Autonomous Vehicles: MMW Radar Backscattering Modeling of Traffic Environment, Vehicular Communication Modeling, and Antenna Designs

by

Xiuzhang Cai

A dissertation submitted in partial fulfillment
of the requirements for the degree of
Doctor of Philosophy
(Electrical and Computer Engineering)
in the University of Michigan
2020

Doctoral Committee:

Professor Kamal Sarabandi, Chair
Professor Anthony Grbic
Professor Huei Peng
Professor Fawwaz Ulaby

Xiuzhang Cai

caixz@umich.edu

ORCID iD: 0000-0003-1314-1892

Dedication

To my daughter Sophie and my wife Qianying.

Acknowledgements

The completion of this thesis could not be possible without the help and support from so many people. First of all, I want to express my sincere thanks to my research advisor, Professor Kamal Sarabandi. His endless passion and curiosity for science and knowledge are so contiguous and is the first reason for me to pursue a Ph.D. degree. I want to thank him for his always patient and inspiring guidance on not only my research but also the philosophy for a Doctor of Philosophy: envision the big picture, remain critical thinking on the details and always find the beauty in your work. Besides the work, he is also a great friend and gave me many valuable advices that I can benefit for my entire life.

I would like to thank Professor Fawwaz Ulaby, Professor Anthony Grbic and Professor Huei Peng for being my dissertation committee members and giving me many constructive advices to improve my dissertation. I would also like to thank the University of Michigan, the EECS department and many other extraordinary professors including Professor Eric Michielssen, Professor Amir Mortazawi, Professor Leung Tsang, Professor Mark Kushner and etc. to offer excellent classes for me to build a solid foundation of knowledge and to broaden my horizons on different disciplines.

I would like to thank the current and previous members in Radlab that I worked with. I want to express my special thanks to Michael Giallorenzo for being my research partner in many radar measurements, Dr. Adib Nashashibi for his constant help in lab work, Dr. Jiangfeng Wu for his help in my early Ph.D. study, Dr. Shurun Tan and Jiyue Zhu for the insightful discussion, Dr. Chong Han for many constructive advices and collaboration. I am also grateful to all other

colleagues and friends in Radlab whose names may not all be mentioned. I want to thank Dr. Mani Kashanianfard, Dr. Armin Jam, Dr. Amr Ibrahim, Dr. Jihun Choi, Dr. Mohammad Amjadi, Dr. Behzad Yektakhah, Dr. Gurkan Gok, Dr. Yang Liu, Dr. Han Guo, Dr. Weitian Sheng, Dr. Abdulkadir C. Yucel, Dr. Tai Qiao, Dr. Huangting Huang, Dr. Shuo Huang, Dr. Nikolaos Chiotellis, Dr. Shiyu Luo, Dr. Changjiang Deng, Dr. Jordan Budbu, Dr. Najme Ebrahimi, Zhe Jian, Michael Benson, Navid Barani, Mostafa Zaky, Menglou Rao, Tanner Douglas, David Geroski, Abdulrahman Alaqeel, Abdelhamid Nasr, Jinkai Wu, Kaleo Roberts, Tianlin Wang, Weihui Gu, Haokui Xu, Zhanni Wu, Chenhui Qu, Brian O. Raeker, Frank Salas, Luke Szymanski, Cody Scarborough and many others.

I want to acknowledge Ford Motor Company as the sponsor of my research project for financial supporting me to fulfill many works in this thesis. I would like to thank Dr. Douglas Blue and Marc Klinger from Ford Motor Company for constantly providing feedbacks and requirements to my research projects, which gives me confidence on the direction we are working on and improves the quality of this dissertation. I want to also thank Dr. Bruno Camps-Raga and Praveen Nair from Aptiv PLC for collaboration in some of my thesis work.

Last but most important, I would like to express my gratitude to my family. I wouldn’t achieve anything without the support and love from my parents Shugui Cai and Jinzhu Lai. I also want to thank my mother-in-law Dafen Peng for taking care of my daughter, my wife and me in this special period of time. My ordinary language cannot express all my appreciation to my wife Qianying Zeng. Qianying, meeting you is the best thing happening to my life, and I am really grateful for your unconditional support and love, for the happiness you brought to me and for the great sacrifices you have done for me. In the end, I would like to dedicate this dissertation to my

newborn daughter Sophie. Sophie, you give me the strength and faith to be a better person, and to fight for a better world.

Xiuzhang Cai

Summer, 2020

Table of Contents

List of Tables

List of Figures

Abstract

77 GHz Millimeter-wave (mmWave) radar serves as an essential component among many sensors required for autonomous navigation. High-fidelity simulation is indispensable for nowadays' development of advanced automotive radar systems because radar simulation can accelerate the design and testing process and help people to better understand and process the radar data. The main challenge in automotive radar simulation is to simulate the complex scattering behavior of various targets in real time, which is required for sensor fusion with other sensory simulation, e.g. optical image simulation.

In this thesis, an asymptotic method based on a fast-wideband physical optics (PO) calculation is developed and applied to get high fidelity radar response of traffic scenes and generate the corresponding radar images from traffic targets. The targets include pedestrians, vehicles, and other stationary targets. To further accelerate the simulation into real time, a physics-based statistical approach is developed. The RCS of targets are fit into statistical distributions, and then the statistical parameters are summarized as functions of range and aspect angles, and other attributes of the targets. For advanced radar with multiple transmitters and receivers, pixelated-scatterer statistical RCS models are developed to represent objects as extend targets and relax the requirement for far-field condition. A real-time radar scene simulation software, which will be referred to as Michigan Automotive Radar Scene Simulator (MARSS), based on the statistical models are developed and integrated with a physical 3D scene generation software (Unreal Engine

4). One of the major challenges in radar signal processing is to detect the angle of arrival (AOA) of multiple targets. A new analytic multiple-sources AOA estimation algorithm that outperforms many well-known AOA estimation algorithms is developed and verified by experiments. Moreover, the statistical parameters of RCS from targets and radar images are used in target classification approaches based on machine learning methods.

In realistic road traffic environment, foliage is commonly encountered that can potentially block the line-of-sight link. In the second part of the thesis, a non-line-of-sight (NLoS) vehicular propagation channel model for tree trunks at two vehicular communication bands (5.9 GHz and 60 GHz) is proposed. Both near-field and far-field scattering models from tree trunk are developed based on modal expansion and surface current integral method. To make the results fast accessible and retractable, a macro model based on artificial neural network (ANN) is proposed to fit the path loss calculated from the complex electromagnetics (EM) based methods.

In the third part of the thesis, two broadband (bandwidth > 50%) omnidirectional antenna designs are discussed to enable polarization diversity for next generation communication system. The first design is a compact horizontally polarized (HP) antenna, which contains four folded dipole radiators and utilizing their mutual coupling to enhance the bandwidth. The second one is a circularly polarized (CP) antenna. It is composed of one ultra-wide-band (UWB) monopole, the compact HP antenna and a dedicatedly designed asymmetric power divider based feeding network. It has about 53% overlapping bandwidth for both impedance and axial ratio with peak RHCP gain of 0.9 dBi.

Chapter 1 Introduction

1.1 Motivation

Autonomous vehicle, a concept often seen in Sci-Fi films is coming to reality brought by the integration of many advanced technologies including sensors, control, communication and artificial intelligence. This topic of research is of importance to automotive industry, academia and policy makers as it is believed to benefit the society in many aspects including improving the road safety, relieving traffic congestion and parking problem, reducing the transportation cost and providing more mobility for young, old and disabled people [1]. Unlike many other technological innovations in this information era including computer, internet, cell phone and smart home devices, the failure or malfunction for autonomous vehicle is unacceptable since the mistake or failure of autonomous car may lead to injury or even death. Thus, before an autonomous car can be offered to the market, the autonomous vehicle's performance is required to be tested for almost all traffic scenarios. In fact, millions of miles of road test is required for the autonomous car as an established standard by many well-known companies including Google/Waymo, Tesla, GM/Cruise, Ford, and etc. [2]. Sensors including radar, camera and Lidar must satisfy the requirements of performance and reliability in the road test as well.

Sensors of the autonomous vehicle detect the environment and generate data to represent the surroundings. Among the three commonly seen sensors, camera and Lidar can provide higher resolution images than radar, but radar has the advantages of low cost and target range and speed measurement capability [3]. Radar has been installed on vehicles for decades. In the middle 1970s,

many automobile manufacturers like AEG-Telefumkenl/Bosch, Daimler-Benz/SEL and Lucas start to put radars on their products [4], and their main purpose was for collision warning/avoidance [5]. Advanced radars with beam-steering capabilities by either mechanical or digital beam-forming technique are also developed to produce radar images [6]-[9]. The radar images can be used in target recognition by itself or fused with the data obtained from other sensors for autonomous vehicle.

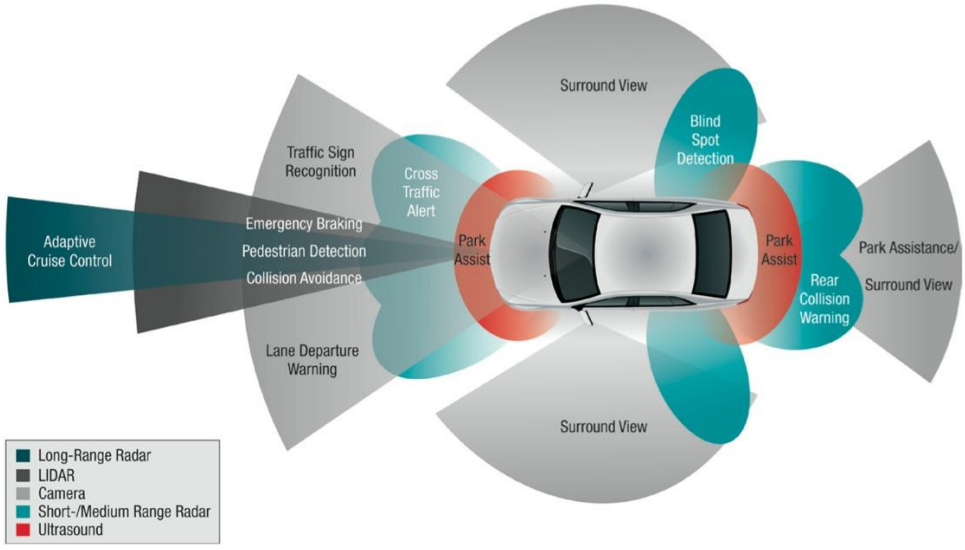

Figure 1.1. Sensors distribution for a typical autonomous car [12]

Automotive radars nowadays are regulated to mainly operate on two different bands: 24 GHz and 77 GHz [7]. Among them, 77 GHz is more popular due to its potential higher resolution and smaller antenna dimensions. The 77 GHz millimeter wave (mmWave) band can be further divided into two bands: one from 76 GHz to 77 GHz is mainly used for long-range or medium-range radar, and the other from 77 GHz to 81 GHz is usually applied by short-range radar [10]. The long-range mmWave radar is usually placed on the front of the car and the short-range radar could be on front, side or the back of the vehicle as is shown in Figure 1.1. The long-range radar has narrow beamwidth and is preferred beam-steering capabilities. The short-range radars have wide beamwidth for broad coverage, and wide bandwidth for accurate range resolution. They are

mainly used for collision detection/avoidance. The worldwide market size for automotive radar is 4.7 billion dollars in 2018 and is expected to grow to 7.9 billion dollars in 2021 [11]. The growth of market demanding accelerate the emergence of advanced radar system with better performance.

During the continuous measurements in road test, it is difficult to compare the ground truth with measured data to evaluate the performance especially for the radar. The traffic scenes are usually complex and dynamic systems, and the ground truth information can hardly be monitored accurately and thoroughly. On the other hand, high-fidelity simulations are not only costing much less money and time, but also can provide all ground truths of the surroundings of the car. Besides, it can easily repeat scenes for more careful examinations about some important scenarios that rare occur in real life, e.g. traffic accidents. Moreover, radar simulation is more demanding than camera and Lidar since the data acquired by camera and Lidar are purely images and easier to be recognized by human, the corresponding targets can be more clearly identified and labeled manually for supervised learning. By contrast, the physical behaviors of radar signals are more complicated, counterintuitive and need more effort to be compared with ground truth. Therefore, simulations for radar response are more challenging and very valuable for autonomous car research.

Besides the automotive radar, another emerging application of mmWave technology in autonomous vehicle is the mmWave vehicular communication. The vehicular communication includes vehicle-to-vehicle (V2V), vehicle-to-infrastructure (V2I) and vehicle-to-everything (V2X) communication systems [13]. In vehicular communication, one vehicle is linked to other vehicles or infrastructure, the shared information may be for the safety or entertainment / working purpose. Information like accidents, road and weather condition, speed-warning message or sensory data from other vehicles are useful in improving the safety and comfort of passengers in the vehicle [14]. A wireless network in vehicles and infrastructures can also be applied in the intelligent

transportation system. The system is designed to provide higher level of security and convenience for vehicles and pedestrians, for example, it may coordinate the vehicles in changing lanes or choosing routes [14] [15]. A standard IEEE 802.11p has been assigned for vehicular communication with frequency band at 5.9 GHz and 75MHz bandwidth [15]. For autonomous vehicles' communication, the demand in data rate could be hundreds of Mb/s to several Gb/s in sensory sharing system or video streaming [13], which drive the spectrum selection to mmWave range to achieve wider bandwidth. The potential mmWave (30-300 GHz) bands could be used in vehicular communication are unlicensed 60 GHz band, 5G band at 28 GHz and 38 GHz, and automotive radar bands (24 GHz and 77 GHz) [16]. The 60 GHz band is most promising in vehicular communication since it has the least interference with other communication / radar systems, and its 7 GHz bandwidth from 57 to 64 GHz is largest among all the bands [16][17]. The drawback of 60 GHz is the high signal attenuation in air due to the oxygen absorption with attenuation rate ranges from 7 to 15.5 dB/km [16], thus it is only suitable for short range communication system. Nevertheless most links in vehicular communication is in short range so it is still a good candidate band.

1.2 MMW automotive radar response simulation and signal processing

Figure 1.2. Simplified block diagram of FMCW radar signals in (a) time domain and (b) frequency domain

Radar can detect the range, speed, angle of arrival and radar cross section (RCS) of the targets. The simulation or signal processing for detecting range and speed has been well studied [18]-[22]. Depending on the type of radar, different mechanisms are utilized to detect range and speed. Frequency modulated continuous wave (FMCW) radar is the most popular type in automotive radar application due to its fast response time, low cost and low power consumption. The simplified block diagram of FMCW radar is shown in Figure 1.2 (a). Transmitter will generate frequency modulated signals and send EM wave signals out by antennas, then the signals get reflected by targets and captured by receivers. For FMCW radar, the received signals are mixed with transmitted signals by a frequency mixer, and by examining the spectrum domain of the IF signal, one can extract the range and speed information of targets. The same process in frequency domain is depicted in Figure 1.2 (b). The procedure that wave propagating in air and scattered back to receiver can be treated as a system $G(f)$, and the received signal $S_r(f) = S_t(f) \cdot G(f)$. The mixed signal in IF band is the convolution of the two signals in frequency domain.

Simulation for the RCS of targets, i.e. the frequency response of the system $G(f)$ is more complicated than signal processing simulation as RCS simulation relies on deep understanding of the electromagnetic (EM) scattering phenomenon from all types of targets. Typical traffic targets are electrically large, for example, a 1.8 m tall pedestrian is more than 400 wavelengths at 77 GHz, which makes it almost computationally impossible to be simulated by full-wave simulation methods like method of moment (MoM) [23], finite element method (FEM) [24] and finite-difference time-domain method (FDTD) [25]. There are many high-frequency asymptotic methods for electrically large problems, including physical optics method (PO) [26]-[28], geometric optics (GO) or ray-tracing based shooting and bouncing rays method (SBR) [29] [30], and uniform geometric theory of diffraction (UTD) [31] [32]. Each of them has its own advantages and best

applicable scenarios. PO calculates scattered field from integral of equivalent surface current, and it is accurate for convex surface whose radii of curvature is much larger than the wavelength, but it is inefficient in calculating multi-scattering or higher order solutions. SBR treats EM wave propagation as light, and on boundary the wave gets reflected and/or refracted with GO rule. It can solve the multi-scattering problem so usually it is applied for concave geometry like cavities. UTD includes the diffraction field that neglected in GO solution and make it more accurate for edge or vertices scattering problem.

Another type of targets for automotive radar is distributed targets, i.e., the road surface. The road surface condition includes material, roughness, debris or pothole, weather related conditions like wet, icy or snowy. Correct recognition of road surface condition is important for driving safety especially in severe weather such as heavy rain, snow. Some researches use the speed sensor, GPS and/or accelerometer to detect the slip or friction coefficient between tire and road to identify the road conditions [33]-[35]. The drawback of such detection is that it could only detect the road condition under the vehicle with ignorance of the condition of front road, which cause potential danger to the autonomous vehicle as it may be too late to react for terrible or slippery road condition. The usage of optical sensors and cameras in recognition of the front road condition are reported in literatures as well [36] [37]. Compared to radar, optical sensor or camera has higher resolution and more sensitive to the change of roughness, but they are also more severely affected by weather conditions. Some radar measurements are reported for various road conditions at 24 GHz [38] and 94 GHz [39]. They show promising results in using radar to identify different road conditions. For mmWave radar, the backscattering from road surface are contributed by two parts: the surface scattering and volumetric scattering as described in Figure 1.3. The volumetric scattering from road surface is very difficult to evaluate numerically. Because first the

distribution of permittivity of the ingredients in the road is unknown and varies from different types of road. Second, the dimensions the ingredients could be smaller or larger than wavelength in mmWave range so asymptotic methods may fail for this problem, besides full-wave methods requires too many computational resources that normal computers can acquire to accurately evaluate such problem.

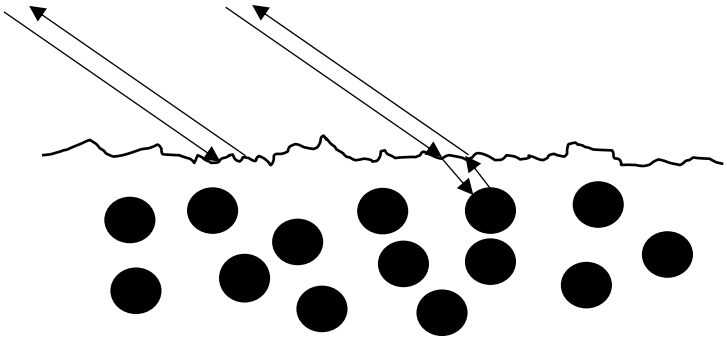

Figure 1.3. mmWave Backscattering from road can be divided into two parts: from rough surface and inhomogeneous medium of road

In standard FMCW radar signal processing, during one chirp period of the FMCW radar, the frequency of the signal sent by FMCW radar is monotonic with time. For stationary targets, by taking Fourier transform (FT) of the mixed signal in time domain, one can obtain the frequency difference between received signal and transmitted signal, which is corresponding to the time difference between the two signals and the range information of targets [18]. If the target is moving relative to radar, the phase of the mixed signal contains a Doppler shifting term varying from chirp to chirp, by applying second FT, the speed information can be revealed [19][20]. To obtain the angle of arrival (AOA) or direction of arrival (DOA) information from targets, a straight forward solution is to scan its main beam either by mechanical scanning or digital beamforming through antenna array or MIMO array [21][22]. If the targets with the same range and Doppler bin are sparse, super-resolution AOA estimation algorithms for multiple sources can be applied to identify

the AOA with resolution much smaller than the beam width. There are many known AOA estimation algorithms such as subspace methods MUSIC [40][41], ESPRIT [42] and optimization approach maximum likelihood method [43]. In subspace methods, the essential idea is to obtain the correlation matrix of the signals, which requires at least M snapshot to have good performance, where M is the number of channels. However, in automotive radar application, a single snapshot AOA estimation is desired as vehicles could move very fast and different snapshots may be corresponding to different AOA. Maximum likelihood method is applicable but the computational complexity increases dramatically with the number of targets. Therefore, to support the real-time signal processing for highly dynamic systems like autonomous vehicles, a more efficient AOA estimation algorithm based on small number of or even single snapshot is needed.

The RCS information of target are useful not only in high-fidelity radar simulations, but also in target identification and classification. Radar has the ability of detecting target in further range than camera or Lidar, and target in far range can be considered as point target. Because of the complex geometry of traffic targets, the RCS usually fluctuates a lot as a function of frequency or aspect angles, however, statistically the RCS of different types of targets are distinct and the RCS of same types could be similar. For example, the RCS difference between an adult and a kid should be much smaller than that between an adult and a car. Some studies on target identification by Radar are based on the range or Doppler information [44] [45]. This thesis is focusing on classifying targets based on their RCS information.

1.3 MMW propagation model for vehicular communication

Wireless communication in real life often suffers from non-line-of-sight (NLoS) propagation issues like multipath or signal blockage. In mmWave band, such problem is more significant as obstacles are electrically larger for shorter wavelength and therefore can scatter and

block signals more severely. The obstacles in typical traffic scene include vehicles, buildings, pedestrians and cylindrical shape objects like tree trunk, lamp post, traffic light post, and etc. The complexity of traffic scene makes it very difficult to simulate the mmWave wave propagation in such environment, and many researchers are trying to characterize the mmWave propagation channel model by measurements [46]-[48]. Those linear or exponential models for the pathloss given in those literatures are simple and easy to use, but the variation of the measured data is significantly high among different locations with the same range, which indicates limited accuracy when applied to other scenarios. Compare to modeling the pathloss for the entire traffic scene, it will be easier and more accurate to model the pathloss for specific types of obstacles. The path loss due to NLoS propagation through vehicles and pedestrians in mmWave range are characterized by measurements in literatures [49]-[51]. They show rapidly changing in pathloss with small disturbance to the system, e.g. movement of vehicles or pedestrians. Because of the complexity of the wave scattering phenomenon, the pathloss is fitted into linear or exponential function of distance.

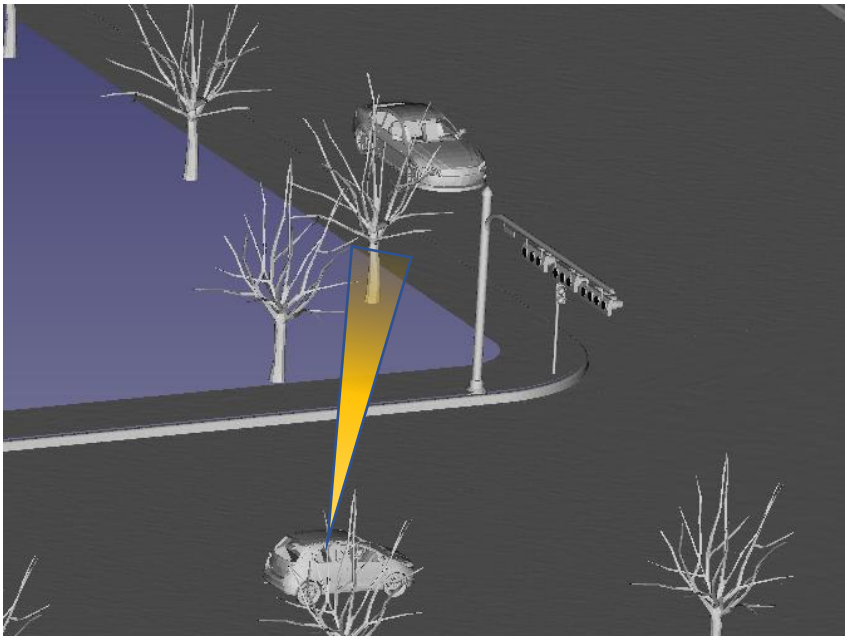

Figure 1.4. Illustration of NLoS propagation in V2V scenario

1.4 Broadband Omnidirectional antenna design

Omnidirectional antenna is favorable in many wireless communication applications since it can have largest signal coverage. With MIMO or synthetic aperture radar (SAR) techniques, high gain antenna pattern with beam-steering ability can be achieved by combining many omnidirectional antennas. Besides, broadband feature can enhance the data rate in communication and improve the resolution in radar system. Therefore, it is also desired in the vehicular communication and 5G communications, and in advanced radar system [54].

Dipole and monopole antennas are the most commonly seen omnidirectional antennas and have been widely used in many types of communication systems like cellular base station, Wi-Fi router, and radios. The usage of such antennas has a long history and can be traced back to 1887 by Heinrich Hertz [55]. Those antennas usually have simple structure and easily achieve small gain variance in azimuth direction, and high radiation efficiency. Since more than a decade ago, several wideband or ultra-wideband (UWB) monopole or dipole antennas have been reported [56][57][58]. Compared to traditional linear wire antennas, these antennas have large dimension in azimuth directions, therefore can form multipole resonances for the current. They can reach more than 100% impedance bandwidth.

A dipole or monopole antenna is vertically polarized (VP) and has an omnidirectional radiational pattern. For better communication systems and polarimetric radar where polarization diversity is considered, horizontally polarized (HP) omnidirectional antenna is required. Ideally small loop antenna can be treated as magnetic dipole and thus provide HP omnidirectional radiation pattern [55], but because of its small impedance, small loop antenna has poor radiation efficiency and extreme narrow bandwidth. One way to overcome those issues is to increase the

size of loop antenna. Some modified large loop antennas are reported to generate HP omnidirectional patterns [59]-[63], but still they all have limited bandwidth (<30%). To achieve wider bandwidth, many designs utilize square array geometry with four wideband horizontally polarized elements [64]-[66]. These antennas are reported to have bandwidth of 30%~41%. To further increase the bandwidth, one design employs 8-element array with octagonal shape [67]. It has about 62.5% bandwidth, however, its dimension is quite large (~0.79λ×0.79λ, λ is the wavelength for lowest operating frequency) and the gain variation is more than 3 dB in azimuth direction.

In addition to linear polarization like VP and HP, another popular polarization in use is circular polarization (CP). CP wave has the property that the polarization of E field keeps rotating with time and distance from the antenna, therefore CP wave is insensitive to the orientation of transmitter's or receiver's antenna and has been widely used in satellite communication where ionosphere may alter the polarization of EM wave. Besides, the first reflection of CP wave from surfaces generates cross-polarization CP wave, i.e., if original CP wave is right-handed CP (RHCP), the reflected wave is left-handed CP (LHCP). This feature will benefit the communication system with less multipath impact as in many cases the strongest multipath effect is from the first order [68]. For radar system, CP antenna can largely reduce the crosstalk between transmitter and receiver and enhance the performance of radar imaging [54]. Hence, CP antennas have the potential to be applied in more advanced communication and radar systems.

Several omnidirectional CP antennas have been reported in the literature [69]-[79]. In some omnidirectional CP dielectric resonator antenna (DRA) design [69] [70], CP is created by adding parasitic slots [69] or dielectric wave polarizer [70] around an omnidirectional vertically polarized (VP) DRA. In such way the radiated VP fields are converted into CP fields. The DRA

using parasitic slots has usable bandwidth (overlapping of both axial ratio (AR) and impedance bandwidth) of 22% and the other design produces a conical radiation pattern with usable bandwidth of 41%. Another omnidirectional CP antenna based on circular TE_{21} modes is reported in [71]. The antenna combines two orthogonal TE_{21} modes and forms a 16-element circular array to create omnidirectional CP. Besides, it utilizes low-pass/high-pass phase shifter to create wideband phase shifting for enhancing the bandwidth. This antenna has an effective bandwidth of 58%, but due to the return loss and resistive loss in feeding network, the lowest efficiency is only about 63%.

Circular polarized EM field can be implemented by the superposition of two perpendicular linear polarized fields with same magnitude and 90° phase difference. The 90° phase difference is often achieved by the electrical length difference between the vertically polarized (VP) and horizontally polarized (HP) fields either in feeding or radiating stage. This setup has been successfully implemented in many omnidirectional CP antennas [72]-[79]. When a circular patch antenna or DRA is feed at the center of the circle, TM modes can be excited to radiate VP fields, and the HP fields are generated by several rotationally symmetric monopole or dipole like radiators around the antenna [72]-[77]. Besides this type of CP antennas, a CP Antenna composed of four inverted L-shape monopoles is reported in [78], and the VP and HP fields are generated by the horizontal and vertical part of the bended monopoles. For another compact omnidirectional CP antenna in [79], a slot antenna with fourfold parallel plate waveguide is designed to produce omnidirectional HP field, and VP field is excited by two PIFA antennas on the sides of the slot antenna. The antennas reported above have good omnidirectional CP property, but most have limited bandwidth (<10%). One idea to increase the bandwidth is to create multipole resonances with different exciting modes. The usable bandwidth is increased to 14.4% [74] and 51.7% [75],

however, these two antennas have a conical radiation pattern and doesn't generate CP field in horizontal plane. Recently, a wideband central-feed CP patch antenna is proposed [77]. Due to the symmetry of ground plane and antenna, this antenna's main beam is on azimuth plane, and it utilizes capacitive feed instead of direct feed to increase the bandwidth to about 30%.

1.5 Dissertation Overview

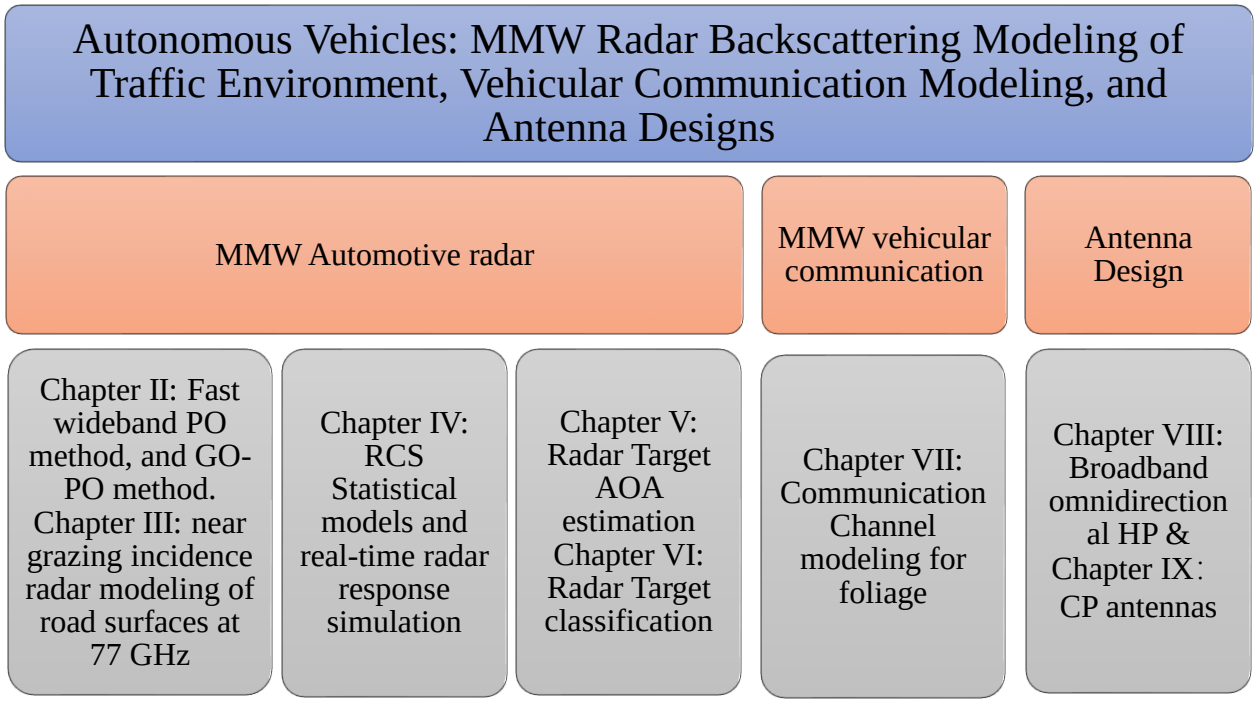

Figure 1.5. Overview of Thesis

Chapter 2: Fast wideband PO method, and GO-PO method

Most targets in traffic scene like pedestrians, vehicles, tree trunks have convex geometry with large radii of curvature of the surface compared to the wavelength (~ 4 mm), therefore physical optics (PO) method is suitable to be applied here. In Chapter II, a novel fast wideband PO method will be discussed. Traditional PO method is only for single frequency, and to get the response for a wide band, all calculations are needed to repeat for different frequencies. In this

modified PO method, the phase term of far-field scattering E field, which is the only part changing rapidly with frequency, is separated from the total expression to be evaluated for all frequencies. Other calculation and the rest parts of the expression remain almost constant within the band and thus they only need to be computed once.

For concave geometry that higher order solutions cannot be neglected, the PO method is combined with GO ray tracing technique to compute the higher order solutions more efficiently. The GO-PO method employs KD-tree data structure and adaptive rays' refinement for fast computation. The developed numerical methods are then applied for simulating RCS for different traffic targets with a typical antenna pattern for automotive radar.

Chapter 3: Near grazing incidence radar modeling of road surfaces at 77 GHz

The backscattering from roads in mmWave range can be divided into two parts: surface scattering and volumetric scattering. Compared to volumetric scattering, surface scattering problem has less unknowns and can be solved by full-wave methods thanks to the recently emerging high-performance computing (HPC) technology. In this chapter, simulation for surface backscattering coefficients from random rough surfaces are presented. The simulation is conducted in commercial simulation software AnsysEM (HFSS) with FEM method. In the simulation, the random rough surface is generated with exponential correlation function and about $5\lambda \times 5\lambda$ dimensions, and then simulated with periodic boundary conditions on the four sides and impedance boundary in the bottom. After many Monte Carlo simulations, the polarimetric backscattering coefficients (RCS per unit area) are modeled as functions of incident angles, permittivity of road and surface roughness. In order to find the volumetric scattering component for road surfaces, measurements are taken, and the volumetric scattering is analyzed based on radiative transfer (RT) method [39].

Chapter 4: Statistical models and real-time radar response simulation

RCS of complex traffic targets is highly fluctuating with frequency, aspect angle and range. The traffic targets include but are not limited to pedestrians with different genders, heights and weights, various types of vehicles, stationary targets and animals. To characterize the pattern of RCS behind its random nature, we utilize statistical approach. The RCS data for a small range of aspect angles (±5°) and all frequency points are treated as independent samples and then fitted into given distribution. The parameters of the probability density function (PDF) of certain distribution then are modeled as functions of range and aspect angle, for pedestrians those parameters are further modeled as functions of action, gender, weight and height. For radar with small angular resolution and able to scan its main beam, 2D range-angle image can be generated for different targets. The neighboring pixels may not be independent random variables, and they can be considered as correlated random variables with multivariate distribution. With these statistical models for various targets, we can generate traffic scene RCS simulation in almost real time. In this thesis, such real-time simulation is implemented in a 3D simulation software Unreal Engine 4 with C++, the simulation can achieve more than 10 fps just in an ordinary PC.

Chapter 5: A Fast Analytic Multiple-Sources Radar Targets AOA estimation Algorithm

Traditionally, the angle of arrival (AOA) estimation problem for multiple sources is considered as a nonlinear problem with no analytic solutions. In this chapter, an analytic iterative multiple-source AOA algorithm (AIMA) is presented for fast and accurate estimation of the AOA. The approach is most useful for automotive MIMO radars where there can be a large number of scatterers in the scene. The AOA estimation problem is divided into two main tasks: (1) estimate one AOA with the prior knowledge of all other AOA; (2) estimate all AOA by iteratively solving Task 1. It can be shown that for a uniform linear array (ULA) Task 1 has analytic solutions and

Task 2 converges very fast, which makes this method effective, efficient and practical for real-time processing. Unlike many other AOA estimation methods, this approach doesn't need the information about the number of sources and can be applied for coherent signals and single snapshot as well.

Chapter 6: Machine Learning-Based Target Classification for MMW Radar in Autonomous Driving

As a result of recent development of artificial intelligence technology, many excellent machine learning software/libraries include Caffe [80], TensorFlow [81], and Matlab are available for researchers and publics. Those frameworks have good performance and efficiency and are easy to use for non-expert in machine learning. In this chapter, a machine learning based radar target classification is presented. Different forms of radar data are considered for target classification based on the type of radar and applicable scenario: when targets are in middle or far range (>50m), the targets may be treated as point targets, the statistical features of the RCS and the range-distributed RCS are used in classification. If the targets are in near range and the radar has the beam-steering ability, radar images in range-azimuth angle domain or in 3D (x-y-z) domain are considered in target classification. Statistical features of RCS and time domain RCS are classified by supervised learning approach artificial neural network (ANN) and the radar images are classified by deep learning approach convolutional neural network (CNN). The traffic targets are divided into three major categories: pedestrians, vehicles and stationary targets. In particular, the targets include but are not limited to pedestrians with different poses, genders, heights and weight, vehicles like bike, motorcycle, sedan, SUV, trucks, buses, and stationary objects like signs, lamp posts, tree, bus stops etc., and animals like dog, deer, horse, etc. It is shown that good performance

(~90% accuracy) can be achieved for this classification approach in both scenarios with the gigantic dataset we generated for such targets.

Chapter 7: Communication Channel Modeling for Foliage

Foliage is commonly encountered in traffic scene and is possible to block the LoS wave propagation as well, and for V2V scenario, the main component of foliage blocking signals is the tree trunk. The tree trunk can be approximated as dielectric cylinders, and the far-field scattering from circular cylinder has been well studied [52][53]. For mmWave vehicular communication, the vehicles are most likely to be in near-field range of tree trunk, and discussion on such case is hardly found in literature. In Chapter VII, a thorough analysis on the mmWave scattering from tree trunk in both near field and far field is performed. To make the model accessible for people not familiar with EM theory and convenient usage, the path loss model is further fitted by artificial neural network (ANN) as function of distance from transmitter to trunk, distance from receiver to trunk, azimuth angle, trunk's radius and height. Besides, a multiple scattering model for tree trunks based on the infinite-long cylinders approximation is developed for the V2V communication channel model in the forest environment. Massive Monte-Carlo simulations have been conducted and generalized into a reduced path loss model for easy usage.

Chapter 8: A Compact Broadband Horizontally Polarized Omnidirectional Antenna using Planar Folded Dipole Elements

In this chapter, two broadband omnidirectional antenna designs are developed. First one is a broadband omnidirectional HP antenna. It is composed of four modified folded dipole antennas arranged around the perimeter of a small square box. The antenna presents a smaller form factor compared to other wideband HP omnidirectional antennas (size of $0.34\lambda \times 0.34\lambda$), while maintain

a relatively low gain variation as a function of azimuth angle in the band of operation. The folded dipole antenna is chosen since it is reported to have a fractional bandwidth that can exceed 50%. One of the main issues of such array geometry is the mutual coupling between different dipole elements will degrade the performance of antenna, to compensate for the mutual coupling of different dipole elements and increase the bandwidth, the geometry of the antenna is carefully Optimized. Four modified folded dipole elements are fed with microstrip baluns and connected by an appropriate matching network to a coaxial feed. The matching network, the baluns, and the geometrical modification of the elements are codesigned to mitigate the mutual coupling effects and achieve the required bandwidth while minimizing the antenna array dimension. Their distances are carefully chosen to achieve best omnidirectional property.

Chapter 9: Broadband Omnidirectional Circularly Polarized Antenna with Asymmetric Power Divider

Another design is broadband CP antenna. For an omnidirectional CP antenna based on VP and HP radiators, the challenges of broad bandwidth (>50%) include broad impedance bandwidth for both VP and HP radiators, maintaining omnidirectional pattern within the band, and maintaining small magnitude difference and 90º phase difference between VP and HP fields for all operating frequencies. In this design, divide-and-conquer strategy is used in achieving a broadband omnidirectional CP antenna. We first design an ultra-wide band (UWB) monopole antenna and broadband HP antenna which can meet the requirement for impedance bandwidth and almost constant radiation pattern. Since their gain difference are not constant but a function of frequency, then a dedicated optimized asymmetric power divider with wideband phase shifter is proposed to compensate the irregular gain difference between VP and HP as a function of frequency and maintain almost 90º phase difference over the entire band. A systematic analysis

for asymmetric power divider is performed as well. The main beam for the proposed antenna is on azimuth plane and the usable bandwidth reaches 53.4%.

Chapter 2 Fast Wideband PO Method, and GO-PO Method

2.1 Introduction

Automotive radar is of the critical sensors for the autonomous cars nowadays and is expected to be in the future. However, because of the complex nature of electromagnetic scattering from traffic targets, the full potential of automotive radar has not been fully investigated yet. To understand the radar signals comprehensively, one should first understand the EM scattering phenomenon. Compare to measurements, simulation is far more convenient, lower cost and more flexible.

One of the major challenges in radar simulation is to the complexity and heterogeneity involved complicated targets. Theoretically, the electromagnetic wave scattering, and propagation can be accurately described by numerical methods based on Maxwell's equations. Depending on the form of Maxwell's equations (e.g. integral or differential equations), different numerical methods such as method of moment (MoM), finite element method (FEM) and finite-difference time-domain method (FDTD) are developed. However, these so called full-wave methods are prohibitively inefficient for electrically large objects. With proper approximations for the wave propagation and boundary conditions at high frequencies where the typical dimensions of the objects are large compared to the wavelength, there exist many asymptotic methods. These methods include physical optics method (PO), geometric optics method (GO) and uniform geometric theory of diffraction (UTD) which can provide excellent computational efficiency and

reasonable accuracy to many scattering problems. In this thesis, we focus on PO, GO and hybrid of GO-PO for higher order solutions.

2.2 Wideband Physical Optics method

2.2.1 EM scattering formulation using PO method

Scattered fields calculated based on PO method are obtained from approximate surface electric (for metallic objects) or electric and magnetic (for dielectric objects) currents using far field approximation of Huygens principle [83]. The scattered electric field can be computed from:

$$\vec{E}_s = \frac{ik_0 e^{i\vec{k}_s\cdot\vec{r}}}{4\pi r}\left(\bar{\bar{I}} - \hat{k}_s\hat{k}_s\right)\iint\left[Z_0\vec{J}_s(r') - \hat{k}_s \times \vec{M}_s(r')\right]e^{-i\vec{k}_s\cdot\vec{r'}}ds', \tag{2.1}$$

where k_0 is the wavenumber, $\hat{k}_s$ is the direction of scattering, $\vec{r}$ is the position of observation point, $\bar{\bar{I}}$ is the dyadic idemfactor, Z_0 is the characteristic impedance of free space, and $\vec{J}_s$, $\vec{M}_s$ are the equivalent electric and magnetic surface currents. Because the scattered fields from PO method are derived from Huygens principle, diffraction of EM waves are naturally included in this method. In the full-wave method MoM, the scattered far fields are also calculated by (2.1) and the difference between PO and MoM is in computing the equivalent surface currents. In MoM, the surface currents are obtained by solving integral equations, which is very accurate but computationally inefficient. If the radii of curvature of the target's surface is much larger than the wavelength, the reflected fields (locally) are similar to that of infinitely large plane tangent to the surface. These fields are given by [28],

$$\vec{E}_r = \left[-Z_0\vec{H}_i\cdot\hat{t}R_{TM}\left(\hat{k}_r\times\hat{t}\right) + \vec{E}_i\cdot\hat{t}R_{TE}\hat{t}\right]e^{i\vec{k}_i\cdot\vec{r}}, \tag{2.2}$$

$$\vec{H}_r = 1/Z_0\left[\vec{E}_i\cdot\hat{t}R_{TE}\left(\hat{k}_r\times\hat{t}\right) + Z_0\vec{H}_i\cdot\hat{t}R_{TM}\hat{t}\right]e^{i\vec{k}_i\cdot\vec{r}}, \tag{2.3}$$

where $\vec{E}_i$ and $\vec{H}_i$ are the incident electric and magnetic fields, $\hat{t}$ is the tangential vector on the surface, defined as $\hat{t} = (\vec{k}_i \times \hat{n})/|\vec{k}_i \times \hat{n}|$, $\vec{k}_i$ is the incident direction unit vector, $\hat{n}$ is the normal

vector of the surface, R_{TM} and R_{TE} are the Fresnel reflection coefficient of the surface for TM and TE cases. Then the equivalent surface currents can be simply expressed as:

$$\vec{J}_s = \hat{n} \times \left(\vec{H}_i + \vec{H}_r\right) = \frac{1}{Z_0}\left[Z_0\vec{H}_i \cdot \hat{t}(1 + R_{TM})(\hat{n} \times \hat{t}) + \vec{E}_i \cdot \hat{t}(\hat{n} \cdot \hat{k}_i)(R_{TE} - 1)\hat{t}\right]e^{i\vec{k}_i \cdot \vec{r}}, \quad (2.4)$$

$$\vec{M}_s = -\hat{n} \times \left(\vec{E}_i + \vec{E}_r\right) = \left[Z_0\vec{H}_i \cdot \hat{t}\left(\hat{n} \cdot \hat{k}_i\right)(R_{TM} - 1)\hat{t} - \vec{E}_i \cdot \hat{t}(1 + R_{TE})(\hat{n} \times \hat{t})\right]e^{i\vec{k}_i \cdot \vec{r}}. \quad (2.5)$$

The Fresnel reflection coefficients R_{TM} and R_{TE} are given by,

$$R_{TE} = (\eta_2 cos\theta_1 - \eta_1 cos\theta_2)/(\eta_2 cos\theta_1 + \eta_1 cos\theta_2)\,, \quad (2.6)$$

$$R_{TM} = (\eta_1 cos\theta_1 - \eta_2 cos\theta_2)/(\eta_1 cos\theta_1 + \eta_2 cos\theta_2). \quad (2.7)$$

Where η_1 and η_2 are the characteristic impedance of air and target, θ_1 and θ_2 are the incident and refraction angle with respect to the surface of targets.

The continuous surface of target can be discretized into many small triangular meshes with a CAD software. Each small triangular facet can be assumed to be illuminated by plane wave locally if the radar is in the far field of the facet, and then the equivalent surface currents on a facet can be expressed as:

$$\vec{J}_s(n, \vec{r}\,') = \vec{J}_{sm}(n)e^{i\vec{k}_i \cdot (\vec{r}\,' - \vec{r})}, \quad (2.8)$$

$$\vec{M}_s(n, \vec{r}\,') = \vec{M}_{sm}(n)e^{i\vec{k}_i \cdot (\vec{r}\,' - \vec{r})}. \quad (2.9)$$

Where $\vec{r}\,'$ is a point on the facet n, and $\vec{J}_{sm}(n)$ and $\vec{M}_{sm}(n)$ are constant vectors for all points on facet *n*, which are given by:

$$\vec{J}_{sm}(n) = \frac{1}{Z_0}\left[Z_0\vec{H}_i \cdot \hat{t}(1 + R_{TM})(\hat{n} \times \hat{t}) + \vec{E}_i \cdot \hat{t}(\hat{n} \cdot \hat{k}_i)(R_{TE} - 1)\hat{t}\right], \quad (2.10)$$

$$\vec{M}_{sm}(n) = Z_0\vec{H}_i \cdot \hat{t}\left(\hat{n} \cdot \hat{k}_i\right)(R_{TM} - 1)\hat{t} - \vec{E}_i \cdot \hat{t}(1 + R_{TE})(\hat{n} \times \hat{t}). \quad (2.11)$$

Therefore, for each facet, the equivalent surface currents and scattered E field can be calculated based on (2.1):

$$\vec{E}_{sn} = \frac{ik_0 e^{i(\vec{k}_{sn} - \vec{k}_{in}) \cdot \vec{r}}}{4\pi r_n}\left(\bar{\bar{I}} - \hat{k}_{sn}\hat{k}_{sn}\right)\left[Z_0\vec{J}_{sm}(n) - \hat{k}_{sn} \times \vec{M}_{sm}(n)\right] \iint e^{i(\vec{k}_{in} - \vec{k}_{sn}) \cdot \overrightarrow{r'}} ds', \quad (2.12)$$

Automotive radars are licensed to operate at a wide bandwidth from 76 GHz to 81 GHz. Hence scattering simulations is required over a wide frequency range. Traditionally PO method is used in evaluating scattered field at a single frequency and therefore calculation for wideband is rather time consuming. This is done by applying PO method to a discrete set of frequency points within the band. To expedite this calculation, we notice the scattered field for facet *n* in (2.12) can be divided into multiplication of two parts, the first part $\frac{i}{4\pi r_n}\left(\bar{\bar{I}}-\hat{k}_{sn}\hat{k}_{sn}\right)\left[Z_0\vec{J}_{sm}(n)-\hat{k}_{sn}\times\vec{M}_{sm}(n)\right]$ has almost no dependence on frequency (if the medium of target is dispersive, then this term will change with frequency), and second part $k_0 e^{i(\vec{k}_{sn}-\vec{k}_{in})\cdot\vec{r}}\iint e^{i(\vec{k}_{in}-\vec{k}_{sn})\cdot\overrightarrow{r'}}ds'$ can be highly fluctuating when frequency changes. To more efficiently calculate the wideband scattered field from targets, the first part that has no frequency dependence is evaluated once for all frequency points and the second part is calculated at all frequencies.

The phase integral term in (2.12) integrates the phase $e^{i(\vec{k}_{in}-\vec{k}_{sn})\cdot\overrightarrow{r'}}$ for all points on one polygon facet (usually is triangle), and such integral can be converted into a summation based on the formulation introduced by Gordon [84]. Consider a triangular facet S_n shown in Figure 2.1, with three vertices of it located at $\vec{v}_1$, $\vec{v}_2$ and $\vec{v}_3$ respectively. The unit normal vector to the triangle is denoted by $\hat{n}$, and the incident wave vector is $\vec{k}_{in}$ and the scattered wave vector is $\vec{k}_{sn}$. $\vec{O}'$ is point on the center of the facet, and $\vec{r}'$ is an arbitrary point on the facet.

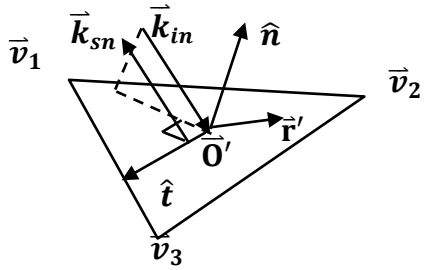

Figure 2.1. Demonstration of phase integral of a triangular facet

Let $\vec{k} = \vec{k}_{in} - \vec{k}_{sn} = \vec{k}_n + \vec{k}_\alpha$, where $\vec{k}_n$ is the component in $\hat{n}$ direction, $\vec{k}_n = (\vec{k} \cdot \hat{n})\hat{n}$, and $\vec{k}_\alpha$ is the component on the surface of the facet. $\hat{t}$ is a tangential unit vector on the surface perpendicular to $\vec{k}$. The integral can be rearranged as:

$$\begin{aligned}\iint e^{i(\vec{k}_{in}-\vec{k}_{sn})\cdot\overrightarrow{r'}} ds' &= e^{i\vec{k}\cdot\vec{O}'} \iint e^{i(\vec{k}_n+\vec{k}_\alpha)\cdot(\vec{r}'-\vec{O}')} ds' = e^{i\vec{k}\cdot\vec{O}'} \iint e^{i\vec{k}_\alpha\cdot(\vec{r}'-\vec{O}')} ds' \\ &= e^{i\vec{k}\cdot\vec{O}'} \iint e^{i\vec{k}_\alpha\cdot(\vec{x}')} dx',\end{aligned} \tag{2.13}$$

where $\vec{x}' = \vec{r}' - \vec{O}'$. Note that $\vec{k}_\alpha \cdot \hat{t} = 0$, we can define $\hat{\alpha}$ such that $\vec{k}_\alpha = k_\alpha\hat{\alpha} + k_t\hat{t}$, where $k_t = 0$, and $\vec{x}' = x_\alpha\hat{\alpha} + x_t\hat{t}$. Then the phase integral becomes,

$$\iint e^{i\vec{k}_\alpha\cdot(\vec{x}')} ds' = \iint e^{ik_\alpha x_\alpha} dx_\alpha dx_t. \tag{2.14}$$

Since $\frac{\mathrm{d}e^{ik_\alpha x_\alpha}}{dx_\alpha} = ik_\alpha e^{ik_\alpha x_\alpha}$, then we have

$$e^{ik_\alpha x_\alpha} = \frac{1}{ik_\alpha}\left(\frac{d(e^{ik_\alpha x_\alpha})}{dx_\alpha}\right), \tag{2.15}$$

$$\iint e^{ik_\alpha x_\alpha} dx_\alpha dx_t = \frac{1}{ik_\alpha} \iint \left(\frac{d(e^{ik_\alpha x_\alpha})}{dx_\alpha}\right) dx_\alpha dx_t. \tag{2.16}$$

Recall the Green's theorem,

$$\oint_{L'} (f_1 dx_\alpha + f_2 dx_t) = \iint \left(\frac{\partial f_2}{\partial x_\alpha} - \frac{\partial f_1}{\partial x_t}\right) dx_\alpha dx_t. \tag{2.17}$$

Let $f_2 = e^{ik_\alpha x_\alpha}$ and $f_1 = 0$, then

$$\frac{1}{ik_\alpha} \iint \left(\frac{d(e^{ik_\alpha x_\alpha})}{dx_\alpha}\right) dx_\alpha dx_t = \frac{1}{ik_\alpha} \oint_{L'} e^{ik_\alpha x_\alpha} dx_t. \tag{2.18}$$

For each triangular facet, the edge vector is defined as:

$$\vec{e}_i = \vec{v}_{i+1} - \vec{v}_i. \quad (i = 1,2,3, \vec{v}_4 = \vec{v}_1) \tag{2.19}$$

$$\vec{x}(l) = \vec{v}_i + l\vec{e}. \quad (0 \le l \le 1) \tag{2.20}$$

Therefore,

$$d\vec{x}(l) = \vec{e}_i \mathrm{d}l, \qquad dx_t = \vec{e}_i \cdot \hat{t}\mathrm{d}l, \qquad x_\alpha = \vec{x}(l) \cdot \hat{\alpha}, \tag{2.21}$$

$$\frac{1}{ik_\alpha}\oint_{L'} e^{ik_\alpha x_\alpha} dx_t = \frac{1}{ik_\alpha}\sum_1^3 \int_0^1 e^{ik_\alpha(\vec{v}_i + l\vec{e}_i)\cdot\hat{\alpha}}\vec{e}\cdot\hat{t}\mathrm{d}l \tag{2.22}$$

$$= \frac{1}{ik_\alpha}\sum_1^3 \vec{e}_i \cdot \hat{t}\frac{e^{ik_\alpha \vec{v}_i\cdot\hat{\alpha}}\left(e^{ik_\alpha \vec{e}_i\cdot\hat{\alpha}} - 1\right)}{ik_\alpha \vec{e}_i \cdot \hat{\alpha}}$$

$$= \frac{1}{ik_\alpha}\sum_1^3 \vec{e}_i \cdot \hat{t}\frac{e^{ik_\alpha(\vec{v}_i + \vec{v}_{i+1})\cdot\hat{\alpha}/2}\sin(\frac{1}{2}k_\alpha \vec{e}_i \cdot \hat{\alpha})}{\frac{1}{2}k_\alpha \vec{e}_i \cdot \hat{\alpha}}$$

Then the phase integral is in summation form:

$$\iint e^{i(\vec{k}_{in} - \vec{k}_{sn})\cdot\overrightarrow{r'}} ds' = e^{i\vec{k}\cdot\vec{0}'}\frac{1}{ik_\alpha}\sum_1^3 \vec{e}_i \cdot \hat{t}\frac{e^{ik_\alpha(\vec{v}_i + \vec{v}_{i+1})\cdot\hat{\alpha}/2}\sin(\frac{1}{2}k_\alpha \vec{e}_i \cdot \hat{\alpha})}{\frac{1}{2}k_\alpha \vec{e}_i \cdot \hat{\alpha}}. \tag{2.23}$$

As is discussed in Section 1.2 the goal of the numerical simulation is to find the radar response of targets $G(f)$, which is defined as $G(f) = S_r(f)/S_t(f)$, where $S_r(f)$ and $S_t(f)$ are the complex signal or voltage at the transmitter and receiver. The relation between $G(f)$ and the scattered E field for one facet in (2.12) is given by,

$$G(f) = \frac{\lambda}{4\pi}\sum_n \frac{E_s^n F_{tn} F_{rn}}{E_i^n R_{tn} R_{rn}} \mathrm{e}^{ik(R_{tn} + R_{rn})}. \tag{2.24}$$

where E_s^n/E_i^n is the scattering coefficient from facet n, F_{tn}, F_{rn} are the transmitter and receiver's antenna's far field at facet n, where $|F_n|^2$ is the corresponding antenna's gain, R_{tn}, R_{rn} are the distance between transmitter, receiver and facet n.

2.2.2 Visibility algorithm

Since PO method assumes the current only exists on lit region of the surface of targets, another challenge for PO method is to decide which part of the surface is lit and which part is shadowed. This is a classical visibility problem in computer graphics or computer geometry, and one of the most efficient algorithm is called z-buffering or depth-buffering algorithm [85][86]. The z-buffering algorithm can be simply described as following:

Table 2 - 1. Z-buffering Algorithm

Algorithm: Z-buffering

1. **Rotate the coordinate such that the direction of radar view is along z axis**
2. **In x-y plane of new coordinate, divide the entire region occupied by the targets into n by m equal size rectangular sub-regions R_{mn}, and initialize all $R_{mn} \rightarrow \emptyset$**
3. For each **facet of target f_i**
   If **f_i overlap with R_{mn}** then
   $R_{mn} \rightarrow \{R_{mn}, i\}$
4. **Initialize all facets as lit facets, i.e. $L_i \rightarrow$ true**
5. For each **facet of target f_i, find the sub-region R_{mn} contains the center of f_i, denotes as O_i**
   For each **f_j overlapped with R_{mn} but $j \neq i$**
   If **a ray from radar to O_i is blocked by f_j,** then
   $L_i \rightarrow$ false

Notice in the algorithm the way to determine whether a ray from radar to the center of one facet O_i is blocked by a second facet is to first exam whether the projection of the point in x-y plane is within the triangular projection of the second facet, and if so, then compare the z value of the intersect point on the second facet with O_{iz}. If O_{iz} is larger, then the first facet is shaded by the second facet.

2.3 GO-PO method for multi-scattering problem

For target with convex geometry where multiple scattering is insignificant, and the scattered field calculated by the first order PO solution dominates. If the target has concave component, then the multi-scattering effects cannot be ignored. In this case higher order PO calculations must be carried out to account for multi-scattering phenomena. Typically, there are two methods for higher order PO, one is called iterative PO and the other is called geometric optics PO (GO-PO). In the iterative PO approach, the higher order incident fields are calculated based on Huygens principle with the currents from lower order solutions, and then the higher order currents are derived from the new incident fields by following a similar process used for first order PO. It is noted that in iterative PO, the multi-scattering is assumed to be established between any two

facets that have direct light-of-sight (LoS), and it means the computational time complexity will be $O(n^2)$, where n is the number of facets or points on the surface. This requires extremely heavy computation for electrically very large objects like vehicles and human bodies in our application.

Note that if the surface has a much larger radii of curvature compared to the wavelength, the main direction of wave scattering will be very similar to that for light, and that phenomenon can be described by GO. Since only the facet/point in the specular direction is considered for higher order PO calculation, ideally the time complexity is reduced to $O(n)$. However, in practical algorithm the time complexity is not simply $O(n)$ but rather $O(n\log(n))$. This is due to the fact that the most challenging part of this method is not in calculating currents or fields in PO, but in ray tracing with GO. With tree-type data structure like KD-tree or BSP, the ray tracing time complexity can be as low as $O(\log(n))$. This algorithm will be discussed later.

To illustrate higher order GO-PO, we can first take a look at the second order GO-PO. As is shown in Figure 2.2, $\vec{r}$ is the location of the radar, and $\vec{r}'$ and $\vec{r}''$ are the hitting point of ray on first order and second order facets. $d\vec{r}'$ and $d\vec{r}''$ are two small vectors along the tangential direction of first order and second order facets. $\vec{k}_1$, $\vec{k}_2$ and $\vec{k}_3$ are the three wavenumber vectors of the ray's propagation.

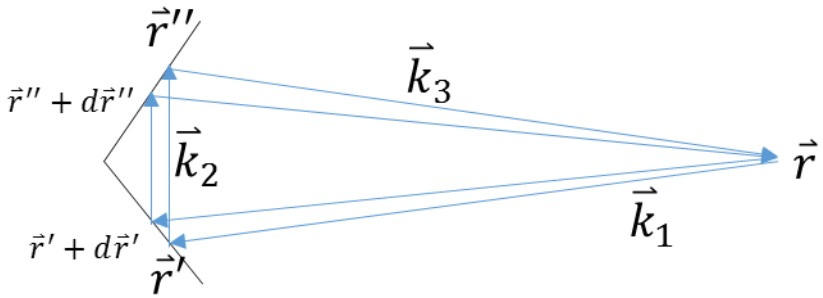

Figure 2.2. Illustration of second order GO-PO multi-scattering link

In GO approximation, the incident field at $\vec{r}'$ is given by spherical wave function:

$$\vec{E}_i\left(\vec{r}^{'}\right) = \frac{\vec{E}_0 e^{i\vec{k}_1\cdot\left(\vec{r}'-\vec{r}\right)}}{\left|\vec{r}'-\vec{r}\right|}, \tag{2.25}$$

$$\vec{H}_i\left(\vec{r}^{'}\right) = \frac{\hat{k}_1 \times \vec{E}_i\left(\vec{r}^{'}\right)}{Z_0}, \tag{2.26}$$

where $\hat{k}_1$ is the unit vector indicating the direction of incidence. The reflected fields are given by (2.2) :

$$\vec{E}_r\left(\vec{r}^{'}\right) = \left[-\hat{k}_1 \times \vec{E}_0 \cdot \hat{t}R_{TM}\left(\hat{k}_r \times \hat{t}\right) + \vec{E}_0 \cdot \hat{t}R_{TE}\hat{t}\right]e^{i\vec{k}_1\cdot\left(\vec{r}'-\vec{r}\right)}/\left|\vec{r}'-\vec{r}\right|, \tag{2.27}$$

$$\vec{H}_r\left(\vec{r}^{'}\right) = 1/Z_0 * \left[\vec{E}_0 \cdot \hat{t}R_{TE}\left(\hat{k}_r \times \hat{t}\right) + \hat{k}_1 \times \vec{E}_0 \cdot \hat{t}R_{TM}\hat{t}\right]e^{i\vec{k}_1\cdot\left(\vec{r}'-\vec{r}\right)}/\left|\vec{r}'-\vec{r}\right|. \tag{2.28}$$

Let $\vec{E}_{r1} = \left[-\hat{k}_1 \times \vec{E}_0 \cdot \hat{t}R_{TM}\left(\hat{k}_r \times \hat{t}\right) + \vec{E}_0 \cdot \hat{t}R_{TE}\hat{t}\right]$, $\vec{H}_{r1} = 1/Z_0 * \left[\vec{E}_0 \cdot \hat{t}R_{TE}\left(\hat{k}_r \times \hat{t}\right) + \hat{k}_1 \times \vec{E}_0 \cdot \hat{t}R_{TM}\hat{t}\right]$, then the incident field at $\vec{r}''$ can be expressed as:

$$\vec{E}_i\left(\vec{r}^{''}\right) = \frac{\vec{E}_{r1}e^{i\vec{k}_1\cdot\left(\vec{r}'-\vec{r}\right)}e^{i\vec{k}_2\cdot\left(\vec{r}''-\vec{r}^{'}\right)}}{\left|\vec{r}'-\vec{r}\right| + \left|\vec{r}''-\vec{r}'\right|} = \frac{\vec{E}_{r1}e^{i(\vec{k}_1-\vec{k}_2)\cdot\vec{r}'}e^{-i\vec{k}_1\cdot\vec{r}}e^{i\vec{k}_2\cdot\vec{r}''}}{\left|\vec{r}'-\vec{r}\right| + \left|\vec{r}''-\vec{r}'\right|}, \tag{2.29}$$

$$\vec{H}_i(\vec{r}'') = \frac{\vec{H}_{r1}e^{i(\vec{k}_1-\vec{k}_2)\cdot\vec{r}'}e^{-i\vec{k}_1\cdot\vec{r}}e^{i\vec{k}_2\cdot\vec{r}''}}{\left|\vec{r}'-\vec{r}\right| + \left|\vec{r}''-\vec{r}'\right|}. \tag{2.30}$$

Similar to equation (2.4) and (2.5), the equivalent surface current on $\vec{r}''$ is:

$$\vec{J}_s(\vec{r}'') = \frac{\left[Z_0\vec{H}_{r1}\cdot\hat{t}(1+R'_{TM})(\hat{n}\times\hat{t}) + \vec{E}_{r1}\cdot\hat{t}(\hat{n}\cdot\hat{k}_i)(R'_{TE}-1)\hat{t}\right]e^{i(\vec{k}_1-\vec{k}_2)\cdot\vec{r}'}e^{-i\vec{k}_1\cdot\vec{r}}e^{i\vec{k}_2\cdot\vec{r}''}}{Z_0(|\vec{r}'-\vec{r}|+|\vec{r}''-\vec{r}'|)}, \tag{2.31}$$

$$\vec{M}_s(\vec{r}'') = \frac{\left[Z_0\vec{H}_{r1}\cdot\hat{t}(\hat{n}\cdot\hat{k}_i)(R'_{TM}-1)\hat{t} - \vec{E}_{r1}\cdot\hat{t}(1+R'_{TE})(\hat{n}\times\hat{t})\right]e^{i(\vec{k}_1-\vec{k}_2)\cdot\vec{r}'}e^{-i\vec{k}_1\cdot\vec{r}}e^{i\vec{k}_2\cdot\vec{r}''}}{|\vec{r}'-\vec{r}|+|\vec{r}''-\vec{r}'|}, \tag{2.32}$$

where R'_{TM} and R'_{TE} are the reflection coefficients in TM and TE case on the second order facet.

Again, we can denote $\vec{J}_{sm2} = \left[Z_0\vec{H}_{r1}\cdot\hat{t}(1+R'_{TM})(\hat{n}\times\hat{t}) + \vec{E}_{r1}\cdot\hat{t}\left(\hat{n}\cdot\hat{k}_i\right)(R'_{TE}-1)\hat{t}\right]/Z_0$, and $\vec{M}_{sm2} = Z_0\vec{H}_{r1}\cdot\hat{t}\left(\hat{n}\cdot\hat{k}_i\right)(R'_{TM}-1)\hat{t} - \vec{E}_{r1}\cdot\hat{t}(1+R'_{TE})(\hat{n}\times\hat{t})$, such that:

$$\vec{J}_s(\vec{r}'') = \frac{\vec{J}_{sm2}e^{i(\vec{k}_1-\vec{k}_2)\cdot\vec{r}'}e^{-i\vec{k}_1\cdot\vec{r}}e^{i\vec{k}_2\cdot\vec{r}''}}{(|\vec{r}'-\vec{r}|+|\vec{r}''-\vec{r}'|)}, \tag{2.33}$$

$$\vec{M}_s(\vec{r}'') = \frac{\vec{M}_{sm2}e^{i(\vec{k}_1-\vec{k}_2)\cdot\vec{r}'}e^{-i\vec{k}_1\cdot\vec{r}}e^{i\vec{k}_2\cdot\vec{r}''}}{|\vec{r}'-\vec{r}|+|\vec{r}''-\vec{r}'|}. \tag{2.34}$$

The scattered E field of second order solution given by (2.1) is rearranged as:

$$\vec{E}_s^{(2)} = \frac{ik_0 e^{i\vec{k}_3\cdot\vec{r}}}{4\pi\left|\vec{r}^{''}-\vec{r}\right|}\left(\bar{\bar{I}}-\hat{k}_3\hat{k}_3\right)\iint\left[Z_0\vec{J}_{sm2}-\hat{k}_s\times\vec{M}_{sm2}\right]\frac{e^{i\left(\vec{k}_1-\vec{k}_2\right)\cdot\vec{r}^{'}}e^{-i\vec{k}_1\cdot\vec{r}}e^{i\vec{k}_2\cdot\vec{r}^{''}}e^{-i\vec{k}_3\cdot\vec{r}^{''}}}{\left|\vec{r}^{'}-\vec{r}\right|+\left|\vec{r}^{''}-\vec{r}^{'}\right|}ds'' = \frac{ik_0 e^{i(\vec{k}_3-\vec{k}_1)\cdot\vec{r}}}{4\pi\left|\vec{r}^{''}-\vec{r}\right|}\left(\bar{\bar{I}}-\hat{k}_3\hat{k}_3\right)\left[Z_0\vec{J}_{sm2}-\hat{k}_s\times\vec{M}_{sm2}\right]\iint\frac{e^{i\left(\vec{k}_1-\vec{k}_2\right)\cdot\vec{r}^{'}}e^{i(\vec{k}_2-\vec{k}_3)\cdot\vec{r}^{''}}}{\left|\vec{r}^{'}-\vec{r}\right|+\left|\vec{r}^{''}-\vec{r}^{'}\right|}ds'' \tag{2.35}$$

Note that when the intersected point of ray and second order facet changes from $\vec{r}''$ to $\vec{r}''+d\vec{r}''$, the intersected point of the ray and the first facet will change from $\vec{r}'$ to $\vec{r}'+d\vec{r}'$, and $\left(\vec{k}_1-\vec{k}_2\right)\cdot\left(\vec{r}'+d\vec{r}'\right)=\left(\vec{k}_1-\vec{k}_2\right)\cdot\vec{r}'$ as the vector $\left(\vec{k}_1-\vec{k}_2\right)$ is normal to the first facet. Because $\left|d\vec{r}^{'}\right|\ll|\vec{r}'-\vec{r}|$, and $\left|d\vec{r}^{''}\right|\ll|\vec{r}''-\vec{r}'|$, $|\vec{r}'-\vec{r}|+|\vec{r}''-\vec{r}'|$ is approximated as a constant. Therefore, the second order scattered E field for the second facet can be written as:

$$d\vec{E}_s^{(2)} = \frac{ik_0 e^{i(\vec{k}_3-\vec{k}_1)\cdot\vec{r}}e^{i\left(\vec{k}_1-\vec{k}_2\right)\cdot\vec{r}^{'}}}{4\pi\left|\vec{r}^{''}-\vec{r}\right|\left(\left|\vec{r}^{'}-\vec{r}\right|+\left|\vec{r}^{''}-\vec{r}'\right|\right)}\left(\bar{\bar{I}}-\hat{k}_3\hat{k}_3\right)\left[Z_0\vec{J}_{sm2}-\hat{k}_s\times\vec{M}_{sm2}\right]\iint e^{i(\vec{k}_2-\vec{k}_3)\cdot\vec{r}^{''}}ds'' \tag{2.36}$$

The higher order scattered E field with order *m* can be expressed in similar manner,

$$d\vec{E}_s^{(m)} = \frac{ik_0 e^{i\left[\left(\vec{k}_{m+1}-\vec{k}_1\right)\cdot\vec{r}+\left(\vec{k}_1-\vec{k}_2\right)\cdot\vec{r}^{(1)}+\left(\vec{k}_2-\vec{k}_3\right)\cdot\vec{r}^{(2)}+\cdots+\left(\vec{k}_{m-1}-\vec{k}_m\right)\cdot\vec{r}^{(m-1)}\right]}}{4\pi\left|\vec{r}^{(m)}-\vec{r}\right|\left(\left|\vec{r}^{(1)}-\vec{r}\right|+\left|\vec{r}^{(2)}-\vec{r}^{(1)}\right|+\cdots+\left|\vec{r}^{(m)}-\vec{r}^{(m-1)}\right|\right)}\left(\bar{\bar{I}}-\hat{k}_{m+1}\hat{k}_{m+1}\right)\left[Z_0\vec{J}_{sm}^{(m)}-\hat{k}_s\times\vec{M}_{sm}^{(m)}\right]\iint e^{i(\vec{k}_m-\vec{k}_{m+1})\cdot\vec{r}^{(m)}}ds^{(m)}, \tag{2.37}$$

where $\vec{k}_m$ is the k vector of the ray at m^{th} bounce, $\vec{J}_{sm}^{(m)}$ and $\vec{M}_{sm}^{(m)}$ are the induced surface electrical and magnetic current on the facet with m^{th} bounce of the ray.

One of the major challenges in GO-PO method is to efficiently locate the positions where the rays hit. This is a classical ray tracing problem in computer graphic [87], and is known as shooting and bouncing ray (SBR) in asymptotic computational electromagnetics [29][30]. The surface of target can be divided into many triangular facets, and hence the problem of finding intersected point of ray and target can be divided into two steps: first to find the facet intersecting with the ray, and second to find the intersected point on the facet. To search the targeting facet,

first all facets should be rearranged into a certain order or in certain data structure that can be located easily. The most efficient way for searching is to store all facets in a hierarchy manner, or tree-type data structure, which has a searching time complexity of O(log(n)) for one ray, where n denotes the number of facets. There are two popular data structures for storing the facets, one is called K-D tree and the other is known as binary space partitioning (BSP) [88].

In K-D tree data structure, the 3D space that is occupied by the target is divided into two equal-size boxes for each level, and in different levels, the division happens in different dimensions. For example, at level 1, the space is divided in x direction into two boxes, and at level 2, the resulting two boxes are divided in y direction, and etc. as shown in Figure 2.3 (a). Those boxes with certain dimensions are nodes in K-D tree data structure, and the facets are leaves. The relationship between nodes and leaves are shown in Figure 2.3 (b). The iteration stops when a specific requirement is meet. For instance, we can set a maximum level or a minimum dimension of the box, and when the iteration reaches the maximum level or the dimension of space at one level is smaller than the minimum dimension then it stops. When the iteration stops, the facet is put into that node. This data structure is relatively easy to implement compared to BSP, with the drawback that K-D tree can be an unbalanced tree because the target may not be symmetric. Since the focus of the study is not to develop an algorithm to maximize the computational efficiency, K-D tree data structure is applied here.

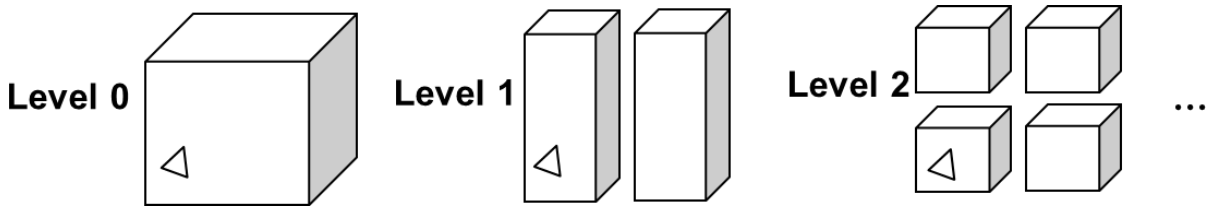

(a)

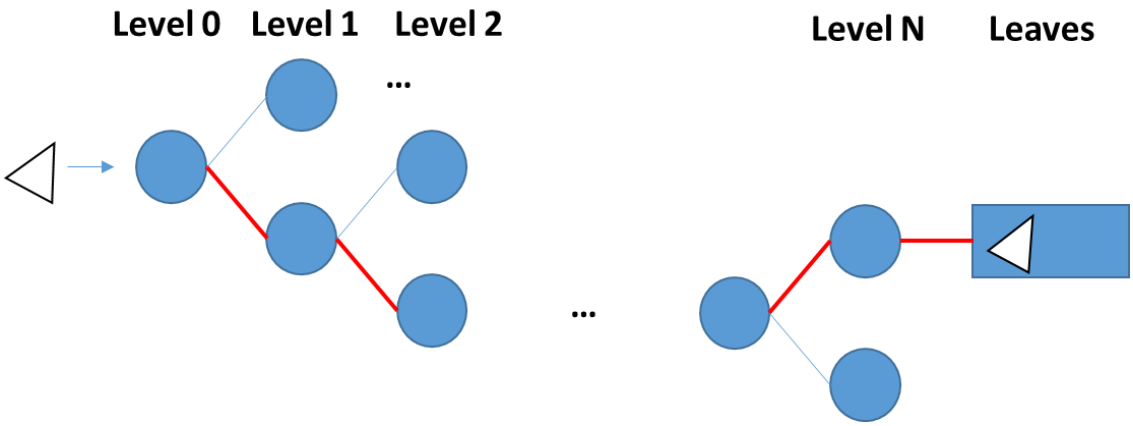

(b)

Figure 2.3. Example of putting one facet into K-D tree data structure

As mentioned, the main task is to search where the ray hits on the target, or equivalently, to find which facet of the surface of target intersects with the ray. In the K-D tree data structure, the search process is also in a hierarchical manner as illustrated in Figure 2.4. The simplified ray tracing algorithm is described in Table 2 - 2.

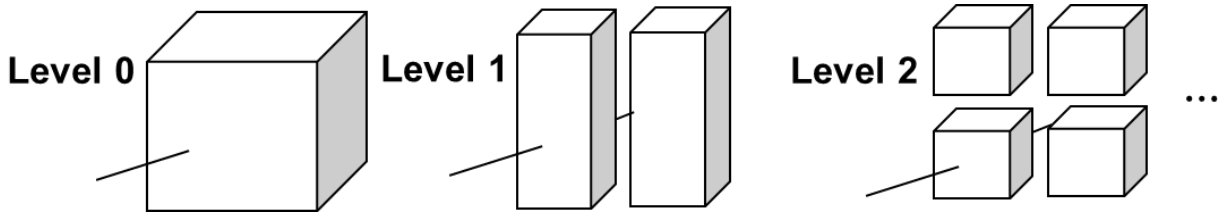

Figure 2.4. Example of searching intersected facet in K-D tree data structure

Table 2 - 2. Ray tracing algorithm with K-D tree

Algorithm: Ray tracing

1. **Generating rays regarding the dimensions, orientation of target(s)**
2. For each **ray R_j set the current order $\gamma \rightarrow 0$, intersected facets set $\Phi_\gamma \rightarrow \emptyset$**
   If $\gamma < \gamma_{max}$ **then** set the current node as root node
3. If **the ray intersects with current node** then
   If the ray intersects with any leaf f_i of the node **then**
   Put f_i into Φ_γ
   If the ray intersects with any child node of current node **then**

Repeat the process in step 3 for the child node(s)

4. For each **intersected facet in Φ_γ**
   Find the most front facet and find the hitting point on the facet $P_{j\gamma}$
5. For each **order γ**
   For each **triangle with vertices of $P_{j\gamma}$ by neighboring rays**
   If **the three vertices are on the same plane on the target,** then
   Perform the EM calculation to find the scattered field

2.4 Numerical results and validation of PO method

In this section, the accuracy of the proposed GO-PO method is examined by simulating the backscattering RCS of some targets with known RCS values. Then it shows the numerical results for some real targets and the comparison of measurements. In the end, the contributions of different order of PO solutions are discussed for commonly seen traffic targets like pedestrian and vehicles.

For electrically very large sphere, circular cylinder, and trihedral (corner reflector), there are theoretical solutions for their backscattering RCSs [89]. The backscattering RCS of an electrically large metallic sphere is:

$$\sigma = \pi r^2, \tag{2.38}$$

where r is the radius of sphere. The backscattering RCS of circular cylinder is:

$$\sigma = \frac{2\pi r h^2}{\lambda}, \tag{2.39}$$

where r is the radius of cylinder, and h is the height of the cylinder and λ is the wavelength. The backscattering RCS of trihedral is given by:

$$\sigma = \frac{4\pi L^4}{3\lambda^2}, \tag{2.40}$$

where L is the length of edge connecting a vertex to the corner as shown in Figure 2.5 (c).

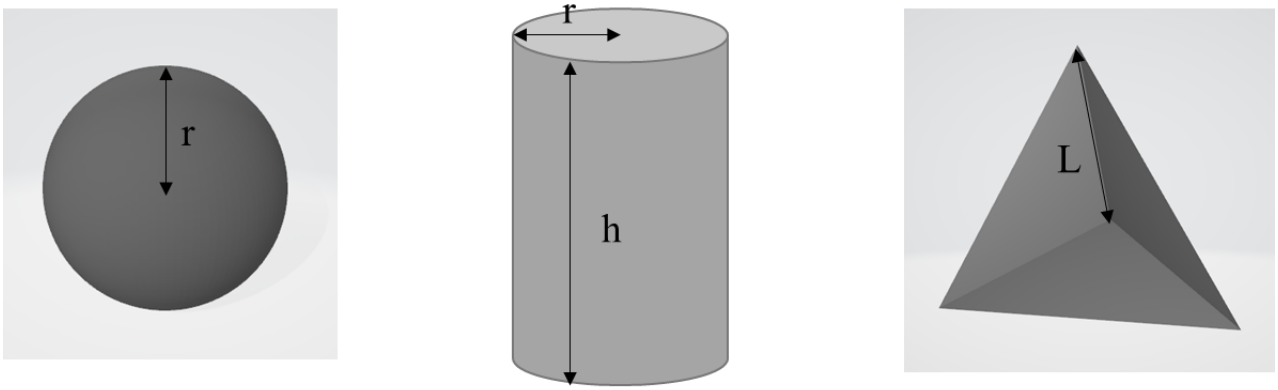

(a) (b) (c)

Figure 2.5. Geometry of known backscattering RCS targets: (a) sphere, (b) circular cylinder, and (c) trihedral.

The RCS for a metallic sphere with 0.1 m radius, a circular cylinder with r = 0.05m and h = 0.2m, and a trihedral with L = 0.1 m are simulated at 77 GHz and compared with theoretical solutions as demonstrated in Table 2 - 3. The difference between theoretical solutions and simulations are within 0.3 dB for all three targets, therefore, excellent accuracy of the proposed GO-PO method is shown for targets whose radii of surface is much larger than wavelength.

Table 2 - 3. Comparison between simulated and theoretical backscattering RCS

Backscattering RCS (dBsm)	sphere	Circular cylinder	trihedral
Theoretical solution	-15.03	5.08	8.16
Simulation	-15.29	5.09	7.99

In addition, the GO-PO method is tested against measurements for some targets commonly seen in traffic scene. Metallic square posts are widely used as post for traffic signs or parking signs as shown in Figure 2.6 (a). The radar's view usually has narrow beam width in elevation direction, thus the main backscattering for a traffic sign is from the post. The RCS of a square post with 2.5 in by 2.5 in is measured in the anechoic chamber in the University of Michigan (by my colleague

Michael Giallorenzo) shown in Figure 2.6 (b). Figure 2.6 (c) depicts the CAD model of a metallic square post with the same dimension as the measured one.

(a) (b) (c)

Figure 2.6. (a) Picture of a stop sign with square post, (b) the measurement setup of a square post inside anechoic chamber, and (c) A CAD model for the same square post in measurement.

In the measurement, the square post is put on a turn table and a radar with 3 degree antenna beam width in both the elevation and azimuth direction is used to perform the measurement. The RCS of the target is measured at a distance of 18 m. Due to the rotational symmetry, the square post is measured for azimuth direction from -45 degree to 45 degree, and 0 degree represents one face of the square post is perpendicular to the direction of incidence. In the numerical simulation, the same setups are applied to find the RCS of square post. The comparison of measurement and simulation for all angles from -45 degree to 45 degree are shown in Figure 2.7 and the comparison of ±5º averaged RCS is given in Figure 2.8. Both figures show good agreements between the measured and simulated results. Notice that ±5º averaged RCS has excellent agreement, which means the statistical data from simulation can be more accurate and may be more meaningful.

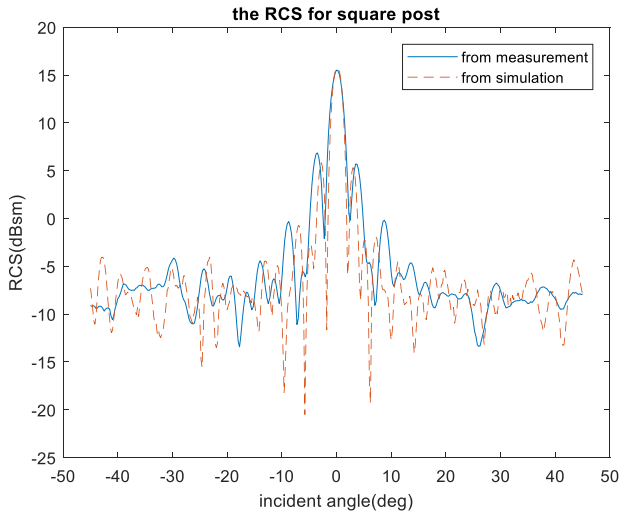

Figure 2.7. Comparison between measured and simulated RCS as a function of incident angle for a metallic square post

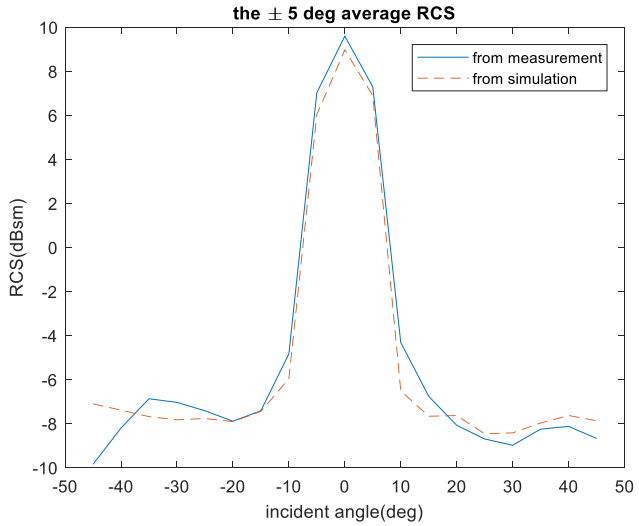

Figure 2.8. Comparison between measured and simulated ±5º average RCS as a function of incident angle for a metallic square post

Besides the square post measurement inside an anechoic chamber, an outdoor measurement for a vehicle is performed and the RCS results are compared with simulation as well. In the measurement, a sedan is driven into a large turn table, and several wave absorbers with height

about 0.3 m are placed in front of car to block the response from turn table as shown in Figure 2.9. The turn table can only operate manually, so we cannot measure the data with an accurate azimuth angle. In this situation, we roughly labeled angles from -90 to 90 degree for each 10 degrees on the ground, and at each angle, the car was slightly rotated for several angles and the averaged RCS of them are collected. The distance between the radar and the target changes from 10 m to 20 m. The antenna beam width for the radar is 3 degree in both elevation and azimuth direction, and the bandwidth of radar is from 76 to 79 GHz.

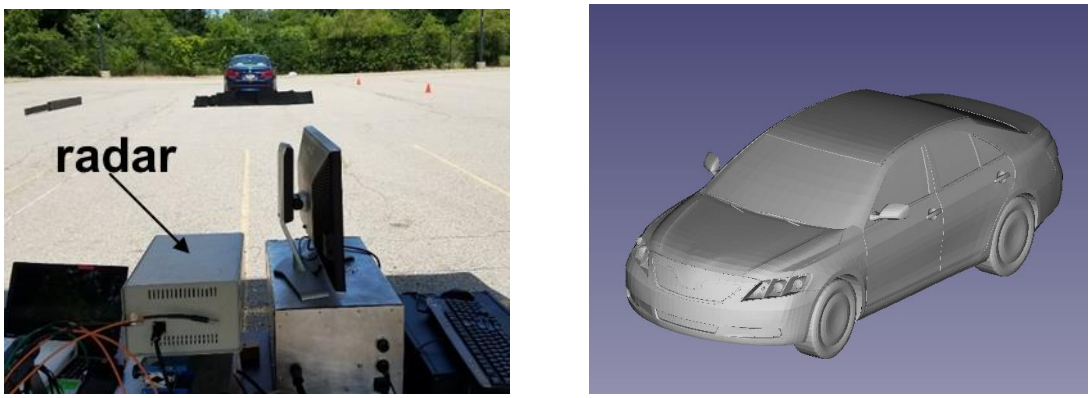

(a) (b)

Figure 2.9. (a) Picture of the outdoor measurement for the RCS of a sedan and (b) a CAD model of a sedan

The comparison between the measurements and simulated RCS results for a sedan at 10 m and 20 m is shown in Figure 2.10. In the figure, each data point represents the ±3 degrees and frequency averaged RCS. As can be seen, at both ranges, the averaged RCS values as a function of incident angle from simulation and measurement are similar. Because the CAD model is not exactly the same as the car under measurement, it is understood that the simulation and measurement results will not be the same. The good agreement between the simulated and measured averaged RCS indicates that the statistical features obtained from simulation and measurement behave similarly.

(a)

(b)

Figure 2.10. Measured and simulated averaged RCS as a function of incident angle for (a) range of 10 m and (b) 20 m

Higher order solutions of the GO-PO methods are corresponding to multiple reflection of EM waves. It will be interesting to exam how large the higher order responses are for typical traffic targets like pedestrian and vehicles.

2.5 Conclusion

Radar simulation can help to better understand the radar signals from different targets, guide and test the radar design to meet the requirement of autonomous driving. Meanwhile, the simulation for mmWave radar is quite challenging as most traffic targets are complex and electrically very large. In this chapter, asymptotic methods based PO and GO-PO approaches are introduced to obtain high-fidelity radar response simulation results. To accelerate traditional PO method in a wideband problem, separation of variables is applied to largely reduce redundant calculation for different frequency points. In GO-PO method, the most challenging part ray-tracing technique with KD-tree data structure is described in detail. The accuracy of the proposed PO and GO-PO methods are validated through comparison with theoretical solution of simple geometry targets and measurements.

Chapter 3 Near Grazing Incidence Radar Modeling of Road Surfaces at 77 GHz

3.1 Introduction

Road surfaces are usually rough, inhomogeneous and can be considered as random rough surfaces. The roughness of road will cause MMW scattering in backward direction and can detected by an MMW radar. The commonly seen types of road include asphalt, concrete and soil as shown in Figure 3.1. Depending on the weather, the road may also have different conditions like dry, wet, ice- or snow-covered. Different types of road surfaces and road with different conditions may result in different level of backscattering power. This phenomenon indicates that radars can also function for identifying road conditions, which is a very important function for enabling autonomous navigation. Because radar is usually mounted on the front or side of a vehicle and the fact that road surface assessment is needed at a distant point away from the vehicle, such EM scattering problem is for near grazing incident angle (> 80°) on the road surface.

Figure 3.1. Different road types: asphalt, concrete and soil road

The radar backscattering from road surface is more complicated than that from regular targets such as vehicles and pedestrians because the roughness feature of road surface is smaller than or comparable to the wavelength at millimeter wave range and the extent of the illuminated area is much larger than the wavelength. As a result, high-frequency asymptotic methods including PO and GO are not suitable for calculation of scattering from such targets. In low frequency regime where both the RMS height and the correlation length are much smaller than the wavelength, analytical approaches such as small perturbation method [94], [95] can be used to find the radar backscattering from random rough surfaces. For scattering problems at very high frequency regime, where the roughness of the surface can locally be considered flat (the radii of curvature of the surface is much larger than the wavelength), then Kirchhoff approximation [96] can be applied to the scattering problems. In the mmWave radar application, the wavelength is about 4 mm, and both RMS height and correlation length of typical road surfaces are comparable to the wavelength,

which results in both small perturbation method or Kirchhoff approximation not applicable in this problem.

Generally, the radar backscattering from ground can be divided into two parts: surface scattering and volumetric scattering. Road surfaces are usually made up of heterogeneous materials having different permittivity values and different particle size distributions. This causes the volume scattering that is difficult to model electromagnetically and hence the scattering per unit volume of such materials is usually obtained through measurement or using semi-empirical methods [39], [90]. Since both low-frequency and high-frequency approximation fails in the surface scattering problem, full-wave numerical approach is used to study the surface scattering component in this chapter.

3.2 Road surface statistics and profile measurement

The ground surface is considered as a random rough surface with certain statistical features. The statistical features include root-mean-square (RMS) height, autocorrelation function and the correlation length related to the autocorrelation function [91], [92], [93]. RMS height of a rough surface is defined as:

$$s = \sqrt{\frac{1}{A}\iint_A (z(x,y) - \bar{z})^2 dxdy}, \tag{3.1}$$

where $z(x,y)$ is the height on the surface at position (x, y), A is the area of integration, and $\bar{z}$ is the average height of the surface.

Correlation function is used to describe how rapidly the height of surface changes with position (x, y), and is defined as following [93]:

$$C(x-x', y-y') = \frac{1}{s^2}\langle z(x,y), z(x',y')\rangle, \tag{3.2}$$

Exponential autocorrelation function and Gaussian autocorrelation function are the most commonly used autocorrelation functions to describe rough surface. The exponential autocorrelation function is given by [93]:

$$C(x-x', y-y') = \exp(-\sqrt{[(x-x')^2 + (y-y')^2]}/l^2), \quad (3.3)$$

where l is the correlation length. The Gaussian correlation function is:

$$C(x-x', y-y') = \exp(-[(x-x')^2 + (y-y')^2]/l), \quad (3.4)$$

In general, the rough surface with exponential correlation function is much rougher than that with Gaussian correlation function, and the rough surface generated from different correlation function may have quite different radar backscattering response. Therefore, it is important to find out the autocorrelation function of real road surfaces before further analysis. We use a laser profilometer on a linear stage to detect the height of ground surface as is shown in Figure 3.2. The laser profilometer can very accurately estimate the profile of ground surface in one dimension. The RMS height, autocorrelation function and correlation length can be calculated based on the measurement data, and by repeating the measurement for the same type of ground for many times, the averaged RMS height and correlation length can be obtained.

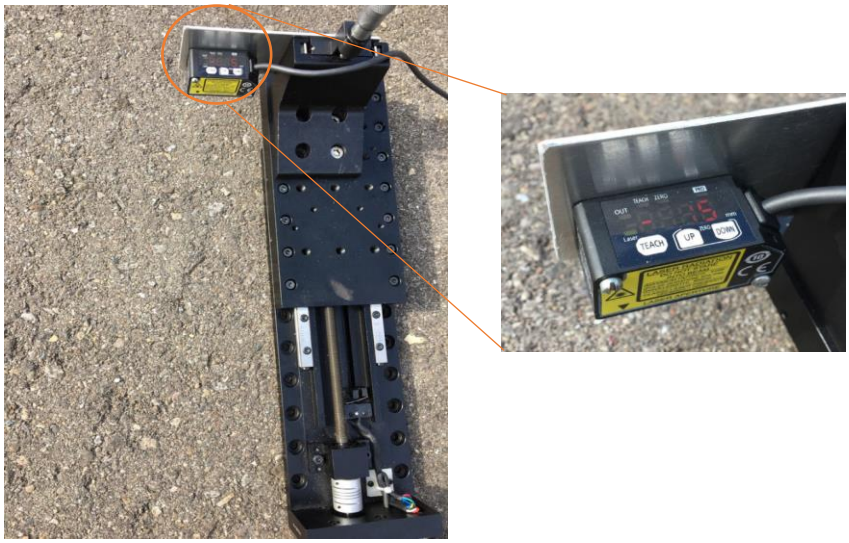

Figure 3.2. Laser profilometer used to measure the roughness of ground surface

Some examples of the correlation function obtained from measurements for asphalt are depicted in Figure 3.3. It can be seen that the correlation function created by measured data is closer to exponential function than Gaussian function, and therefore in future analysis exponential correlation function is assumed. Another interesting observation is that the correlation length varies largely for different samples. This indicates that the roughness of road surface is not homogenous even for measurements are taken in a local area.

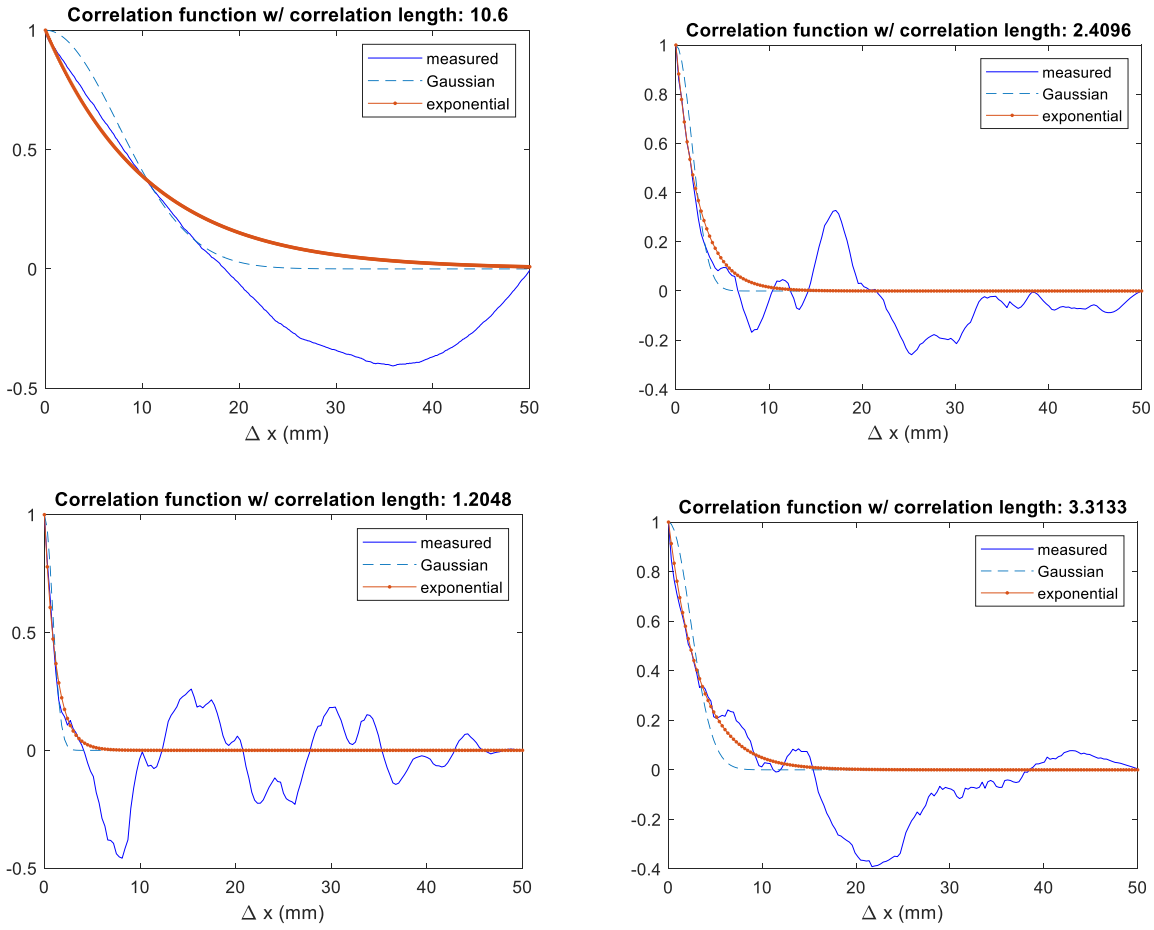

Figure 3.3. Two examples of correlation function comparison between measurement, Gaussian and exponential.

The measurements are taken with the help from another graduate student (Michael Giallorenzo). The profile of concrete, new asphalt and weathered asphalt ground surfaces are

measured and each of them has more than 50 samples. Their averaged RMS height and correlation lengths are shown below:

Table 3 - 1. RMS height and correlation length for measured samples

Ground Type	$\bar{s}$ (mm)	$\sigma(s)$ (mm)	$\bar{l}$ (mm)	$\sigma(l)$ (mm)
Weathered asphalt	1.24	1.17	2.71	2.48
New asphalt	0.81	0.49	1.80	1.66
Concrete	0.20	0.08	13.2	4.51

In the table above, $\bar{s}$ denotes the average RMS height, and $\sigma(s)$ refers the standard deviation of RMS heights from all samples. It is shown that concrete surface has much smaller RMS height and larger correlation length than asphalt surface, which indicates that concrete surface is smoother than asphalt surface. Similarly, the weathered asphalt is rougher than new asphalt. The standard deviation on the correlation length is large for both asphalt and concrete surfaces, which is also a proof that the ground surface is not homogenous in roughness.

3.3 Full-wave numerical method for surface scattering from near grazing incidence

In reality the extent of road surfaces is much larger than the radar antenna footprint. Thus, in numerical simulations, we have to truncate the dimensions of the road surface to have feasible simulation. To eliminate the edge effect of the finite rough surface in simulation, one approach is called tapered incident wave [97], [98]. Instead of using planar incident wave, this approach creates an artificial wave front such that there would be little incident field on the edge of the rough surface. However, in order to have good convergence, the dimensions of the rough surface must be increased with incident angle, and this will lead to requiring hundreds of wavelengths for incident angle more than 80° for accurate results [97]. Alternatively, periodic boundary conditions can be

applied to eliminate edge effect as well [99], [100]. With periodic boundary condition, the incident wave can be plane wave and the dimensions of rough surface don't depend on the incident angle.

In this thesis, FEM based commercial software AnsysEM (HFSS) is chosen to perform simulations because first, FEM method is an accurate single frequency solver and AnsysEM has industrial standard adaptively meshing techniques for reducing the number of unknowns. Second, it provides periodic boundary condition to eliminate edge effect of rough surface. Figure 3.4 gives an example of the simulation setup for a dielectric random rough surface. The random rough surface in the example is generated with exponential correlation function with $s = 0.8\text{mm}$ and $l = 1.8$ mm. On the top of the rough surface is the air layer, and above the air layer is a perfect-match layer (PML) to prevent wave reflection from to top boundary of air layer. Below the rough surface is the road layer, in this example, the road layer is considered as homogeneous dielectric. Below the road layer is an impedance boundary whose impedance is calculated such that almost no reflection from the bottom of the road layer. On the four sides of the entire model, the periodic boundary conditions are enforced. The total dimensions of the example model are about 20 mm by 20 mm by 10 mm (~5λ × 5λ × 2.5λ), and mesh size is about 0.1 λ.

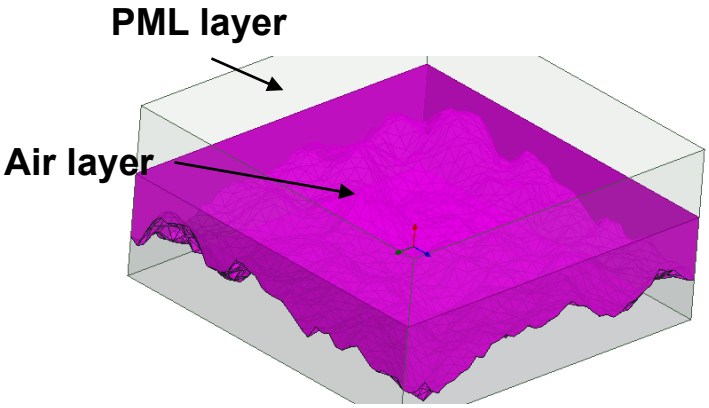

(a)

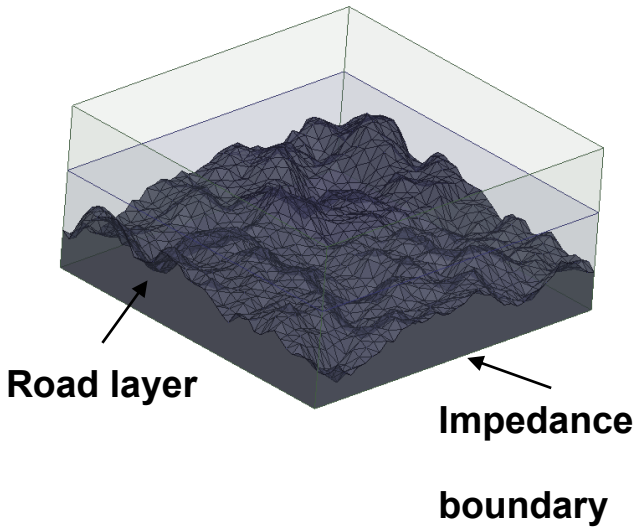

(b)

Figure 3.4. Simulated setup of a rough surface in AnsysEM

After perform simulation in AnsysEM for the rough surface model in Figure 3.4, the scattered tangential electric field on the top surface of air layer can be collected and drawn in Figure 3.5. Because the model has periodic boundary condition, the scattered E field outside the boundary will be the field inside the boundary times some phase term related to the incident phase difference. Hence, the scattered tangential E field everywhere with the same height can be obtained. According to equivalence theorem, the scattered electric far field can be calculated by near-field and far-field transformation [101].

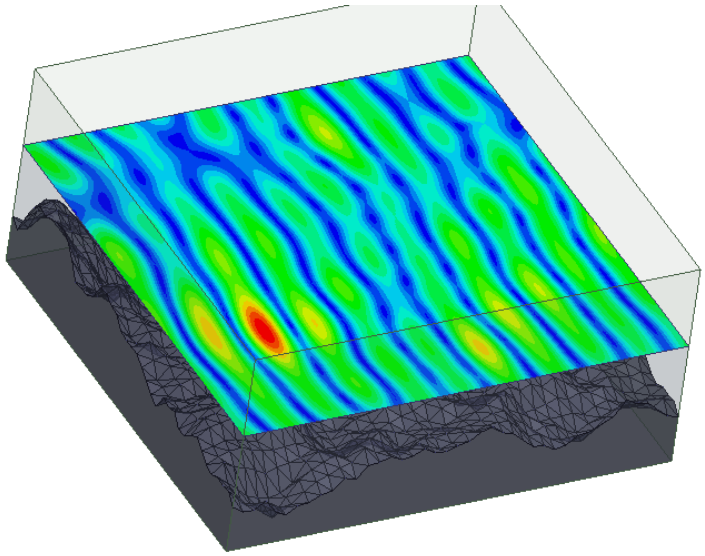

Figure 3.5. Simulated scattered tangential E field on the top of air layer from one rough surface example

The detail of near-field and far-field transformation is given below. The cell shown in Figure 3.5 has periodicity in both x and y directions. Let the period in x direction is L_x and in y direction is L_y. Any point with coordinate values of (x', y', z) can be represented as $(x + nL_x, y + mL_y, z)$, with $0 \leq x < L_x$, $0 \leq y < L_y$, $n, m \in \mathbb{Z}$. Due to the periodic boundary condition, the E field at (x', y', z) is given by:

$$\boldsymbol{E}(x + nL_x, y + mL_y, z) = \boldsymbol{E}(x, y, z)e^{jk_0(nL_x sin\theta_i cos\phi_i + mL_y sin\theta_i cos\phi_i)}, \quad (3.5)$$

where θ_i and ϕ_i are the incident elevation and azimuth angle with respected to the surface. The E field inside the cell $\boldsymbol{E}(x, y, z)$ can be expressed as Fourier transform of its spectral domain value:

$$\boldsymbol{E}(x, y, z) = \frac{1}{4\pi^2} \iint_{-\infty}^{\infty} \boldsymbol{A}(k_x, k_y, z)e^{-jk_z z}e^{-jk_x x - jk_y y}dk_x dk_y, \quad (3.6)$$

$\boldsymbol{A}(k_x, k_y, z)$ is the inverse Fourier transform of $\boldsymbol{E}(x, y, z)$:

$$\boldsymbol{A}(k_x, k_y, z) = e^{jk_z z_0} \iint_{-\infty}^{\infty} \boldsymbol{E}(x, y, z_0)e^{jk_x x + jk_y y}dxdy, \quad (3.7)$$

In far field approximation, the electrical far field can be expressed as [101]:

$$E_\theta(\theta,\phi,r) = jk_0\frac{e^{-jk_0r}}{2\pi r}\left(A_x cos\phi_s + A_y sin\phi_s\right), \tag{3.8}$$

$$E_\phi(\theta,\phi,r) = jk_0\frac{e^{-jk_0r}}{2\pi r}cos\theta_s\left(A_y cos\phi_s - A_x sin\phi_s\right), \tag{3.9}$$

where θ_s and ϕ_s are the elevation and azimuth direction of observation point. Thus, the task is to find the value of A_x and A_y for a given incident wave. Let the tangential A be $\mathrm{A_t} = A_x\hat{x} + \mathrm{A_y}\hat{y}$. We also have:

$$\boldsymbol{A_t}\left(k_x,k_y,z_0\right) = e^{jk_zz_0}\iint_{-\infty}^{\infty}\boldsymbol{E_t}(x,y,z_0)e^{jk_xx+jk_yy}dxdy =$$

$$e^{jk_zz_0}\sum_{n=-N}^{N}e^{jk_0(nL_xsin\theta_icos\phi_i)}\,e^{jk_xnL_x}\sum_{m=-M}^{M}e^{jk_0(mL_ysin\theta_isin\phi_i)}\,e^{jk_ymL_y}\times \tag{3.10}$$

$$\int_0^{L_y}\int_0^{L_x}\boldsymbol{E_t}(x,y,z_0)e^{jk_xx+jk_yy}dxdy.$$

Note that the summation term is a sinc function, which becomes a delta function if N and M goes to infinite:

$$\sum_{n=-N}^{N}e^{jk_0(nL_xsin\theta_icos\phi_i)}\,e^{jk_xnL_x} = \begin{cases} 1+2N, & k_x = -k_0sin\theta_icos\phi_i + \frac{2\pi n}{L_x} \\ negligible, & k_x \neq -k_0sin\theta_icos\phi_i + \frac{2\pi n'}{L_x} \end{cases} \tag{3.11}$$

It indicates that it only has solutions for the discretized angles or called Bragg angles [102] with k_x and k_y satisfied the following conditions:

$$k_x = -k_0\,sin\,\theta_i\,cos\,\phi_i + 2\pi n/L_x, n \in \mathbb{Z}, \tag{3.12}$$

$$k_y = -k_0\,sin\,\theta_i\,sin\,\phi_i + 2\pi m/L_y, m \in \mathbb{Z}. \tag{3.13}$$

Since our interested scattering direction is in the back, the value of L_x and L_y are carefully chosen such that $\hat{k}_s = -\hat{k}_i$. The equation (3.10) can be rewritten as:

$$\begin{aligned}\boldsymbol{A_t}\left(k_x,k_y,z_0\right) &= e^{jk_zz_0}(1+2N)(1+2M)\int_0^{L_y}\int_0^{L_x}\boldsymbol{E_t}(x,y,z_0)e^{jk_xx+jk_yy}dxdy \\ &= e^{jk_zz_0}(1+2N)(1+2M)\boldsymbol{A_{t_0}}.\end{aligned} \tag{3.14}$$

Where $\boldsymbol{A_{t0}}$ represents the integration of simulated tangential E fields, and can be numerically evaluated.

The main contribution of the backscattering field from a random rough surface is incoherent field, therefore, a term called scattering coefficient is used to characterize the radar response of the rough surface. Scattering coefficient is defined by the RCS per unit area, or:

$$\langle \sigma_{pq}^0 \rangle = \lim_{R\to\infty} \frac{4\pi R^2}{A_0} \frac{|\hat{p}\cdot \boldsymbol{E}^s|^2}{|\hat{q}\cdot \boldsymbol{E}^i|^2}, \tag{3.15}$$

where p and q are polarizations, usually is specified as horizontal or vertical polarization. In this application, A_0 is the area of one unit cell, and $\boldsymbol{E^s}$ is obtained by substituting $\boldsymbol{A_{t0}}$ into equation (3.8) and (3.9).

3.4 Surface backscattering simulation results

To examine the accuracy of FEM method with AnsysEM (HFSS) for this surface scattering problem, we first perform the simulation to find the scattered field from a flat dielectric surface in specular direction. The reflection coefficients for flat surface in specular direction is given by Fresnel's equations [89]. The simulated reflection coefficients are simply the ratio between the magnitude of scattered E field and incident E field:

$$|R|_{sim} = \frac{|E_s|}{|E_i|}, \tag{3.16}$$

An example of the simulation for flat dielectric surface in both TM and TE cases are shown in Figure 3.6. It has dimensions of about 4mm by 4mm (λ × λ), dielectric constant of 3.18+0.1i, and is illuminated by a planewave with $\theta_i = 80°$. The real part of the scattered E fields is depicted in the figure, and it appears to be a sine function as expected. The reflection coefficients are 0.458 for TM case and 0.791 for TE case according to Fresnel equations in this problem. It can be observed from Figure 3.6 that the simulated reflection coefficients are 0.442 for TM case and 0.794

for TE case. Therefore, the error between simulated and theoretical results are very small (<0.016) which validate the accuracy of this simulation approach.

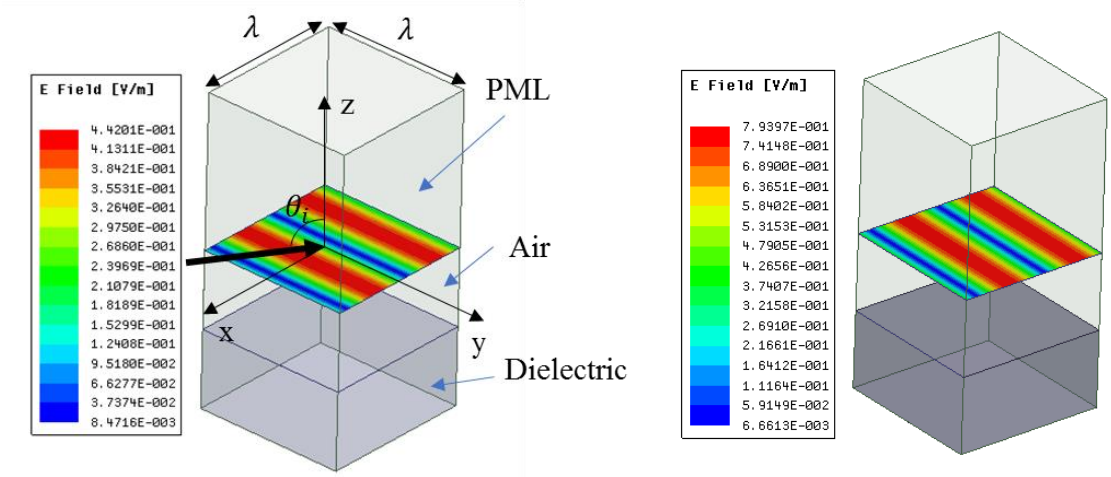

(a) (b)

Figure 3.6. The simulated scattered tangential E field on the top of air layer from a flat surface for (a) TM case and (b) TE case

The rough surfaces are random, therefore, their backscattering responses are random variables as well. In order to characterize the randomized behavior of the backscattering response, Monte Carlo simulations are performed. First question to ask is how many realizations are needed to achieve reliable results. In one example, Figure 3.7 depicts the simulated average backscattering coefficients as a function of number of realizations of the rough surfaces with the same statistical features (RMS height, autocorrelation function and correlation length). In the figure, VV, HH, VH/HV stand for different polarizations, in particular, V is for vertical polarization or TM polarization, and H is for horizontally polarization or TE polarization. VH means the transmitter is in V polarization and the receiver is in H polarization, etc. Due to the reciprocity of EM wave, the backscattering coefficients of VH coincides with that of HV, therefore only one curve is used to represent the two polarization states. It can be seen that after 30 realizations, the backscattering

coefficients for all polarizations converge. Therefore, 30 realizations are sufficient to achieve a relatively accurate result. In the following discussion, data are collected for about 40 realizations.

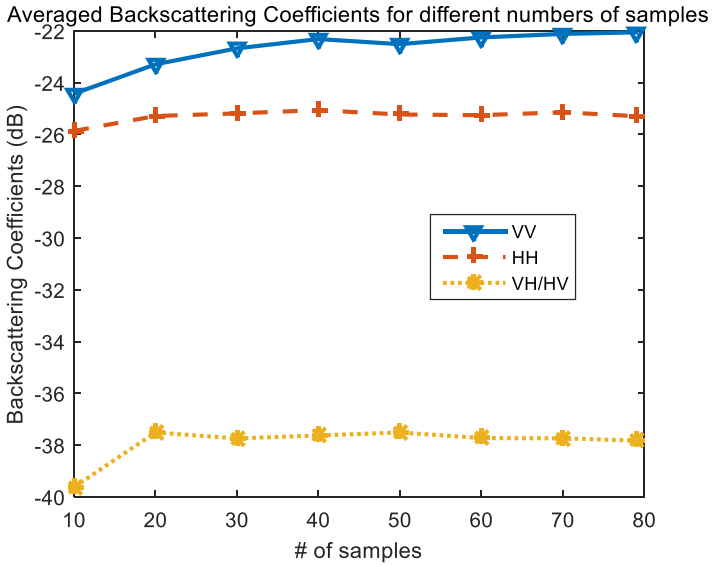

Figure 3.7. The backscattering coefficients averaged from many realizations of random rough surfaces with the same statistical features

The time complexity and memory increase dramatically with the dimensions of rough surface in FEM simulation, meanwhile, the rough surface may not exhibit the correct statistical information if the dimensions are too small. Therefore, it is desired to find the smallest dimensions of the rough surface model that has good convergence to save the time and memory. Table 3 - 2 gives the comparison of simulated backscattering coefficients and the computational costs between the rough surfaces with different dimensions. All randomly generated rough surfaces have the same statistical parameters (s = 0.5mm and h = 1.2 mm) and same incident angle (θ = 70 º). σ_{pq}^{0} denotes the backscattering coefficients with incident field of p polarization and scattered field of q polarization, and CPU time and memory are the averaged values for all 40 realizations. It is shown from the table that when the dimensions increase from 21mm (~5 λ) to 31 mm (~ 8λ), the variation in backscattering coefficients are lower than 1.5 dB for all polarizations but the CPU time

is increased by more than 3 times and memory is increased by 1.5 times. Hence, considering the tradeoff between accuracy and computational cost, 5 λ by 5 λ is used as the dimensions of rough surfaces in following simulations.

Table 3 - 2. Comparison of the backscattering coefficients and computational resources for the rough surfaces with different dimensions and same statistics

Dimensions (mm)	σ_{vv}^0 (dB)	σ_{vh}^0 (dB)	σ_{hh}^0 (dB)	CPU time (hrs)	Memory (GB)
~21×21	-22.0	-37.9	-25.1	7.99	105
~25×25	-22.6	-38.6	-27.1	14.37	156
~31×31	-23.0	-39.4	-26.5	32.47	250

The backscattering coefficients are treated as random variables. Characterizing the statistical features of the backscattering coefficients can help us better understand the scattering mechanism from random rough surfaces. In one example, the rough surface has RMS height equal to 0.8mm, correlation length of 1.8mm, and is illuminated by a plane wave with $\theta_i = 70°$. Its backscattering coefficients are found to follow exponential distribution as is shown in Figure 3.8. In the figure the results for HV polarization are not shown because they are the same as those for VH polarization. The exponential distribution can be described with one parameter μ, and its probability density function (PDF) is given by [103]:

$$f(x) = \begin{cases} e^{-x/\mu}/\mu & x \geq 0 \\ 0 & x < 0 \end{cases}, \tag{3.17}$$

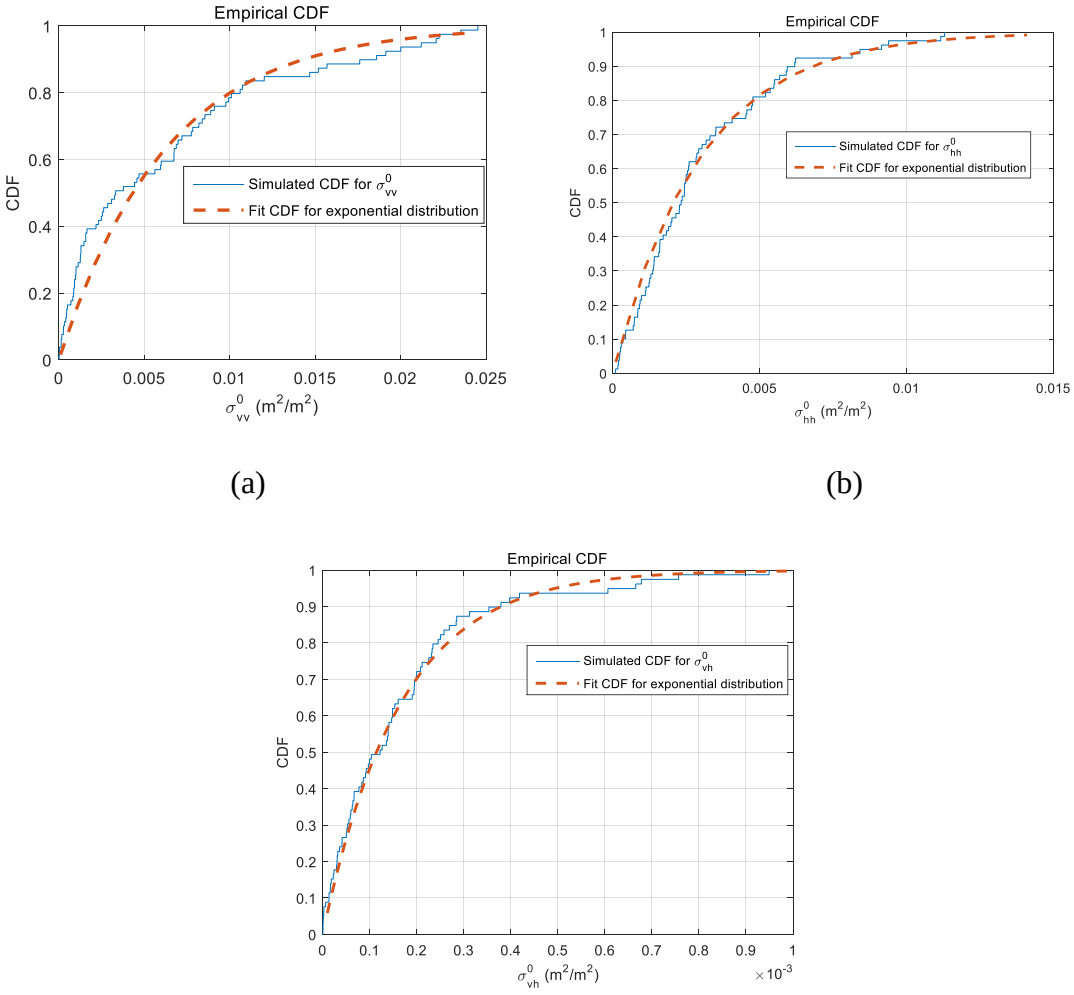

Figure 3.8. The comparison of empirical and fitted cumulative density function of backscattering coefficients with (a) VV polarization, (b) HH polarization and (c) VH polarization for the rough surfaces with the same statistical features

The mean value of the exponential distribution is μ, and in the example of Figure 3.8, the parameter μ for the backscattering coefficients with different polarizations are: $\mu_{vv} = 6.23e-3$, $\mu_{hh} = 2.96e-3$, $\mu_{vh} = 1.65e-4$. Notice that since the backscattering coefficients are defined as RCS per unit area, they have unit of m^2/m^2 or are unitless. One interesting property of exponential distribution is memoryless, which can be described as:

$$P(X > x + x_0 | X > x_0) = P(X > x), \quad \forall x, x_0 \geq 0 \tag{3.18}$$

In this rough surface radar backscattering problem, the backscattering power is dominated by incoherent summation, which means the total backscattering power can be treated as the sum of the backscattering power from all scatterers on the rough surface. The memoryless equation can be interpreted as: the probability of the occurrence of one strong scatterer on the rough surface is independent of the existing backscattering power of the rough surface. This is naturally true since the points on the rough surface are quickly uncorrelated, and thus the scatterers should be independent as well. It is shown that only one parameter μ is needed to describe the statistical features of backscattering coefficients. In the following discussion, parameter μ of the backscattering coefficients for different polarizations is studied, and the relation between μ and other parameters are discussed.

3.5 Reduced surface backscattering models

The Monte Carlo simulations for polarimetric radar backscattering coefficients are performed for the random rough surfaces with many different profile features and incident directions. In particular, the profile features are characterized as RMS height, correlation length, and dielectric constant. The simulated instances have RMS height from 0.4 mm to 1 mm, and correlation length from 1 mm to 3mm. The dielectric constant for road varies from 2 to 10, and the incidence angle ranges from 65º to 85º.

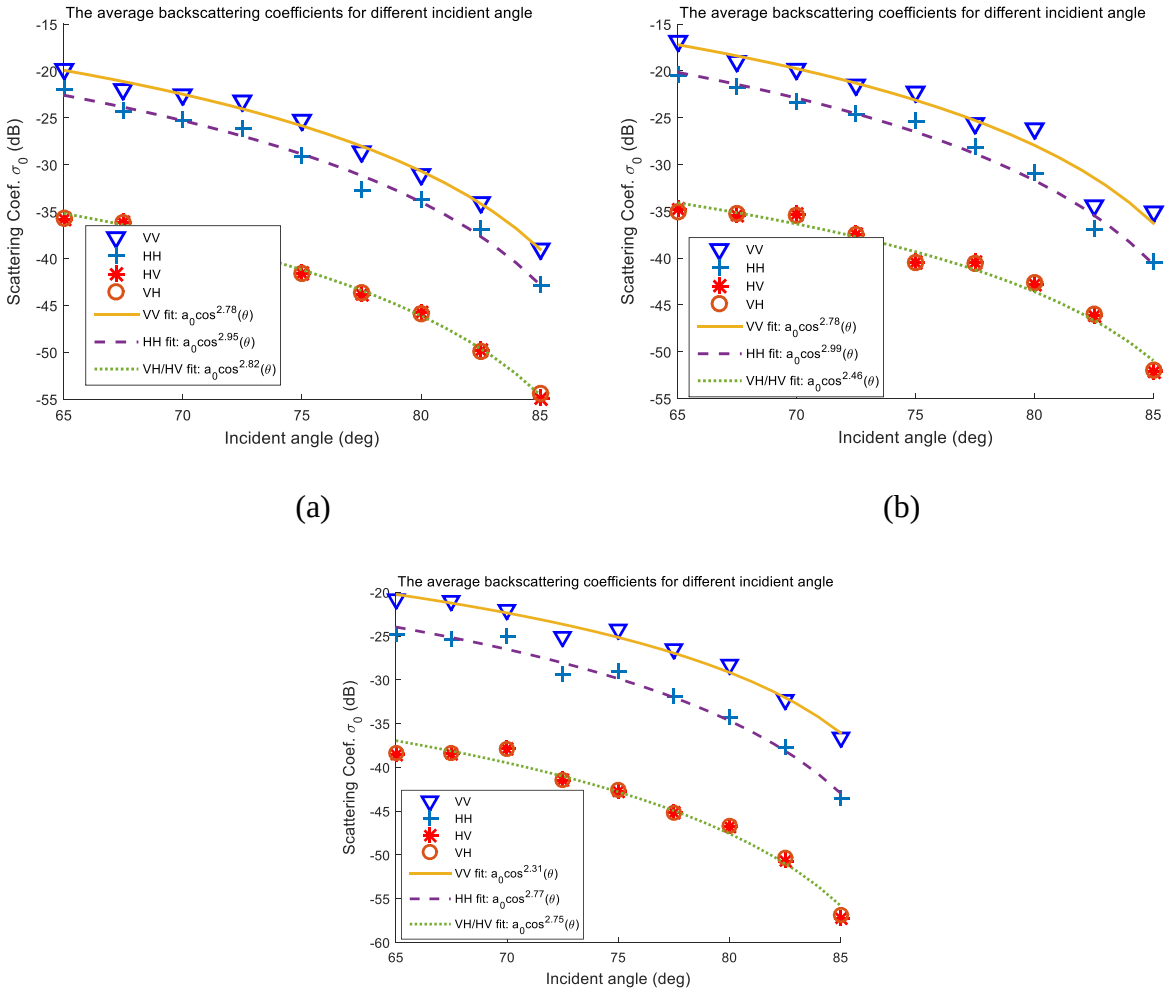

Figure 3.9. The backscattering coefficients with different polarizations as functions of incident angle for the rough surfaces with (a) $ks = 1.29, kl = 3.23, \varepsilon_r = 3.18 + 0.1i$, (b) $ks = 1.29, kl = 2.41, \varepsilon_r = 3.18 + 0.1i$ and (c) $ks = 0.81, kl = 1.93, \varepsilon_r = 3.18 + 0.1i$.

To quantitatively examine the relations between polarimetric backscattering coefficients and road surface properties and incident angles, method of control variable is applied. To obtain a more general relations in the MMW band where automotive radar operates (76~81 GHz), though

the simulations are only performed for 77 GHz, we use unitless variables ks and kl instead of RMS height s and correlation length l. k is the wavenumber defined as $\frac{2\pi}{\lambda}$.

The relation between backscattering coefficients and incident angles are depicted in Figure 3.9. In the three figures, variables ks, kl and ε_r maintain the same values and the mean value μ of backscattering coefficients vary with incident angle only. They show that the backscattering coefficients can be modeled as functions of incident angle in the following form:

$$\sigma_{pq}^{0} = a_0 \cos^{b_0} \theta_i \,, \quad p, q = h \; or \; v, \tag{3.19}$$

where a_0 and b_0 are functions of other variables ks, kl and ε_r.

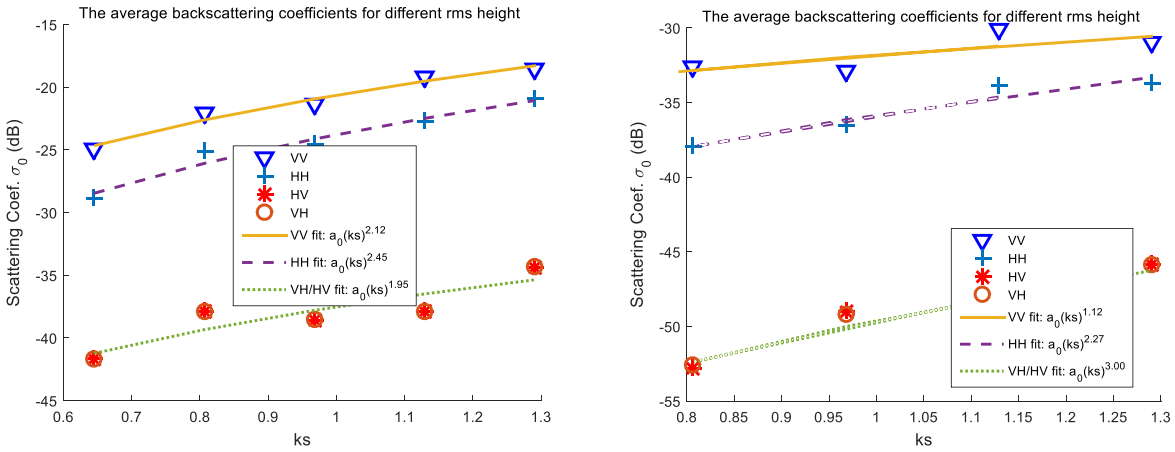

(a) (b)

Figure 3.10. The backscattering coefficients with different polarizations as functions of ks for the rough surfaces with (a) $kl = 1.93, \varepsilon_r = 3.18 + 0.1i, \theta_i = 70°$, and (b) $\theta_i = 80°, kl = 3.23, \varepsilon_r = 3.18 + 0.1i$

Figure 3.10 depicts how the backscattering coefficients change with RMS height while other variables remain constant. Figure 3.10 (a) and (b) have different kl and incident angle values.

In both situations the backscattering coefficients σ_{pq}^0 are proportional to ks^{b_1}, b_1 can be a function of incident angle.

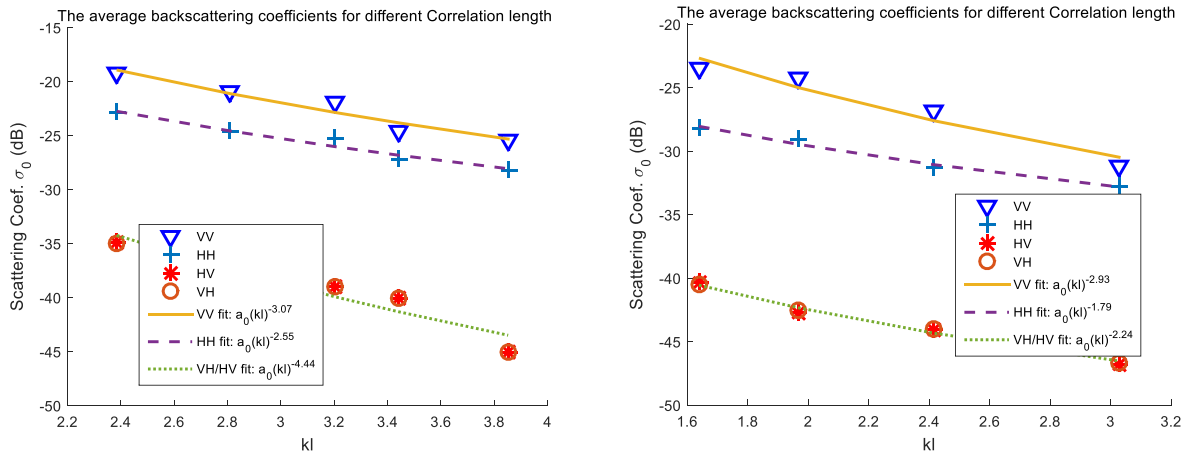

(a) (b)

Figure 3.11. The backscattering coefficients with different polarizations as functions of kl for the rough surfaces with (a) $ks = 1.29, \varepsilon_r = 3.18 + 0.1i, \theta_i = 70°$, and (b) $\theta_i = 75°, ks = 0.81, \varepsilon_r = 3.18 + 0.1i$

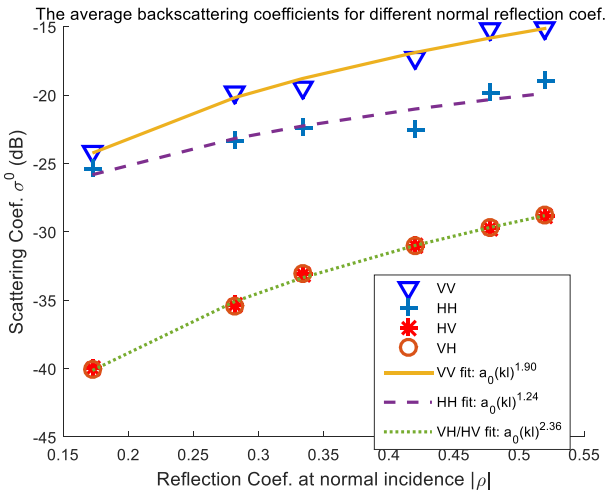

Figure 3.12. The backscattering coefficients with different polarizations as functions of normal incidence reflection coefficient ρ_0 for the rough surfaces with $ks = 1.29, kl = 2.41, \theta_i = 70°$

The mean values of backscattering coefficients as functions of kl are given in Figure 3.11. Similar to the previous analysis, σ_{pq}^0 is found to be proportional to kl^{-b_2}. In Figure 3.12, the mean values of backscattering coefficients are modeled as functions of normal incidence reflection coefficient ρ_0. The normal incidence reflection coefficient is defined as:

$$\rho = \frac{\sqrt{\varepsilon_1}-\sqrt{\varepsilon_0}}{\sqrt{\varepsilon_1}+\sqrt{\varepsilon_0}}, \tag{3.20}$$

where ε_1 is the permittivity of the road, equal to $\varepsilon_r\varepsilon_0$, and ε_0 is the permittivity of air. From Figure 3.12, it is observed that the mean backscattering coefficient σ_{pq}^0 is proportional to $\rho_0^{b_3}$, which in fact is a function of the dielectric constant of the road.

Synthesize all the observations shown above, the mean values of backscattering coefficients are modeled as the following function:

$$\sigma_{pq}^0 = A\frac{\cos^{\alpha_1}\theta\,|\rho_0|^{\alpha_2}\,(ks)^{\alpha_3 cos\theta+\alpha_4}}{(kl)^{\alpha_5 cos\theta+\alpha_6}}\left(\frac{m^2}{m^2}\right), \qquad p,q = h\ or\ v \tag{3.21}$$

In the function, the coefficients A, α_1 to α_6 are obtained by curve fitting from the simulated data, and are different for different polarizations. The values of those coefficients are shown in Table 3 - 3.

Table 3 - 3. Coefficients of the reduced backscattering model for different polarizations

Coefficient	σ_{vv}^0	σ_{hh}^0	σ_{hv}^0 or σ_{vh}^0
A	10.77	2.73	0.927
α_1	2.67	3.15	2.96
α_2	1.86	1.24	2.61
α_3	5.40	1.38	-2.27
α_4	0.47	1.94	3.42
α_5	0.78	1.16	0.83
α_6	2.38	1.86	2.43

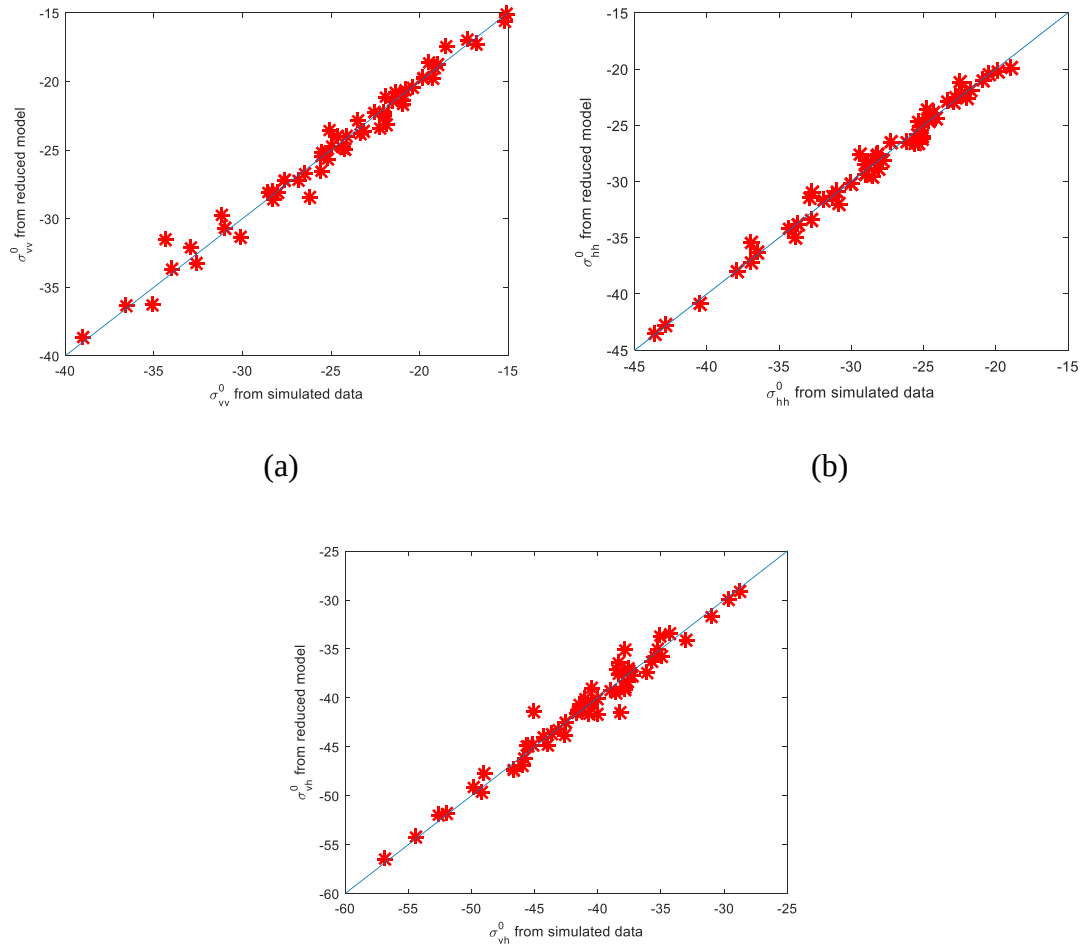

Figure 3.13. The regression performance of the proposed reduced backscattering model for (a) VV polarization, (b) HH polarization and (c) VH/HV polarization

The linear regression performance of the reduced backscattering model described in (3.21) is shown in Figure 3.13. The x axis represents the original data and the y axis represents the data calculated from the reduced model. Very good agreements between original data and the results generated by reduced model can be observed from the figures. The root-mean-square error for VV polarization is 0.76 dB, that for HH polarization is 0.69 dB and that for VH/HV polarization is 1.05 dB. Therefore, the accuracy of the proposed reduced empirical model is validated.

3.6 Semi-empirical volumetric backscattering models

The reduced backscattering models derived in previous section can only be applied to surface backscattering problem with homogeneous random rough surface. In the homogeneous rough surface assumption, the permittivity of the rough surface is constant in different locations, and the RMS height and correlation length are statistically identical in different locations. However, in real road like asphalt road, the homogeneous assumption is invalid and the volumetric backscattering due to the inhomogeneity of the material contributes largely to the entire backscattering power. To characterize the volumetric backscattering coefficients, the radiative transfer equation methods [89] [104] are applied. The radiative transfer equation is given by [90] [105],

$$\frac{d\boldsymbol{I}(\boldsymbol{r},\hat{s})}{ds} = -\kappa_e \boldsymbol{I}(\boldsymbol{r},\hat{s}) + \int_{\boldsymbol{4\pi}} \boldsymbol{P}(\hat{s},\hat{s}')\boldsymbol{I}(\boldsymbol{r},\hat{s}')d\Omega', \tag{3.22}$$

where $\boldsymbol{I}(\boldsymbol{r},\hat{s})$ is specific intensity at location $\boldsymbol{r}$ and radiating to direction $\hat{s}$, s denotes the path length in the direction $\hat{s}$, κ_e is extinction coefficient contributed by both absorption and scattering, $\boldsymbol{P}(\hat{s},\hat{s}')$ denotes phase matrix from incident direction $\hat{s}'$ to scattering direction $\hat{s}$.

Because the random property of the permittivity, density and geometry of scatterers inside different roads are unknown, it is difficult to obtain the extinction coefficient and phase matrix by theoretical analysis or numerical simulation. Therefore, a semi-empirical model is proposed in [90] to find the backscattering coefficients, and the backscattering coefficients for different polarizations are given by:

$$\begin{aligned}
\sigma_{vv}^0 &= 4\pi\cos\theta_0 \,|t_{01}^v|^2|t_{10}^v|^2 \frac{p_1}{2\kappa_e},\\
\sigma_{hh}^0 &= 4\pi\cos\theta_0 \left|t_{01}^h\right|^2\left|t_{10}^h\right|^2 \frac{p_1}{2\kappa_e},\\
\sigma_{vh}^0 &= 4\pi\cos\theta_0 \left|t_{01}^h\right|^2|t_{10}^v|^2 \frac{p_2}{2\kappa_e},\\
\sigma_{hv}^0 &= 4\pi\cos\theta_0 \,|t_{01}^v|^2\left|t_{10}^h\right|^2 \frac{p_2}{2\kappa_e},
\end{aligned} \tag{3.23}$$

where θ_0 denotes the incident angle, t_{01}^{v} denotes the transmission coefficient from air to the road with vertical polarization or TM wave, and t_{10}^{h} denotes the transmission coefficients from the road to air with horizontal polarization or TE wave, p_1 and p_2 are the terms in phase matrix related to co-polarization and cross-polarization, respectively.

The values of $\frac{p_{1,2}}{2\kappa_e}$ are obtained from measurement data, and therefore the equation (3.23) is called semi-empirical model. Three different types of road, weather asphalt, new asphalt and concrete, are measured with 77 GHz continuous wave radar. The pictures of the roads are shown below:

(a) (b) (c)

Figure 3.14. Radar measurements for (a) weathered asphalt, (b) fresh asphalt and (c) concrete road

Figure 3.14 shows the pictures of measurement for different types of ground. The radar is scanning its main beam in elevation direction manually, and at each elevation angle, the radar can scan its beam in azimuth direction mechanically, resulting in more than 30 samples of radar backscattering measurement, and the backscattering coefficients are obtained from the RCS values divided by the beam's footprint area as is shown in Figure 3.14 (a). From the measured backscattering coefficients, the values for $\frac{p_{1,2}}{2\kappa_e}$ can be found and are given in Table 3 - 4.

Table 3 - 4. Values of $\frac{p_{1,2}}{2\kappa_e}$ for different types of road

Roads	$\frac{p_1}{2\kappa_e}$	$\frac{p_2}{2\kappa_e}$
Weathered asphalt	0.0064	0.0015
Fresh asphalt	0.0029	0.00085
Concrete	0.00083	0.0000167

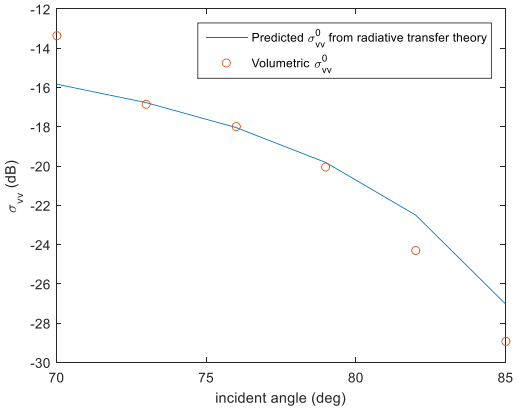

(a)

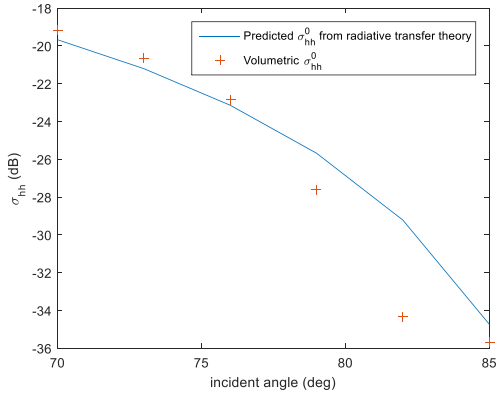

(b)

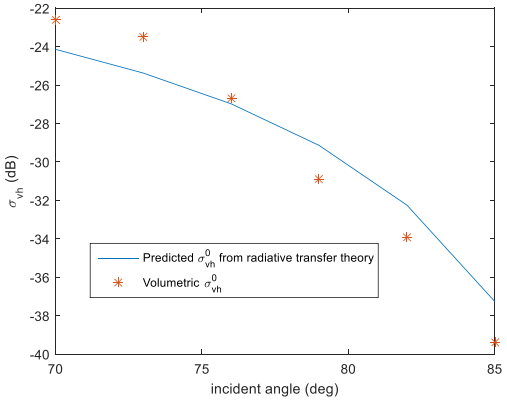

(c)

Figure 3.15. Comparison of backscattering coefficients between measurements and semi-empirical model for weathered asphalt with (a) VV polarization, (b) HH polarization and (c) VH polarization

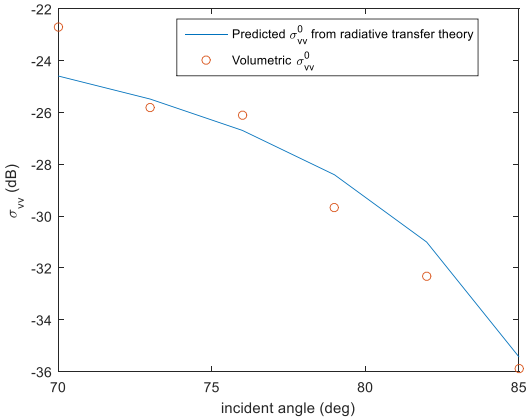

(a)

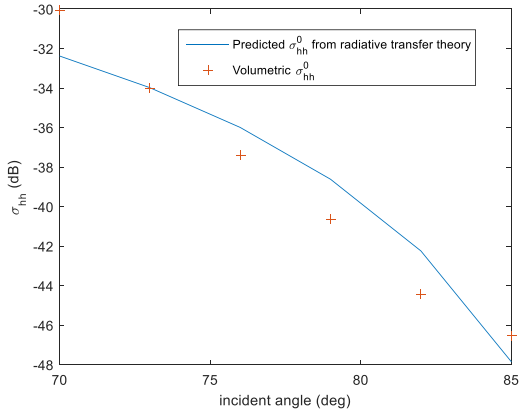

(b)

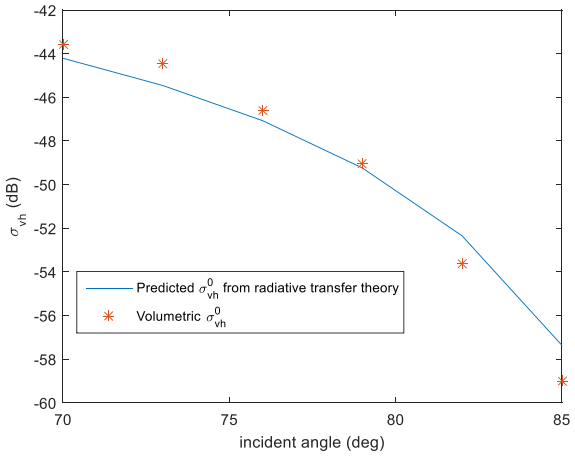

(c)

Figure 3.16. Comparison of backscattering coefficients between measurements and semi-empirical model for concrete with (a) VV polarization, (b) HH polarization and (c) VH polarization

The comparison of measured data and the data from radiative transfer models are shown in Figure 3.15 and Figure 3.16. Good agreement is found between measurement data and the data

generated by semi-empirical model. It should be noted that the values of $\frac{p_{1,2}}{2\kappa_e}$ may only be applied to the road conditions of the samples under test and could be different for the same type of road but with different conditions.

3.7 Conclusion

In this chapter, millimeter wave backscattering coefficients with different polarizations for various road surfaces are studied. The backscattering power from road is divided into two parts: surface scattering and volumetric scattering. For surface scattering, the road surface profiles are measured, and their statistical features are obtained. Then the random rough surfaces with different statistical features are generated and simulated by full-wave numerical simulation software. By applying the near field and far field transformation, the backscattering coefficients can be derived from the full-wave simulation and the average backscattering coefficients are obtained through Monte-Carlo simulations. Finally, the backscattering coefficients with different polarizations are modeled as reduced analytical functions of the road surfaces' statistical features, dielectric constant and incident angle.

Volumetric scattering usually dominates the backscattering power from road. The study of volumetric scattering is based on radiative transfer theory. The backscattering models utilizing measurement data are presented in this chapter. The measured roads including fresh asphalt, new asphalt and concrete roads. Good agreements are observed between the measured data and the semi-empirical models.

Chapter 4 Radar Statistical Models and Real-time Radar Response Simulation

4.1 Introduction

The traffic targets are usually complex and electrically very large in MMW band. As a result, their radar cross-section (RCS) often fluctuate rapidly as a function of incident angle and frequency. This phenomenon can be addressed with PO simulations. For example, the RCS of a 1.8 m tall walking man is simulated at the range of 50 m for all incident azimuth directions at 77 GHz is shown in Figure 4.1 (a). It is shown that the simulated backscattering RCS may change more than 20 dB if the incident angle alters slightly. The RCS of targets could fluctuate with frequency as well. In another example, the RCS as a function of frequency for a sedan is shown in Figure 4.1 (b). More than 15 dB RCS variation is observed with frequency. Therefore, statistical approach should be applied to reveal the intrinsic property of the apparently randomized data.

The study on the statistical behavior of RCS for complex target can be traced back to 1950s by Peter Swerling, and the proposed statistical models are also called Swerling target models [109]. The Swerling models can be generalized as Chi-square distribution models, which are actually special cases of gamma distribution [110]. For example, Swerling I model, which has been widely used in aviation targets, is gamma distribution with shape parameter k=1, or exponential distribution. Besides gamma distribution, other statistical distributions like Lognormal distribution [111], [112] and Weibull Distribution [113], [114], [115] have been used to characterize the fluctuation of RCS for different types of targets including aircrafts, ships, vehicles and sea clusters

in different frequency band. However, the statistical models for traffic targets like pedestrians and vehicles in MMW band hasn't been reported in literature yet.

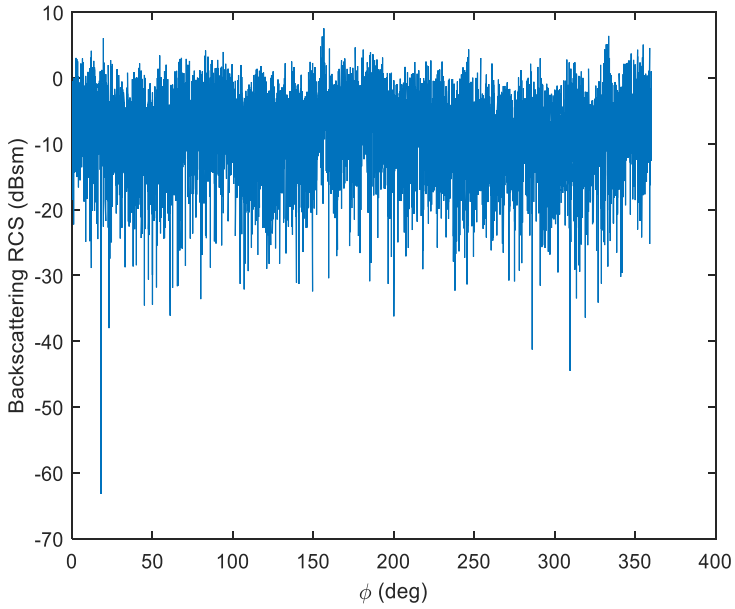

(a)

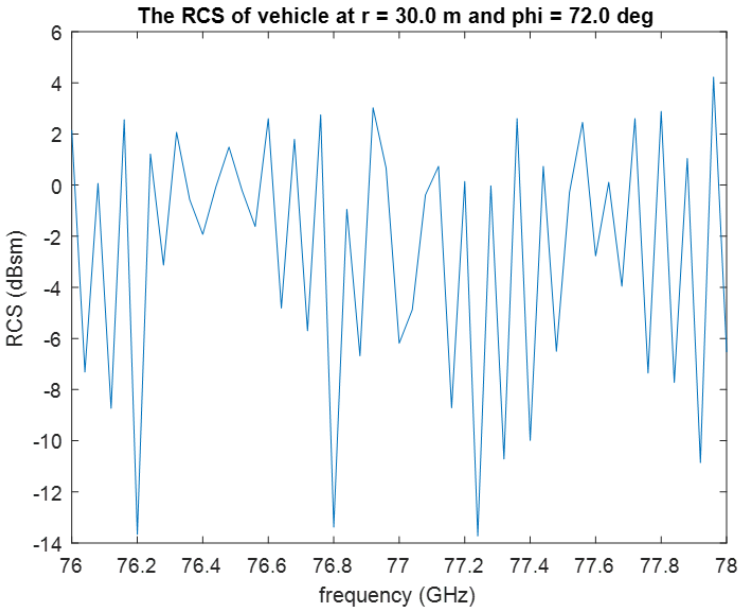

(b)

Figure 4.1. Simulated RCS as a function of (a) incident angle for a 1.8m pedestrian, and (b) frequency for a sedan

Accurately characterize the RCS statistical features for pedestrians and vehicles can enable fast radar simulation and assist the autonomous car to identify targets as well. In this chapter, numerous RCS data are generated first for various targets including pedestrians, vehicles and other stationary targets. Pedestrians are examined with different weights, heights, ages, genders and poses, vehicles include sedans, SUVs, hatchbacks, buses, trucks, bike and motorcycles, other stationary targets include traffic lights, traffic signs, lamp posts, trash bins, tree trunks, animals etc. Then the RCS data of one target with similar ranges, frequencies and incident angles are fit to several known statistical distributions, and the statistical parameters are summarized and recorded. In the end, the statistical RCS models are utilized to perform real-time Radar response simulation from traffic scene in Unreal Engine 4.

4.2 RCS statistical models of pedestrians for real-aperture radar

For real-aperture or beam-steering radar that has one transmitter and one receiver, a traffic target can be represented by one RCS value. The RCS value is treated as a random variable whose features could be a function of incidence angle, range and other parameters of targets. Regarding the driving safety, pedestrians are the most important targets and therefore, the first priority is to study the RCS behavior of pedestrians.

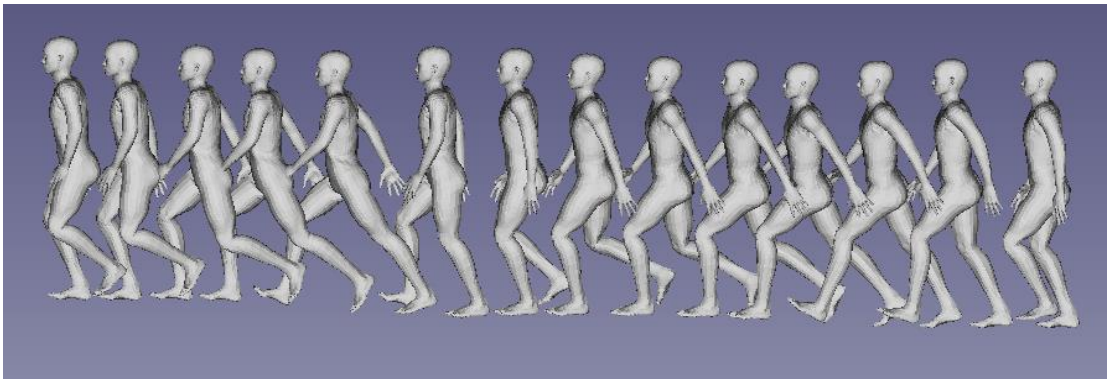

(a)

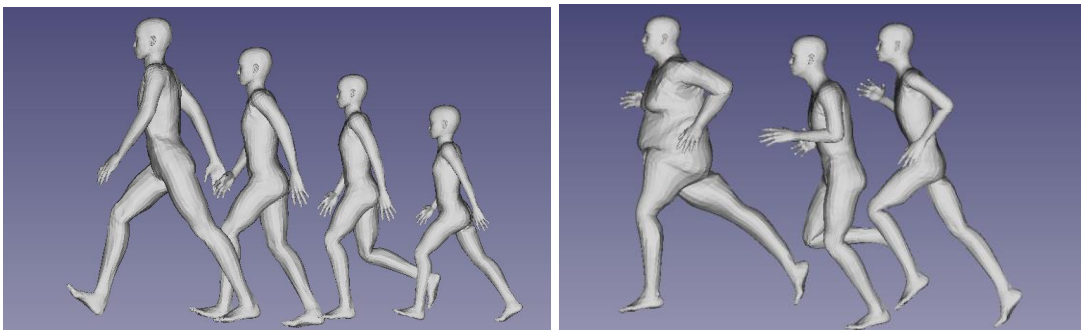

(b) (c)

Figure 4.2. CAD models of male pedestrians for (a) different poses during one period of walking, (b) different heights with walking motion and (c) different weights with jogging motion (same height)

One of the major challenges in simulation for the RCS of pedestrians is the dynamic behaviors of pedestrians. In traffic scene, pedestrians usually exhibit various poses during walking or jogging motion. To capture the features of RCS response from different behaviors, we first generate the computer-aid-design (CAD) models for human with multiple poses of one motion (walking or jogging). Some examples of human CAD models with different poses, heights and weights are depicted in Figure 4.2. The CAD model for a human with arbitrary height and body shape is created by an open-source software MakeHuman [106], and the poses during walking and jogging are obtained from CMU's motion capture database [107]. Finally, the poses are integrated into a given pedestrian CAD model in another open source 3D computer graphic software Blender [108]. The CAD models are generated for different genders as well. For each gender, CAD models are created for more than five different heights, and for each height, there are five different body shapes. For pedestrian with specific gender, height and weight, CAD models are further created for two motions: walking and jogging. For each motion, more than 10 poses are generated for each person. The hierarchy structure of CAD models for pedestrians are illustrated in Figure 4.3.

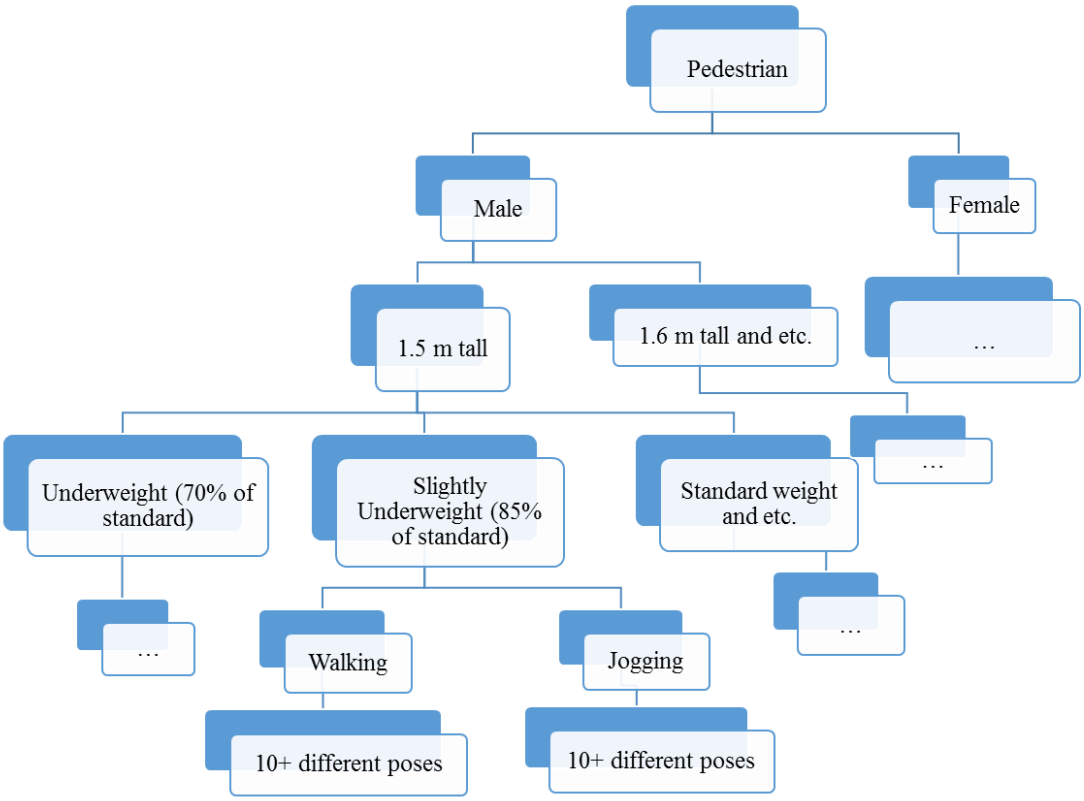

Figure 4.3. Hierarchy of CAD models generated for pedestrians

In the numerical simulation, the antenna's beamwidth of the radar is assumed to be 3º, and the first side-lobe level is compressed to -26 dB lower than the main lobe. The radiation pattern of the antenna is given in Figure 4.4. The radiation pattern is corresponding to a 2D antenna array with triangular tapered current distribution among antenna array elements.

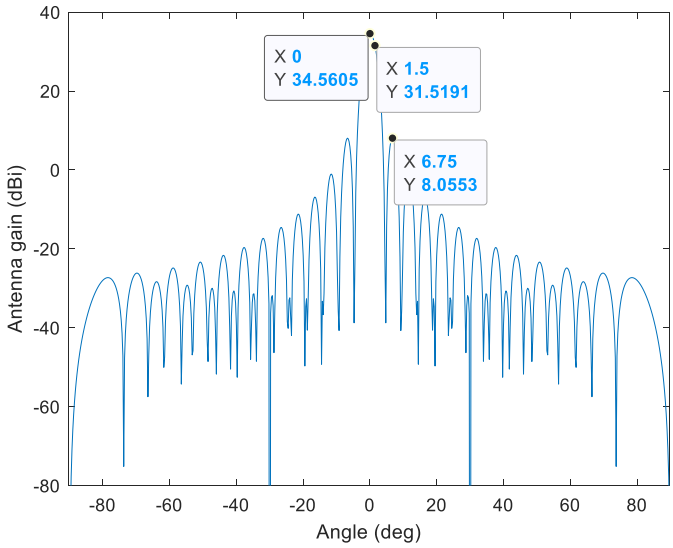

Figure 4.4. Radiation pattern of the antenna employed in simulation

CAD models of 10+ continuous poses of one period of walking or jogging motion for one pedestrian are used in the simulation, and their RCS values may differ for the same range and incident angle. Because it is difficult to track the exact incident angle and pose of one pedestrian, the simulated RCS data of one pedestrian with different poses at one range and ±5º incident angles are considered as independent samples in statistical analysis. For example, Figure 4.5 shows the averaged RCS and standard deviation of RCS from different incident angles at range of 100 m for a 1.7m tall walking woman. The averaged RCS has peak values at 0º, 90º, 180º and 270º, which are corresponding to the two sides, front and back of the person. Due to the rotational symmetry of pedestrians, it is found that the mean values can be fit by a Fourier series up to fourth order of incident angle ϕ, which is given by:

$$< \sigma_{vv}(\phi) >= \sum_{n=1}^{4} a_n cos(n\phi) + b_n sin(n\phi) + c_0(m^2), \tag{4.1}$$

where c_0 denotes the average RCS value of all azimuth angles, and a_n, b_n are coefficients of Fourier series, which determine the variation of mean RCS at different azimuth angles. The values

of a_n, b_n can be obtained from curve fitting for the 10º averaged RCS as a function of azimuth angle.

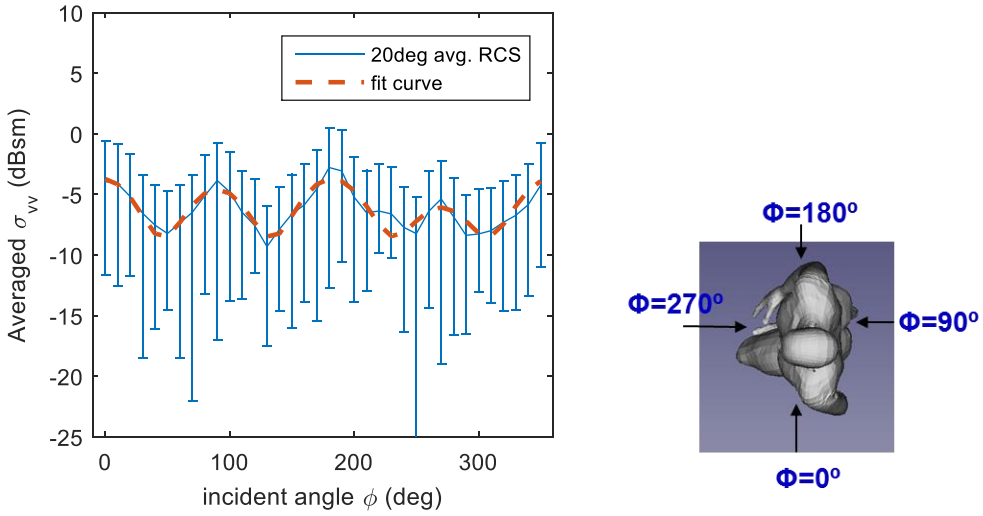

Figure 4.5. Mean values and mean ± standard deviation values of RCS as a function of incident angles for a 1.7m tall walking woman in the range of 100 m

Notably, the concept of RCS is for point target, and point-target approximation requires the radar to be in the far-field range of the target. The far-field range equation is given in (4.2), where D is the largest dimension of target and λ is the wavelength. In one example, the far-field range for a 1.8m tall pedestrian is more than 1600 m at 77 GHz. Hence, the radar usually operates in the near-field range of traffic targets. Besides, depending on the range and beamwidth, the pedestrian may be partially illuminated, which results in the RCS value to be a function of range. Therefore, the Fourier coefficients a_n, b_n and c_0 should be functions of range as well.

$$l = \frac{2D^2}{\lambda}. \tag{4.2}$$

To find how those values change with range, first massive simulations are performed for pedestrians at different ranges from 5 m to 100 m. The averaged RCS values of all azimuth angles and all poses can be displayed as a function of range as depicted in Figure 4.6. It shows that at near range where the pedestrian is partially illuminated, the averaged RCS is almost a linear function

with range, and after the range where the pedestrian is fully illuminated, the RCS gradually increases with the distance to the radar. Therefore, we can define a reference range R_{ref} denotes the range that the target is fully illuminated. In this example of a 1.8 m tall pedestrian and 3° beamwidth radar, $r_{ref} = 42\ m$.

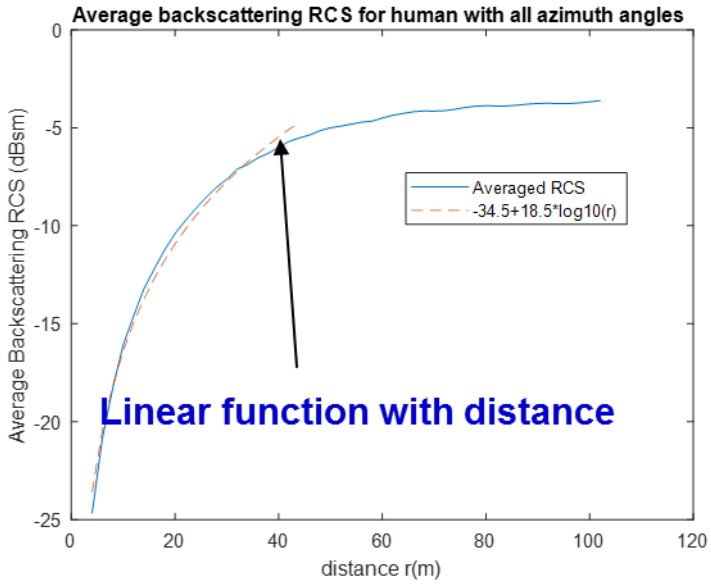

Figure 4.6. Backscattering RCS for a 1.8m tall walking man averaged for all azimuth angles and poses as a function range

While 20° averaged RCS can be properly fit by an analytic function shown in Figure 4.5, the corresponding standard deviation cannot. To best describe the statistical property of RCS from pedestrians, the RCS data are fitted by known statistical distributions to obtain the corresponding statistical parameters instead of just mean values and standard deviations. In the example shown in Figure 4.7, the RCS data are fitted into Weibull, lognormal and gamma distribution.

The probability density function (PDF) for Weibull distribution is given by:

$$f(x|A,B) = \frac{B}{A}\left(\frac{x}{A}\right)^{B-1} exp\left\{-\left(\frac{x}{A}\right)^{B}\right\}, \tag{4.3}$$

where A and B are two parameters of Weibull distribution. That for lognormal distribution is:

$$f(x|\mu,\sigma) = \frac{1}{x\sigma\sqrt{2\pi}} exp\left\{-\frac{(\ln x - \mu)^2}{2\sigma^2}\right\}, \tag{4.4}$$

where μ and σ are two parameters of lognormal distribution. The PDF for gamma distribution is:

$$f(x|a,b) = \frac{1}{b^a \Gamma(a)} x^{a-1} exp\left\{-\frac{x}{b}\right\}, \tag{4.5}$$

where a is a shape parameter and b is a scale parameter of gamma distribution, and $\Gamma(a)$ is Gamma function.

Figure 4.7 depicts the fitting performance of the three distributions described above for the RCS of a 1.8 m tall walking man with range of 15 m and incident angle of 45°. It shows that both Weibull distribution and gamma distribution have excellent fitting performance in this example. To quantitatively evaluate the fitting performance, a fitting error in CDF is defined as:

$$\delta = \sqrt{\frac{\sum_1^N \left(F_{fit}(x) - F_{emp}(x)\right)^2}{N}}, \tag{4.6}$$

where $F_{fit}(x)$ is the CDF fitted to a known distribution, $F_{emp}(x)$ is the empirical CDF.

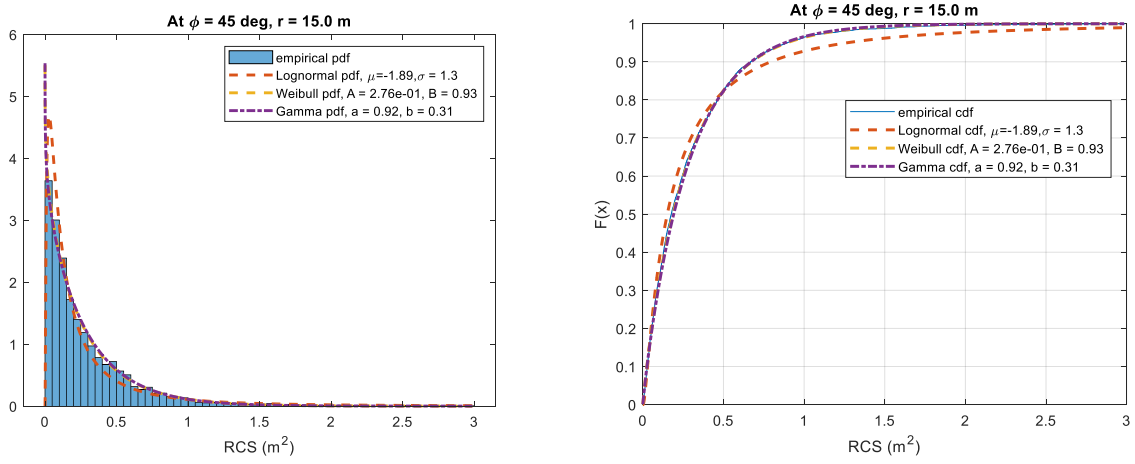

(a) (b)

Figure 4.7. (a) Probability density functions and (b) cumulative density functions comparisons between empirical data and several statistical distributions

The fitting error is evaluated for all ranges and incident angles, and the performance for different distributions are given in Table 4 - 1. It shows that Weibull distribution has the best fit to the RCS of 1.8 m tall pedestrian. Similarly, the simulated RCS data for other pedestrians can be best fitted by Weibull distribution as well. Therefore, Weibull distribution is chosen as the statistical distribution of RCS in the following discussion.

Table 4 - 1. Fitting errors δ of different statistical distributions for the RCS of a 1.8 m tall walking man

Distribution	Lognormal	Weibull	Gamma
Fitting error	0.0368	0.0159	0.0256

In Weibull distribution, A is scale parameter and B is shape parameter. When B = 1, Weibull distribution is reduced to exponential distribution (Swerling I model), which has been successfully applied to represent the fluctuation of RCS for many aircrafts in the far field. As mentioned, the radar is operating in the near field range of pedestrians, and the RCS is a function of range as shown in Figure 4.6. To find proper analytic expressions for the Weibull parameters as functions of incident angle and range, control variable method is applied. The parameters A and B are first fitted as functions of incident angle in fixed range by Fourier series and then the Fourier coefficients are modelled as functions of range. For example, Figure 4.8 depicts the Weibull parameters A and B as functions of incident angle for different ranges for a 1.8 m tall walking man. The functions of incident angle are fitted by the following Fourier series:

$$A(\phi,r) = \beta_{1a}(r)sin(\phi) + \alpha_{2a}(r)cos(2\phi) + \beta_{3a}(r)sin(3\phi) + \alpha_{4a}(r)cos(4\phi) + \gamma_{0a}(r)(m^2), \quad (4.7)$$

$$B(\phi,r) = \beta_{1b}(r)sin(\phi) + \alpha_{2b}(r)cos(2\phi) + \beta_{3b}(r)sin(3\phi) + \alpha_{4b}(r)cos(4\phi) + \beta_{5b}(r)sin(5\phi) + \alpha_{6b}(r)cos(6\phi) + \gamma_{0b}(r). \quad (4.8)$$

The Fourier coefficients α_i and β_j for Weibull parameters A and B as functions of range are shown in Figure 4.9. Those coefficients then are fitted by polynomial functions of range. Notice that the range shown in the Figure is the normalized range, which is defined as r/r_{ref}.

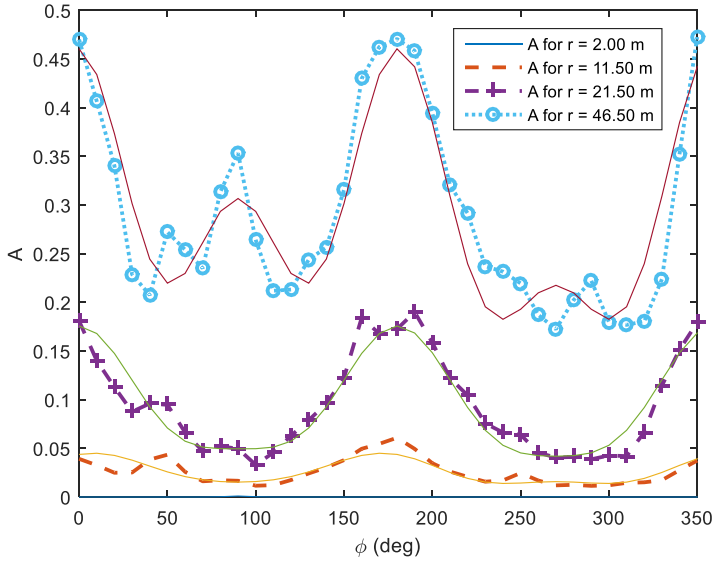

(a)

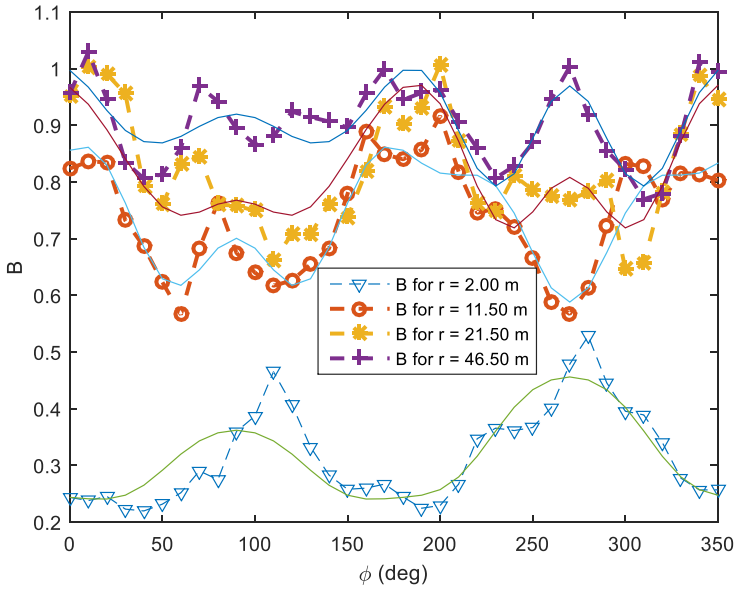

(b)

Figure 4.8. Values of Weibull parameters (a) A and (b) B as functions of incident angle in different ranges and their fitted curves by Fourier series (solid lines)

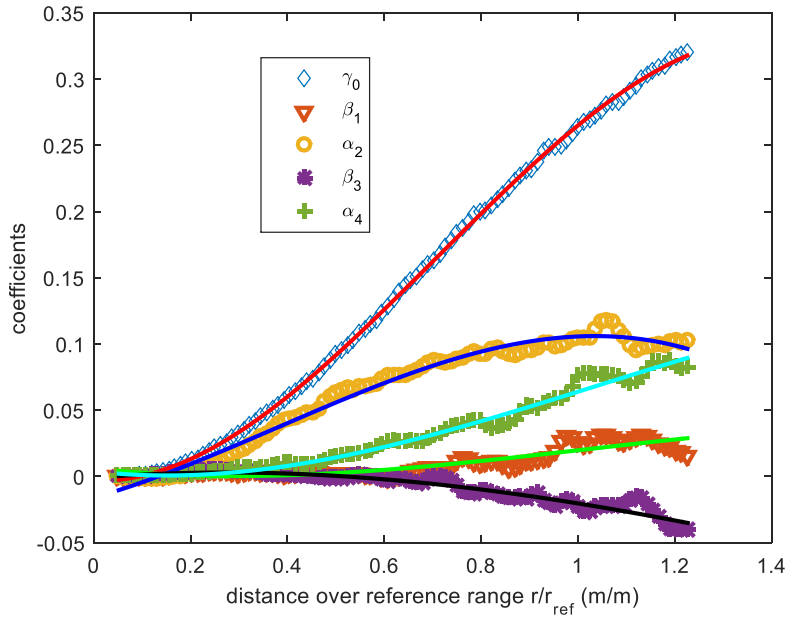

(a)

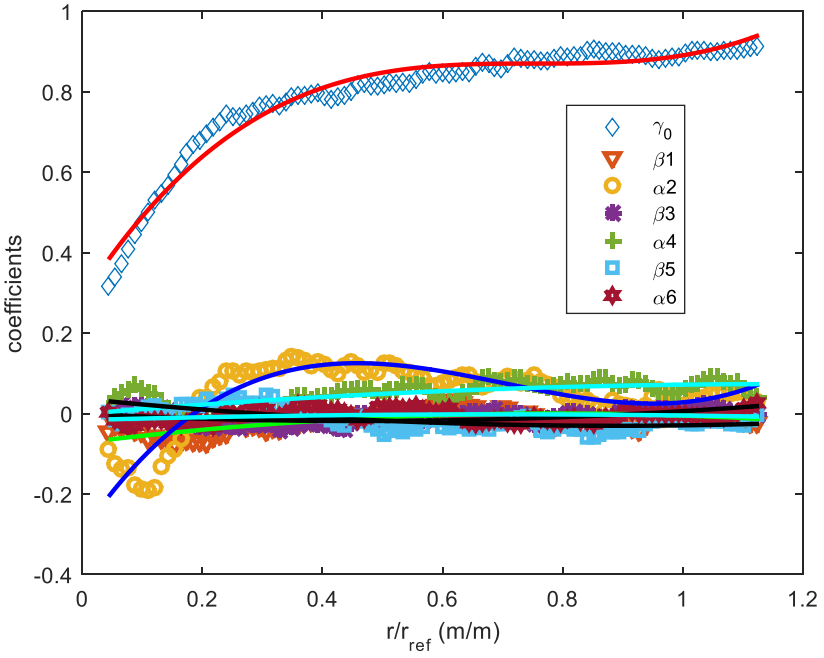

(b)

Figure 4.9. Fourier coefficients for Weibull parameters (a) A and (b) B as functions of range and are fitted by polynomial functions (solid lines)

In one example of 1.8 m tall walking man, the coefficients α_i and β_j, which are shown in Figure 4.9, are expressed in the following functions. For parameter A:

$$\gamma_{0a} = -0.029 - 0.0184\frac{r}{r_{ref}} + 0.542\left(\frac{r}{r_{ref}}\right)^2 - 0.256\left(\frac{r}{r_{ref}}\right)^3$$
$$\beta_{1a} = 0.006 - 0.041\frac{r}{r_{ref}} + 0.082\left(\frac{r}{r_{ref}}\right)^2 - 0.027\left(\frac{r}{r_{ref}}\right)^3$$
$$\alpha_{2a} = -0.016 + 0.104\frac{r}{r_{ref}} + 0.14\left(\frac{r}{r_{ref}}\right)^2 - 0.123\left(\frac{r}{r_{ref}}\right)^3$$
$$\beta_{3a} = -0.0011 + 0.031\frac{r}{r_{ref}} - 0.06\left(\frac{r}{r_{ref}}\right)^2 + 0.01\left(\frac{r}{r_{ref}}\right)^3$$
$$\alpha_{4a} = 0.0039 - 0.042\frac{r}{r_{ref}} + 0.151\left(\frac{r}{r_{ref}}\right)^2 - 0.048\left(\frac{r}{r_{ref}}\right)^3 \quad (4.9)$$

For parameter B:

$$\gamma_{0b} = 0.288 + 2.\ 12\,{}^{r}/_{r_{ref}} - 2.58({}^{r}/_{r_{ref}})^2 + 1.04({}^{r}/_{r_{ref}})^3$$
$$\beta_{1b} = -0.073 + 0.17\,{}^{r}/_{r_{ref}} - 0.099({}^{r}/_{r_{ref}})^2$$
$$\alpha_{2b} = -0.296 + 2.01\,{}^{r}/_{r_{ref}} - 2.98({}^{r}/_{r_{ref}})^2 + 1.29({}^{r}/_{r_{ref}})^3$$
$$\beta_{3b} = -3.05e-4 - 0.072\,{}^{r}/_{r_{ref}} + 0.071({}^{r}/_{r_{ref}})^2$$
$$\alpha_{4b} = -0.0013 + 0.117\,{}^{r}/_{r_{ref}} - 0.046({}^{r}/_{r_{ref}})^2$$
$$\beta_{5b} = 0.0369 - 0.139\,{}^{r}/_{r_{ref}} + 0.072({}^{r}/_{r_{ref}})^{2^2}$$
$$\alpha_{6b} = -0.0162 + 0.038\,{}^{r}/_{r_{ref}} - 0.025({}^{r}/_{r_{ref}})^2 \quad (4.10)$$

Notice that for different pedestrians the coefficients of the functions can be different. Particularly, people with different weight and height may have different coefficients on the

Weibull parameters. It is understood that the weight and height are highly correlated, that a tall person usually has more weight than a shorter person given the same body shape. In order to isolate the impact of height on weight, two concepts are introduced. The first one is called standard weight (w_0), which is the weight for a given height normal shape person. We used the standard of normal shape defined by the human CAD generation software MakeHuman. It is noted that the standard weight is different for man and woman, and the standard weight as a function of height is given by:

$$w_0(h) = 64.38h^2 - 112.1h + 65.78\ (kg), \qquad \text{for man} \tag{4.11}$$

$$w_0(h) = -0.714h^2 + 91.73h - 95.02(kg), \qquad \text{for woman} \tag{4.12}$$

where h is the height of the person, with unit in *m*, and ranging from 1.4 m to 2 m.

The second quantity is called shape factor (*sf*) and is defined as w/w_0. Shape factor is used to represent how a person's weight deviated from its standard weight. For example, the standard weight for a 1.7 m tall woman is 57.4 kg according to (4.12), and a woman with 1.7 m height and 50 kg weight then has shape factor of 0.871. Figure 4.10 illustrates the CAD models of 1.7 m tall woman with different body shapes. The demonstrated body shapes include skinny shape (#1) to overweighted shape (#7), and their weights and body factors are given in Table 4 - 2. The weight is measured by multiplying the volume of the CAD model and density of human body (0.985 g/ml). Many software including autoCAD can evaluate the volume of a CAD model, and one of the algorithm is to divide the entire CAD model into many small tetrahedrons, and for each tetrahedron, there is analytical solution to calculate the volume [116].

The statistical analysis and curve fitting process mentioned before are repeated for the pedestrians with different genders (man and woman), actions (walking and jogging), heights (1.4m to 2m) and shape factors (0.65 to 2.2). The coefficients α_i, β_j and γ_0 as functions of range are

recorded and tabulated for all different pedestrians. The tabulated statistical data can be applied to quickly generate RCS values of a pedestrian given the information of range and aspect angle in a real-time radar simulation application. For a pedestrian with arbitrary weight and height, his/her shape factor will be calculated first, and his/her corresponding statistical parameters will be calculated based on linear interpolation from the lookup table generated from massive simulations.

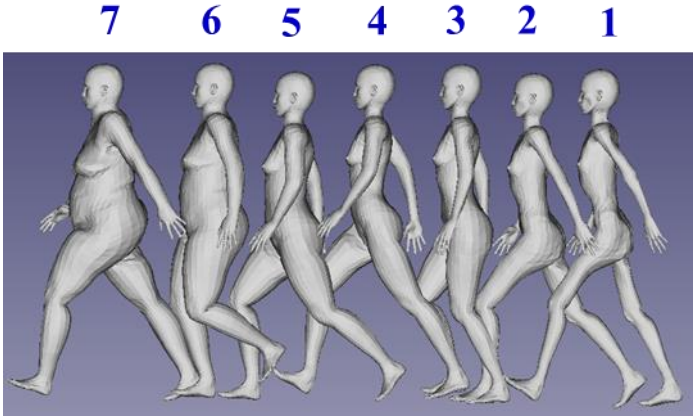

Figure 4.10. CAD models for 1.7 m tall walking woman with different shape factors

Table 4 - 2. Weights and shape factors for different samples of 1.7 m tall woman

Sample #	1	2	3	4	5	6	7
Weight (kg)	38.4	48.6	57.4	59.2	72.9	88.8	104.0
Shape factor	0.67	0.85	1	1.03	1.27	1.55	1.81

This semi-lookup table semi-analytic model can be efficiently used to find the RCS value of a given pedestrian. Here gives an example to fast generate RCS value of a 1.75 m tall walking man with weight of 70 kg, and he faces the radar at the range of 30 m. The first task is to evaluate the corresponding Weibull parameters A and B of the RCS, and then we can generate the RCS value through Weibull distribution random number generator. The standard weight for a 1.75 m tall man is 66.77 kg according to (4.11). Thus, his shape factor is 1.05. Because in the tabulated

library, there is no male model with 1.75 m tall and shape factor of 1.05, but instead there are models for 1.7 m tall man and 1.8 m tall man, and shape factor of 1 and 1.25. To calculate the Weibull parameters A and B in this example, first the values of Weibull parameters A and B for four different cases are evaluated: (1) 1.7 m tall walking man with shape factor of 1, (2) 1.7 m tall walking man with shape factor of 1.25, (3) 1.8 m tall walking man with shape factor of 1, and (4) 1.8 m tall walking man with shape factor of 1.25. The Weibull parameters A and B for those models can be evaluated from analytical fitted curve with the methods described previously. The parameters for those four models at range of 30m and azimuth angle of 90º (front view) are given in Table 4 - 3, and the estimated Weibull parameters for a 1.75 m tall waking man with weight of 70 kg is: A = 0.127 and B = 0.853. Notice that the Weibull parameters for the pedestrians with small difference in weight and height are quite similar and the differences are smaller than the differences between Weibull parameters from different aspect angles for one pedestrian. Therefore, the statistical RCS information cannot be used to identify a person's weight and height.

Table 4 - 3. Weibull parameters for the four pedestrians with different height and weight in the range of 30 m and azimuth angle of 90º

Weibull Parameters:	A	B
1.7 m tall man with shape factor of 1	0.137	0.863
1.7 m tall man with shape factor of 1.25	0.112	0.851
1.8 m tall man with shape factor of 1	0.120	0.840
1.8 m tall man with shape factor of 1.25	0.117	0.868

4.3 RCS statistical models of vehicles and other targets for real-aperture radar

Other than pedestrians, there are many other important targets can be detected by MMW radar in a traffic scene. Those targets include but are not limited to vehicles like bikes, motorcycles, sedans, SUVs, trucks, buses and etc., other targets like lamp posts, traffic lights, traffic signs, tree trunks, dogs, and etc. The failure of detecting those targets may also result in serious accidents. Similar to pedestrians, those targets are usually electrically very large, and the RCS values are fluctuating with both frequency and aspect angle. In this situation, the statistical approach is applied as well. Compared to the pedestrians, vehicles are larger in size and thereby when a beam-steering radar is scanning in azimuth directions, it might just illuminate different portion of the vehicle, and the RCS values different portions may be correlated rather than independently distributed.

In the following discussion, we take a sedan (Mazda 6) as an example to demonstrate the statistical analysis for large targets such as vehicles. The CAD model of the sedan is shown in Figure 4.11. The radar used in simulation has 3° beam width in both azimuth and elevation direction. Notice that in near range, the radar may only illuminate a portion of the vehicle, and in the initial study, the RCS values are collected when the radar is focusing on the center of the vehicle. It is illustrated in Figure 4.1 (b) that its RCS value is a function of frequency with a given aspect angle and range.

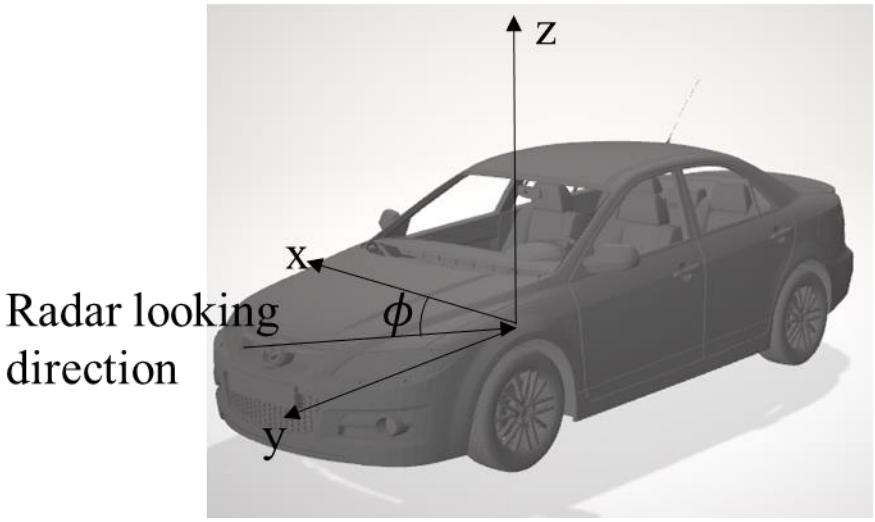

Figure 4.11. CAD model for a sedan with model of Mazda 6

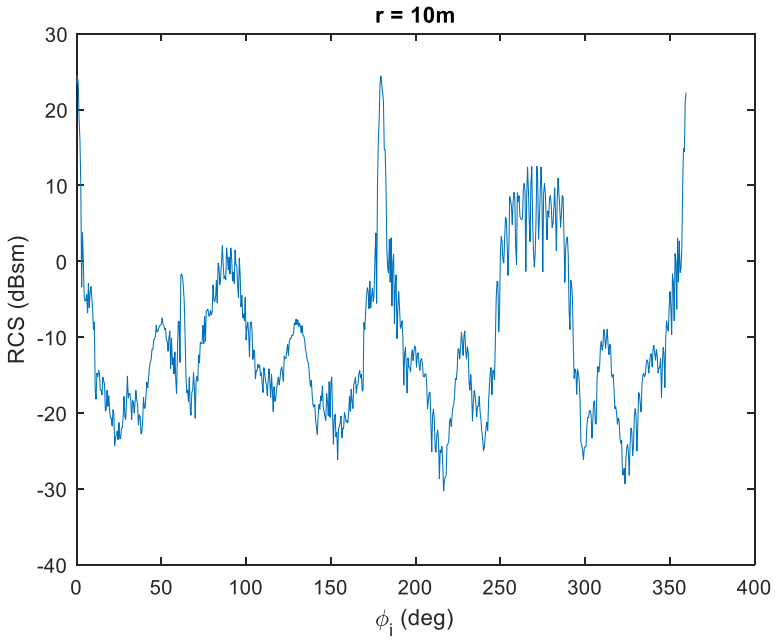

(a)

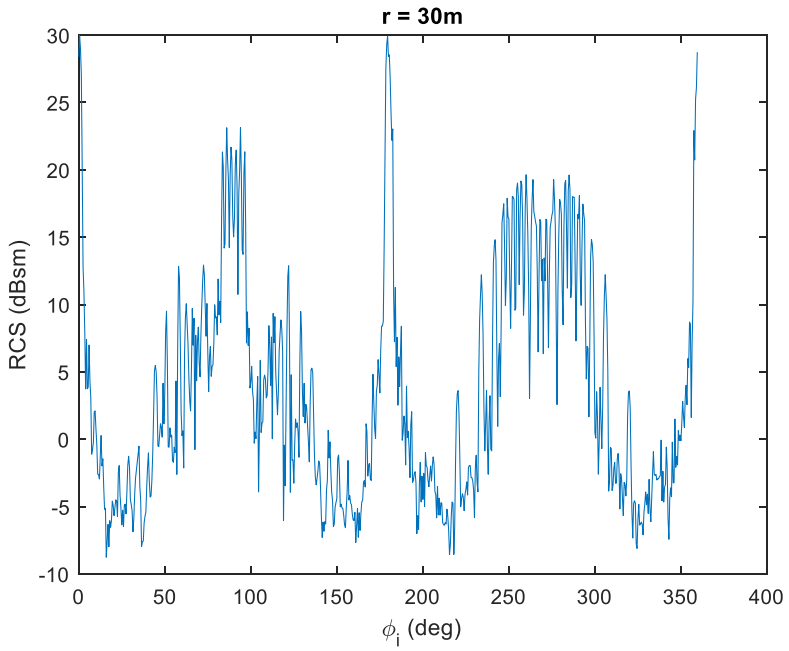

(b)

Figure 4.12. RCS of a Mazda 6 sedan as a function of azimuth angle for (a) range of 10 m and (b) range of 30 m

The frequency averaged RCS values as a function of aspect angle is given in Figure 4.12. In the figures, aspect angle of 0° refers to the right side of the car and 90° refers the front of the car. It is shown that the frequency averaged RCS values still vary more than 30 dB with the aspect angle of the car.

The RCS data in one range, aspect angle $\phi \pm 2.5°$, and different frequencies are considered have the same statistical distribution, and those values are fitted to known distributions such as Weibull distribution and Lognormal distribution as described in section 4.2. Some examples of the fitting performance of different statistical distributions are shown in Figure 4.13. It is shown that for some aspect angle and range, Weibull distribution has better fit, while for some other aspect angle and range, Lognormal fitting has better performance.

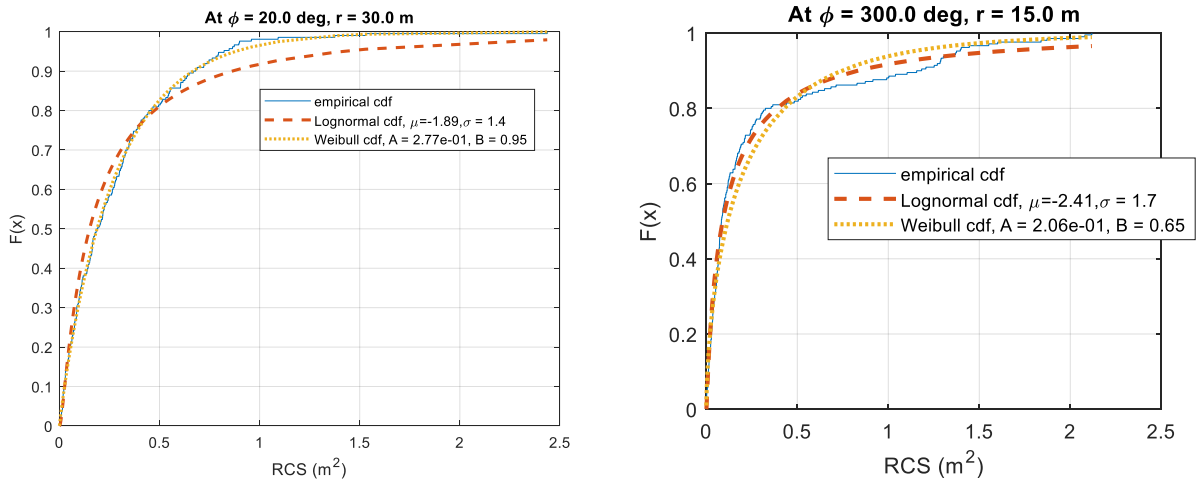

(a) (b)

Figure 4.13. The comparison between empirical CDF and fitted Lognormal and Weibull CDF for (a) range of 30 m, aspect angle of 20° and (b) range of 15 m, aspect angle of 300°

To best characterize the statistical features of the RCS for a vehicle, the following strategy is applied: first, fit the RCS data in one range, at one aspect angle ± 2.5°, and at different frequencies into both Weibull ($W_{A,B}(r,\phi)$) and Lognormal distribution ($L_{\mu,\sigma}(r,\phi)$), and this process is repeated for all ranges and angles, and all data are recorded into a library. In this example, the Weibull parameters A and B as functions of range and aspect angle are shown in Figure 4.14 and the Lognormal parameters μ and σ as functions of range and aspect angle are shown in Figure 4.15. Because the radar is in the near field range of the sedan, the statistical parameters will be functions of range, and those values change rapidly with aspect angles as well.

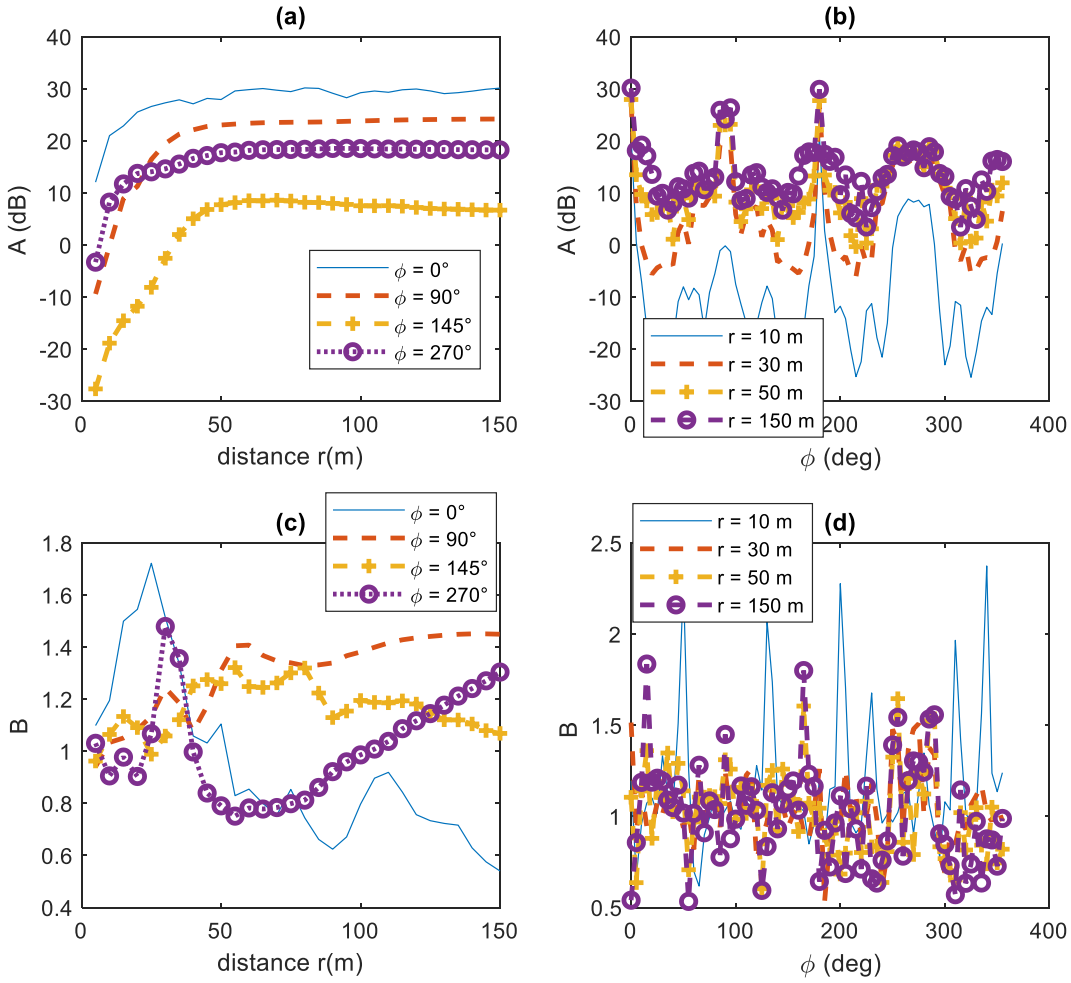

Figure 4.14. The fitted Weibull parameters (a) A and (c) B as a function of range for different azimuth angles, and (b) A and (d) B as a function of angle for different ranges

Second, find the RMS error between the fitted CDF and empirical CDF for the data of each range and each angle set and record the distribution with the smallest RME error. This is referred as the hybrid statistical distribution, and can be expressed as:

$$D(r,\phi) = \begin{cases} W_{A,B}(r,\phi), & if\ RMSE\left(W_{A,B}(r,\phi)\right) \le RMSE\left(L_{A,B}(r,\phi)\right) \\ L_{\mu,\sigma}(r,\phi), & otherwise \end{cases}, \tag{4.13}$$

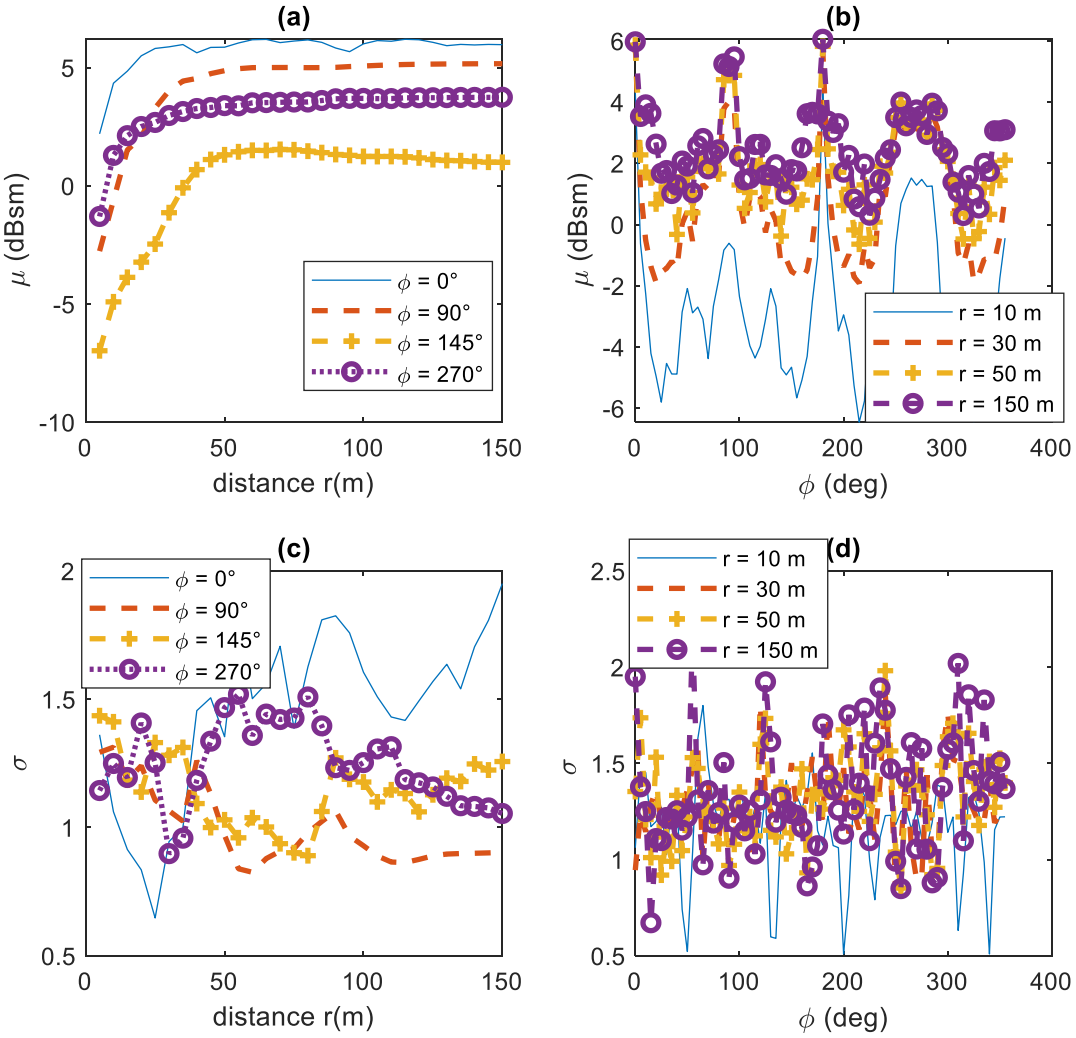

Figure 4.15. The fitted Lognormal parameters (a) μ and (c) σ as a function of range for different azimuth angles, and (b) μ and (d) σ as a function of angle for different ranges

Finally, the statistical features can be calculated for any range and aspect angle of the vehicle with the following steps. Step 1: navigate the specific range and angle set in the library; step 2: use the statistical distribution with the smallest RMS error; step 3: obtain the statistical parameters from linear interpretation method.

Figure 4.16 depicts the RMS error of the CDF for different statistical distributions. It shows that in the range of 50 m, Weibull distribution has the better performance in some angles, and

Lognormal distribution has the better fit in the rest angles. Figure 4.16 (b) shows the error performance of the hybrid distribution $D(r, \phi)$, and the overall averaged RMS error for $L_{\mu,\sigma}$, $W_{A,B}$ and D at 50 m are 0.054, 0.038 and 0.033 respectively.

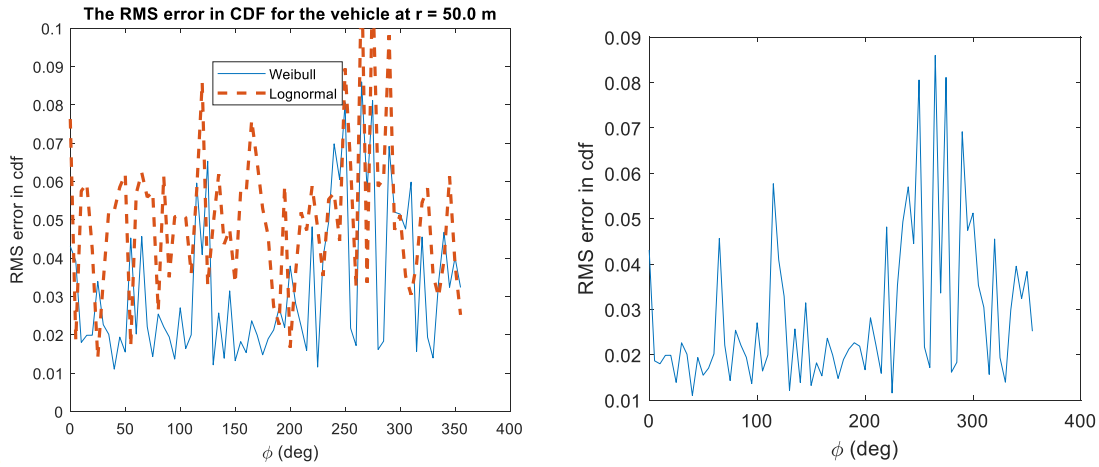

(a) (b)

Figure 4.16. The RMS error in CDF for (a) Weibull ($W_{A,B}(r, \phi)$) and Lognormal distribution ($L_{\mu,\sigma}(r, \phi)$) and (b) the best of the two distributions $D(r, \phi)$ for the sedan at 50 m and different azimuth angles

When a vehicle is in the near range of a radar, the radar may see different parts of the vehicle if it can scan its narrow main beam as illustrated in Figure 4.17. In the Figure, the coordinate is defined in the same way as shown in Figure 4.11, and the radar scanning angle is denoted as ψ. $\psi = 0°$ means the radar is looking at the center of the vehicle. For each value of ψ, the corresponding detected RCS value can be treated as a random variable. Because the shapes of different parts of a vehicle are usually well-defined, the radar response from different parts of the vehicle may be correlated. Therefore, the random variables representing RCS with different values of ψ should be correlated and treated as multivariant random variables with a given correlation matrix/covariance matrix. For example, suppose the radar locates at $r = 20\ m$ and $\phi = 45°$, and

the scanning angle ψ is between $-6°$ and $6°$ with 1.5° step. There are in total 9 random variables for different value of ψ in this case: $[-6°, -4.5°, -3°, -1.5°, 0°, 1.5°, 3°, 4.5°, 6°]$. The mean values of the RCSs for different ψ are illustrated in Figure 4.18 (a). Notice that $\psi = 0°$ only means the radar is focusing on the center of the car, and the detected RCS at $\psi = 0°$ may not be the highest value. In the example shown in Figure 4.18, the beam with $\psi = -3°$ has the highest mean RCS value.

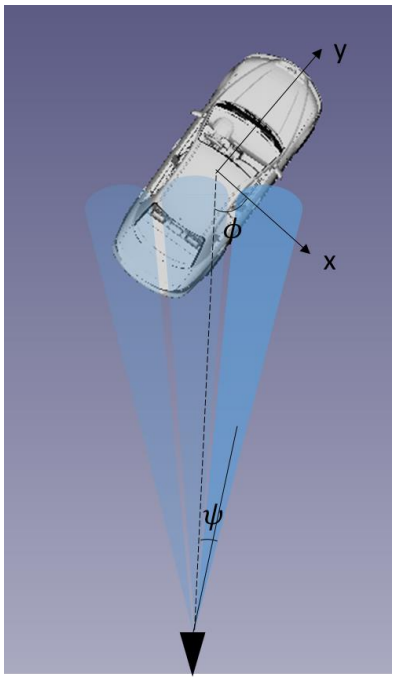

Figure 4.17. Coordinate system used in the scenario when radar is scanning main beam

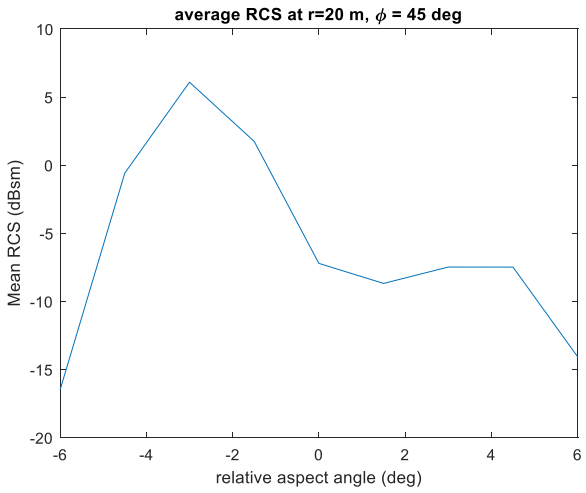

(a)

9x9 double

	1	2	3	4	5	6	7	8	9
1	1	0.3795	0.2000	0.1167	-0.0833	-0.0295	0.0323	0.1365	0.1851
2	0.3795	1	0.9637	0.8583	-0.0917	-0.0392	-0.0474	-0.1395	-0.1805
3	0.2000	0.9637	1	0.9370	-0.0627	-0.0212	-0.0597	-0.2096	-0.2774
4	0.1167	0.8583	0.9370	1	0.1184	0.0089	-0.0720	-0.2690	-0.3531
5	-0.0833	-0.0917	-0.0627	0.1184	1	0.3819	-0.0364	-0.2217	-0.3062
6	-0.0295	-0.0392	-0.0212	0.0089	0.3819	1	0.4296	-0.0729	-0.1904
7	0.0323	-0.0474	-0.0597	-0.0720	-0.0364	0.4296	1	0.5133	0.2005
8	0.1365	-0.1395	-0.2096	-0.2690	-0.2217	-0.0729	0.5133	1	0.8574
9	0.1851	-0.1805	-0.2774	-0.3531	-0.3062	-0.1904	0.2005	0.8574	1

(b)

Figure 4.18. (a) Mean RCS values as a function of scanning angle for a sedan and (b) the correlation matrix of the RCS random variables with different scanning angles

The correlation coefficient of two random variables X and Y is defined by:

$$\rho_{X,Y} = \frac{E[(X-\mu_X)(Y-\mu_Y)]}{\sigma_X \sigma_Y}, \tag{4.14}$$

where $E[*]$ is the expected value, and μ_X and σ_X are the mean value and standard deviation of variable X, respectively.

It is known that correlation coefficient with value of 1 means linearly dependent and 0 means independent. The correlation coefficients between each pair of the nine RCS random

variables define the correlation matrix, and the correlation matrix for the example described above is shown in Figure 4.18 (b). It shows that the highly correlated region is between the angle ψ between $-4.5°$ and $-1.5°$, which are the angles with the highest mean RCS values.

Use the correlation matrix to generate multivariant random variables of radar response can provide better fidelity for large and/or near target. The multivariant random variables for normal distribution have been well studied [117]. The generation of multivariant normal distribution variables is available in MATLAB with function name of "mvnrnd", and in C++, the generation of multivariant random variables with normal distribution can be implemented with "Eigen" library [118] as well. The multivariant random variables for other distributions, like Weibull and Lognormal distribution in this case, can be obtained from the transformation of multivariant normal distribution random variables [119].

The task is to generate multivariant random variables $\vec{X} = (\vec{x}_1, \vec{x}_2 \dots, \vec{x}_\mathrm{n})^\mathrm{T}$, and each variable follows a given statistical distribution. The mean value, variance of each variable, and the covariance matrix *C* is given as well. The covariance matrix is defined as:

$$\mathrm{C_X} = \mathrm{E}\left[(\vec{X} - \vec{\mu})(\vec{X} - \vec{\mu})^T\right]. \tag{4.15}$$

To start with, we first generate multivariant normal distribution random variables $\vec{Z} = (\vec{z}_1, \vec{z}_2 \dots, \vec{z}_\mathrm{n})^\mathrm{T}$ with zero mean, variance of 1 and the same covariance matrix C as $\mathrm{C_X}$. This can be done by applying the library in C++ or MATLAB, or a method called Cholesky decomposition [120]. In Cholesky decomposition approach, n independent normal distribution random variables with 0 mean and variance of 1 $\overrightarrow{Z'} = (\vec{z}'_1, \vec{z}'_2 \dots \vec{z}'_\mathrm{n})$ are generated first. Because variables in $\overrightarrow{Z'}$ are independent, the covariance matrix of $\overrightarrow{Z'}$ is $C_{Z'} = E\left[\overrightarrow{Z'}\overrightarrow{Z'^T}\right] = \bar{\bar{I}}$, and $\bar{\bar{I}}$ is identity matrix. Notice that the covariance matrix is symmetric, and always positive semi-definite. The covariance matrix

is positive definite if there are no two variables are linearly dependent to each other [121]. Then, the covariance matrix $\mathrm{C_X}$ can be decomposed by [120]:

$$\mathrm{C_X} = \mathrm{LL^T}, \tag{4.16}$$

where L is a lower triangular matrix. Then,

$$\mathrm{C_X} = \mathrm{LL^T} = \mathrm{C} = \mathrm{LL^T} = \mathrm{L}E\left[\overrightarrow{Z'}\overrightarrow{Z'^T}\right]\mathrm{L^T} = E\left[L\overrightarrow{Z'}\overrightarrow{Z'^T}L^T\right]. \tag{4.17}$$

Meanwhile, recall that $\mathrm{C_X} = E\left[\vec{Z}\vec{Z}^T\right]$, thus the multivariant normal distribution random variables $\vec{Z}$ can be generated from *n* independent normal distribution random variables $\overrightarrow{Z'}$:

$$\vec{Z} = L\overrightarrow{Z'}. \tag{4.18}$$

Next step is to convert the multivariant normal distribution random variables to the multivariant random variables with given distributions. This can be done by utilizing the property of CDF function. For a random variable *V*, if *V* has continuous and strictly increasing CDF F_V, then $y = F_V$ has uniform distribution on $0 \leq y \leq 1$ [122]. With this property, a random variable with a given distribution whose CDF is continuous and strictly increasing can be related to a normal random variable by:

$$X = F_X^{-1}(y) = F_X^{-1}(F_Z(Z)), \tag{4.19}$$

where X is the targeting random variable, $F_X^{-1}(y)$ is the inverse cumulative distribution function of distribution for X, Z is the normal random variable, and F_Z is the cumulative distribution function of normal distribution.

The cumulative distribution function of normal distribution is given by [123]:

$$F(x|\mu,\sigma) = \frac{1}{\sigma\sqrt{2\pi}}\int_{-\infty}^{x} e^{\frac{-(t-\mu)^2}{2\sigma^2}}dt = \frac{1}{2}\left[1 + erf\left(\frac{x-\mu}{\sigma\sqrt{2}}\right)\right], \tag{4.20}$$

where erf () is the error function.

The targeting distributions are Weibull or Lognormal distribution, and both distributions have continuous and strictly increasing CDF, therefore, their random variables can be generated from the method described above. The inverse CDF for Lognormal distribution is:

$$x = F^{-1}(p|\mu,\sigma) = exp\left[\sigma\left(-\sqrt{2}\text{erfcinv}(2p) + \mu\right)\right], \tag{4.21}$$

where p is the CDF random variable and erfcinv() is the inverse error function. The inverse CDF for Weibull distribution is:

$$x = F^{-1}(p|A,B) = A(-\ln(1-p))^{1/B}. \tag{4.22}$$

Table 4 - 4. Comparison between targeting Lognormal parameters and the measured parameters from randomly generated data

Parameters	Variable 1	Variable 2	Variable 3
μ_{target}	1	2	3
μ_{data}	0.968	1.977	2.973
σ_{target}	1	1.2	1.5
σ_{data}	0.973	1.167	1.460
Targeting Correlation Matrix	$\begin{bmatrix} 1 & 0.96 & 0.86 \\ 0.96 & 1 & 0.94 \\ 0.86 & 0.94 & 1 \end{bmatrix}$		
Measured Correlation Matrix	$\begin{bmatrix} 1 & 0.94 & 0.74 \\ 0.94 & 1 & 0.88 \\ 0.74 & 0.88 & 1 \end{bmatrix}$		

To validate the approach described above, about 1000 set data samples for multivariate random variables with given distributions are generated and analyzed. The comparison between targeting statistical parameters and measured statistical parameters of generated data for one example of Lognormal multivariate random variables are shown in Table 4 - 4, and that for Weibull multivariate random variables are displayed in Table 4 - 5. In both cases, there are good agreements between statistical parameters for single variable (μ, σ or A, B), and the strong correlation between random variables are observed from the data as desired. There are some errors in correlation matrix,

which are due to the non-linearity of the CDF and inverse CDF operation, but after all the strong correlation are simulated, which can improve the fidelity of real-time radar simulation.

Table 4 - 5. Comparison between targeting Weibull parameters and the measured parameters from randomly generated data

Parameters	Variable 1	Variable 2	Variable 3
A_{target}	1	2	3
A_{data}	0.93	1.94	2.96
B_{target}	0.5	1	1.5
B_{data}	0.48	0.96	1.43
Targeting Correlation Matrix	$\begin{bmatrix} 1 & 0.96 & 0.86 \\ 0.96 & 1 & 0.94 \\ 0.86 & 0.94 & 1 \end{bmatrix}$		
Measured Correlation Matrix	$\begin{bmatrix} 1 & 0.86 & 0.69 \\ 0.86 & 1 & 0.92 \\ 0.69 & 0.92 & 1 \end{bmatrix}$		

The multivariate statistical analysis is performed for many different types of vehicles and other stationary targets. The types of vehicles include but are not limited to sedan, SUV, pickup truck, heavy truck, RV, bus, motorcycle and bicycle, the other targets include bus station, trees, lamp post, traffic sign, traffic light, trash bins and animals like dog, deer and horse. All data are stored in one library and can be used to simulate the radar response in real-time traffic scene simulation for autonomous driving.

4.4 Real-time radar image simulation for real-aperture beam steering radar

A typical radar signal processing is first do 2D FFT to obtain the range-Doppler image and then find the angle-of-arrival (AOA) of each target. For a narrow-beamwidth beam-steering radar, the AOA of target can be simply obtained by the scanned angle. Beam-steering ability can be done either by digital/analog beamforming, MIMO techniques or mechanically scanning. Practically, the automotive radar only scans on azimuth direction due to the limitation of cost. In many

scenarios, the 2D range-azimuth angle images are sufficient for separation of targets, given that the radar has narrow beam in elevation direction. In some cases, Doppler information may not be needed in targets separation, for example, If the Doppler information is used to isolate the response of targets involving a pedestrian, the pedestrian might be falsely considered as multiple targets due to multiple Doppler bins exhibited by a pedestrian. Notably, there are some cases the Doppler information is required for separation of targets, for example, in a scenario where a car is moving under a bridge. If Doppler information is not used to separate signals, the car might be miss-detected. In our preliminary research, the scenarios where two objects overlapping in elevation direction are not studied and the 2D range-azimuth angle images of dynamic traffic scenes are presented.

The objective of the radar simulation is to generate radar data as close to those in the physical world as possible. To demonstrate the similarity, some radar images from measured data and simulation are presented and compared. One example of the 2D radar image from measurement is shown in Figure 4.19. Figure 4.19 (a) depicts the photograph of a parking lot under measurement. The MMW radar in use has 3-degree antenna beam width, and its beam is scanned manually with 1.5-degree step from -30 degree to 30 degree in azimuth plane. Many cars in the measuring scene can be identified from the radar images shown in Figure 4.19 (b). Figure 4.24 shows another 2D radar image example generated by simulation. In Figure 4.24 (a), a traffic scene with cars, trees and pedestrians are shown. Figure 4.24 (b), (c) and (d) depicts the 2D radar images with 2°, 3° and 1.5° antenna beamwidth and -13 dB, -26 dB and -26 dB side-lobe levels, respectively. In general, the image generated by narrower beam width, and lower side-lobe level radar has better image quality that can reduce the false detection rate. Notably, in PO numerical

simulation, the simulation time for one frame is around 30 minutes for a single core CPU in an ordinary PC.

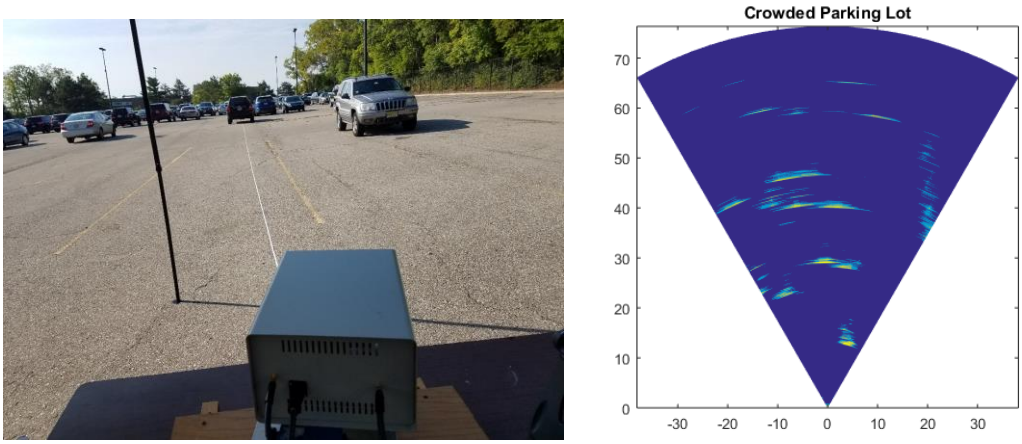

(a) (b)

Figure 4.19. (a) Radar measurement in a parking lot (b) The corresponding 2D radar images

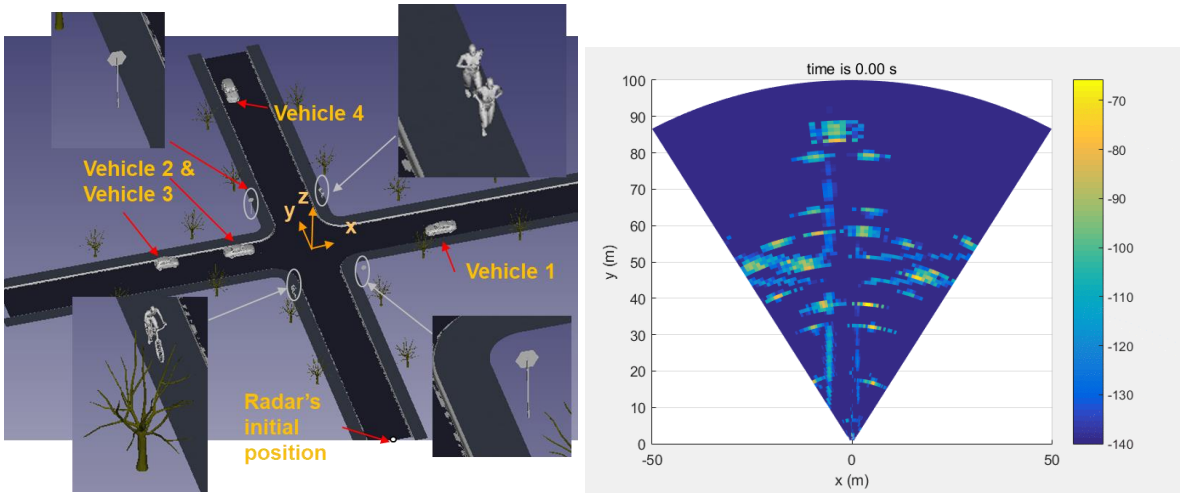

(a) (b)

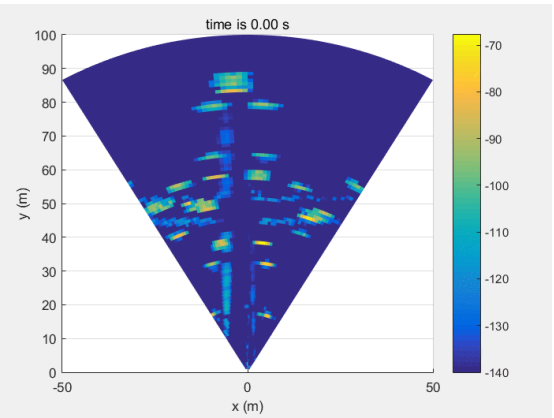

(c)

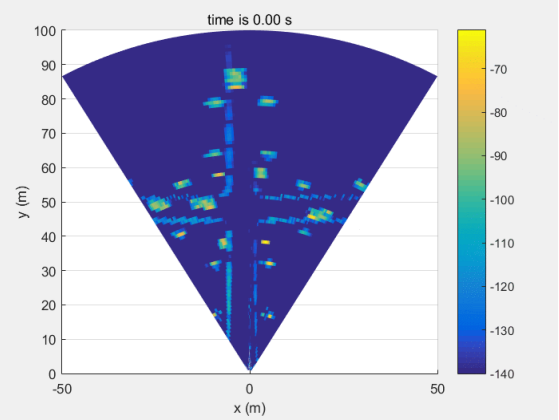

(d)

Figure 4.20. (a) A crossroad traffic scene for numerical simulation with PO. The corresponding 2D radar images for (a) 2° beamwidth and -13 dB sidelobe radar, (b) 3° beamwidth and -26 dB sidelobe radar and (c) 1.5° beamwidth and -26 dB sidelobe radar

To accelerate the simulation into real time, statistical models are applied. The real-time radar simulation is performed in Unreal Engine 4 [124], which is best known as a game engine for many popular 3D video games. It can generate 3D scene and run video animation efficiently, which makes it a good candidate for autonomous driving simulation software. In this real-time simulation, the radar response from ground surface is simulated as well. One example of a traffic scene created in Unreal Engine 4 is displayed in Figure 4.21. There are many vehicles including sedans, SUVs, bus and motorcycles, trees, bus station, and pedestrians in the traffic scene. Among the two asphalt roads displayed, one road is covered by fresh snow. The statistical model for snow is derived from semi-empirical scattering models.

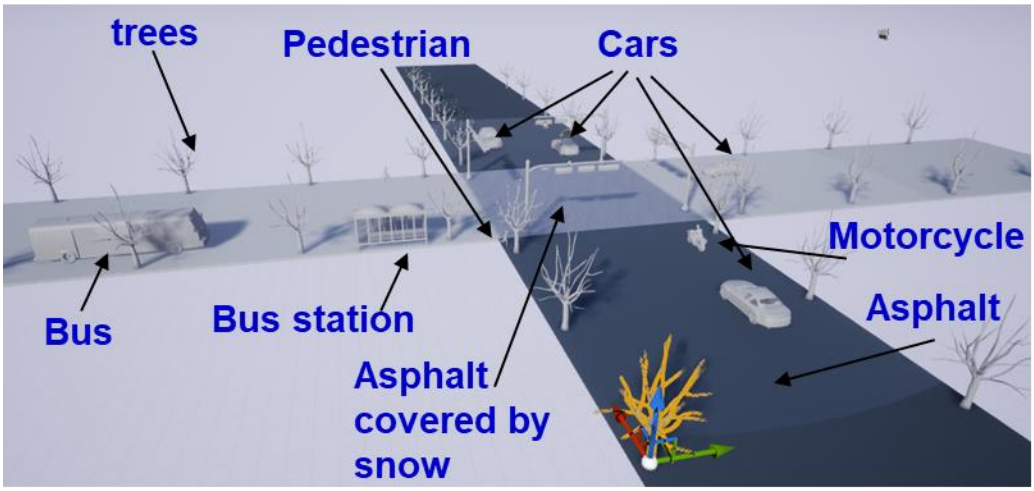

Figure 4.21. A dynamic crossroad traffic scene built in Unreal Engine 4 for real-time radar images simulation

In the simulation setup, each target is initialized with its own radar statistical models, depending on the aspect angle and range to the radar during simulation, a set of statistical parameters for RCS are calculated and the RCS values are generated by random number generators. Then the received power level at each radar scanning angle is derived from the radar equation with RCS values and corresponding antenna's gains. The simulation is performed for a dynamic environment, where the objects can move in their pre-programed traces.

The dynamic traffic simulation with setup shown in Figure 4.21 is displayed in Figure 4.22. It shows three frames from a continuous simulation. The large sector shows the 2D radar image generated for a forward-looking radar, and the radar used in this example has 1.5° beam width, -26 dB side-lobe level, 0.5 m range resolution and 1.5° angular resolution. The two small sectors below are corresponding to a near-grazing looking radar. The two images are corresponding to VV and HH polarizations. The results for cross-polarization is not shown because the power level for it is much lower than VV and HH, and usually below the noise floor.

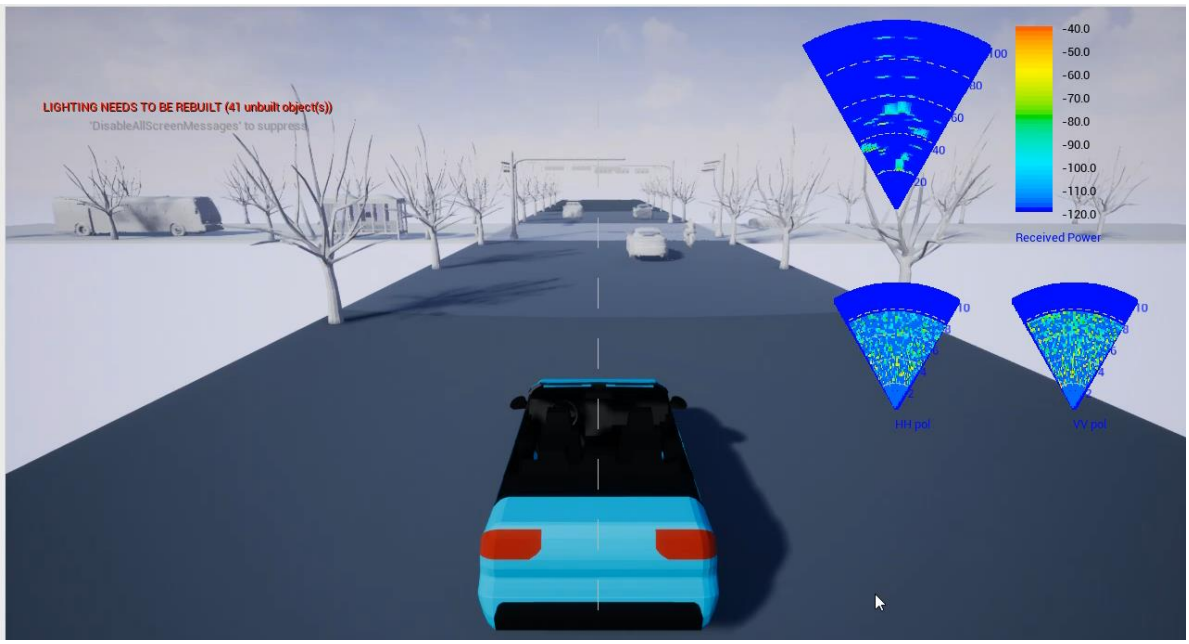
LIGHTING NEEDS TO BE REBUILT (41 unbuilt object(s))
'DisableAllScreenMessages' to suppress
-40.0
-50.0
-60.0
-70.0
-80.0
-90.0
-100.0
-110.0
-120.0
Received Power
HH pol
VV pol

(a)

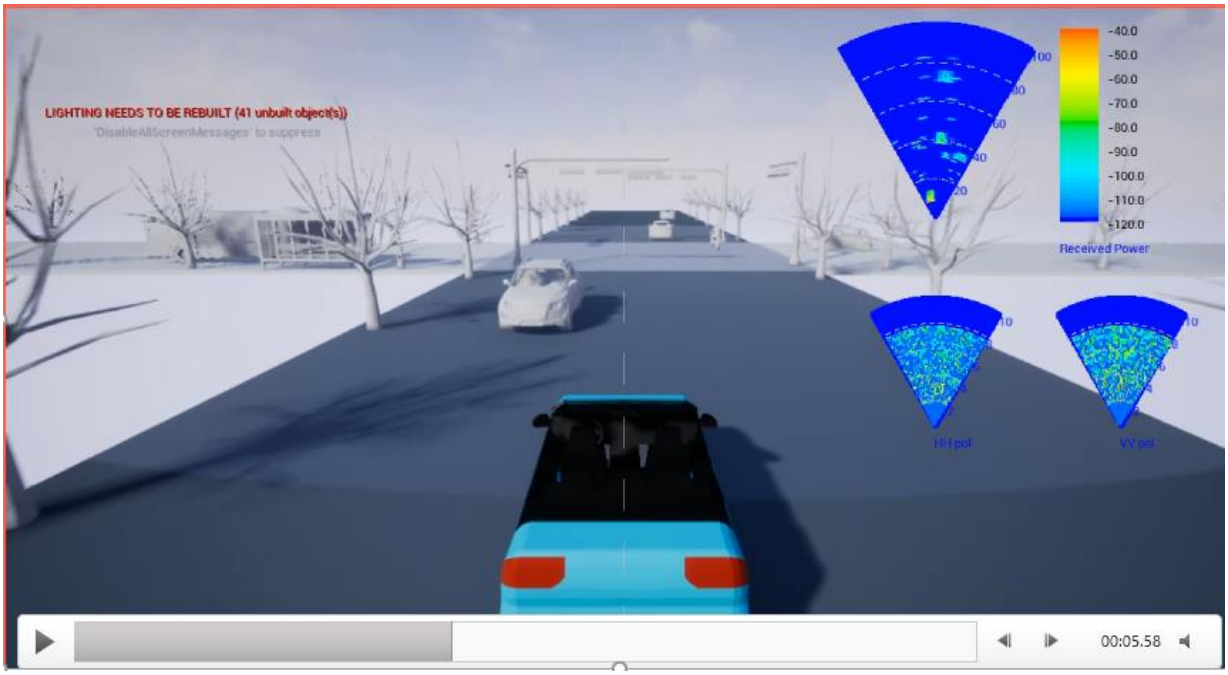
LIGHTING NEEDS TO BE REBUILT (41 unbuilt object(s))
'DisableAllScreenMessages' to suppress
-40.0
-50.0
-60.0
-70.0
-80.0
-90.0
-100.0
-110.0
-120.0
Received Power
HH pol
VV pol
00:05.58

(b)

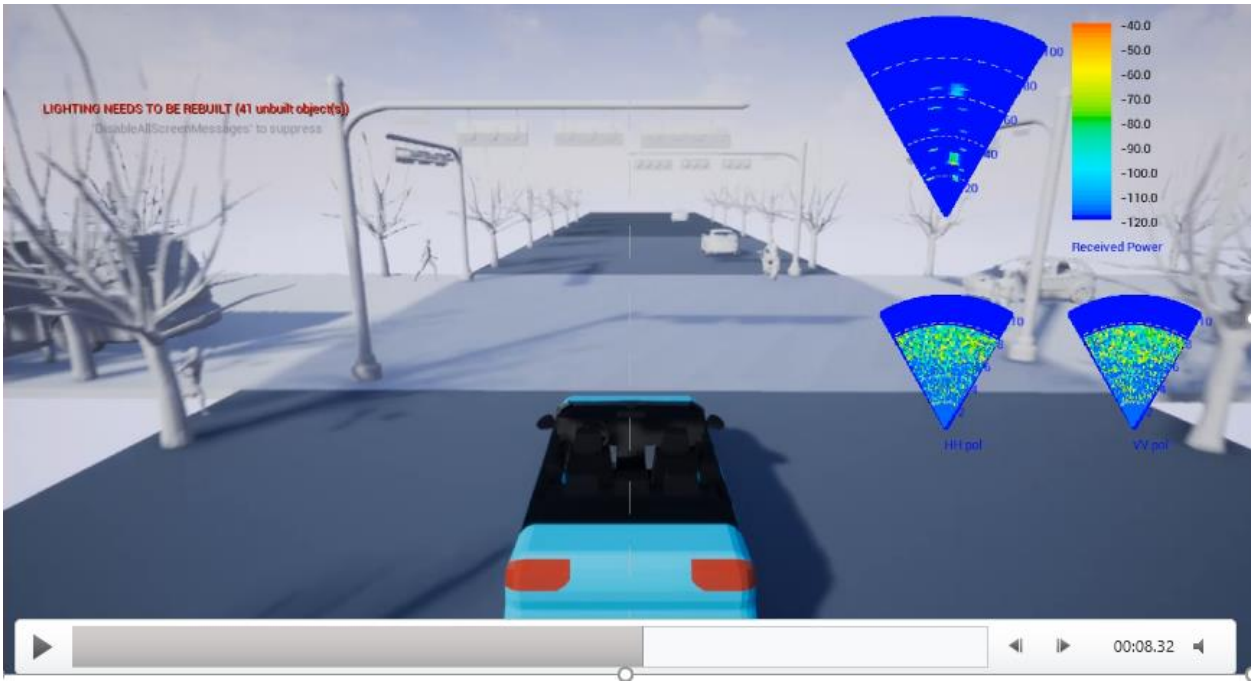

(c)

Figure 4.22. A dynamic traffic scene simulation in Unreal Engine 4 of (a) starting frame, (b) middle frame 1, and (c) middle frame 2.

In Figure 4.22 (a), the major targets including vehicles, trees and bus station can be clearly observed from the radar images. Figure 4.22 (b) shows that near targets has stronger radar response. The snow backscattering is detected in Figure 4.22 (c), where in the lower radar images, a boundary showing the different backscattering level between ordinary asphalt and snow covered asphalt can be identified.

The radar images simulation in Unreal Engine 4 has more than 20 frame-per-second (FPS) (or <50 ms per frame) on an ordinary PC with Intel i7-7700 CPU for the traffic example described above. Depending on the complexity of traffic scene and simulation platform, the simulation speed can be faster or slower. The program can export the radar image data out for future signal processing as well.

4.5 Multi-scatterer RCS statistical models for MIMO radar

For MIMO radar system where more than one transmitter/receiver are considered, the RCS statistical models should be further extended to multi-scatterers for better fidelity. In MIMO radar system, the signal processing for angle-of-arrival (AOA) is different from that for beam-steering radar and is derived from the phase and amplitude distribution among different communication channels (transmitters/receivers). Therefore, it is crucial to have accurate simulation of the relative phase and amplitude of different channels. In the aforementioned statistical models for traffic targets, one target is considered as one scatterer, which will result in uniform magnitude distribution for different channels. This is unlikely to happen in real radar measurement especially for large traffic targets like vehicles as the targets are not far enough to be considered as point targets. For example, for a car with largest dimension of 2.5 m on the cross section, its far-field range is 3125 m according to equation (4.2), and the typical radar operation range is within 300 m. Therefore, to capture the correct magnitude and phase distribution for different channels, multiple-scatterer model is developed. In multiple-scatterer model, the targets are represented by more than one scatterers. One challenge of multiple-scatterer model is to identify the position of each scatterer. Besides, similar to the single-scatterer statistical model, the RCS values of each scatterer may also be fluctuating with incident angle, which requires further statistical analysis.

A scatterer is defined as a point target, which means it has a position and an RCS value but no volume. Any point on the surface of a target can be considered as a scatterer. As a result, there could be infinite number of scatters. On the other hand, it is known that if the radar is locating in the far field of target, the response from different scatterers on the target can be approximated by the response from one scatterer. Therefore, the problem can be simplified by dividing the entire

target into many small portions such that for each portion, the radar is in the far field range. Thereby the scatterers on one portion can be considered as one scatterer.

In this model, the entire space occupied by the target is divided into small pixels with dimensions of 0.1m by 0.1m by 0.1m. This value is chosen because the far-field range for target with dimension of 0.1 m is about 5 m at 77 GHz. In the other words, if the radar is more than 5 m away from the target, this approximation is valid. The RCS of each scatterer is considered as a random variable, and the statistical features of each random variable are summarized from massive numerical simulations from small variation of incidence angles in both elevation and azimuth direction. Notably, since each scatterer is a point target, its RCS value should be constant for different frequencies and ranges greater than 5 m.

The RCS statistical features for each scatterer are summarized in $\pm 2.5°$ in both azimuth and elevation direction with 100 samples. The data are fitted into Gamma distribution, and some examples of the fitting results for the RCS of one scatterer on a sedan from one angle are shown in Figure 4.23. It shows Gamma distribution has a good fit to the empirical data. In the pixelated model, every $(0.1\text{m})^3$ volume may be considered as one scatterer, however, many volumes are empty or have very small RCS values, and to reduce the complexity of the problem, the scatterers with RCS value less than -40 dBsm are ignored. The positions and randomly generated RCS values of the significant scatterers for some typical targets in traffic scenes including a sedan, a man riding a bike and a pedestrian are displayed in Figure 4.24. In Figure 4.24 (a), a sedan is illuminated from the back, and it shows the strongest scatterers locate on the back of the car. Figure 4.24 (b) depicts the scatterers distribution for a man riding a bike when radar is on the side. It shows the major scattering happens on the bike, while the human body also has some contribution. Figure 4.24 (c) and (d) depict the scatterer distribution for a jogging man illuminated by the radar from the side

and the back, respectively. The scatters form the shape of human body, and the strong scatters locate on the surface of human body whose normal vector is almost parallel to the radar direction.

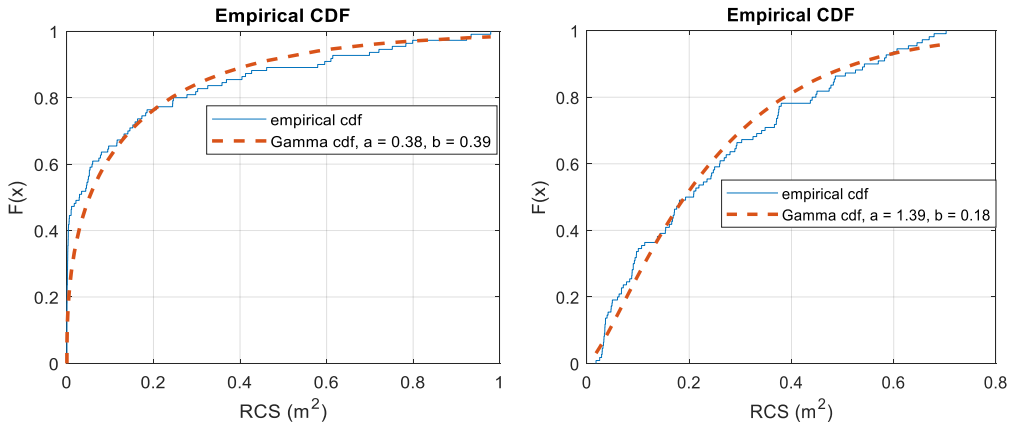

Figure 4.23. Comparison of empirical and fitted CDF for the RCS of two scatterer on a sedan

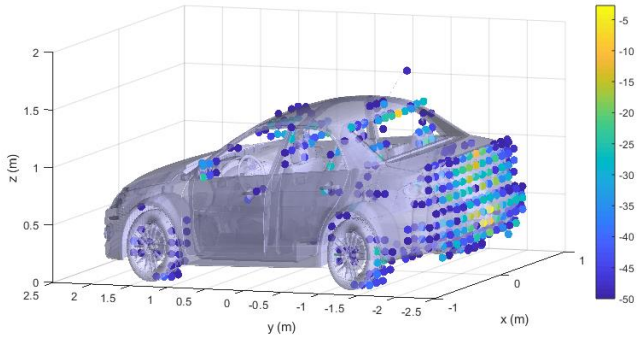

(a)

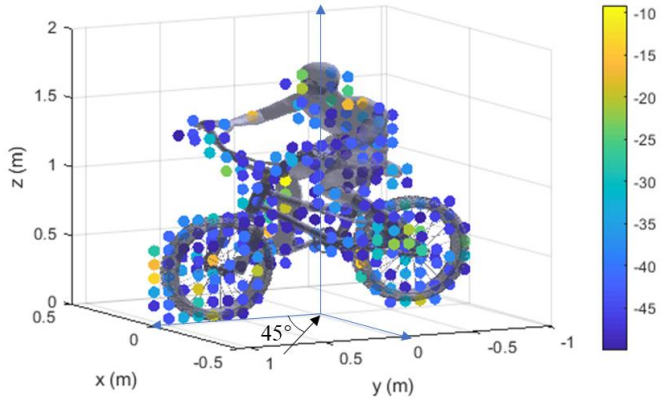

(b)

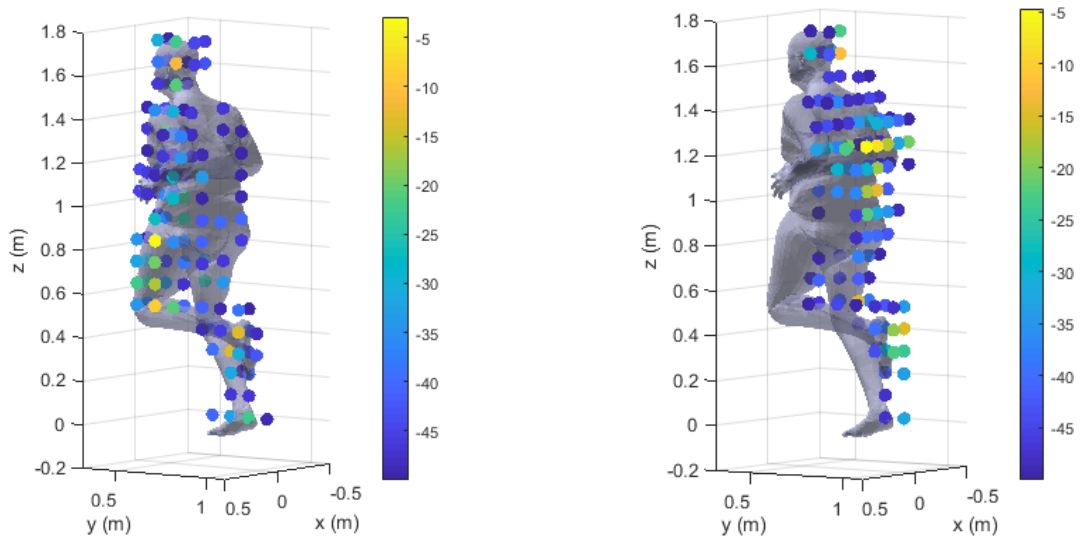

(c) (d)

Figure 4.24. The positions and randomly generated RCS values of scatters for (a) a sedan illuminated from the back, (b) a man on a bike illuminated from 45° off to the front, and a jogging man (c) illuminated from the side and (d) illuminated from the back.

4.6 Real-time radar response simulation for MIMO radar

In FMCW MIMO radar system, the voltage at the ith receiver's antenna can be calculated by the radar equation:

$$V_{ji} = \frac{\sqrt{P_{tj} Z_i}\lambda}{(4\pi)^{3/2}} \sum_l \frac{\sqrt{\sigma_l} F_{li} F_{lj}}{R_{li} R_{lj}} e^{ik_0(R_{li}+R_{lj})}, \tag{4.23}$$

where P_{tj} is the transmitted power from the jth transmitter, Z_i denotes the impedance of ith receiver's antenna, λ is the wavelength, k_0 is the wave number, and both λ and k_0 are functions of freuqncy, σ_l is the RCS for scatterer l, F_{li}, F_{lj} are the antenna far field for scatterer l with respect to jth transmitter and ith receiver , and R_{li}, R_{lj} are the distance from lth scatterer to jth transmitter and ith receiver, respectively.

Notice that FMCW radar transmits and receives wideband and multipole-chirp signals during one frame of operation as depicted in Figure 4.25. In (4.23), the parameter $\boldsymbol{\lambda}$ and $\boldsymbol{k_0}$ are functions of frequency and $\boldsymbol{R_{li}}$, $\boldsymbol{R_{lj}}$ are functions of chirp (time). As a result, the received signals of one frame requires the calculation of (4.23) for all frequencies and chirps.

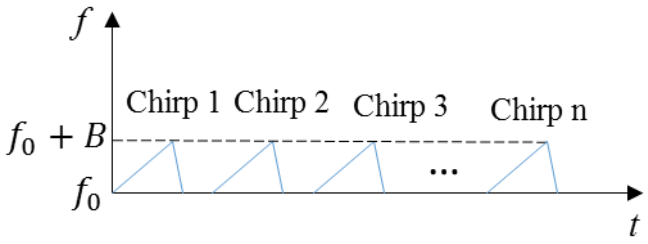

Figure 4.25. The transmitted signal's frequency as a function of time during one frame for a typical FMCW radar

A single frame of FMCW radar signals usually contain tremendous data. For example, a MIMO radar with range resolution of 0.3m, maximum unambiguity range of 150 m, speed resolution of 0.3 m/s, and maximum unambiguity speed of 80 m/s has 256 chirps in one frame, and 512 frequency points for each chirp. Assume the MIMO radar has three transmitters and four receivers, or equivalently 12 communication channels for the radar, and then the number of total data samples in one frame is 1,572,864 (512*256*12). In order to generate such amount of data in real time (< 100 ms), parallel computing with both CPU and GPU should be applied. The parallel computing with CPU is implemented by OpenMP library [125], and NVIDIA parallel programing tool CUDA [126] is utilized for GPU parallel computing. To test the performance of parallel computing, the radar simulation of one frame is performed for different hardware with the scene containing 100 scatterers. The radar setup has 12 channels, 512 frequency samples and 256 chirps. The computer that runs the simulation utilizing the CPU of Intel Core i7-7700 (4 cores, 3.6 GHz) and the GPU of Nvidia GeForce GTX 1060 (1280 cores, 1.7 GHz). The comparison of simulation

time for the one frame simulation between different hardware is shown in Table 4 - 6. It is shown that compared to single core CPU, parallel computing with GPU is about 60 times faster and able to be run in real time (< 100 ms) with an ordinary GPU for a PC.

Table 4 - 6. Comparison of the simulation time for different hardware

	Single core, CPU	Four cores, CPU	GPU (double precision)	GPU (single precision)
Simulation time	5.8 s	1.5 s	270 ms	94 ms

The GPU-based radar response simulation module has been developed and referred as Michigan Automotive Radar Scene Simulator (MARSS). It can be run as a standalone program with given traffic scene information or it can be integrated into Unreal Engine 4 (UE4) as part of the real-time autonomous driving simulation as well. In both simulation environment it will generate the same results, so in this dissertation we just show the results in UE4 as examples. One example of the simulation process is depicted in Figure 4.26. In this example, the simulation is set to operate every 100 ms. When the unreal Engine starts, it will load the MARSS dynamic link library (DLL) and other libraries and initialize the solver. During the radar simulation, it will first read ground truth data from the traffic scene in UE, and then convert the traffic scene into a plurality of scatterers, and afterwards calculate the radar response for all the scatterers. It provides options to export the radar response data for external signal processing as well. In the next step, the simulated data will be put into the signal processing module, which will output the positions, speeds and angles of all detected targets. The signal processing module will be our future work.

Figure 4.27 shows an example of traffic scene for radar signal simulation in UE4. The radar has the same setup as described before (512 frequency points, 256 chirps, 12 channels), and there are 4 vehicles in the traffic scene. The shadowing effect is considered in the simulation, which means the scatterers of one target blocked by others will be excluded in the simulation.

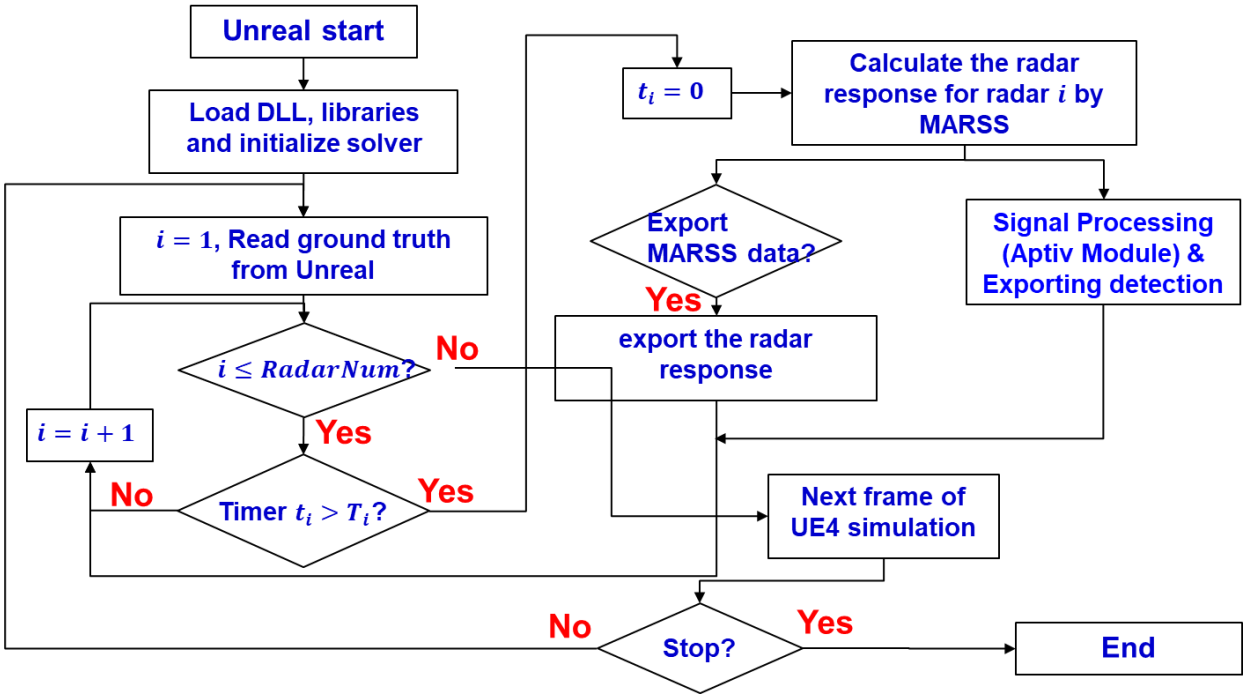

Figure 4.26. The flow chart of radar response simulation for multiple radars with Unreal Engine 4

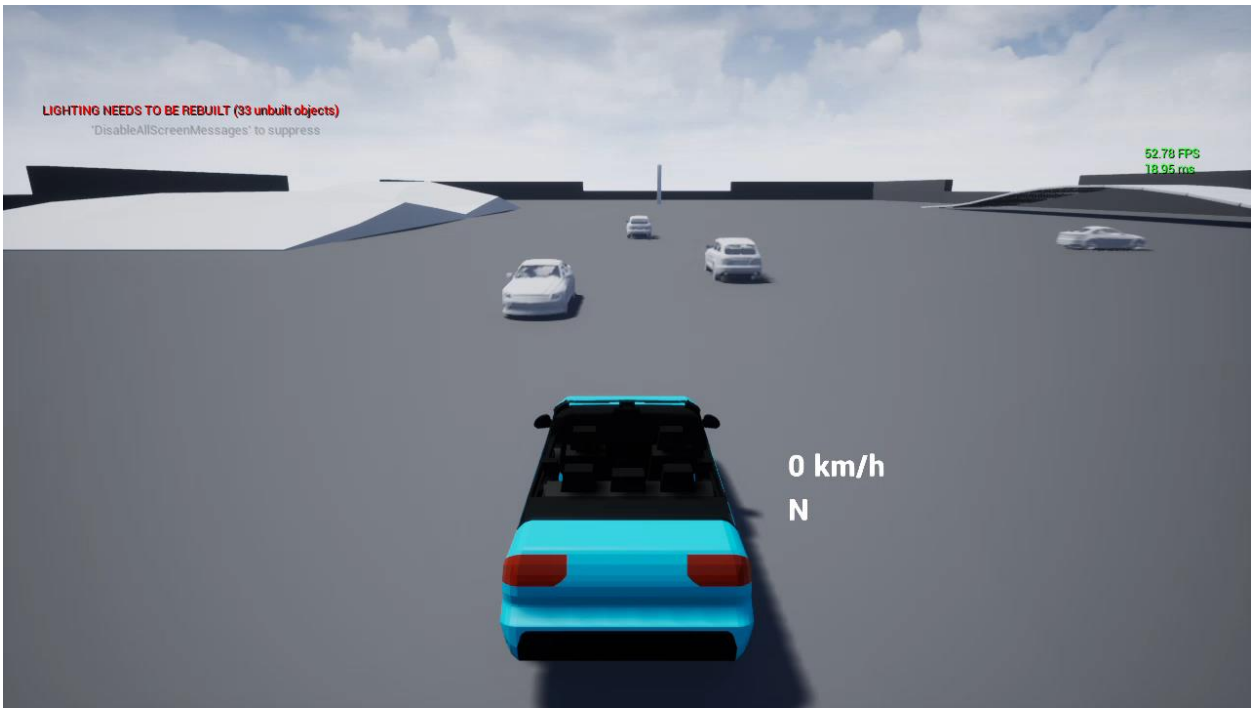

Figure 4.27. The example of a static traffic scene built in Unreal Engine 4

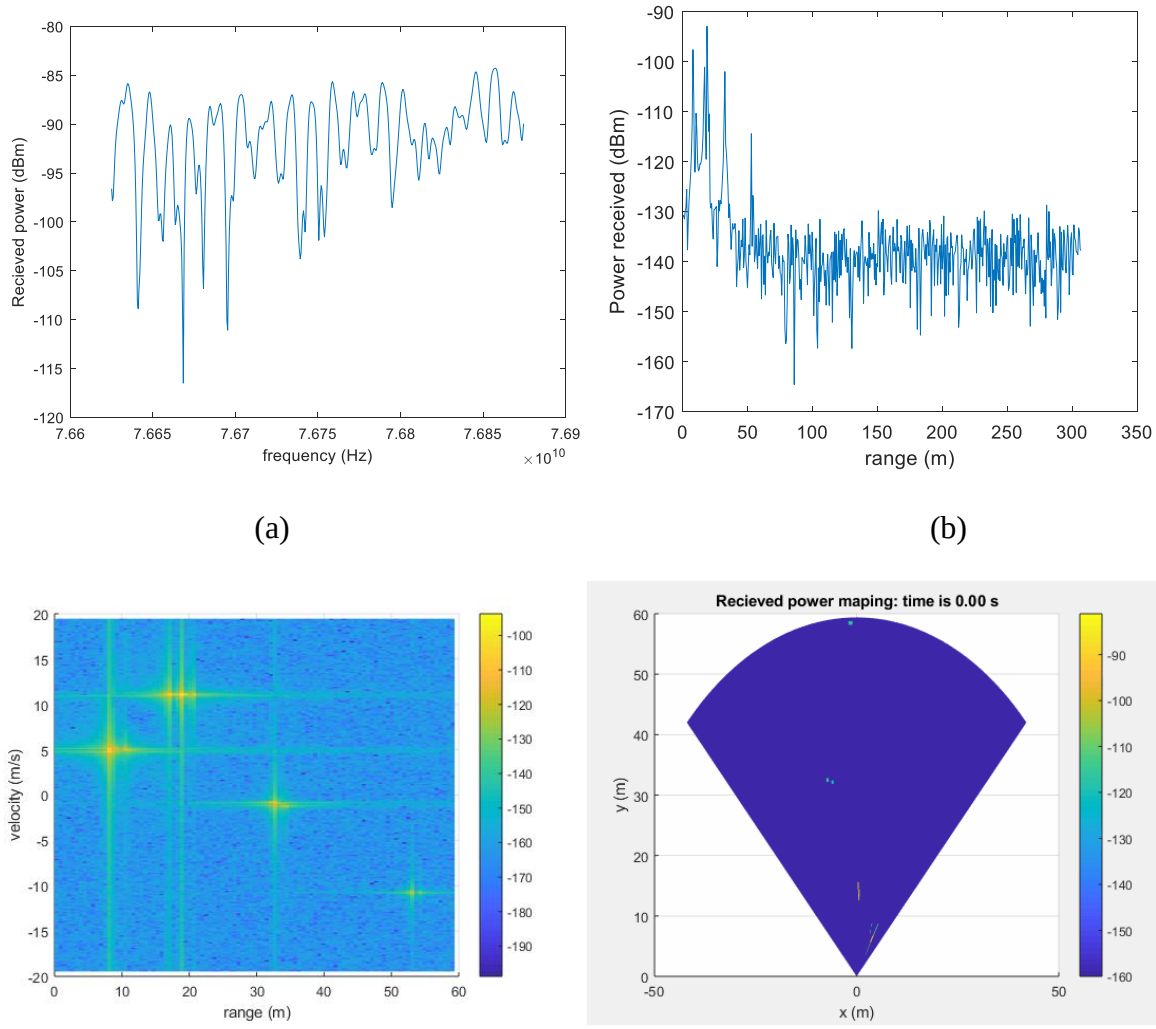

(a) (b)

(c) (d)

Figure 4.28. (a) The received power in frequency domain for one channel and one chirp, (b) The received power as a function of range (time domain response after Fourier transform), (c) the range-Doppler image (2D Fourier transform to the 256 chirps, 512 frequencies per chirp data) and (d) 2D radar image for the traffic scene (after angle of arrival estimation)

The simulated radar response and radar images after signal processing are displayed in **Figure 4.28**. The received power of one channel and one chirp as a function of frequency is shown **Figure 4.28** (a). The received power is defined as $\left|V_{ji}\right|^2/Z_i$, and V_{ji} is calculated by (4.23), Z_i by

default is 50 Ω. **Figure 4.28** (b) shows the received power of one channel as a function of range. It is derived from the FFT of the radar response in frequency domain. It is shown that some targets can be detected in the scene. Combining the response of many chirps, the range-Doppler image is given in **Figure 4.28** (c). The last task is to find the angle of arrival of targets. The range-Doppler images are generated for all 12 channels, and for each cluster of the range-Doppler image, a single target AOA estimation algorithm is applied. The range-azimuth angle radar images then can be constructed and is shown in **Figure 4.28** (d).

The MARSS simulator for UE4 can also simulate the radar response for more than one radar and display the radar detections on the screen. Because the signal processing module is not covered in this thesis, the displayed detections are just the true positions of targets shown in Figure 4.29. It shows the positions of each scatterer detected by each radar, and to have better visibility, the z position of scatterers are moved above the targets. It also provides the option to display the radial speed of detected scatterers. In this six-target and two-radar simulation example, the simulation time is about 130 ms per frame (with ~6 million data).

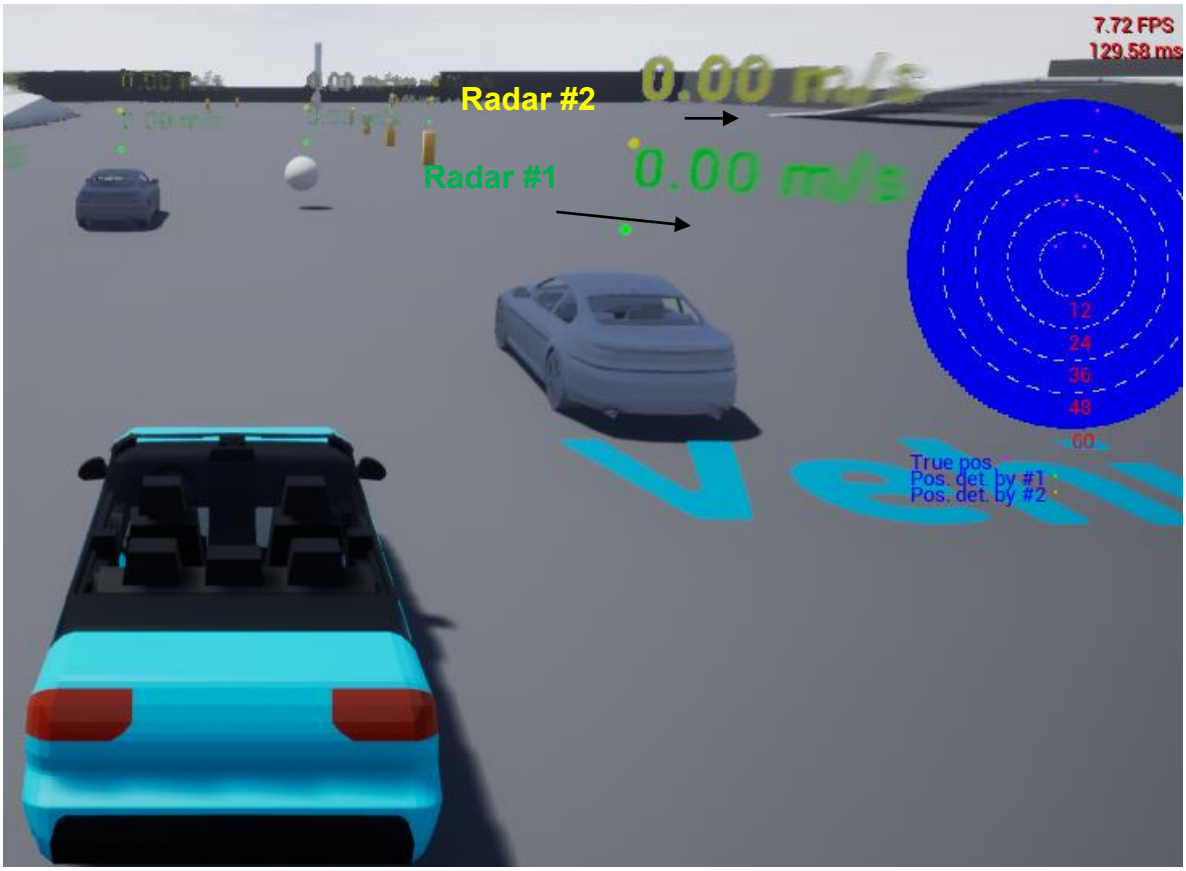

Figure 4.29. The display of radar detection module of MARSS in the UE4 editor, the green and yellow dots represent the scatterers detected by different radars.

4.7 Conclusion

In the first part of this chapter, the RCS statistical models for traffic targets including pedestrians, vehicles and other targets are presented, and then a real-time radar image simulation for real-aperture radar with Unreal Engine 4 is demonstrated. The radar statistical models are based on a massive databases of RCS values generated by fast wideband PO method from Chapter 2, and the RCS values are modeled as Weibull, Lognormal or Gamma distributions. The statistical features of one target is further modeled as functions of range and aspect angle and other property of targets, for example, the weight and height of a pedestrian.

In the second part, near and large traffic targets are represented by multi-scatterer RCS statistical models. In this model, targets are discretized into small scatterers with separation of 0.1 m. The RCS of each scatterer is found to be best fitted by Gamma distribution. The multi-scatterer RCS statistical model enables high-fidelity real-time radar response simulation, which is referred as MARSS, and examples of real-time FMCW radar response simulation performing in Unreal engine 4 (>30 FPS) is demonstrated.

Chapter 5 A Fast Analytic Multiple-Sources AOA Estimation Algorithm for Automotive MIMO Radars

5.1 Introduction

Direction finding (DF) of wireless signals is a classical problem with a long history. The angle (direction) of arrival (AOA/DOA) estimation has a wide range of applications in the wireless communication and radar systems. For example, it can be used to improve channel quality, reduce jamming impact, and find the positions of signal sources or radar targets [127]. Particularly, high-resolution multiple-signal AOA estimation with single snapshot can enhance the performance of multiple-input multiple-output (MIMO) automotive radars [128].

Traditionally, many high-resolution multiple-signal AOA estimation algorithms can be divided into two categories: subspace based methods like MUSIC [40][41] or ESPRIT [42][130], and optimization based method maximum likelihood estimation (ML) [43][131][132][133]. The subspace methods require many snapshots to construct correlation matrix and the number of sources needs to be known in advance. ML performs N-dimensional optimization (N is the number of signals) and becomes computationally inefficient for large N. Recently, many new AOA estimation methods are proposed, including nulls-synthesis signal segregation method ASSIA [134][135] and machine learning [136]-[138] or compressed sensing [139] based approaches. Signal segregation method requires signal's angular spacing is larger than the array beamwidth, and it also relays complicated nulls-synthesis and beam-steering process in each iteration of subtraction of signals, which is computationally expensive. Machine learning based methods are only applicable to a specific band and array arrangement, and requires large amount of data for

sources in different directions and with different power and noise levels for training. Because machine learning approach cannot be applied to the data outside the range of training data, the training data size increases dramatically with the number of sources, which makes it difficult to detect more than three sources.

To support the real-time signal processing for highly dynamic systems like autonomous vehicles, a more efficient AOA estimation algorithm based on small number of or even single snapshot is required. In this thesis, a novel analytic iterative multiple-source AOA algorithm (AIMA) is proposed to meet the requirement. In this method, the AOA estimation problem is divided into two main tasks: (1) estimate one AOA with the prior knowledge of all other AOA; (2) estimate all AOA by iteratively solving Task 1. It can be shown that for a uniform linear array (ULA) Task 1 has analytic solutions and Task 2 converges very fast, which makes this method effective, efficient and practical for real-time processing.

5.2 Signal model

In the classical AOA estimation signal model for a uniform linear array (ULA) as shown in Figure 5.1 (a), the measured signals on an M-element antenna array from N signal sources are given by:

$$\vec{x} = A(\theta)\vec{s} + \vec{n}, \tag{5.1}$$

where $\vec{x}$ is a $M \times 1$ vector, $A(\theta)$ is the $M \times N$ steering matrix with $A_{ij} = e^{ikd_i \sin\theta_j}$, k is the wavenumber, d_i denotes the position of i^{th} element and $d_i = di$ in uniform linear array (ULA) with array spacing d. θ_j is defined as angle deviated from the boresight of the antenna array for j^{th} source, $\vec{s}$ is a $N \times 1$ vector denoting the amplitude of signals from N sources, and $\vec{n}$ is a $M \times 1$ zero-mean Gaussian random vector and denotes the noise.

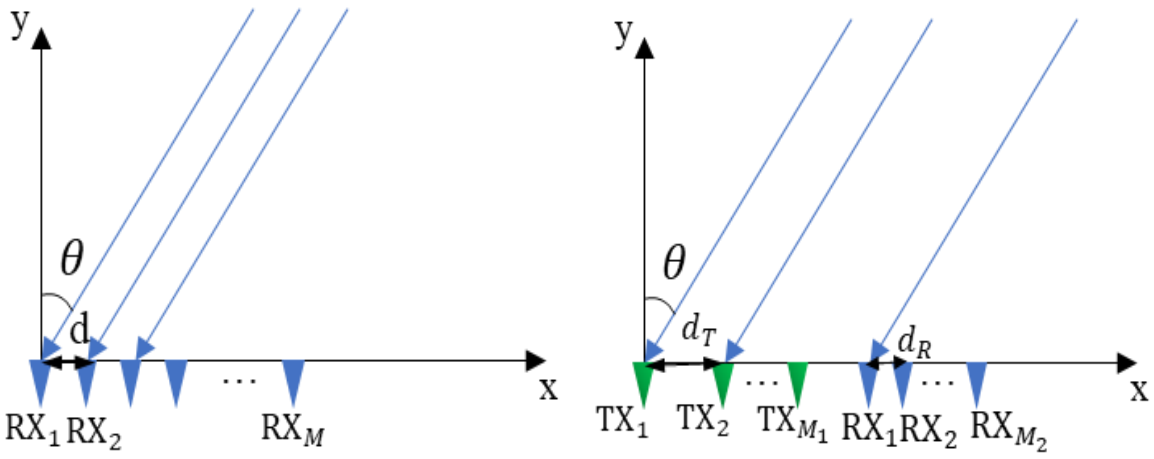

(a) (b)

Figure 5.1. The coordinate system for (a) the classic signal model and (b) the MIMO radar signal model

Similar model can be derived for radar signals. The transmitters (TXs) and receivers (RXs) coordinate for the signal model is depicted in Figure 5.1 (b). Assuming there are M ULA channels from N major targets/scatterers, then the received signal at m^{th} channel by radar equation can be represented by:

$$x_m = \frac{\lambda}{4\pi}\sum_{n=1}^{N}\frac{S_n FF_{mn}^t FF_{mn}^r}{R_{mn}^t R_{mn}^r} e^{ik(R_{mn}^t + R_{mn}^r)} V_m + n_m, \tag{5.2}$$

Where λ is the wavelength at center frequency, S_n is the scattering coefficient of nth target, FF_{mn}^t, FF_{mn}^r are the transmitter and receiver antenna far field, and $|FF_{mn}^t|^2 = G_{mn}^t$, G_{mn}^t denotes the gain of the transmitted antenna for m^{th} channel in the direction of the n^{th} target. R_{mn}^t, R_{mn}^r denote the distance between transmitter and receiver to the n^{th} target, respectively. V_m is the voltage for the transmitted signal, and n_m denotes the noise term for m^{th} channel. For simplicity, we can assume the targets locate in the far field of the radar, and the transmitter and receiver has the same gain. Then (5.2) can be rewritten as:

$$x_m \approx \frac{\lambda}{4\pi}\sum_{n=1}^{N}\frac{S_n G_n}{R_n^2} e^{ik(2R_n+\sin\theta_n d_m)} V_m + n_m, \tag{5.3}$$

where G_n is the antenna's gain in the direction of the n^{th} target, and R_n denotes the distance between the first transmitter (TX) of radar and the n^{th} scatterer. Also $d_m = d_{m_t} + d_{m_r}$, where d_{m_t} is the distance between the first TX the TX for m^{th} channel and d_{m_r} is the distance between the first TX and the RX for the m^{th} channel.

In matrix form, the signal model is the same as (5.1), with

$$A(\theta) = \begin{bmatrix} e^{iksin\theta_1 d_1} & \dots & e^{iksin\theta_N d_1} \\ \dots & \dots & \dots \\ e^{iksin\theta_1 d_M} & \dots & e^{iksin\theta_N d_M} \end{bmatrix}, and\ \vec{s} = [s_1, \dots, s_N]^T \tag{5.4}$$

where $s_n = \frac{\lambda V_t}{4\pi}\frac{S_n G_n}{R_n^2} \mathrm{e}^{ik2R_n}$.

5.3 Analytic solution of Nth AOA for ULA

If there is only one source, its AOA can be easily estimated from the phase difference of signals between antenna elements of the ULA array.

$$\sin\theta_1^{(1)} = E\left[\frac{\arg\left(\frac{x_m}{x_{m-1}}\right)}{kd}\right] \tag{5.5}$$

where E[*] is the expected value, arg($\frac{x_m}{x_{m-1}}$) returns the phase different of mth element and (m-1)th element. The next question to ask is if there are two sources, can the AOA of the second source be evaluated analytically if the AOA of the first source is known? To simplify the problem, the noise-free situation is examined first. The noise-free signal $\vec{x}'$ can be defined as:

$$\vec{x}' = \vec{x} - \vec{n} = A(\theta)\vec{s} \tag{5.6}$$

In the two-source problem,

$$x_m' = e^{ikdm\sin\theta_1} s_1 + e^{ikdm\sin\theta_2} s_2. \tag{5.7}$$

Assume θ_1 is known, and multiply the both sides of (5.7) by $e^{-ikdm\sin\theta_1}$, we have

$$e^{-ikdm\sin\theta_1}x'_m = s_1 + e^{ikdm(\sin\theta_2-\sin\theta_1)}s_2 \tag{5.8}$$

We can eliminate s_1 by subtracting the $(m-1)^{th}$ equation from m^{th} equation:

$$\begin{aligned} &e^{-ikdm\sin\theta_1}x'_m - e^{-ikd(m-1)\sin\theta_1}x'_{m-1} \\ &\qquad = (e^{ikdm(\sin\theta_2-\sin\theta_1)} - e^{ikd(m-1)(\sin\theta_2-\sin\theta_1)})s_2 \end{aligned} \tag{5.9}$$

we can eliminate s_2 and end up with

$$e^{ikd(\sin\theta_2-\sin\theta_1)} = \frac{e^{-ikd\sin\theta_1}x'_m - x'_{m-1}}{x'_{m-1} - e^{ikd\sin\theta_1}x'_{m-2}} \tag{5.10}$$

Then $\sin\theta_2$ can be found by

$$\sin\theta_2 = \frac{\arg\left(\frac{e^{-ikd\sin\theta_1}x'_m - x'_{m-1}}{x'_{m-1} - e^{ikd\sin\theta_1}x'_{m-2}}\right)}{kd} + \sin\theta_1, \tag{5.11}$$

where $3 \le m \le M$.

Moreover, in a ULA for any $N \in [2, M-1]$, there exists an analytic solution such that $\sin\theta_N$ can be expressed as a function of θ_1 to θ_{N-1}. Let $\sin\theta_n$ be T_n, and with some mathematic manipulation, the following relations can be shown:

$$e^{ikd(T_N - T_{N-1})} = \frac{\Gamma_{m,N-1}^{(1,2,\ldots,N-1)'}}{\Gamma_{m-1,N-1}^{(1,2,\ldots,N-1)'}}, \quad N+1 \le m \le M, \tag{5.12}$$

where $\Gamma_{m,n}^{(l,2,3,\ldots,n)'}$ can be obtained recursively:

$$\Gamma_{m,n}^{(l,2,3,\ldots,n)'} = \frac{\Gamma_{m,n-1}^{(l,2,\ldots,n-1)'}}{\Gamma_{m,n-1}^{(n,2,\ldots,n-1)'}} - \frac{\Gamma_{m-1,n-1}^{(l,2,\ldots,n-1)'}}{\Gamma_{m-1,n-1}^{(n,2,\ldots,n-1)'}}. \tag{5.13}$$

The initial conditions for $\Gamma_{m,n}^{(l,2,3,\ldots,n)'}$ are:

$$\Gamma_{m,1}^{(1)'} = e^{-ikdmT_1}x'_m - e^{-ikd(m-1)T_1}x'_{m-1}, \tag{5.14}$$

$$\Gamma_{m,1}^{(n)'} = e^{ikdm(T_n-T_1)} - e^{ikd(m-1)(T_n-T_1)}, n \ne 1. \tag{5.15}$$

The proof of (5.12) can be given by mathematic induction. The proof can be divided into three steps:

1, prove that if there are l signals, the follow equation is true:

$$\Gamma_{m,l-1}^{(1,2,\dots,l-1)'} = \Gamma_{m,l-1}^{(l,2,\dots,l-1)'} s_l, 2 \le l \le M-1,\ \ l \le m \le M \tag{5.16}$$

2, prove that

$$\frac{\Gamma_{m,n-1}^{(n,2,\dots,n-1),}}{\Gamma_{m-1,n-1}^{(n,2,\dots,n-1),}} = e^{i(kd)(T_n - T_{n-1})}, 2 \le n \le M-1,\ \ n+1 \le m \le M \tag{5.17}$$

3, Final step, show that

$$\frac{\Gamma_{m,n-1}^{(1,2,\dots,n-1),}}{\Gamma_{m-1,n-1}^{(1,2,\dots,n-1),}} = e^{ikd(T_n - T_{n-1})}, \qquad n+1 \le m \le M \tag{5.18}$$

To start with, assume there are two sources with magnitude of s_1 and s_2 and AOA of θ_1 and θ_2. From (5.5), we have:

$$x_m' = e^{ikd_m T_1} s_1 + e^{ikd_m T_2} s_2, \qquad 1 \le m \le M \tag{5.19}$$

By eliminating s_1 from the equations, the following relations can be obtained:

$$e^{-ikd_m T_1} x_2 - e^{-ikd_{m-1} T_1} x_1 = (e^{ikd_m (T_2 - T_1)} - e^{ikd_{m-1}(T_2 - T_1)}) s_2, 2 \le m \le M \tag{5.20}$$

(5.14) shows the initial condition of step 1 is true, which is $l = 2$ case, and

$$\begin{aligned} \Gamma_{m,1}^{(1)'} &= e^{-ikd_m T_1} x_2 - e^{-ikd_{m-1} T_1} x_1, \\ \Gamma_{m,1}^{(2)'} &= (e^{ikd_m (T_2 - T_1)} - e^{ikd_{m-1}(T_2 - T_1)}) \end{aligned} \tag{5.21}$$

Suppose when $l = p$, step 1 is true, which is,

$$\Gamma_{m,p-1}^{(1,2,\dots,p-1)'} = \Gamma_{m,p-1}^{(p,2,\dots,p-1)'} s_p, \qquad 2 \le p \le M-1,\ \ p \le m \le M \tag{5.22}$$

Then if (5.10) is also true for $l = p+1$, it is true for all $l \ge 2$ by mathematic indcution.

When $l = p + 1$, a new signal with magnitude of s_{p+1} and AOA of θ_{p+1} is added to the system. Because of the linearity of the system, the following condition holds:

$$\Gamma_{m,p-1}^{(1,2,\dots,p-1)'} = \Gamma_{m,p-1}^{(p,2,\dots,p-1)'} s_p + \Gamma_{m,p-1}^{(p+1,2,\dots,p-1)'} s_{p+1}, \qquad p \le m \le M \tag{5.23}$$

One can validate the (5.17) by considering $s_p = 0$, then there are still p sources in the system, and (5.17) is reduced to (5.16) by replacing $\Gamma_{m,p-1}^{(p,2,\dots,p-1)'} s_p$ with $\Gamma_{m,p-1}^{(p+1,2,\dots,p-1)'} s_{p+1}$. In (5.17), both sides are divided by $\Gamma_{m,p-1}^{(p,2,\dots,p-1)'}$:

$$\frac{\Gamma_{m,p-1}^{(1,2,\dots,p-1)'}}{\Gamma_{m,p-1}^{(p,2,\dots,p-1)'}} = s_p + \frac{\Gamma_{m,p-1}^{(p+1,2,\dots,p-1)'}}{\Gamma_{m,p-1}^{(p,2,\dots,p-1)'}} s_{p+1}, \qquad p \le m \le M \tag{5.24}$$

(5.18) is the m^{th} equation, and subtract the m^{th} equation by $(m-1)^{th}$ equation for $p + 1 \le m \le M$. It leads to:

$$\frac{\Gamma_{m,p-1}^{(1,2,\dots,p-1)'}}{\Gamma_{m,p-1}^{(p,2,\dots,p-1)'}} - \frac{\Gamma_{m-1,p-1}^{(1,2,\dots,p-1)'}}{\Gamma_{m-1,p-1}^{(p,2,\dots,p-1)'}} = \left(\frac{\Gamma_{m,p-1}^{(p+1,2,\dots,p-1)'}}{\Gamma_{m,p-1}^{(p,2,\dots,p-1)'}} - \frac{\Gamma_{m-1,p-1}^{(p+1,2,\dots,p-1)'}}{\Gamma_{m-1,p-1}^{(p,2,\dots,p-1)'}} \right) s_{p+1}, \tag{5.25}$$

Recall the recursive relation given in (5.7), and (5.19) becomes:

$$\Gamma_{m,p}^{(1,2,\dots,p)'} = \Gamma_{m,p}^{(p+1,2,\dots,p)'} s_{p+1}, \quad p + 1 \le m \le M \tag{5.26}$$

Then the step 1 is true for all $2 \le l \le M - 1$.

In step 2, the initial condition is $n = 2$, and the left hand side can be expressed as:

$$\frac{\Gamma_{m,1}^{(2)'}}{\Gamma_{m-1,1}^{(2)'}} = \frac{e^{ikd_m(T_2-T_1)} - e^{ikd_{m-1}(T_2-T_1)}}{e^{ikd_{m-1}(T_2-T_1)} - e^{ikd_{m-2}(T_2-T_1)}} = \frac{e^{ik(d_m-d_{m-1})(T_2-T_1)} - 1}{1 - e^{ik(-d_{m-1}+d_{m-2})(T_2-T_1)}} \tag{5.27}$$

In ULA, $d_m - d_{m-1} = d_{m-1} - d_{m-2} = d$, therefore,

$$\frac{\Gamma_{m,1}^{(2)'}}{\Gamma_{m-1,1}^{(2)'}} = \frac{e^{ik(d)(T_2-T_1)} - 1}{1 - e^{ik(-d)(T_2-T_1)}} = e^{ikd(T_2-T_1)} \tag{5.28}$$

Thus it shows that for $n = 2$, the equation in step 2 is true.

Suppose when $n = p$ (5.11) is true:

$$\frac{\Gamma_{m,p-1}^{(p,2,\ldots,p-1),}}{\Gamma_{m-1,p-1}^{(p,2,\ldots,p-1),}} = e^{i(kd)\left(T_p - T_{p-1}\right)}, 2 \le p \le M-1,\ \ p+1 \le m \le M \tag{5.29}$$

When $n = p + 1$, we have

$$\frac{\Gamma_{m,p}^{(p+1,2,\ldots,p),}}{\Gamma_{m-1,p}^{(p+1,2,\ldots,p),}} = \frac{\dfrac{\Gamma_{m,p-1}^{(p+1,2,\ldots,p-1)'}}{\Gamma_{m,p-1}^{(p,2,\ldots,p-1)'}} - \dfrac{\Gamma_{m-1,p-1}^{(p+1,2,\ldots,p-1)'}}{\Gamma_{m-1,p-1}^{(p,2,\ldots,p-1)'}}}{\dfrac{\Gamma_{m-1,p-1}^{(p+1,2,\ldots,p-1)'}}{\Gamma_{m-1,p-1}^{(p,2,\ldots,p-1)'}} - \dfrac{\Gamma_{m-2,p-1}^{(p+1,2,\ldots,p-1)'}}{\Gamma_{m-2,p-1}^{(p,2,\ldots,p-1)'}}} = \frac{\dfrac{e^{ikd(T_{p+1}-T_{p-1})}}{e^{ikd(T_p-T_{p-1})}} - 1}{1 - \dfrac{e^{ikd(-T_{p+1}+T_{p-1})}}{e^{ikd(-T_p+T_{p-1})}}} \tag{5.30}$$

$$= \frac{e^{ikd(T_{p+1}-T_p)} - 1}{1 - e^{ikd(T_p-T_{p+1})}} = e^{ikd(T_{p+1}-T_p)}$$

This is the same form as (5.11) in step 2, therefore, the statement of step 2 is proved. The proof of statement in step 3 is relatively easy: use the equation (5.10) in step 1, and divide the m^{th} equation by $(m-1)^{th}$ equation of (5.10):

$$\frac{\Gamma_{m,l-1}^{(1,2,\ldots,l-1)'}}{\Gamma_{m-1,l-1}^{(1,2,\ldots,l-1)'}} = \frac{\Gamma_{m,l-1}^{(l,2,\ldots,l-1)'}}{\Gamma_{m-1,l-1}^{(l,2,\ldots,l-1)'}} = e^{ikd(T_l - T_{l-1})},\ \ l+1 \le m \le M \tag{5.31}$$

It will be interesting to check the equations in the three steps when the array is a nonuniform linear array. It can be observed that equations in step 1 and 3 can be applied to the nonuniform linear array, but (5.11) in step 2, the left hand side cannot be simplified into the right hand side.Let the left hand side of (5.11) to be $\Lambda_{m,n-1}^{(n,2,\ldots,n-1)}$, and from the recursive relation (5.7), we have:

$$\Lambda_{m,n-1}^{(n,2,\ldots,n-1)} = \frac{\Gamma_{m,n-1}^{(n,2,\ldots,n-1),}}{\Gamma_{m-1,n-1}^{(n,2,\ldots,n-1),}} = \frac{\dfrac{\Gamma_{m,n-2}^{(n,2,\ldots,n-2)'}}{\Gamma_{m,n-2}^{(n-1,2,\ldots,n-2)'}} - \dfrac{\Gamma_{m-1,n-2}^{(n,2,\ldots,n-2)'}}{\Gamma_{m-1,n-2}^{(n-1,2,\ldots,n-2)'}}}{\dfrac{\Gamma_{m-1,n-2}^{(n,2,\ldots,n-2)'}}{\Gamma_{m-1,n-2}^{(n-1,2,\ldots,n-2)'}} - \dfrac{\Gamma_{m-2,n-2}^{(n,2,\ldots,n-2)'}}{\Gamma_{m-2,n-2}^{(n-1,2,\ldots,n-2)'}}} = \frac{\dfrac{\Lambda_{m,n-2}^{(n,2,\ldots,n-2)}}{\Lambda_{m,n-2}^{(n-1,2,\ldots,n-2)}} - 1}{1 - \dfrac{\Lambda_{m-1,n-2}^{(n-1,2,\ldots,n-2)}}{\Lambda_{m-1,n-2}^{(n,2,\ldots,n-2)}}} \tag{5.32}$$

The initial condition of $\Lambda_{m,n-1}^{(l,2,\dots,n-1)}$ is when $n = 2$, which is $\Lambda_{m,1}^{(l)}$, and it is with the same form as (5.21):

$$\Lambda_{m,1}^{(l)} = \frac{e^{ik(d_m - d_{m-1})(T_l - T_1)} - 1}{1 - e^{ik(-d_{m-1} + d_{m-2})(T_l - T_1)}} \tag{5.33}$$

Thereby, for nonuniform linear array, $\Lambda_{m,n-1}^{(n,2,\dots,n-1)}$ can be represented as a function of $(T_1, \dots, T_n)$, and T_n is the only unknown. Notes in (5.25), we have:

$$\frac{\Gamma_{m,n-1}^{(1,2,\dots,n-1)'}}{\Gamma_{m-1,n-1}^{(1,2,\dots,n-1)'}} = \frac{\Gamma_{m,n-1}^{(n,2,\dots,n-1),}}{\Gamma_{m-1,n-1}^{(n,2,\dots,n-1),}} = \Lambda_{m,n-1}^{(n,2,\dots,n-1)} \tag{5.34}$$

The left hand side can be derived from $\theta_1, \dots \theta_{N-1}$ and $\vec{x}$. Hence, the only unknown T_n can be calculated from this sophisticated equation (5.28). Because it is a complicated nonlinear equation, an analytic solution is hard to find while it can always be solved numerically. Therefore, for nonuniform linear array, the proposed method can still find the AOA of last source but not efficiently.

Notice that the analytic solutions are for ULA with noise-free case, and they are derived from the noise-free signal x', not the measured signal x. To deal with the noise, we can start from the initial condition of $\Gamma_{m,l-1}^{(l,2,\dots,l-1)'}$ in (5.8) and (5.9). (5.8) can be rewritten as:

$$\Gamma_{m,1}^{(1)\prime} = e^{-ikdmT_1} x_m - e^{-ikd(m-1)T_1} x_{m-1} + n_m^{(1)}, \tag{5.35}$$

where $n_m^{(1)}$ is a zero mean Gaussian noise,

$$n_m^{(1)} = -e^{-ikdmT_1} n_m + e^{-ikd(m-1)T_1} n_{m-1} \tag{5.36}$$

In (5.9), $\Gamma_{m,1}^{(n)\prime}$ has no noise term. It can be shown that $\Gamma_{m,n}^{(l,2,\dots,n)\prime}$ doesn't contain the noise term if $l \neq 1$, and $\Gamma_{m,n}^{(1,2,\dots,n)\prime} = \Gamma_{m,n}^{(1,2,\dots,n)} + n_m^{(1,2,\dots,n)}$. Where $\Gamma_{m,n}^{(1,2,\dots,n)}$ is the same form of $\Gamma_{m,n}^{(1,2,\dots,n)\prime}$ except substituting x'_m by x_m, and $n_m^{(1,2,\dots,n)}$ denotes a zero mean Gaussian noise. This can also be

proved by mathematic induction from the recursive relations (5.7). The initial condition of the statement is true as given in (5.29) and (5.30). Suppose at $n = p$, it is true, which is:

$$\Gamma_{m,p}^{(l,2,\ldots,p)'} = \begin{cases} \Gamma_{m,p}^{(1,2,\ldots,p)} + n_m^{(1,2,\ldots,p)}, & l = 1 \\ \Gamma_{m,p}^{(l,2,\ldots,p)}, & l \neq 1 \end{cases} \tag{5.37}$$

When $n = p + 1$, and $l = 1$, we have:

$$\begin{aligned} \Gamma_{m,p+1}^{(1,2,\ldots,p+1)'} &= \frac{\Gamma_{m,p}^{(1,2,\ldots,p)'}}{\Gamma_{m,p}^{(p+1,2,\ldots,p)'}} - \frac{\Gamma_{m-1,p}^{(1,2,\ldots,p)'}}{\Gamma_{m-1,p}^{(p+1,2,\ldots,p)'}} \\ &= \frac{\Gamma_{m,p}^{(1,2,\ldots,p)} + n_m^{(1,2,\ldots,p)}}{\Gamma_{m,p}^{(p+1,2,\ldots,p)}} - \frac{\Gamma_{m-1,p}^{(1,2,\ldots,p)} + n_{m-1}^{(1,2,\ldots,p)}}{\Gamma_{m-1,p}^{(p+1,2,\ldots,p)}} \\ &= \frac{\Gamma_{m,p}^{(1,2,\ldots,p)}}{\Gamma_{m,p}^{(p+1,2,\ldots,p)}} - \frac{\Gamma_{m-1,p}^{(1,2,\ldots,p)}}{\Gamma_{m-1,p}^{(p+1,2,\ldots,p)}} + \frac{n_m^{(1,2,\ldots,p)}}{\Gamma_{m,p}^{(p+1,2,\ldots,p)}} - \frac{n_{m-1}^{(1,2,\ldots,p)}}{\Gamma_{m-1,p}^{(p+1,2,\ldots,p)}} \\ &= \Gamma_{m,p+1}^{(1,2,\ldots,p+1)} + n_m^{(1,2,\ldots,p+1)}, \end{aligned} \tag{5.38}$$

where $n_m^{(1,2,\ldots,p+1)}$ follows the recursive relation and is a zero mean Gaussian noise,

$$n_m^{(1,2,\ldots,p+1)} = \frac{n_m^{(1,2,\ldots,p)}}{\Gamma_{m,p}^{(p+1,2,\ldots,p)}} - \frac{n_{m-1}^{(1,2,\ldots,p)}}{\Gamma_{m-1,p}^{(p+1,2,\ldots,p)}} \tag{5.39}$$

If $l \neq 1$, the $n = p + 1$ case is simple to derive:

$$\begin{aligned} \Gamma_{m,p+1}^{(l,2,\ldots,p+1)'} &= \frac{\Gamma_{m,p}^{(l,2,\ldots,p)'}}{\Gamma_{m,p}^{(p+1,2,\ldots,p)'}} - \frac{\Gamma_{m-1,p}^{(l,2,\ldots,p)'}}{\Gamma_{m-1,p}^{(p+1,2,\ldots,p)'}} = \frac{\Gamma_{m,p}^{(l,2,\ldots,p)}}{\Gamma_{m,p}^{(p+1,2,\ldots,p)}} - \frac{\Gamma_{m-1,p}^{(l,2,\ldots,p)}}{\Gamma_{m-1,p}^{(p+1,2,\ldots,p)}} = \\ &= \Gamma_{m,p+1}^{(l,2,\ldots,p+1)}. \end{aligned} \tag{5.40}$$

Therefore, the statement (5.31) is proved. Next, (5.6) can be rewritten as:

$$e^{ikd(T_N - T_{N-1})} = \frac{\Gamma_{m,N-1}^{(1,2,\ldots,N-1)} + n_m^{(1,2,\ldots,N)}}{\Gamma_{m-1,N-1}^{(1,2,\ldots,N-1)} + n_{m-1}^{(1,2,\ldots,N)}} \tag{5.41}$$

In (5.35), the term $\Gamma_{m,N-1}^{(1,2,\ldots,N-1)}$ can be analytically obtained from the recursive relation given by (5.7) with the known variable $\theta_1, \ldots \theta_{N-1}$ and $\vec{x}$. Moreover, (5.35) can be rearranged as a linear equation:

$$\Gamma_{m,N-1}^{(1,2,\ldots,N-1)} = e^{ikd(T_N - T_{N-1})}\Gamma_{m-1,N-1}^{(1,2,\ldots,N-1)} + n_{m-1}^{(1,2,\ldots,N)\prime}, N+1 \le m \le M \tag{5.42}$$

where $n_{m-1}^{(1,2,\ldots,N)\prime} = e^{ikd(T_N - T_{N-1})}n_{m-1}^{(1,2,\ldots,N)} - n_m^{(1,2,\ldots,N)}$ is also a zero mean Gaussian noise. There are $K(M-N)$ equations of (5.36) for K snapshot angle of arrival. Then the slope term can be estimated by linear regression:

$$[b_0, e^{ikd(T_N - T_{N-1})}] = (X'X)^{-1}X'Y \tag{5.43}$$

where b_0 is the offset term in this linear regression problem, and X and Y are given by,

$$X = \begin{bmatrix} 1 & 1 & \ldots & 1 \\ \Gamma_{N,N-1}^{(1,2,\ldots,N-1)} & \Gamma_{N+1,N-1}^{(1,2,\ldots,N-1)} & \ldots & \Gamma_{M-1,N-1}^{(1,2,\ldots,N-1)} \end{bmatrix}^T \tag{5.44}$$

$$Y = \begin{bmatrix} \Gamma_{N+1,N-1}^{(1,2,\ldots,N-1)} & \Gamma_{N+2,N-1}^{(1,2,\ldots,N-1)} & \ldots & \Gamma_{M,N-1}^{(1,2,\ldots,N-1)} \end{bmatrix}^T \tag{5.45}$$

After solving (5.37), T_N can be obtained from $e^{ikd(T_N - T_{N-1})}$ as well, and finally, θ_N can be derived from T_N.

Another way to interpret (5.35) is

$$\Gamma_{m,N-1}^{(1,2,\ldots,N-1)} + n_m^{(1,2,\ldots,N)} = ae^{ikmd(T_N - T_{N-1})}, N+1 \le m \le M \tag{5.46}$$

where a is some constant. We can take logarithm to both sides of (5.40):

$$\log \Gamma_{m,N-1}^{(1,2,\ldots,N-1)} + \log\left(1 + \frac{n_m^{(1,2,\ldots,N)}}{\Gamma_{m,N-1}^{(1,2,\ldots,N-1)}}\right) = \log a + ikmd(T_N - T_{N-1}) + 2in\pi, n \in \mathbb{Z} \tag{5.47}$$

If $\left|\frac{n_m^{(1,2,\ldots,N)}}{\Gamma_{m,N-1}^{(1,2,\ldots,N-1)}}\right| \ll 1$, $\log\left(1 + \frac{n_m^{(1,2,\ldots,N)}}{\Gamma_{m,N-1}^{(1,2,\ldots,N-1)}}\right) \approx \frac{n_m^{(1,2,\ldots,N)}}{\Gamma_{m,N-1}^{(1,2,\ldots,N-1)}}$, and then (5.38) can be rewritten as:

$$\log \Gamma_{m,N-1}^{(1,2,\dots,N-1)} = \log a + ikmd(T_N - T_{N-1}) - \frac{n_m^{(1,2,\dots,N)}}{\Gamma_{m,N-1}^{(1,2,\dots,N-1)}} + i2l\pi, l \in \mathbb{Z} \quad (5.48)$$

To evaluate $T_N - T_{N-1}$, we just need the imaginary part of (5.42):

$$\arg \Gamma_{m,N-1}^{(1,2,\dots,N-1)} = \arg a + kmd(T_N - T_{N-1}) - \text{imag}\left(\frac{n_m^{(1,2,\dots,N)}}{\Gamma_{m,N-1}^{(1,2,\dots,N-1)}}\right) + 2l\pi, l \in \mathbb{Z} \quad (5.49)$$

Then $T_N - T_{N-1}$ can be found through linear regression as described in (5.37).

Notice that (5.42) contains the phase ambiguity term $i2l\pi$, which may be a problem in claculation. To solve this issue, we can first examine the phase difference between adjacent element (e.g. m and $m-1$ term) of $\Gamma_{m,N-1}^{(1,2,\dots,N-1)\prime}$. For a ULA with element spacing $\lambda/2$, the phase difference of $\Gamma_{m,N-1}^{(1,2,\dots,N-1)\prime}$ and $\Gamma_{m-1,N-1}^{(1,2,\dots,N-1)\prime}$ is $kd(T_N - T_{N-1}) = \pi(T_N - T_{N-1})$. In the ULA assumption, the targets can be detected only on one side of the linear array, which means $-90° < \theta_N < 90°$. Therefore, the phase difference is between $\pi(-1 - T_{N-1})$ and $\pi(1 - T_{N-1})$. In practical situation, due to the limitation of antenna's beamwidth, the angular range of the detectable target is smaller than 180°, and thus can further limit the potential phase difference. This can help in resolving the phase ambiguity if the phase noise is not too large. (5.50) is preferable compared to (5.36) because it is less sensitive to the noise.

5.4 Iterative AOA estimation of all sources

The ultimate AOA estimation task to find the AOA of all sources without piror knowlege of any of them in a single snapshot. In this section, an algorithm that iteratively solving the task described in Sec. 5.3 is proposed to solve this problem effectively and efficiently. The detail of the algorithm is described in Algorithm 5.1. In the beginning of the algorithm, assume there is only one source. Its AOA can be simply estimated based on the antennas elements' phase differences. The sources's magnitude $s_1^{(1)}$ can be estimated by:

$$s_1^{(1)} = \left(A\left(\theta_1^{(1)}\right)\right)^+ \vec{x} \tag{5.51}$$

where $(A)^+$ is the pseudo inverse of A. Then the estimated received signals denotes as $\vec{x}'^{(1)}$ can be obtained by $\vec{x}'^{(1)} = A\left(\theta_1^{(1)}\right)s_1^{(1)}$. Its corresponding root-mean-square error is given by:

$$rms\left(\vec{x} - \vec{x}'^{(1)}\right) = \sqrt{\sum_{i=1}^{M}\left(x_i - x'^{(1)}_i\right)^2} \tag{5.52}$$

Next step, assume there are two sources. The AOA of the second source is estimated from the analytic approach described by 5.3 with the AOA estimated from step 1. Then the AOA of the first source is evaluated from the same approach with the previously estimated AOA of the second source. This process will continue until convergence. Then the second order estimated signal $\vec{x}'^{(2)}$ can be evaluated and so is the $rms\left(\vec{x} - \vec{x}'^{(2)}\right)$. Comparing the RMSE of $\vec{x}'^{(2)}$ and $\vec{x}'^{(1)}$, if they are very close, then there might be just one sources and the algorithm will stop. Otherwise the algorithm will continue until the close RMSE criterion is met.

Algorithm 5.1 Iterative AOA estimation

Input: $\vec{x}$, *d*, *M* **Output:** $\vec{\theta}$, $\vec{s}$
Initial condition: *N*=1 (1 source)

estimate $\theta_1^{(1)}, s_1^{(1)}$ from the antennas' phase differences
while *true*
  N=*N*+1; $\vec{\theta}^{(N)} = \vec{\theta}^{(N-1)}$; $\theta_N^{(N)} = 0$; $\vec{x}'^{(N)} = A\left(\theta^{(N)}\right)\left(A\left(\theta^{(N)}\right)\right)^+ \vec{x}$
  while not converge **or** not reach maximum iteration
    $\vec{x}'^{(N)}_{old} = \vec{x}'^{(N)}$, $\vec{\theta}^{(N)}_{old} = \vec{\theta}^{(N)}$
    for *i* = *N* to 1 **do**
      estimate $\theta_i^{(N)}$ from the rest $\theta_j^{(N)}, j \neq i$
    end for
    $\vec{x}'^{(N)} = A\left(\theta^{(N)}\right)\left(A\left(\theta^{(N)}\right)\right)^+ \vec{x}$
    if (rms($\vec{x} - \vec{x}'^{(N)}$) > rms($\vec{x} - \vec{x}'^{(N)}_{old}$)-$\delta$) **then**
      $\vec{\theta}^{(N)} = \vec{\theta}^{(N)}_{old}$; **break**
    end if
  end while

13: $\vec{s}^{(N)} = \left(A\left(\theta^{(N)}\right)\right)^{+} \vec{x};\ \ \vec{x}'^{(N)} = A\left(\theta^{(N)}\right)\vec{s}$
14: **if** (rms($\vec{x} - \vec{x}'^{(N)}$) > rms($\vec{x} - \vec{x}'^{(N-1)}$) -$\delta$) **then**
15: $\vec{\theta} = \vec{\theta}^{(N-1)}$; $\vec{s} = \vec{s}^{(N-1)}$; **break**
16: **end if**
17: **end while**

5.5 Simulation Results

To demonstrate how the proposed algorithm works and its effectiveness, a three-source AOA estimation example is shown. The basic idea of the iterative approach is to find the AOA of the strongest source first, then find that of the second strongest one and so on. Therefore, the most challenge scenario is when all sources have the same amplitude. In one example, we examine a three-source AOA estimation with a 10-element half-wavelength spacing ULA. The three sources have the same amplitude and different AOA: $s_1 = s_2 = s_3 = 1$, and $\theta_1 = 5.1°$, $\theta_2 = 10.4°$, $\theta_3 = -4.2°$. The signal to noise ratio (SNR) is 30 dB and the analysis are based on just one snapshot. The iteration steps of the algorithm are shown in Figure 5.2. In the beginning, the algorithm assumes there is only one source, and it detects one AOA of 5.4°. Then it assumes there are two sources and in the second iteration, it estimates the two AOA are -4.4° and 11.6°. It converges in two iterations and then it adds one more source to the problem. After four iterations, the convergence condition is met and it gives the estimation of three AOA: -4.31°, 4.90° and 10.34°. Next, it further adds one source to the estimation problem, but the RMSE of ($\vec{x} - \vec{x}'$) doesn't drop significantly, therefore, the algorithm concludes there are only three sources and their estimated AOA are given previously. It shows that the proposed algorithm can quickly estimate the number of sources and the corresponding AOA. The RMS error of the AOA estimation is 0.14°, which shows very good performance with high SNR.

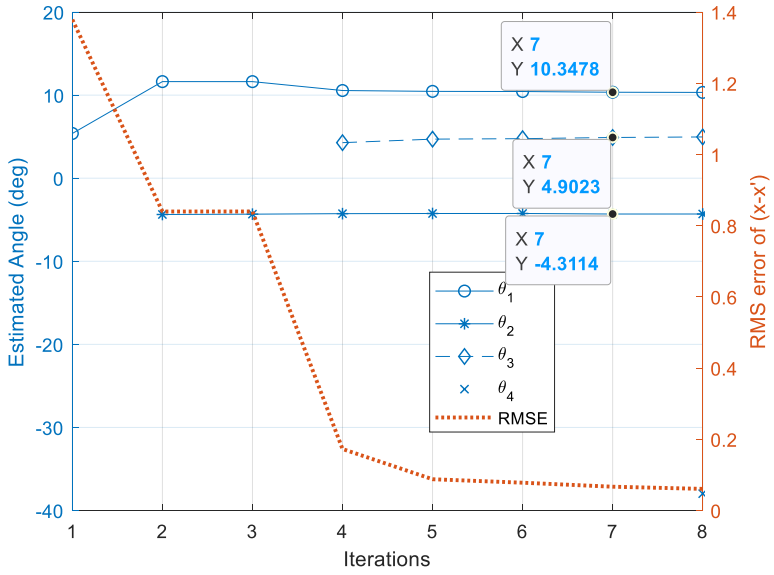

Figure 5.2. The estimated AOA and RMS error as a function of iterations of AIMA for a three-source problem

In some case that there existing two close sources with identical magnitude, the algorithm will converges to one sources with AOA to be in the center of the two sources. To solve this problem, a very small coefficient can be added to all the preknown AOAs. For example, if there are two identical sources with AOA of 5° and 6°, and the SNR is 40 dB. For a 10-element ULA, the first estimation of AOA will be about 5.5°, if there is no perturbation, it is likely the second estimation angle is also 5.5° and then the algorithm will conclude that there is only one source locates at 5.5°. In this example, 0.01° is added to the preknown angle every time performing the analytic method for AOA estimation, and the estimated AOA and the corresponding RMSE of $\vec{x}'^{(l)}$ is depicted in Figure 5.3. It is shown that in 4 iterations the angles converge to 4.97° and 5.96°, respectively.

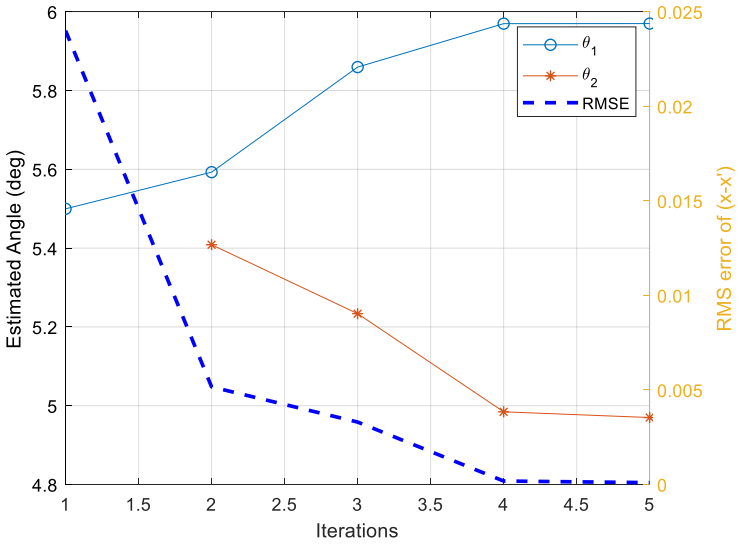

Figure 5.3. The estimated AOA and RMS error as a function of iterations of AIMA for two close targets

The proposed method is compared with some classical AOA estimation algorithms including MUSIC-SS [41], maximum liklihood method with alternating projection (ML-AP) [133], and ASSIA [134]. In the first example, assume there are three equal-amplitude sources with angular spacing larger than the array beamwidth. A 10-element ULA with half wavelength spacing is used to estimate AOA. The half power beam width (HPBW) of this array can be approximately given by $\frac{70\lambda}{d} = 14°$. The AOA and source amplitudes are given as: $\theta_1 = 5.5°$, $\theta_2 = 30.5°$, $\theta_3 = 50°$, $s_1 = s_2 = s_3 = 1$. Because MUSIC-SS requires at least M snapshot to evaluate covariance matrix, in this example, 10 snapshots are used for each algorithm. MUSIC-SS, ML-AP and ASSIA estimate the AOA on grid, and in this example, each of them has angular step of 0.5°, and the number of sources are given in MUSIC-SS and ML-AP algorithm. To evaluate the performance of AOA estimation, the average RMS-error of the three AOA as a function of SNR is shown in Figure 5.4. Figure 5.5 shows the normalized time performance of the four different algorithms. The average RMS-error of AOA for one SNR value is generated by 200 Monte Carlo simulations.

It shows that AIMA has the second-best accuracy to estimate the AOA for SNR < 20 dB, and its average RMSE of all three AOA is less than 0.3° for SNR > 10 dB in this three-source AOA estimation problem. Compared to ML-AP algorithm, AIMA has slightly larger RMSE of AOA but is about 100 times faster. It is also twice faster than MUSIC-SS algorithm in this problem.

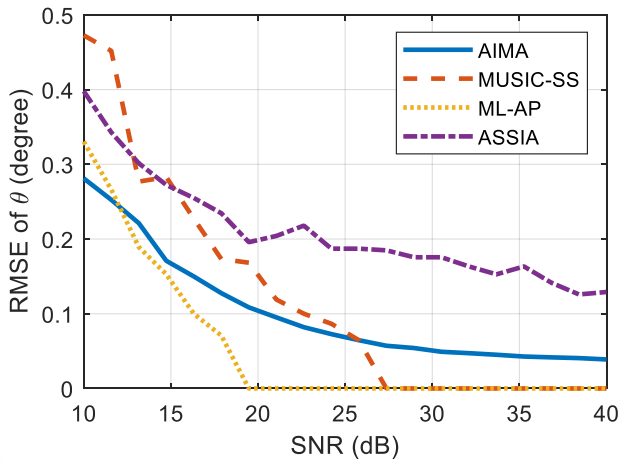

Figure 5.4. The average RMSE of the three estimated AOA ($\theta_1 = 5.5°$, $\theta_2 = 30.5°$, $\theta_3 = 50°$) as a function of SNR for different algorithms with 10 snapshots

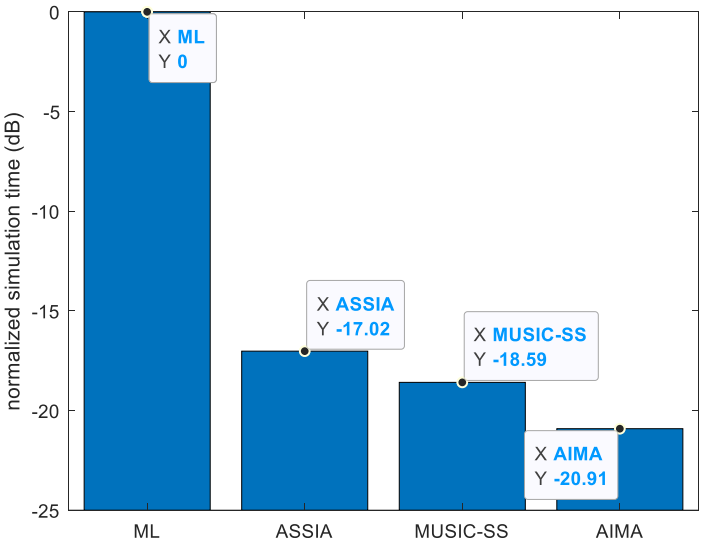

Figure 5.5. The time performance comparison of different algorithms for the three AOA estimation problem ($\theta_1 = 5.5°$, $\theta_2 = 30.5°$, $\theta_3 = 50°$)

In another example, a two-source problem with close angular spacing is used to compare the performances of different AOA estimation algorithms mentioned previously. In this problem, the angular spacing is smaller than the antenna beamwidth: $\theta_1 = 5.2°$, $\theta_2 = 10.3°$. It is noted that these two angles are off-grid for MUSIC-SS, ML-AP and ASSIA. The two sources are assumed to be equal amplitude. A 10-element ULA with half wavelength spacing is used in this example as well. The average RMSE of the two estimated AOA as a function of SNR for different algorithms is depicted in Figure 5.6, and the simulation time comparison for different algorithm is shown in Figure 5.7. It is found that in this close-source AOA problem, AIMA has the second best angular RMSE performance when SNR < 27 dB and has the smallest RMSE when SNR > 35 dB. It is still about 100 time faster than the ML-AP algorithm and about 10 times faster than ASSIA and 3 times faster than MUSIC-SS.

Besides the preferable AOA estimation performance and efficiency, AIMA possesses other advantages like no requirement of prior knowledge of the number of sources, and can be applied in single snapshot problem compared to many classic AOA estimation algorithm.

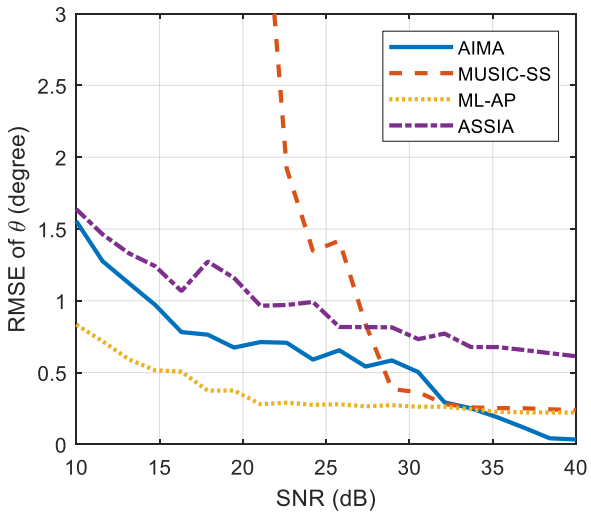

Figure 5.6. The average RMSE of the two close AOA ($\theta_1 = 5.2°$, $\theta_2 = 10.3°$) as a function of SNR for different algorithms with 10 snapshots

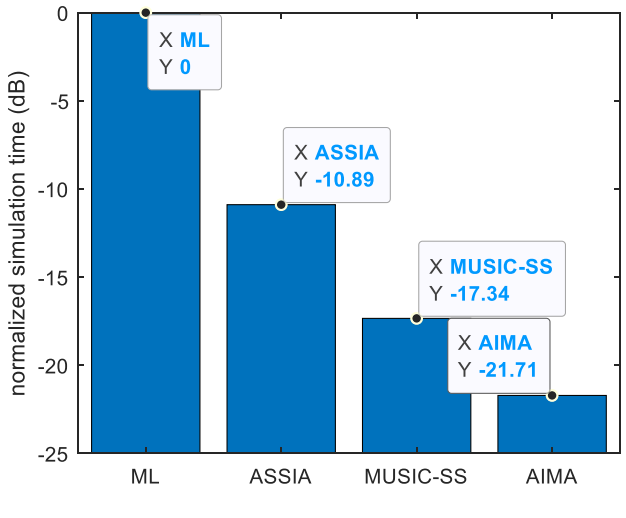

Figure 5.7. The time performance comparison of different algorithms for the two AOA estimation problem ($\theta_1 = 5.2°, \theta_2 = 10.3°$)

Among the four AOA estimation algorithms, AIMA and ASSIA has the advantage of no need to know the number of sources, and the lack of the prior knowledge of number of sources is very common in radar and communication applications. MUSIC algorithm will fail if it predicts a wrong number of sources especially for coherent signals. Regarding ML-AP, if the number of source is not known, it can estimate the number successively. For example, assume the number of source is N (start from N=1), and it can test the RMSE performance of order N and order N+1, if they are close, then it may conclude there are N sources, otherwise it will continue the process to N+2. Because the computational complexity increase dramatically with the number of sources, this process is even more time-consuming than the ordinary ML-AP with number of sources known. Figure 5.8 (a) demonstrates the normalized simulation time for the three algorithms (ML-AP, ASSIA and AIMA) with no prior knowledge of number of sources with 1000 Monte Carlo simulations for a three source problem. It shows that in this condition AIMA is about 200 times faster than ML-AP.

In addition, ASSIA and ML-AP are grid-based algorithm, which means they estimate the AOA with discretized angles. For off-grid AOA estimation, both algorithms could estimate wrong number of sources as additional weak sources may be included to the estimation to compensate the error from off-grid estimation. The over estimation of source number will lead to more processing time as well. Such issue doesn't exist for AIMA as AIMA can estimates the AOA arbitrarily off grid. The time performance comparison of the three algorithms in an off-grid AOA estimation problem is shown in Figure 5.8(b). The simulation time is summarized from 1000 Monte Carlo simulations and normalized. It shows that in this off-grid problem, AIMA is about 400 times faster than ML-AP and more than 20 times faster than ASSIA.

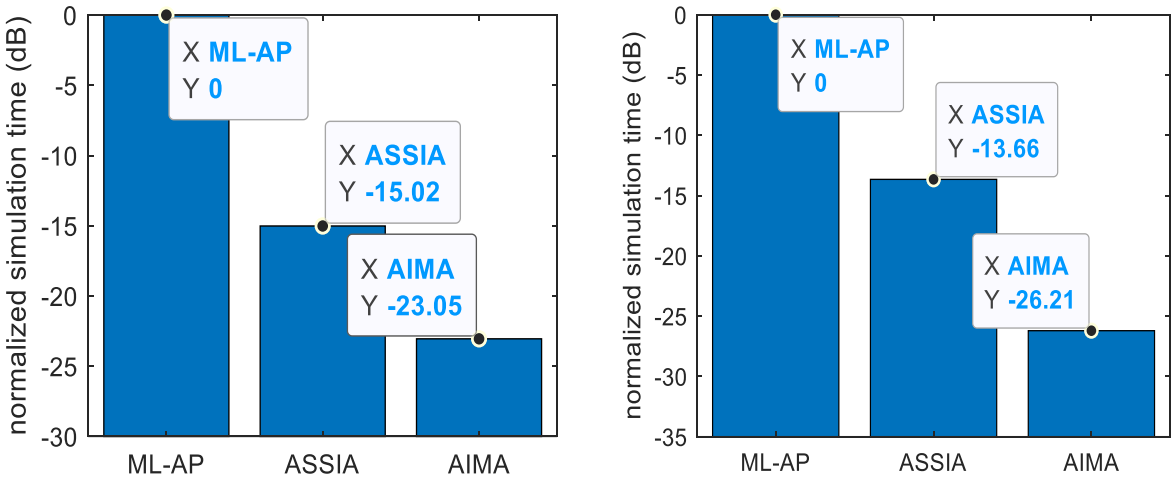

(a) (b)

Figure 5.8. The normalized time performance comparison for different algorithms without knowing the number of sources in (a) a three AOA ($\theta_1 = 5.5°$, $\theta_2 = 30.5°$, $\theta_3 = 50°$) problem and (b) a two AOA ($\theta_1 = 5.2°$, $\theta_2 = 10.3°$) estimation problem.

Besides the SNR and the angular space between signals, the performance of AOA estimation is limited by the number of array elements and the array spacing as well. Theoretically, for an array with *M* elements, the proposed algorithm can be applied to find (*M* - 1) sources because

each iteration of estimation N^{th} angle only requires $(N+1)$ equations. However, only using $N+1$ elements may not get the AOA correctly as there are in total $2N$ unknowns (each source has two unknowns: amplitude and AOA), and requires at least $2N$ equations to solve it. More elements will lead to more accurate results particularly in the single snapshot problem because adding equations can provide better estimation under noise condition.

To demonstrate how the AOA estimation performance is impacted by the number of array elements for the proposed algorithm, the RMSE of the AOA estimated with AIMA is studied for different numbers of array elements with the same array spacing (λ/2). The AOA estimation performance for a two-source estimation problem ($\theta_1 = -15°$, $\theta_2 = 0°$, $\mathrm{SNR}_1 = 30\mathrm{dB}$, $\mathrm{SNR}_2 = 20\mathrm{dB}$) with a single snapshot is shown in Figure 5.9 (a), and that for a three-source estimation problem ($\theta_1 = -15°$, $\theta_2 = 0°$, $\theta_3 = 10°$, $\mathrm{SNR}_1 = 30\mathrm{dB}$, $\mathrm{SNR}_2 = 25\mathrm{dB}$, $\mathrm{SNR}_3 = 20\mathrm{dB}$) with a single snapshot is depicted in Figure 5.9. (b). Each RMSE of AOA is obtained from more than 500 Monte Carlo simulations. It shows that for the two-source problem the RMSE in estimated angle is less than 1 dB when there are more than 6 elements, and for the three-source problem, the RMSE is less than 1 dB when there are more than 8 elements. Therefore, it is recommended to have $2N+2$ or more array elements in this half wavelength spacing ULA to apply the AIMA for estimation of AOA.

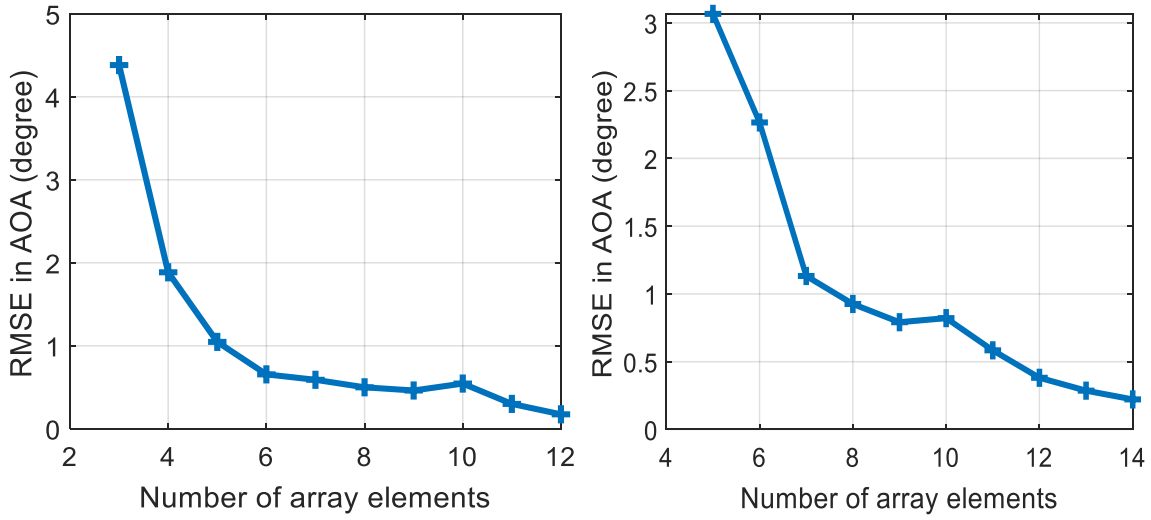

(a) (b)

Figure 5.9. The RMSE of AOA estimated with AIMA as a function of the number of array elements of a half-wavelength spacing ULA for (a) a two AOA ($\theta_1 = -15°$, $\theta_2 = 0°$) problem and (b) a three AOA ($\theta_1 = -15°$, $\theta_2 = 0°$, $\theta_3 = 10°$) estimation problem.

When the number of elements is fixed, the spacing between array elements determines the aperture size of the antenna array. Generally, the larger the aperture size is, the better the antenna array can recognize the sources. In this example, this idea is examined for AIMA algorithm. Figure 5.10 (a) shows the simulated RMSE of the estimated AOA as a function of array spacing of a 6-element ULA in a two-source problem and that of a 8-element ULA for a three-source problem is depicted in Figure 5.10 (b). Each RMSE of the angular spacing is summarized from 500 Monte Carlo simulations. It shows that wide antenna spacing can largely improve the performance of AOA estimation. However, if the spacing is too large, for example, larger than one wavelength, it may introduce grating lobes and causing false detection on some directions.

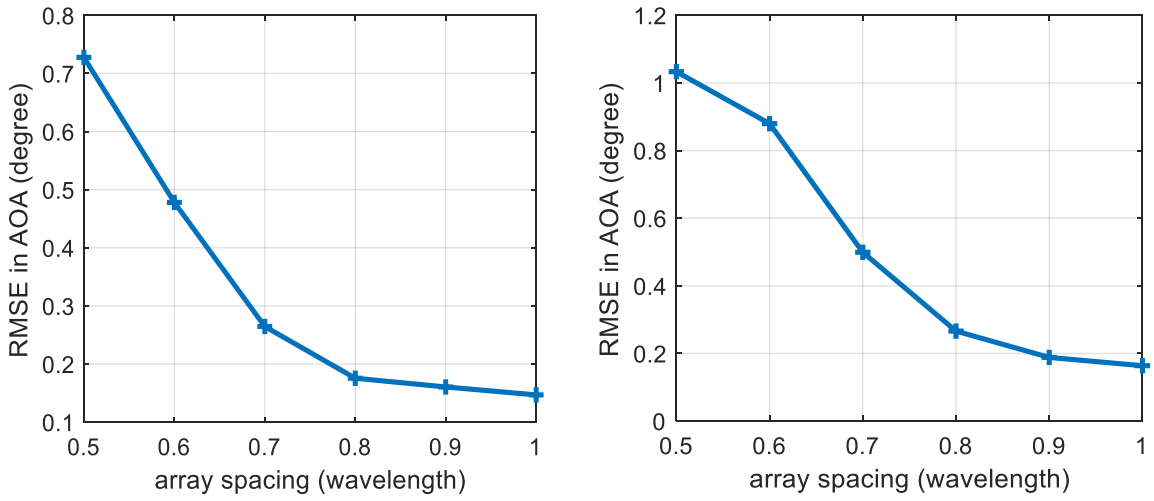

(a) (b)

Figure 5.10. The RMSE of AOA estimated with AIMA as a function of array spacing of (a) a 6-elment ULA for a two AOA (θ_1=-15°, θ_2=0°) problem and (b) a 8-element ULA for a three AOA (θ_1=-15°, θ_2=0°, θ_3=10°) estimation problem.

In the last simulation example, the proposed AOA estimation algorithm AIMA is applied to a radar simulation scenario. The radar system has 12 channels forming a ULA with separation of half wavelength. It operates at 77 GHz as center frequency with bandwidth of 500 MHz. It is a FMCW radar, and there are 512 frequency samples in each chirp, and one frame contains 256 chirps. There are 3 pairs of point targets with similar RCS, range and velocity in the scene, and their positions and velocities are given in Figure 5.11 (a). Because each pair of the targets has the same range and velocity, the six targets turn out to be three points shown in a range-Doppler map of each channel as depicted in Figure 5.11 (b). Some traditional AOA estimation algorithms may fail at this point as they may conclude there are only three targets. In Figure 5.11 (b), the power is normalized with the maximum value as 0 dB, and the SNR is about 30 dB. There are 12 range-Doppler maps for all 12 channels, and therefore for each peak in the range-Doppler maps, there are 12 signals corresponding to each channel. These signals are processed with AIMA algorithm,

and the estimated position is plotted in Figure 5.11 (c). It shows a very good agreement between the true position and estimated position of the six targets.

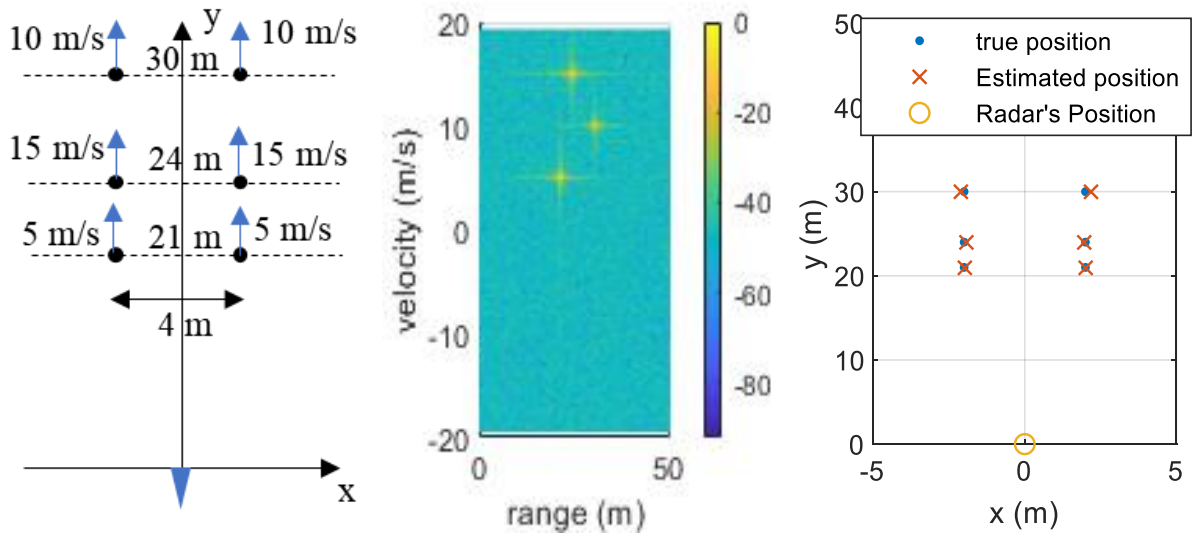

(a) (b) (c)

Figure 5.11. (a) The positions and velocities for the six targets for the radar simulation problem, (b) the normalized range-Doppler map of one channel for the six targets and (c) the comparison between the retrieved positions by AIMA and the true positions of targets.

5.6 Measurement Results

To validate the effectiveness of the proposed algorithm, multiple-source AOA measurements are performed. A six-element antenna array with spacing of half wavelength is used for the measurement. The antenna is an inset-fed rectangular microstrip patch antenna [140] with center frequency of 10 GHz and bandwidth of about 1 GHz, and the 3 dB beamwidth is more than 60°. The photo of the antenna array is shown in Figure 5.12 (a). The six elements are connected to an electrically controlled switch by equal-length transmission lines. Three horn antennas that represent signal sources are demonstrated in Figure 5.12 (b). The three sources are almost in the same range of the antenna array, and because their heights and gains are different, the signal's

amplitude can be quite different. shows that a six-element array is capable to find the AOA of two sources but not good for finding the AOA of three or more sources. Therefore, in this measurement, we only examine the two-source problem.

In the measurement, one port of a vector network analyzer (VNA) is connected to the switch connected to the antenna array, and the other port is connected to the sources. In the first measurement, only Source II in Figure 5.12 (b) is connected, and the S_{21} is measured for each of the array elements, and they can be denoted as $S_{21,i}^{(II)}$, i denotes i^{th} element of the array. These data are used for calibration. The SNR for each element is greater than 20 dB. Next, each pair of the three sources are connected to one port of the VNA through an equally power dividing power divider. Similarly, we measured the S_{21} for each element and denote them as $S_{21,i}^{(I,II)}$, $S_{21,i}^{(I,III)}$ and $S_{21,i}^{(II,III)}$. In one example, both source II and source III are transmitting signals, and Figure 5.13 (a) shows the measured $S_{21,i}^{(II,III)}$ as a function of frequency for different array elements. By taking fast Fourier transform (FFT), the possible multipath from the wall or ground of the chamber can be filtered out and only left the signal directly propagating from sources. Then the signal $\vec{x}$ can be obtained by calibrating the peak value of $S_{21,i}^{(II,III)}$ after FFT:

$$x_m^{(II,III)} = \frac{\max\left(\mathrm{FFT}\left(S_{21,m}^{(II,III)}\right)\right)}{\max\left(\mathrm{FFT}\left(S_{21,m}^{(II)}\right)\right)}, \quad 1 \le m \le M \tag{5.53}$$

The amplitude and phase of the received signals for different array elements are given in Figure 5.13 (b). Those data are put into AIMA algorithm to find the AOA of each source. The comparisons between the estimated AOA and the true AOA are given in Table I. It shows that the proposed algorithm can accurately estimate the AOA with less than 1° error with SNR more than 20 dB. The RMSE in estimated AOA is about 0.6°.

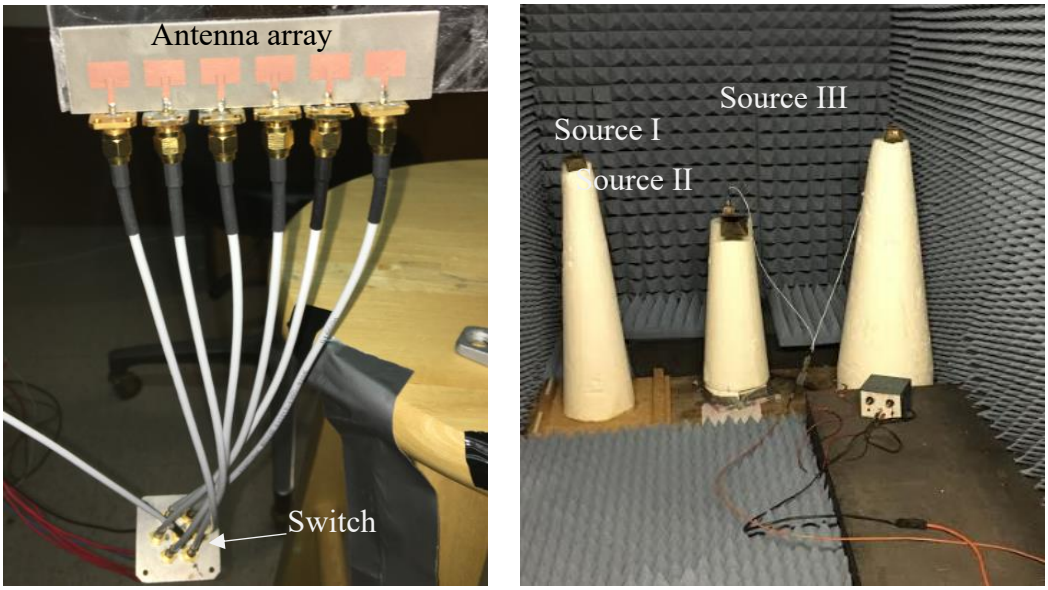

(a) (b)

Figure 5.12. (a) The picture of the six-element antenna array, the six elements are connected to an electrically controlled switch; (b) the picture of the three sources, they are in the same range to the receivers and two of them will be fed the same power in each measurement.

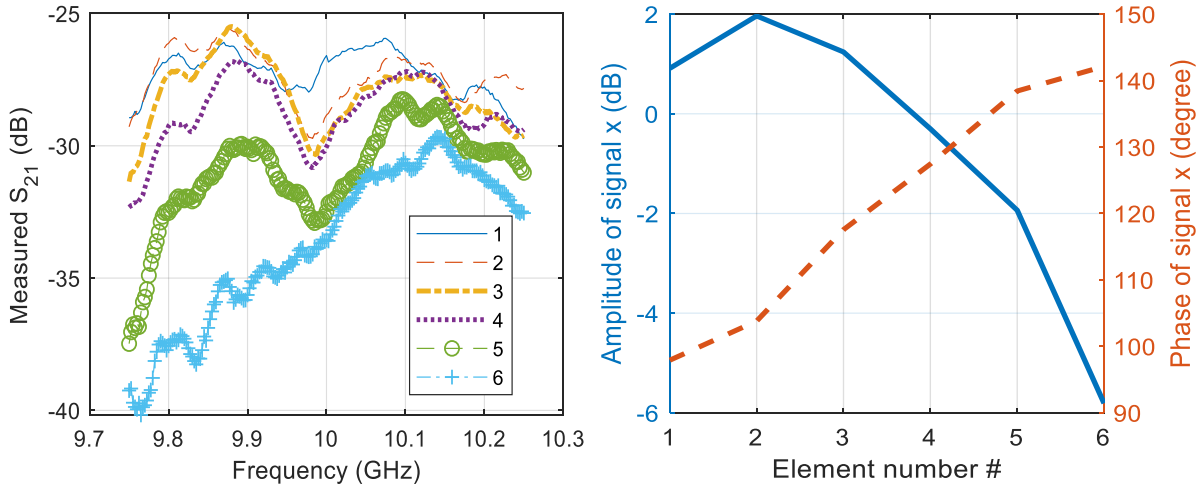

(a) (b)

Figure 5.13. (a) The measured $S_{21,i}^{(II,III)}$ for different array elements as a function of frequency; (b) the amplitude and phase of the received signals $x_m^{(II,III)}$ after calibration for each antenna element.

Table 5 - 1. Performance of the AOA estimation of AIMA with measurement data

	Source I	**Source II**	**Source III**
True AOA (°)	-10.7	0	11.5
I&II only, estimated AOA (°)	-9.78	0.71	NA
I&III only, estimated AOA (°)	-10.75	NA	11.38
II&III only, estimated AOA (°)	NA	-0.04	12.41

5.7 Conclusion

In this paper, a novel analytic iterative algorithm for multiple-source AOA estimation is presented. The algorithm involves two major tasks: 1, analytically evaluate the AOA of the last source from the AOA of all other sources without knowing their amplitude. 2, iteratively solving task 1 to have the smallest RMSE in measured signals and moreover to obtain the number of sources and their AOA and amplitude. This approach doesn't require the knowledge of number of sources, and can be applied in single-snapshot condition. This iterative method converges quickly and outperforms many known algorithms in terms of time efficiency. This method has a wide range of applications particularly in dynamic systems such as automotive radars for autonomous vehicles.

Chapter 6 Machine Learning-Based Target Classification for MMW Radar in Autonomous Driving

6.1 Introduction

The technology for autonomous vehicles with radar was first envisioned in the late 90's [39][90][142][143], but only recently has tremendous progress been made towards the development of these revolutionary vehicles[141]. In autonomous driving, one of the main challenges is to reliably detect and identify all targets in a complex environment. Targets are detected by a multitude of sensors and are represented by different types of data. The most commonly used sensors include optical cameras, lidars and radars. Cameras present targets as 2D colored images , lidars generate 3D point cloud representation of targets[144], and radars measure the range, velocity and the radar cross-section (RCS) of the targets. Each type of sensor has its ownstrengths and wakness, for example, cameras have the highest angular resolution for short distances but are not accurate for range detection and perform poorly at night or in inclement weather conditions (rain, fog, and snow); lidar can measure the distance of targets and has excellent spatial resolution, however it suffers from low sensitivity and it has difficulty detecting highly reflective objects (objects with specular surfaces), in addition to having poor performance in bad weather conditions. On the other hand, radar can detect targets at longest range, it is able to directly measure a target's range and velocity, and its performance is unaffected by poor weather conditions. The drawbacks of radar sensors include poor angular resolution and possible false alarms due to multipath issues [146][146].

For the traffic target classification problem, many studies have been carried out for cameras and lidars [147]-[149] due to their high resolutions and the intuitive nature of data interpretation. However, the performance of cameras or lidars will be largely degraded by poor visibility conditions whereas radar data is, for the most part, unaffected by the atmospheric conditions and the time of day [146]. Hence it is important to develop solutions for target classification using radar data.

Radar based target classification has been studied in the field of remote sensing for decades. Radar classification methods have been applied to aircrafts, military vehicles, and terrestrial targets for various remote sensing applications. Since aircrafts must be detected at long range, they are usually modeled as point targets, and the frequency or time (range) response of the radar signals are used to classify the targets [150][151]. Terrestrial [152] [153] and military vehicles [154][155] can be detected by airbone or satellite synthetic aperture radar (SAR), and therefore the target classification is based on processing the SAR images of targets. For the application at hand, MMW automotive radar can encounter traffic targets at different ranges that may only be partially illuminated and thus cannot always be considered as classical point targets. Synthetic aperture radar methods are obviously not applicable either.

Pedestrians and bicyclists are often encountered in both urban and rural environments, and are considered to be the most important targets to be correctly identified. Because a moving pedestrian will frequenty have different positions on the arms and legs when a pedestrian is moving, it is observed that moving pedestrians exhibit quite different Doppler radar response patterns from those for vehicles. This feature is described and utilized to distinguish pedestrians from vehicles in many studies [156]-[158]. However, when there is no observable Doppler signature, i.e. targets

are stationary or they have zero down range velocity with respect to the radar, these methods are not applicable.

Recent advances in machine learning techniques including convolutional neural network (CNN) [159][160] and convolutional recurrent neural network (RNN) [161] enable new methods for radar target classifications. In [162], multiple frames for the range-Doppler images of a continous movement of a target is put into target classifications models based on RNN. Similar to other Doppler based target classification methods, this approach can only be applied to moving targets. In [163], the phase and magnitude of each antenna element is inputted into a deep neural network to distinguish a pedestrian and a vehicle. While greater than 90% accuracy is achieved, the data samples in the paper are very limited (only based on one vehicle and one pedestrian), which limits the scope and applicability of the model. For some advanced radars that are capable of imaging, the targets then can be represented by radar images in target classification [165][166]. In [165], the proposed algorithm applies CNN to classify static targets as parked vehicles or non-vehicles. In [166], targets are visualized as radar point clouds, where RCS information is discarded, and zero-Doppler data are excluded, which means only dynamic targets are used in classification.

A convincing target classification model based on machine learning requires a comprehensive dataset including an exhaustive list of targets. Measurements can provide reliable data; however, gathering them can be very expensive, time consuming and sometimes impractical for some targets. For example, it is difficult to take the radar measurement from all azimuth directions and any range for a heavy truck or bus as it is almost impossible to put a large vehicle on a turn table for accurate angular variation. By contrast, simulation can be performed for any kind of target from any angle and range with much lower cost. Furthermore, pedestrian models with all ages, weights and heights can easily be generated and examined in simulation, whereas

such measurements usually have very limited samples and can be time consuming and uncomfortable for the test subject.

In this chapter, four traffic target classification approaches for different types of radars regardless of target motion are proposed, and a comparative study of these approaches is performed. The proposed models utilize the statistics of RCS data for different target categories generated by a high-fidelity RCS simulation program. In addition, some measurements are also taken to verify the accuracy of the simulations. In this classification problem, the targets are categorized into three major groups: pedestrians, vehicles, and other objects. For traditional radars, depending on the radar range resolution and the size of the targets, the RCS of targets are examined as point or distributed targets. A novel statistical analysis is proposed that makes use of a large dataset for different targets and an artificial neural network (ANN). This approach is applied to both point and distributed targets. For a radar capable of imaging, 2D or 3D radar images are generated from simulation as well and used in target classifications with CNN. This paper is an extension of our preliminary work in [167], with more data samples, target classification methods, discussions and experimental validations.

This paper is organized as follows: in Section 6.2, the forward scattering model and simulation used for calculation of RCS of targets (both as point or distributed target), and the radar images in 2D and 3D forms are presented. In Section 6.3, the radar target classification models based on machine learning for different types of radar data are implemented and discussed. In Section 6.4, radar measurements for some targets are performed and the radar data are examined with the off-line target classification models for verification. Finally, concluding remarks are provided in Section 6.5.

6.2 High-fidelity radar response simulation for different types of radar

At W band frequencies, traffic targets like vehicles and pedestrians have dimensions on the order of hundreds to thousands of wavelengths. The full-wave methods including method of moment (MoM), finite element method (FEM) and finite-difference time-domain method (FDTD) can generate accurate results but may require exorbitant amounts of time to run the simulations for these electrically very large targets. Asymptotic methods like physical optics method (PO) and physical theory of diffraction (PTD) have been successfully used to evaluate the backscattering RCS of traffic targets at MMW frequency. In this thesis, the PO method is used since most common traffic targets do not often present any sharp edges and are for the most parts convex. The detailed information and validation of PO approach is described in Chapter 2.

6.2.1 RCS simulation results

The RCS of pedestrians, vehicles and other static targets are simulated at different frequencies, aspect angles and ranges. In these simulations, the vehicles are considered as metallic objects and pedestrians and trees are treated as dielectric materials. The complex dielectric constant for human skin is reported in the literature [168]-[170] to be within the ranges of $6.5 \leq \varepsilon_r' \leq 11.6$ and $3.9 \leq \varepsilon_r'' \leq 11.2$. In this research, the dielectric constant model created by Gabriel [169] is used ($\varepsilon_r = 6.57 + 8.92i$ at 77 GHz). Regarding the permittivity of canopies, the dielectric model developed by Matzler [171] is applied, and for a palm tree, the dielectric constant is given as $\varepsilon_r = 4.01 + 3.35i$ at 77 GHz.

The RCS of complex traffic targets fluctuates rapidly with both frequency and aspect angle. For example, Figure 6.1 (b) shows the RCS as a function of frequency for three different targets, a pedestrian, a sedan, and a dwarf palm tree, whose geometries are shown in Figure 6.1 (a). In the simulations, targets are 50 m away from the radar. It is shown that the RCS can fluctuate up to 20 dB over 1 GHz bandwidth, which is less than 1.3% fractional bandwidth. This is mainly due to the

multiple scattering centers on large complex traffic targets that can add constructively or destructively. This argument also holds for the variation of RCS as a function of incidence angle. Note that the average RCS value of a pedestrian and that of a dwarf palm tree from some angles are similar, but the variances are different. This feature may be used in target classification. The RCS statistics is also a function of azimuth incident angle. The frequency averaged RCS as a function of azimuth angle for a 1.8 m tall pedestrian, a sedan and a dwarf palm tree are depicted in Figure 6.1 (c). It shows a significant variation of the RCS over different incident angles for these targets. If the entire target is within the antenna illumination, its statistical information is range independent as shown in Figure 6.1 (d).

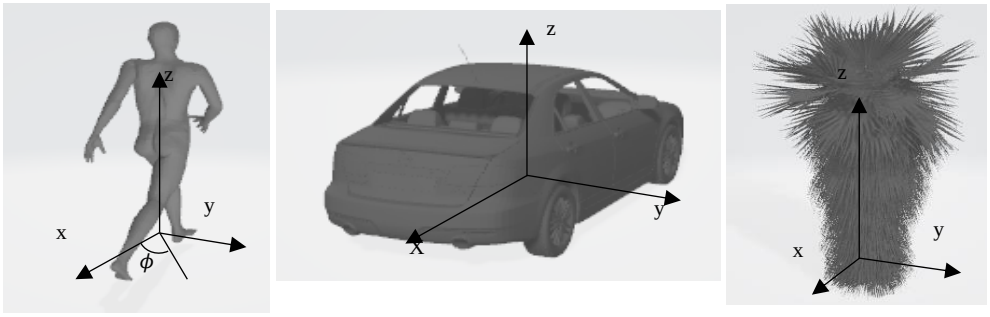

(a)

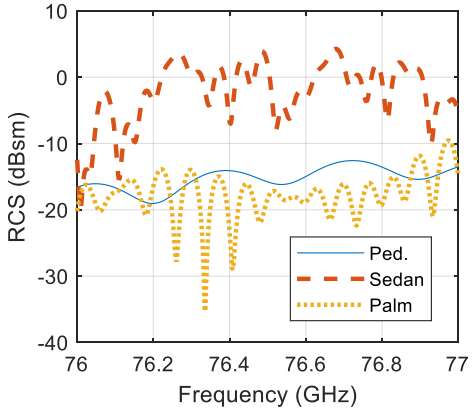

(b)

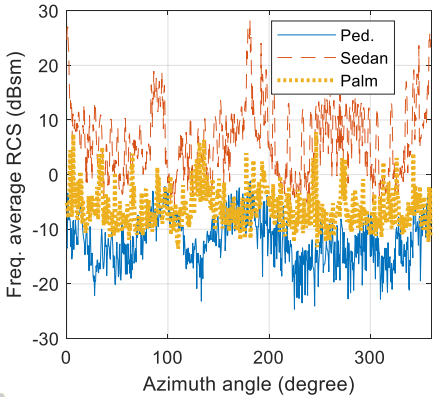

(c)

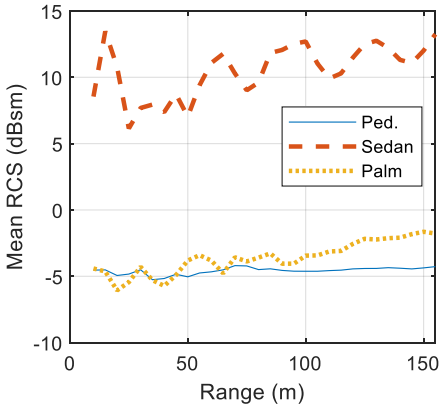

(d)

Figure 6.1. (a) The CAD model of a 1.8 m tall pedestrian, a sedan, and a dwarf palm tree; (b) the simulated RCS as a function of frequency for the three targets from $\phi = 0°, 35°,$ and $105°$, respectively in the range of 50 m; (c) the frequency averaged RCS as a function of azimuth angle in the range of 50 m; (d) the average RCS over all azimuth angles as a function of range for the three targets.

The time domain radar response can be obtained by taking fast Fourier transform (FFT) of the frequency domain data. This will reveal the extent and intensity of scattering centers of the target as a function of range. In the example shown in Figure 6.1 (b), the radar has 1 GHz bandwidth and 512 frequency samples, which corresponds to 0.15 m range resolution and 76.8 m maximum unambiguous range. The time domain responses of the three target in Figure 6.1 (b) is illustrated in Figure 6.2 (a). It is shown that though the RCS level of the pedestrian and that of the dwarf palm are similar, their widths/shapes in the time domain are different and this feature can be used for target classification. Figure 6.2 (b) shows the time domain response of a sedan at different incident angles. The three angles $\phi = 0°, 45°$ and $90°$ correspond to the back, back-right, and the right-side directions. When the car is illuminated from behind, the main scattering points are on the very back of the car while some other illuminated surfaces can contribute some

considerable backscatter. If the car is illuminated at 45°, several scatterers at different ranges from the radar have similar backscatter power level. When the side of the car is perpendicular to the radar, the backscattered power from the door panels dominates and constitutes a single peak in the backscatter direction.

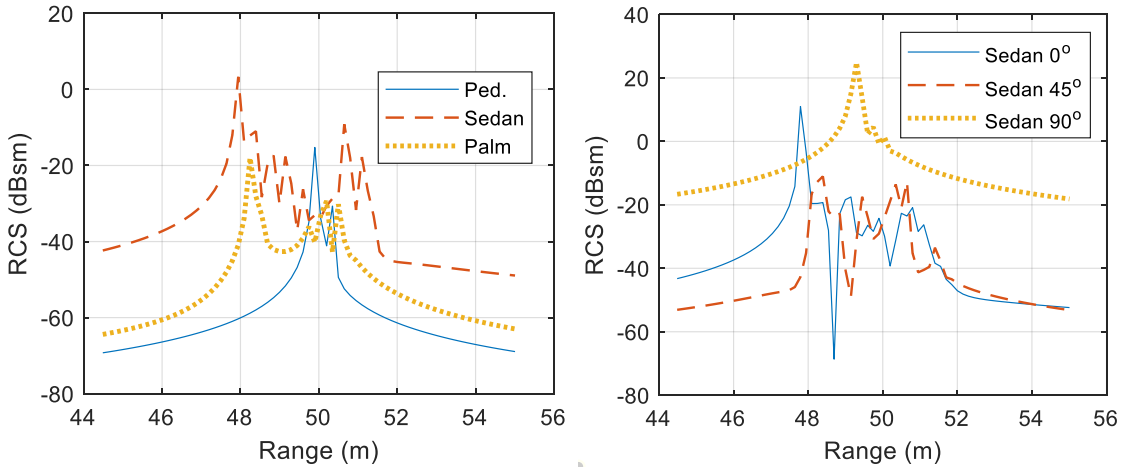

(a) (b)

Figure 6.2. The simulated RCS as a function of range for (a) the three targets in Fig. 6.1 (a) with $\phi = 0°, 35°$, and $105°$, respectively at the range of 50 m, and (b) a sedan with $\phi = 0°, 45°$ and $90°$ in the range of 50 m.

6.2.2 Radar images simulation results

When the radar has beam-steering capability, radar images can be generated, and more features of the target can be obtained. One of the most effective beam steering techniques is digital beamforming with a fixed antenna array. The beamforming is equivalent to synthesizing a narrow beamwidth antenna pattern by properly changing the phase of each element.

It is critical to have low sidelobe levels for radar imaging applications. The low sidelobe level can be created by proper weighting the received signals of the array elements. In this

simulation, a triangular weighting function is applied to a uniform linear array (ULA) to generate lower than -26 dB sidelobe levels. The triangular weighting function is given by:

$$W_i = 1 - \left| \frac{2i}{N+1} - 1 \right|, \quad 1 \le i \le N \tag{6.1}$$

where N is the number of antenna elements. In one example, the triangular weighting function is applied to a 50-element ULA with $\lambda/2$ spacing, and the radiation pattern for the antenna array with main beam at 0° (boresight) or 30° are shown in Figure 6.3. The half-power beamwidth (HPBW) is about 3° when the main beam is at 0° and 3.5° when the main beam is at 30°. The sidelobe levels are less than -26 dB for both cases.

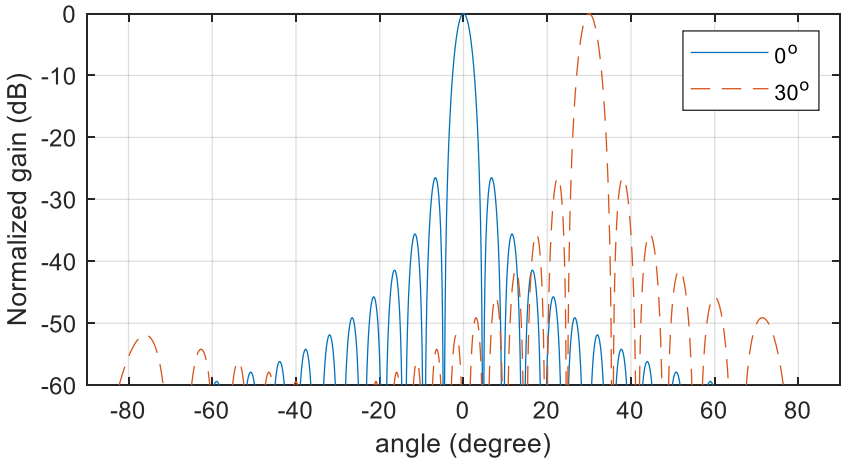

Figure 6.3. The radiation pattern of a 50-element ULA with λ/2 spacing and triangular weighting function.

Different portions of a short-range target can be viewed by the radar with the main beam scanning over the target. For a radar that can scan the beam in azimuth direction, a range-azimuth angle ($r - \phi$) image can be created since the range information is obtained by the time domain response. Consider a radar with a 50-element ULA having inter-element spacing of 0.7 wavelength. This beam-steering radar is capable of providing 2° beamwidth in the boresight direction. Suppose the radar is operating from 76 GHz to 77 GHz and collects 512 frequency samples. Each antenna

element is assumed to have uniform pattern in the azimuthal plane, and to increase the antenna's gain, each element is given about 6° beamwidth in the elevation plane. Figure 6.4 shows the processed radar images for some commonly seen traffic targets. To generate one radar image, the target is simulated for 512 frequency points and 50 transceivers. The radar beam is processed in steps of 1°, and the resulting range-angle images are threshold to maintain a dynamic range of about 30 dB. These images are shown in Figure 6.4 in dB scale and are normalized to their maximum RCS values. It is shown that the shape of large targets like vehicles can be identified to some extent, but the small targets like pedestrians and traffic signpost are hard to be distinguished with the $r - \phi$ radar images.

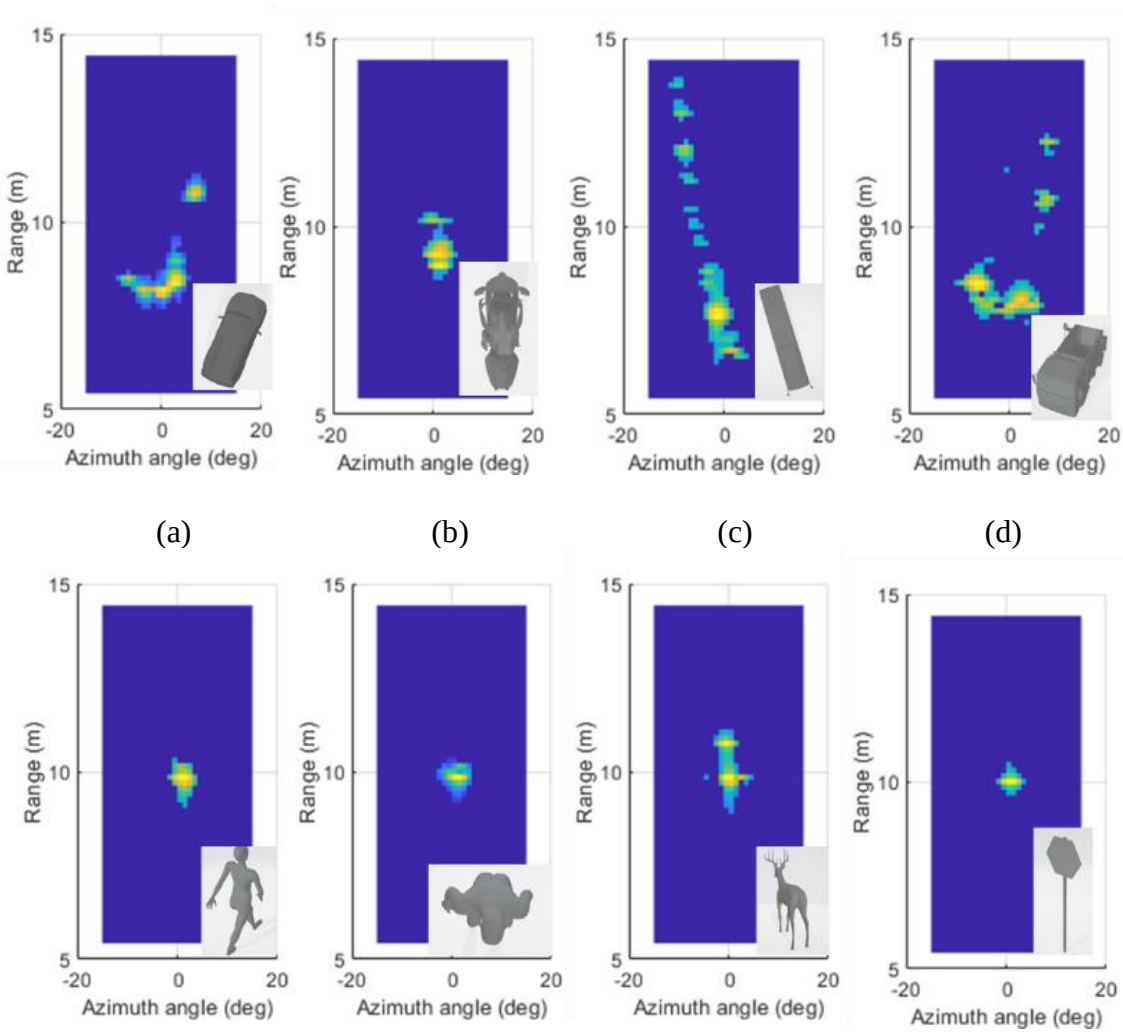

(a) (b) (c) (d)

(e) (f) (g) (h)

Figure 6.4. The simulated range-azimuth angle (rϕ) images for (a) an SUV, (b) a motorcycle, (c) a bus, (d) a truck, (e) a walking pedestrian, (f) a squatting man, (g) a deer and (h) a stop sign in the range of 10 m with a 2° beamwidth radar in azimuth direction.

For more advanced radar with beam steering capability in both azimuth and elevation directions, azimuth-elevation angle ($\phi - \theta$) radar images and 3D (x-y-z) radar images can be obtained. In one simulation example, a MIMO radar has 50 transmitters (TX) in the z direction and 50 receivers (RX) in the x direction, and each have 0.7 wavelength spacing, resulting in about 2° beamwidth in azimuth and elevation at boresight. The radar uses 0.5 GHz bandwidth and 512 frequency samples are recorded. The beam is scanned from -15° to 15° for ϕ and -10° to 10° for θ in steps of 1°. In the signal processing stage, first an FFT to the frequency domain data of all 2500 channels is taken, then for each scanned angle, the triangular weighting function is applied to all channels.

Some examples of the $\phi - \theta$ radar images and 3D radar images are shown in Figure 6.5. The value of one pixel represents the RCS detected for one scan angle, and they are normalized to the maximum value in the image. Because the sidelobe level of the ULA with proposed weighting function is lower than -26 dB, every pixel that has an RCS value 26 dB less than the maximum value is discarded. Figure 6.5 demonstrates the radar images for a pedestrian, a sedan, and a man riding a bike. It is shown that the profile of each target is recognizable from the radar images, and therefore the $\phi - \theta$ radar images or 3D radar images exhibit the best potential for target classification.

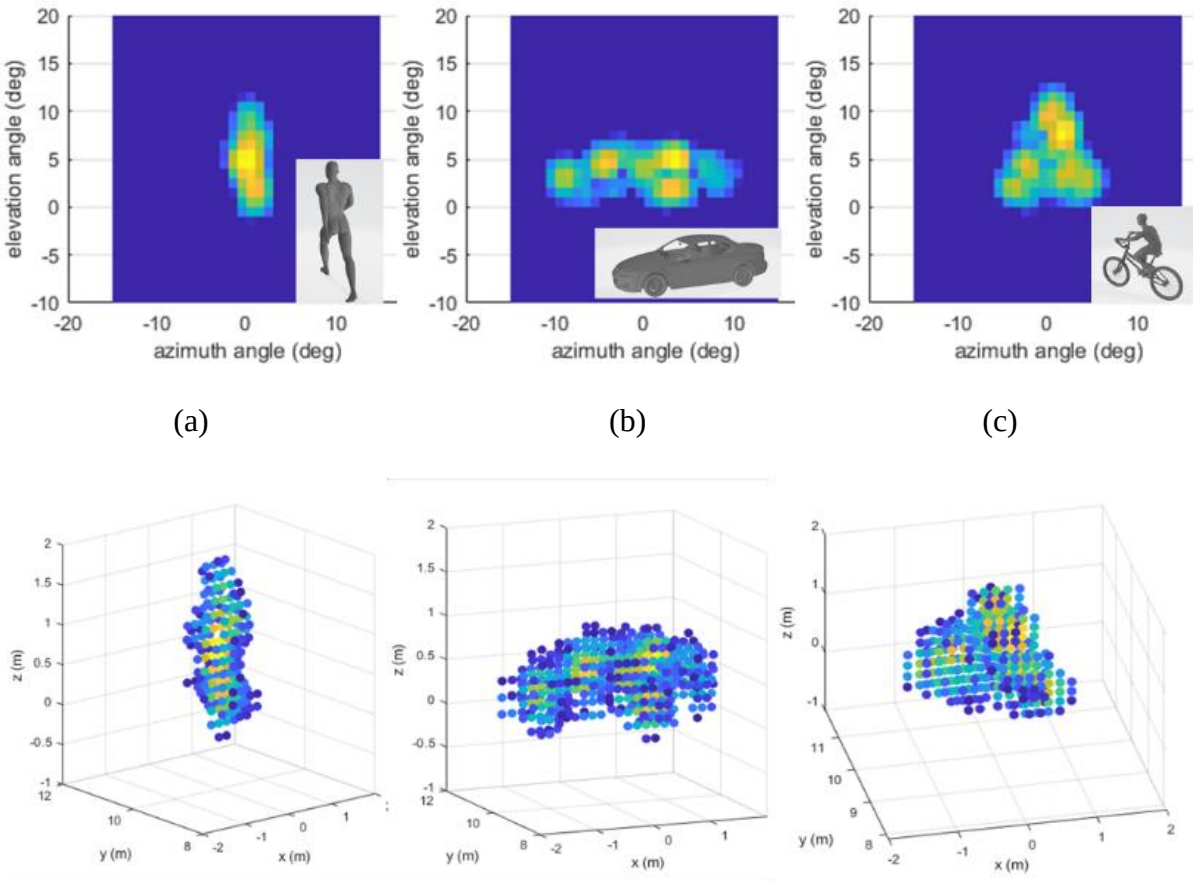

(a) (b) (c)

(d) (e) (f)

Figure 6.5. The simulated azimuth-elevation angle (ϕ-θ) images for (a) a pedestrian, (b) a sedan, (c) a man riding a bike, and their corresponding 3D images (d) (e) and (f) in the range of 10 m with a 2° beamwidth radar.

6.3 MMW Radar Target Classification

In this section, target classification algorithms based on different forms of radar data are developed and compared. Depending on the radar mode of operation, four different forms of radar data are utilized for target classification: statistical RCS information, distributed (time domain) radar response, 2D range-azimuth angle radar images and 3D radar images. If the targets are at long range or the radar doesn't have imaging capabilities, the methods based on statistical RCS

and time domain radar response data are used, and due to the complexity of the problem, the artificial neural network (ANN) approach is used for target classification. If targets are at close range and radar is capable of beam steering, the convolutional neural network (CNN) classification approaches with radar images can be used to provide more accurate classification results.

The forward scattering model is used to generate radar data for many types of traffic targets. Based on the importance of targets, commonly seen traffic targets are divided into three categories: pedestrians, vehicles and all other objects. Simulations are run for a variety of pedestrians ranging from 1.2 m tall children to 70 year olds, including different genders, poses (squat, standing, walking, and jogging), and body types (skinny, average, and overweight). The simulated vehicles include, but are not limited to bikes, motorcycles, sedans, supercars, SUVs, buses, vans, hatchbacks, pickup trucks, and heavy trucks. Other objects include traffic targets other than pedestrians and vehicles, including animals (dogs, deer, horses, etc.), and stationary objects like traffic signs, traffic light posts, traffic drums, lamp posts, trees, trash bins, roadblock, road fence, bus stops, mailboxes, etc. In all approaches described below, more than 6,000 samples of data are created from different incident angles of about 90 different targets for classification, and to avoid bias issues in classification, the number of samples for different categories are kept almost the same.

6.3.1 Target classification based on statistical RCS

For traditional radar without imaging ability, or the target is far enough such that a traffic target can be isolated from range-Doppler map and represented by one or more RCS values. The RCS values are highly fluctuating with aspect angle, frequency and range. To demonstrate the random behavior of the radar response, an example of radar measurement of a sedan on a turn table is given. Figure 6.6 shows the picture of the measurement and the convention used for aspect angle.

Figure 6.7 shows the measured radar response of the sedan in the range of 11 m and aspect angle of 10° and 20°. The radar utilizes a vector network analyzer (VNA) to measure the frequency response of the target, and it operates from 76.5 GHz to 79.5 GHz. It has one transmitter and one receiver with 3° antenna beam width in both elevation and azimuth directions. The response of the sedan can be gated out in time domain, as is shown in Figure 6.7 (a) and (c), where the red dash line refers to the radar response of the sedan. It shows that at different aspect angle, the peak value of the radar response can have more than 10 dB difference. Then the radar response of the sedan in frequency domain can be obtained by taking FFT to the gated time domain response, which is depicted in Figure 6.7 (b) and (d). It shows that the radar response, which is proportional to the RCS, can have up to 20 dB variation at different frequencies.

Figure 6.6. The 77 GHz radar measurement scene for a sedan and the coordinate system.

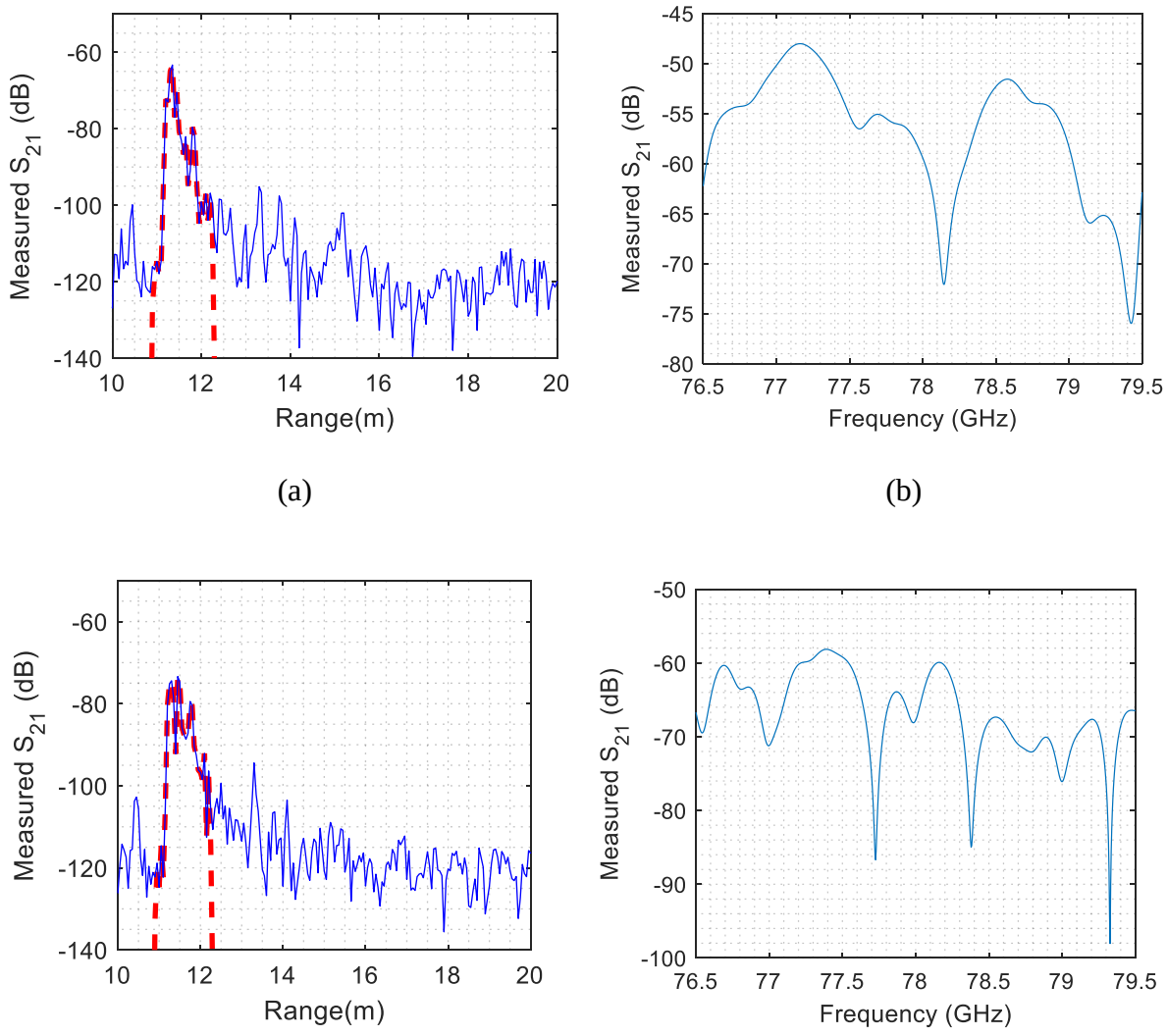

Figure 6.7. The measured S_{21} in time domain as a function of range and the gated response of the sedan in the range of 11 m with (a) $\phi_0 = 10°$ and (c) $\phi_0 = 20°$; the corresponding frequency domain response of the gated S_{21} of the sedan after FFT for (b) $\phi_0 = 10°$ and (d) $\phi_0 = 20°$.

The mean RCS of all azimuth angles is a good indicator in radar target classification, however, it is not praticle to measure the RCS of all azimuth angles of targets during road driving. During road mesurement, it is required that the radar can classify targets in real time.Therefore, the RCS data used in classification are limited, which could be just for slightly changes in aspect

angle and frequency. The RCS values for large targets, e.g. a vehicle, may varies dramatically with azimith aspect angles as is shown in Figure 4.12 in Chapter 4. It is observed that the frequency averaged RCS of a sedan with some aspect angle will not be too different from that for a pedestian (~-10 to -5 dBsm), and therefore, it is hard to distinguish a vehicle from a pedestrian based on the raw RCS data.

The most commonly used statistical information is the mean value and standard deviation. The pairs of mean values and standard deviations for different targets are depicted in Figure 6.8. It is shown that the standard deviation is close to the mean values for all different types of targets, which indicates that the statistical distribution of RCS is close to the exponential distribution. These results agree with the famous Swerling models [109][111] for the RCS of complex targets. Because the mean value and standard deviation are highly correlated, it is difficult to distinguish different types of targets based only on these two features.

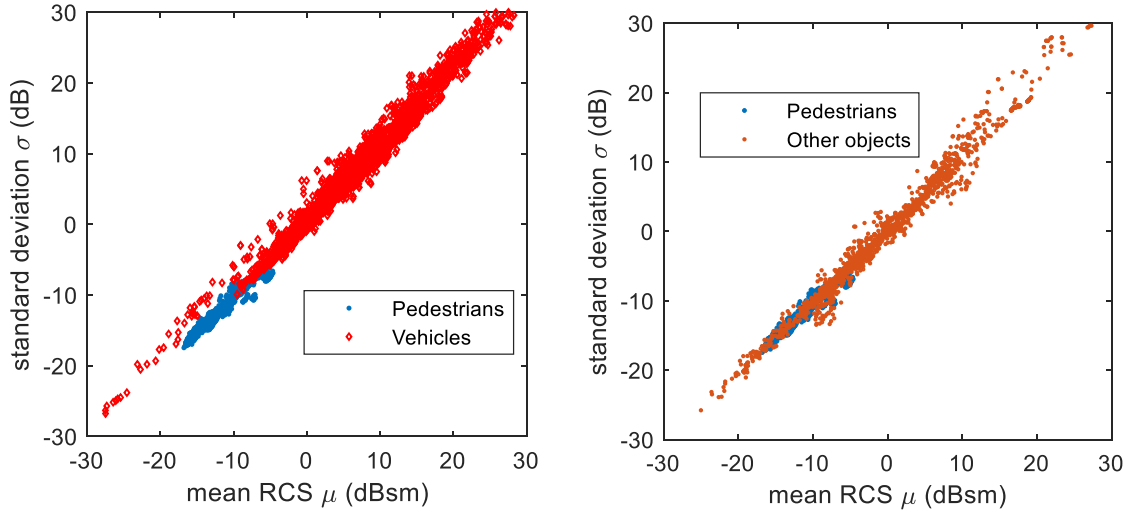

(a) (b)

Figure 6.8. The simulated mean value and standard deviation for different targets with categories in (a) pedestrians and vehicles and (b) pedestrians and other objects.

To achieve a better contrast of the data for different types of targets, it is desirable to have more distinguishable features. It is better to find the statistical distribution of the simulated RCS data. Examining the data carefully, it is found that the Weibull distribution is the best fit for the RCS values of traffic targets in the MMW or sub-MMW band [172][173]. The probability density function (PDF) of the Weibull distribution is given by,

$$f(x|A,B) = \frac{B}{A}\left(\frac{x}{A}\right)^{B-1} \exp\left\{-\left(\frac{x}{A}\right)^{B}\right\}, \tag{6.2}$$

where A is the scale parameter and B is the shape parameter. If B = 1, the Weibull distribution becomes the exponential distribution. Different B parameters can be used to represent how the statistical distribution deviates from the exponential distribution, and therefore the Weibull distribution is used to provide more distinct statistical features.

All groups of RCS data are fitted into the Weibull distribution, and the pairs of A and B parameters are obtained for each dataset. Since the data for different targets may have different fitting performance to Weibull distribution, the fitting error is considered as an additional feature in this classification problem as well. The fitting error is measured by the Kolmogorov-Smirnov (KS) test defined as the RMS error between the empirical cumulative density function of the raw data and the fitted cumulative density function of Weibull distribution with best fitting parameters [173]. The A and B parameters and the fitting errors for different types of targets are displayed in Figure 6.9. Though many parameters still overlap for different target types, compared to Figure 6.8, this approach provides greatly improved distinction for different target types.

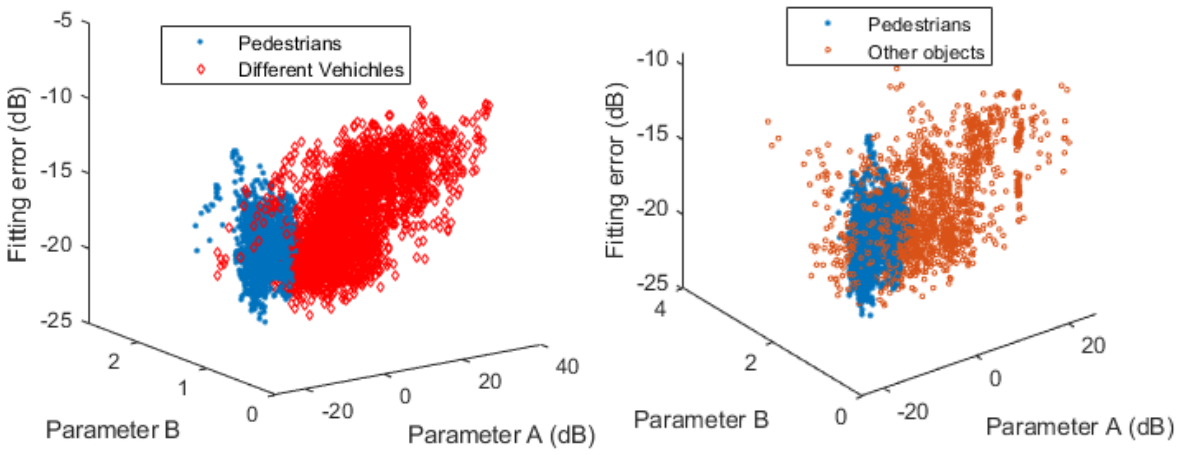

(a) (b)

Figure 6.9. The parameters A and B and the fitting error of Weibull distribution for different targets with categories in (a) pedestrians and vehicles and (b) pedestrians and other objects.

Artifical neural network (ANN) approach is applied to classify the traffic targets based on the statistical features described above. The structure of the ANN used in this classification problem is illustrated in Figure 6.10. In the figure, each black circle represents one value and is called "neuron", and the line with arrow represents a functional relationship. The variables $b_0, \dots, b_m$ are constant 1, and the variables $\hat{x}_{1,2}$ are normalized input values from the training dataset such that the range of $\hat{x}_{1,2}$ are between -1 and 1. $\hat{x}_1$ is normalized from parameter A, $\hat{x}_2$ is normalized from parameter B. The neurons a_{ij} is a function of variables in previous layer. The output values $\hat{y}_{1,2,3}$ have the range between 0 and 1, and they are the probability of being classified as pedestrians, vehicles and other objects, respectively. More specifically, the relations are:

$$\hat{x}_1 = \frac{2(A - \min(A))}{\max(A) - \min(A)} - 1 \tag{6.3}$$

$$\hat{x}_2 = \frac{2(B - \min(B))}{\max(B) - \min(B)} - 1 \tag{6.4}$$

$$a_{1i} = tanh\left(b_0 w_{0i}^0 + \sum_{j=1}^{2} \hat{x}_j w_{ji}^0 \right) \tag{6.5}$$

$$a_{ki} = tanh\left(b_{k-1} w_{0i}^{k-1} + \sum_{j=1}^{n_{k-1}} a_{(k-1)j} w_{ji}^{k-1} \right) \tag{6.6}$$

$$\hat{y}_i = \frac{1}{2}\left[tanh\left(b_m w_{0i}^m + \sum_{j=1}^{n_m} a_{mj} w_{ji}^m \right) + 1 \right] \tag{6.7}$$

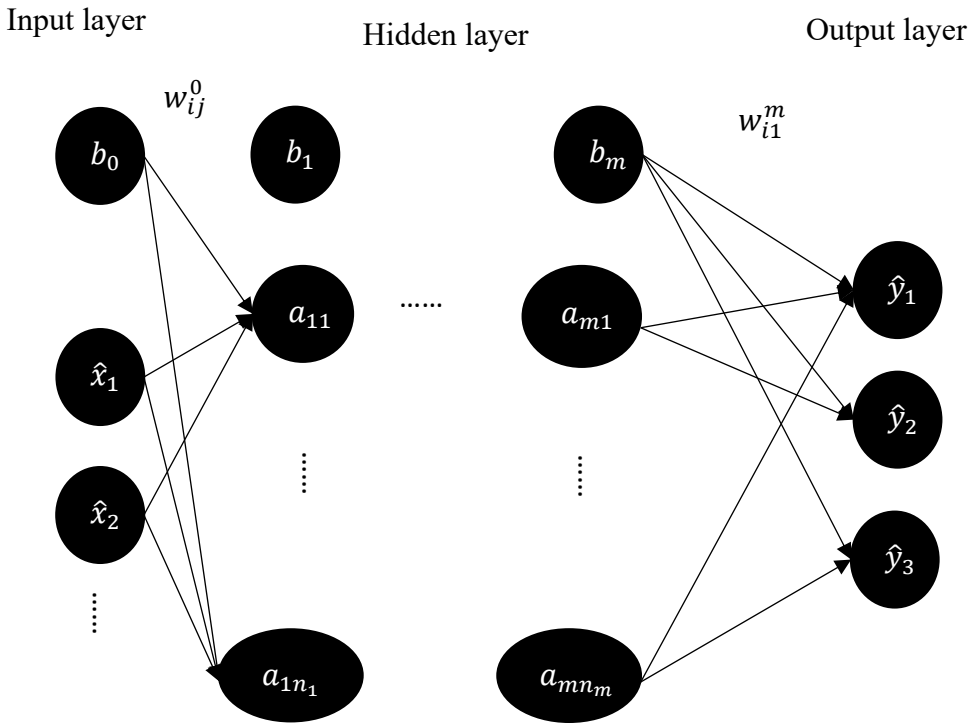

Figure 6.10. Structure of the ANN used for target classification with statistical features

When use the ANN model, it will take the statistical features A and B of the RCS data of one target as inputs and generate output values for $\hat{y}_{1,2,3}$. The target is classified into the category with the highest probability. More than 6000 pairs of parameters A and B for different targets are used to obtain the ANN model. In the training process, 70% data are randomly selected as training set, and 15% of data are used for validation and the rest are test data. The ANN model is trained by Matlab with Levenberg-Marquardt backpropagation algorithm. In this example, an ANN model

with three hidden layers is generated to perform the target classifications. Each layer has 10 neurons.

Table 6 - 1 shows the performance of the target classification model based on the mean values and standard deviations, and the model in Table 6 - 2 is based on the Weibull parameters. It shows that when the data of all three categories are used, the pedestrians and vehicles can be correctly identified with more than 90% accuracy for both models, but the predictions for other objects are very poor. The reason is that the extent of other objects are diverse and as indicated in Figure 6.8, some statistical parameters of the RCS of some objects are similar to those of pedestrians, and those of the others are more close to those of vehicles.

Table 6 - 1. Performance of target classification based on mean RCS values and standard deviations

		Pred. Target			**Pred. Target (Veh. excluded)**	
		Ped.	*Veh.*	*Other Obj.*	*Ped.*	*Other Obj.*
True Target	*Ped.*	**95.3%**	0.3%	4.4%	**95.8%**	4.2%
	Veh.	1.3%	**92.9%**	5.8%	-	-
	Other Obj.	19.7%	51.2%	**29%**	26.4%	**73.6%**

Table 6 - 2. Performance of target classification based on mean RCS values and standard deviations

		Pred. Target			**Pred. Target (Veh. excluded)**	
		Ped.	*Veh.*	*Other Obj.*	*Ped.*	*Other Obj.*
True Target	*Ped.*	**95.4%**	0.2%	4.4%	**96.2%**	3.8%
	Veh.	0.8%	**93.3%**	5.8%	-	-
	Other Obj.	16.3%	47.0%	**36.7%**	17.0%	**83.0%**

If vehicles are static and only pedestrians are needed to be identified, then in both models more than 95% of pedestrians will be correctly identified and less than 10% of non-pedestrians will be wrongly classified since the number of samples of vehicles and other objects are similar. If the vehicles are moving or we only consider the targets near the sidewalk, then we only need to identify the pedestrians from the other static objects. In this case, the model based on mean values and standard deviations of RCS has 95.8% accuracy for pedestrians and 73.6% accuracy for other objects, and the model based on Weibull parameters give even better results of 96.2% accuracy for pedestrian and 83% accuracy for other objects. This shows that the models based on Weibull parameters can provide better classification results.

6.3.2 Target classification based on distributed RCS response (time domain)

The time domain radar response reflects the scattering strength of scatterers distributed over a target. This response can be used in target classification as the target response span in range for different targets can be different. For example, a pedestrian has much smaller extent in azimuth direction than a vehicle, and therefore, the shape of the time domain radar response of a pedestrian is different from that of a vehicle. The time domain response depends on the radar parameters as well. In this paper, a radar is chosen to have a bandwidth of 1 GHz which can provide a range resolution of about 0.15 m. In order to isolate the response of the target for classification, the time domain data samples are truncated into 61 points (9 m in range). Because usually the maximum RCS value occurs at points on the target nearest to the radar, the time domain signal truncation is made such that one third of the points (20 points or 3 m) are before the maximum RCS and two thirds of the points (40 points or 6 m) are after the maximum RCS value.

Compared to the point target data, the distributed (time domain) response is more impacted by the presence of noise since the small scattered power in time domain may not be detected if the

noise level is high. For the example considered next, it is assumed that the signal to noise ratio (SNR) is high enough such that scatterers with -30 dBsm are detectable, and any RCS data in time domain below -30 dBsm is discarded. Some examples of the time domain RCS for different targets with an arbitrary incident angle is shown in Figure 6.11. In the figures, 0 on the x-axis in a relative range representing the location of the RCS peak of the target in time domain. The time domain RCS in Figure 6.11 are distinguishable for different types of targets.

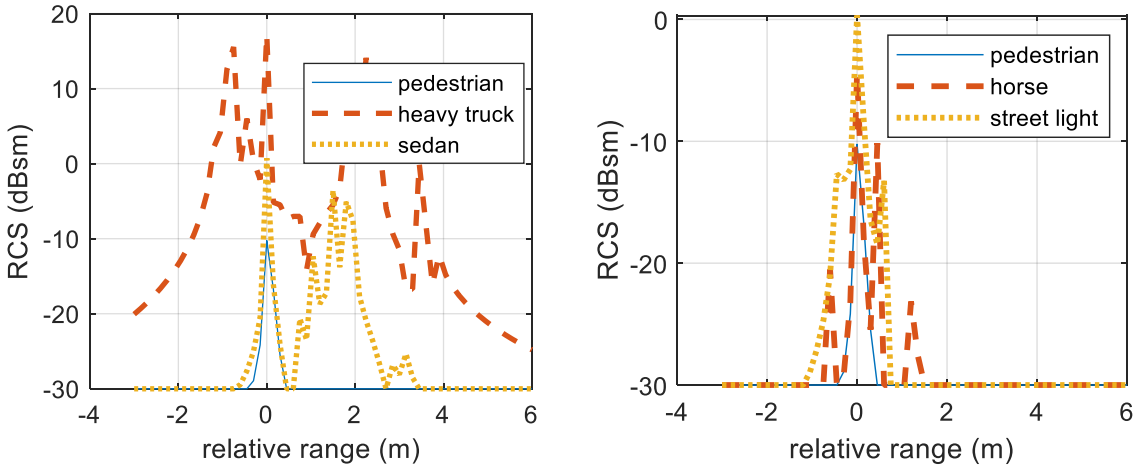

(a) (b)

Figure 6.11. The time domain RCS comparison among (a) a pedestrian, heavy truck and a sedan and (b) a pedestrian, a horse and a streetlight from a randomly selected incident angle.

ANN is applied in the target classification based on time domain RCS. This ANN structure has 61 inputs representing the time domain response, 3 hidden layers with 60, 30 and 20 neurons in each layer and three outputs with values between 0 and 1 referring to the probability of the target being classified as of the three categories. The hidden layers are chosen based on best performance while minimizing the number of layers and neurons and avoiding the overfitting issue. Like the ANN for statistical RCS, 70% of the dataset is randomly picked as training data, and the rest is used as testing and validation data. The ANN is trained in MATLAB as well.

The performance of the classification is provided in Table III. It shows that when all targets are classified, more than 90% of pedestrians and vehicles can be correctly identified, and about 65% of the other objects can be correctly classified. This result outperforms the classification model based on statistical RCS. However, the classification performance when excluding vehicles is not as good as that for the model based on statistical RCS. The advantage of using the time domain response is that it can detect the extent in range of a target, and many targets like traffic signs, traffic lights, tree trunks, etc. have similar azimuth dimensions as pedestrians in terms of the radar's range resolution. Furthermore, the RCS values in classification here are not statistical RCS, therefore the radar response of pedestrians and some other objects may not be differentiable in the time domain.

Table 6 - 3. Performance of target classification based on time domain RCS

		Pred. Target			**Pred. Target (Veh. excluded)**	
		Ped.	*Veh.*	*Other Obj.*	*Ped.*	*Other Obj.*
True Target	*Ped.*	**91.3%**	0.0%	8.7%	**91.6%**	8.4%
	Veh.	0.0%	**94.0%**	6.0%	-	-
	Other Obj.	26.5%	8.0%	**65.5%**	25.8%	**74.2%**

6.3.3 Target classification based on Radar images

One of the major factors that limits the performance of target classification with traditional radar is the number of features. To achieve better accuracy of classification, a radar with imaging capability is desired. Radar images can be created in many different ways and in this simulation, they are generated using digital beamforming. Compared to the frequency domain or time domain RCS classification methods, radar images provide additional dimensions (azimuth and/or elevation) of data and therefore can capture the shape or size of the targets.

The range-azimuth angle ($r-\phi$) images can be generated if the radar can scan its beam in azimuth direction. It is noted that the significant angular features of a target depend on the range, the radar's beamwidth and the angular resolution of scanning angles. To study the effect of range, and radar's beamwidth on the target classification performance, the $r-\phi$ image simulations are performed for targets in different ranges and by varying the number of elements or antenna spacings (resulting in different antenna beamwidths). More than 6000 $r-\phi$ images are generated for different targets from all azimuth angles in each range and radar configuration. Each $r-\phi$ image is truncated into 9m by 30° in azimuth direction, with 61×31 pixels (ranges×angles) and is generated by simulating 25,600 or 51,200 RCS data (512 frequency samples and 50 or 100 antenna elements) for one target. 50 antenna elements generate 3° beamwidth using λ/2 inter-element spacing or 2° beamwidth using 0.7λ inter-element spacing. 100 elements create 1° beamwidth using 0.7λ inter-element spacing at boresight. Some examples of the $r-\phi$ radar images are shown in Figure 6.4.

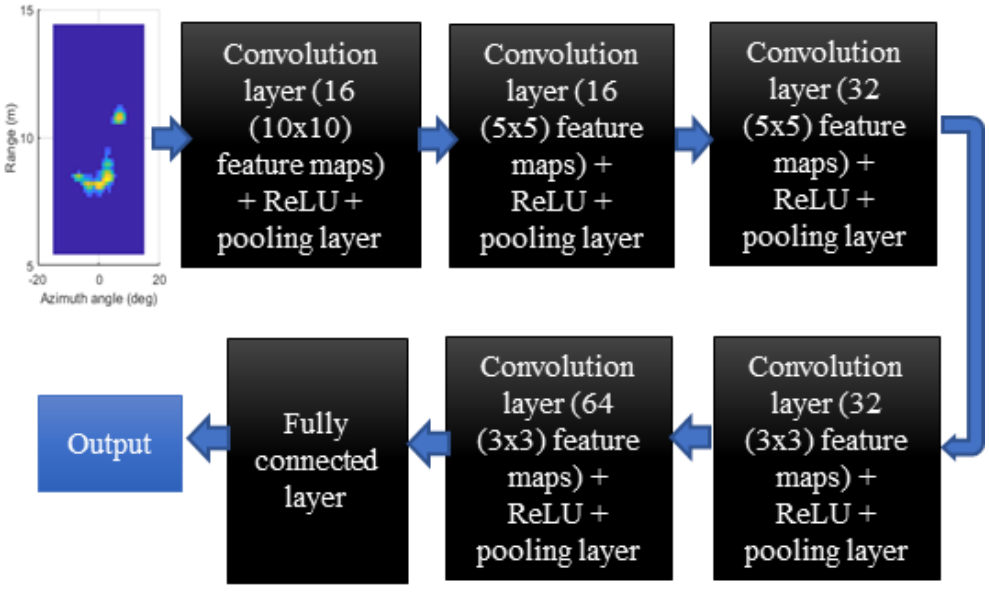

Figure 6.12. The Structure of the CNN used for target classification with rϕ radar images.

The radar image classification algorithm is implemented using CNN. The proposed CNN has five convolutional layers, five rectified linear unit (ReLU) layers, five pooling layers and one fully connected layer as shown in Figure 6.12. The detailed description of each layer can be found in [174]. The CNN is trained using the MATLAB Deep Learning toolbox [177]. 70% of the data is randomly selected as training data and the rest is used as validation data. In the training step, 80 epochs are employed, and each epoch goes through 23 iterations of training process. After training the models, the validation data have similar accuracy as that for training data, which implies the models do not have an overfitting issue. The classification performance of the models for different ranges and beamwidths are given in Table 6-4. For comparison, all models have the same number of layers, and the radar scanning angle step is 1° for all beamwidths. It shows that short range targets have better classification accuracy than long range targets, and the radar with narrow beamwidth can provide better classification performance. This result is intuitive because in the case with nearer targets or narrower radar beamwidth, more useful features of targets can be detected by the radar. Compared to the classification models based on frequency domain or time domain radar response data, the radar images-based models can provide better accuracy for classification at short range.

Table 6 - 4. Performance of target classification based on range-azimuth angle radar images

	True Positive rate with 3° beamwidth		
Range	*Pedestrians*	*Vehicles*	*Other Obj.*
10 m	91.9%	99.5%	91.6%
20 m	93.3%	98.5%	87.0%
30 m	90.8%	98.8%	81.5%
	True Positive rate with 2° beamwidth		
10 m	97.4%	99.6%	91.7%
20 m	93.8%	98.1%	81.4%
30 m	96.4%	97.8%	80.1%
	True Positive rate with 1° beamwidth		
10 m	94.9%	99.1%	93.2%
20 m	94.0%	99.7%	88.4%
30 m	87.0%	96.7%	93.5%

The 3D radar images have the added dimension of elevation compared to $r-\phi$ images. Similarly, more than 6,000 3D radar images are generated for different targets for a given range and radar beamwidth. In this classification example, a 3D radar image has 61×31×31 pixels (9m×31°×31°) and is created by simulation for 1.3 million data with a MIMO radar with 512 frequency samples and 50×50 channels. The equivalent antenna beamwidth is 3° (λ/2 spacing) or 2° (0.7λ spacing). Some examples of 3D radar images with 2° antenna beamwidth are given in Figure 6.5.

CNN is used for target classification with 3D radar images as well. The layers and the convolution operation in the new CNN have three dimensions, unlike the CNN for 2D images. The CNN is trained using the MATLAB Deep Learning toolbox as well. The proposed structure has five convolution layers as shown in Figure 6.13.

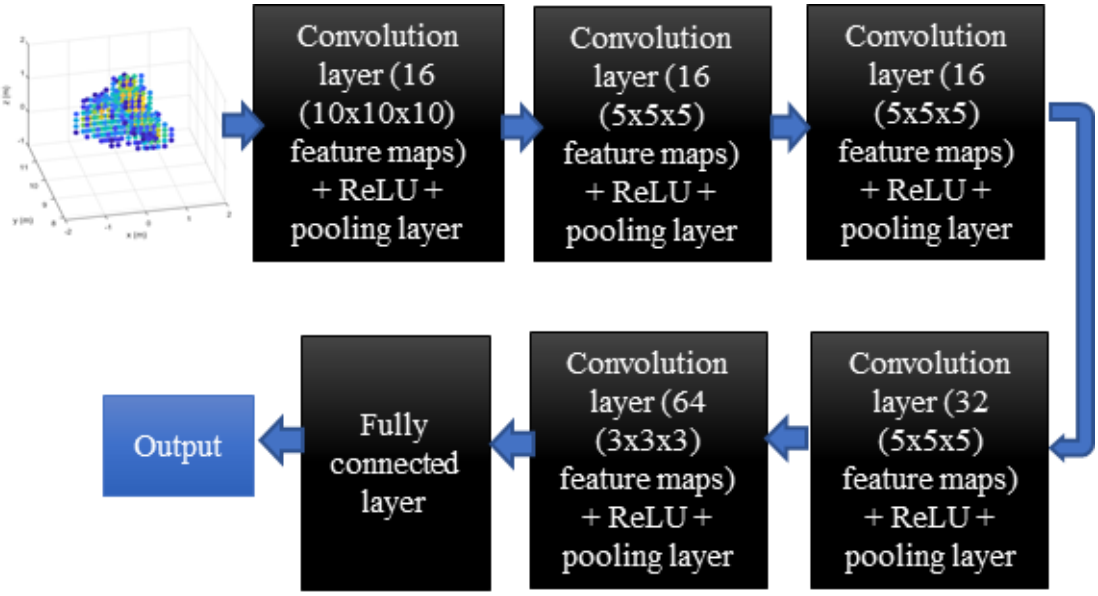

Figure 6.13. The Structure of the CNN used for target classification with 3D radar images.

The classification results for 3D radar images are given in Table V. It shows excellent performance (>98% accuracy for pedestrians and vehicles and >94.5% accuracy for other objects) for both 3° beamwidth and 2° beamwidth for the range from 10 m to 30 m. It is also observed that

the classification accuracy is better if targets are closers and the radar has narrower beamwidth. Because more features can be detected by 3D radar images, it is not surprising that the radar target classification based on 3D radar images outperforms the other models in terms of accuracy. The drawback of the 3D radar images-based target classification is that it requires a more advanced radar and more effort to process the data than other approaches, and the quality of radar images will be degraded for targets at longer ranges.

Table 6 - 5. Performance of target classification based on 3D radar images

	True Positive rate with 3° beamwidth		
10 m	99.5%	99.5%	99.4%
20 m	99.3%	99.2%	97.8%
30 m	98.0%	98.6%	96.5%
	True Positive rate with 2° beamwidth		
10 m	100%	99.9%	99.7%
20 m	100%	99.7%	94.5%
30 m	98.9%	99.0%	97.8%

6.4 Experimental validation of the classification models

In order to validate the proposed radar target classification models, several targets are measured by a 77 GHz instrumental radar. The radar has one transmitter and one receiver with 3° antenna beamwidth in both azimuth and elevation directions. The radar is connected to a vector network analyser (VNA) to sweep over the operating frequency band of 76 GHz to 79 GHz. Due to limitations on the available hardware, this radar cannot generate radar images, and only the model based on statistical RCS with Weibull parameters is examined.

The measured targets include a mannequin covered in a reflective coating in three different poses, two traffic sign posts (one square shape and one U shape) and three vehicles (two sedans and one SUV). Pictures of these measurements are included in Figure 6.14. The targets are on a turntable and measured from all azimuth directions. The mannequin and the traffic sign posts are measured in an anechoic chamber at a range of 18 m, and the vehicles are measured in an open

parking lot with a range of 30 m. The measured data are gated and calibrated to obtain the RCS from which the Weibull parameters are extracted. The parameters A, B, and the fitting errors are depicted in Figure 6.15.

(a)

(b)

(c)

Figure 6.14. The 77 GHz radar measurement for (a) a mannequin with three different poses, (b) two different traffic sign posts and (c) two sedans and one SUV.

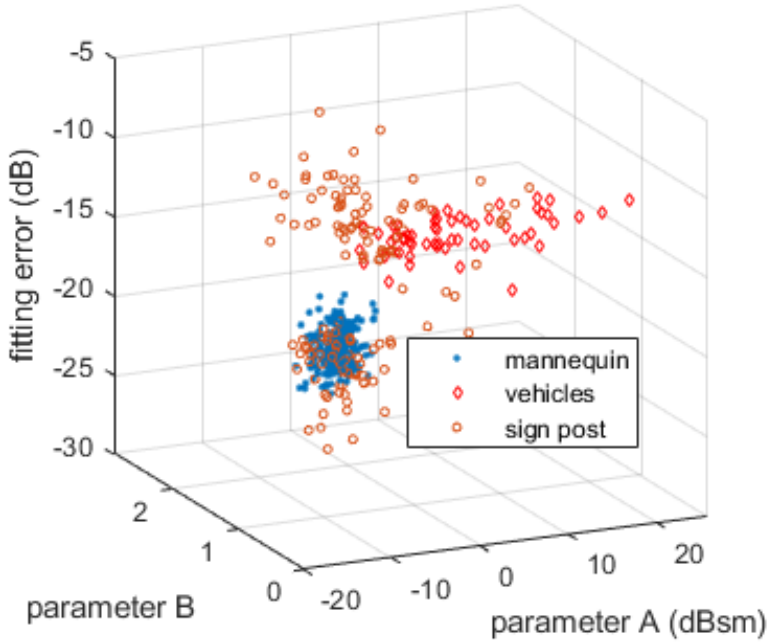

Figure 6.15. The Weibull parameters summarized from the RCS of the measured targets.

The Weibull parameters are put into the off-line models trained in *Sec*. 6.3.1, and the classification performance is given in Table 6-6. It shows that more than 80% statistical RCS data of the mannequin and vehicles can be correctly classified and the classification for traffic sign posts is poor as expected. If the data for the mannequin and the traffic sign posts are put into the

off-line model without vehicle training data, the mannequin can be identified with more than 95% accuracy while the true positive rate for the traffic signposts increases to 57%. The difference between the performance for measured data and for simulated data is due to the lack of samples in the measurement. The simulated other objects include many targets that have RCS values very different from pedestrians, while the RCS of the traffic sign posts have a large overlap with that of pedestrians. It can be observed from Figure 6.15 that many data of traffic sign posts overlap those of the mannequin.

Table 6 - 6. Performance of target classification based on statistical RCS with measured data

		Pred. Target			**Pred. Target (Veh. excluded)**	
		Ped.	*Veh.*	*Other Obj.*	*Ped.*	*Other Obj.*
True Target	*Mann.*	**80.2%**	0.9%	18.9%	**95.6%**	4.4%
	Veh.	5.2%	**86.0%**	8.8%	-	-
	Sign Post	41.0%	20.1%	**38.9%**	43.0%	**57.0%**

6.5 Conclusion

This paper presents four automotive radar target classification models with statistical RCS (point target), time-domain RCS (distributed target in range), range-azimuth angle radar images, and 3D radar images. The four models can be applied in different scenarios using different types of radar: the statistical RCS and time-domain RCS-based models can be applied to traditional radars at both short and long range, and the 2D/3D radar image-based models require a shorter range targets and a radar with imaging capability, but can provide much better classification accuracy. The models are trained with a large high-fidelity simulation dataset, and some models are validated by measurement. The classification models with statistical RCS and time domain RCS are based on ANN approach, and those with 2D and 3D radar images are based on CNN. The performance of different models with targets at different ranges and radar configurations are

compared as well. In the presented example, good classification accuracy has been achieved. This research shows that MMW and sub-MMW radar has great potential to be used for target classification, and that this can improve the situational awareness of an autonomous vehicle, especially in inclement weather conditions when other sensors are compromised, ultimately leading to improved safety for autonomous vehicles and the people around them.

Chapter 7 Vehicular Communication Channel modeling for foliage

7.1 Introduction

Autonomous driving system and intelligent transportation systems (ITS) put strict requirements on reliable and high-speed Vehicle-to-Vehicle (V2V) communications. The upcoming 5G wireless system is expected to support these applications and in particular, 802.11p-based dedicated short-range communications (DSRC) at 5.9 GHz has been specially regulated for vehicular communications[178]. Furthermore, massive connections among vehicles and infrastructure and broadband multimedia sensing and transmissions motivate the adoption of millimeter-wave (mmWave) at 60 GHz for vehicular communications, owing to the multi-GHz bandwidth [13],[179].

The vehicular communication antennas are usually mounted on the top of vehicles to avoid signal blockage from other similar vehicles [180],[181]. In practical V2V wireless communication, the LoS link can be blocked by many obstacles including large vehicles, buildings, foliage and other commonly seen cylindrical shape objects like lamp post and traffic light post. If the V2V LoS is blocked by buildings or a large vehicle like a bus or a truck, the signals are usually totally blocked. On the other hand, when the LoS is blocked by foliage or a cylindrical shape object, the signal is not completely blocked due to the diffraction nature of electromagnetic (EM) waves. Since there are various species, shape and dimensions of foliage, it is challenging to accurately capture the signal attenuation due to the foliage, and make the model efficiently retractable in practical autonomous driving. In a typical V2V communication scenario, the vertical

position of antenna is between 1.2m to 2m above the ground. The analysis of wave propagation can be focused in a 2D plane, where the transmitter and receiver are almost in the same plane[182]. Moreover, due to the extremely narrow beamwidth enabled by the mmWave beamforming technology and/or high gain antenna, the aligned beam from the transmitter is pointed directly to the receiver. As a result, reflection from the ground and scattering from tree branches and leaves can be neglected assuming the lowest branches are above the antenna's height. In this case, the tree trunks are the only scatters that interfere with the signal propagation in mmWave V2V communications, as illustrated in Fig. 1. Such interference is critical in some scenarios, for example, in T-junction or cross-road traffic scene, the LoS link between two vehicles with right angle might be blocked by tree trunks and failure of communication may lead to dangerous consequences.

Literature Review: The literature concerning electromagnetic scattering and propagation through foliage is rather intensive. At a low frequency where the wavelength is greater than the dimensions of trunk and branches, the tree is considered as a homogeneous dielectric cylinder with the equivalent permittivity [52], [53]. At higher frequency where the diameters of branches and trunk are much smaller than the wavelength while length is comparable or greater than the wavelength, the branches and trunk are approximated as 1-D scatter and the corresponding scattering amplitude tensors are derived to calculate the far-field scattering field [183], [184]. As frequency grows, the diameter of cylinder becomes comparable to the wavelength and the length of cylinder is much larger than wavelength. In such case the infinitely-long cylinder approximation can be applied, and the scattered far fields are evaluated analytically [185], [186], [187]. In a forest scenario that many trunks are parallel and closely placed, the higher order scattered fields are computed and the total scattered coefficient from trunks

are modeled as a function of incidence angle by Monte Carlo simulations [186]. In [186], both transmitter and receiver are in the far field of trunks, and it shows the first order scattering dominates for relatively sparse forest. In [187], a statistical approach with the analytical solutions is presented to find the scattered field and path loss inside a forest with frequency from L band to X band. In this model, the transmitter is placed in the far field of trunks as well. For mmWave band, geometric-optics (GO) approximation is applied to find the backscattering response from tree trunk [188], however, GO method is not appropriate for forward propagation direction since it assumes fully blockage of signal in such direction. In [189], the full-wave numerical method finite-difference time-domain method (FDTD) is used to calculate the scattering field of foliage. Although good accuracy can be achieved, the simulation process is prohibitively inefficient, time consuming and not available for the entire trunk simulation. In addition, several empirical models for the path loss caused by foliage based on the measurements have been reported [190]-[193]. In some models, path loss is a function of the distance, tree types and vegetation density at 900 MHz and 2.4 GHz [190], [191]. Since the wave front scattering behaves differently at lower frequencies compared to the mmWave band, these empirical models cannot be directly applied to V2V communications, besides, those models only consider the mean value of the foliage attenuation and the variation or statistical distribution is not presented. Moreover, in V2V communication the scattering from tree trunks can be in the near-field of transmitter and/or receiver while most models are for far-field scattering only. As a result, the efficient near-field tree-trunk scattering model for V2V communications in the mmWave band is still missing. Many methods mentioned in literature are either complex EM scattering analysis or EM numerical methods. Though good accuracy can be achieved, it is difficult to fast extract the solution and evaluate the communication link in real time. The straightforward solution will

be lookup table models, where the results are required to be evaluated for all values of all parameters. Though the lookup table models are simple to implement and apply, the required data points increase dramatically with number of parameters. By contrast, artificial neural network (ANN) model requires relatively much less number of data points in training and can achieve excellent prediction performance [194]. Besides, in ANN models, users only need hundreds of coefficients of neurons to reconstruct the model. On the other hand, to use the lookup table model people need all data points, which could be millions of data. The idea of ANN is inspired by the operation of human brain, and many important study of ANN like backpropagation algorithm can be traced back to 1970s [195], [196],[197]. Recently due to the development of computational ability of computers, ANN becomes one of the most popular tools in machine learning and has been successfully applied to many areas in both science and engineering for data classification, pattern recognition and curve-fitting [198]. There are many other types of neural networks (NN) like convolutional neural network (CNN) [199] or recurrent neural network (RNN) [200], and their typical ap-plications are in image, voice or video recognition. Compared to other NN, ANN has simpler structure and therefore faster to use. In this reduced channel modeling problem, ANN model is sufficient to achieve good performance without making the neural network too complicated.

Our Contributions: In this paper, systematic analysis on the scattering phenomenon from cylindrical trunk in both near-field and far-field regions is performed for V2V communication. To allow for computational tractable simulation of wave scattering and propagation, the complicated EM models are further reduced into a macro-model, by invoking an artificial neural network (ANN). The signal loss through branches and leaves for mmWave V2I communication is studied by Monte-Carlo simulation with commercial ray tracing (RT) software, and its statistical features

are summarized. The main contributions are summarized as follows. First, for V2V communication, we derive semi-exact semi-closed-form formulas for the far-field as well as near-field scattering from a tree trunk for the mmWave V2V communications and then validate them by the full-wave solver and reciprocity [201]. Second, we carry out extensive numerical evaluations on the scattered fields, by varying the position of receiver and transmitter, the trunk radius, the trunk height, the permittivity of the tree, and the frequency. The path loss caused by the tree in the mmWave band varies in a non-linear fashion in terms of the aforementioned parameters. Third, we further invoke the ANN model to provide curve fitting for pathloss. Fourth, in a forest environment, we perform theoretical analysis to accurately estimate the multiple scattering between tree trunks and then massive Monte-Carlo simulations are performed with randomly distributed tree trunks. Finally, the statistical information of the path loss model for foliate and defoliate trees are presented. The resulting macro-model is extracted to compute the overall link analysis in the V2V foliage propagation. The developed macro-model can be integrated as a useful tool to efficiently and accurately analyze real-time mmWave channel quality in vehicular communications. This paper is an extension of our preliminary study in [182], with many more details in near-field validation, path loss analysis and ANN-based macro-model for the path loss caused by the tree scattering.

7.2 Semi-analytic Single Tree Trunk Scattering Model for Millimeter-wave Band

In V2V communications, the presence of a tree may result in attenuation or small enhancement in signal depending on the receiver's and transmitter's locations. The strength of EM signal is proportional to the total electric field, which is equal to the sum of incident field, $\vec{E}_i$, and the scattered field, $\vec{E}_s$, given by:

$$\vec{E}(\vec{r}) = \vec{E}_i(\vec{r}) + \vec{E}_s(\vec{r}) \tag{7.1}$$

where $\vec{r}$ denotes the position of the receiver. The attenuation of the foliage or the path loss in the communication link can be defined as the received power without the foliage over that with the foliage:

$$A_{Fol} = \frac{P_{r_{noFol}}}{P_{r_{Fol}}} = \left| \frac{\vec{E}_i(\vec{r})}{\vec{E}(\vec{r})} \right|^2 = PL^2 \tag{7.2}$$

where PL is defined as $\left| \frac{\vec{E}_i(\vec{r})}{\vec{E}(\vec{r})} \right|$ in this thesis.

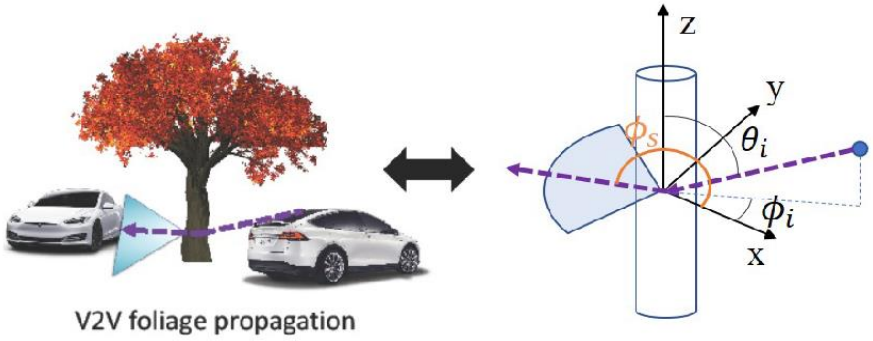

Figure 7.1. V2V foliage propagation and its equivalence to cylinder scattering.

Since any polarization state of electromagnetic wave can be represented by the linear combination of vertical (transverse magnetic (TM) case) and horizontal polarization (transverse electric (TE) case), thus only these two cases need to be considered. Without loss of generality, a coordinate system can be defined as illustrated in Figure 7.1, where the cylinder is along the z axis, and the incident direction is in x-z plane, with angle of θ_i. Later analyses are based on this coordinate system. Because the length of the trunk is much larger than the wavelength at either 5.9 GHz or 60 GHz, the internal field or equivalent surface current can be approximated by those for infinitely long cylinder with the same radius. These fields/currents can be derived from cylindrical

wave expansions [52]. The scattered field of the foliage, $\vec{E}_s(\vec{r})$, is obtained from the equivalent surface current by Huygens Principle, given by,

$$\vec{E}_s(\vec{r}) = \iint_{s'} \left[i\omega\mu_0 \vec{J}_s(\vec{r}') \left\{ \left(\frac{3}{k^2R^2} - \frac{3i}{kR} - 1 \right) \hat{R}\hat{R} + \left(1 + \frac{i}{kR} - \frac{1}{k^2R^2} \right) \bar{\bar{I}} \right\} - \left(ik - \frac{1}{R} \right) (\hat{R} \times \vec{J}_m(\vec{r}')) \cdot \bar{\bar{I}} \right] \frac{e^{ikR}}{4\pi R} ds' \tag{7.3}$$

where k is the wavenumber in free space, $\bar{\bar{I}}$ is the dyadic idemfactor, $\vec{J}_s$ and $\vec{J}_m$ are the equivalent surface electric and magnetic current, respectively, and$R$ is the length of the vector from source point $\vec{r}'$ to observation point $\vec{r}$:

$$\hat{R} = \frac{\vec{r} - \vec{r}'}{|\vec{r} - \vec{r}'|}, \qquad R = |\vec{r} - \vec{r}'|. \tag{7.4}$$

Notice that under far-field approximation ($kR \gg 1$), the scattered field shown in (7.3) reduces to,

$$\vec{E}_s(\vec{r}) = ik(\bar{\bar{I}} - \hat{R}\hat{R}) \cdot \iint_{s'} \left[Z_0 \vec{J}_s(\vec{r}') - (\hat{R} \times \vec{J}_m(\vec{r}')) \right] \frac{e^{ikR}}{4\pi R} ds' \tag{7.5}$$

where Z_0 denotes the characteristic impedance of free space.

The transmitter or receiver can be in either near field of far field of the tree trunk. Depending on the positions of transmitter and receiver, different approximations can be made. For practical applications, the following scenarios are considered: both transmitter and receiver are in the far-field region of the trunk (subsection *7.2.1* and *7.2.2*), transmitter is in the far field while the receiver is in the near-field region of the trunk (subsection *7.2.1* and *7.2.3*), and transmitter is in the near-field region of the trunk regardless of the receiver's position (subsection *7.2.4*).

7.2.1 Transmitter in the Far-field Region

When transmitter is in the far-field of tree trunk, plane wave incidence approximation can be applied. The equivalent electric and magnetic currents on the surface of trunk are derived from

cylindrical modal expansion of plane wave [52]. The electric and magnetic surface currents for TM case in cylindrical coordinate system are given by:

$$\vec{J}_s^{TM}(a,\phi,z) = i\omega\varepsilon_1 e^{ik_z z}\sum_{n=-\infty}^{\infty} C_n k_{1\rho} J_n'(k_{1\rho}a) e^{in\phi}\hat{z}, \tag{7.6}$$

$$\vec{J}_m^{TM}(a,\phi,z) = \frac{e^{ik_z z}k_z}{a}\sum_{n=-\infty}^{\infty} nC_n J_n\left(k_{1\rho}a\right)e^{in\phi}\hat{z} + e^{ik_z z}k_{1\rho}^2\sum_{n=-\infty}^{\infty} C_n J_n\left(k_{1\rho}a\right)e^{in\phi}\hat{\phi}, \tag{7.7}$$

where C_n is the modal coefficient at n^{th} mode, a is the radius of cylinder, ϕ and z are the cylindrical coordinate of one point on the cylinder, and J_n and J_n' are the Bessel function of the first kind and its derivative with order of n. Also $k_z = k_0\cos\theta_i$, $k_\rho = k_0\sin\theta_i$, ε_0 and ε_1 are the permittivity for free space and the dielectric cylinder, $k_{1\rho} = k_\rho\sqrt{\frac{\varepsilon_1}{\varepsilon_0}}$. The solutions for TE case can be easily derived from those for TM case using duality relations, therefore they are not shown in this paper.

By applying boundary condition regarding the continuity of the tangential *E* and *H* fields at $\rho = a$, The unknown coefficient C_n can be obtained and is given by:

$$C_n = E_0(-i)^n\sin\theta_i\frac{k_\rho}{k_{1\rho}^2}\frac{H_n^{(1)}(k_\rho a)J_n'(k_\rho a) - H_n^{(1)\prime}(k_\rho a)J_n(k_\rho a)}{k_{1\rho}H_n^{(1)}(k_\rho a)J_n'(k_{1\rho}a) - k_\rho H_n^{(1)\prime}(k_\rho a)J_n(k_{1\rho}a)}, \tag{7.8}$$

where $H_n^{(1)}$ and $H_n^{(1)\prime}$ are Hankel function and its first derivative with order of n, and E_0 is the magnitude of incident E field at the origin.

7.2.2 Receiver in the Far-field Region

If the receiver is also in the far-field region of the cylinder, after lengthy mathematical manipulations of (7.5) (details are described in Appendix), the electric field in the far-field region can be calculated from:

$$\vec{E}_s(R) = \frac{ik_0 e^{ik_0 R}}{4\pi R}\left(\bar{\bar{I}} - \hat{k}_s\hat{k}_s\right) \cdot b\frac{\sin V}{V}\Upsilon, \tag{7.9}$$

where $V = [k_z k_0 \cos\theta_s]b/2$, b is the length of the cylinder, $\hat{k}_s$ denotes the scattering direction, and Υ is given in the Appendix.

7.2.3 Receiver in the Near-field Region

When the transmitter is in the far-field region, but receiver is in the near field of the tree trunk, the analytical solution in (7.9) becomes inaccurate. However, as transmitter is in the far field, plane wave incidence approximation can still be used to obtain the surface currents on the trunk by (7.6), (7.7) and the scattered field can be calculated numerically by taking integral of surface currents with equation (7.3). This approach is referred to as surface current integral method (SCIM).

7.2.4 Transmitter in the Near-field Region

If the transmitter is in the near-field region of the entire tree trunk, to avoid complex near-field calculation, segmented-cylinder method (SCM) may be applied. In this method, the entire trunk is divided into smaller segments but still large compared to the wavelength, and then the transmitter can be in the far-field range of each small segment. As a consequence, the methods based on plane-wave incidence approximation are still valid for each segment and the total scattered field is the sum of that from all segments, as shown in Figure 7.2.

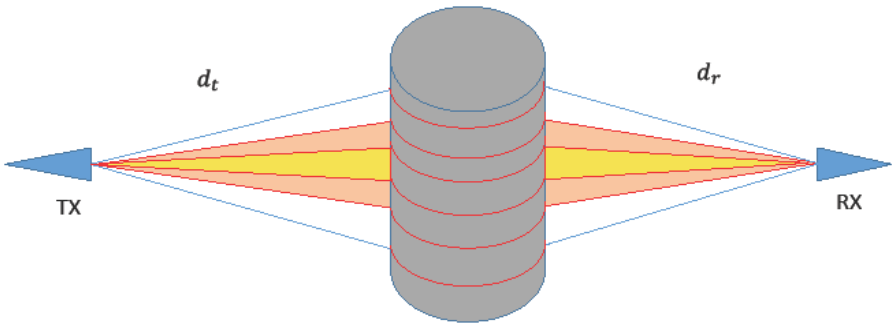

Figure 7.2. The transmitter and receiver locate in the near-field of whole trunk but in the far-field of small segment.

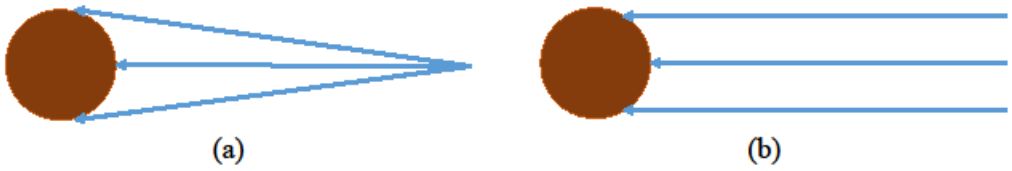

Figure 7.3. Transmitter is in near-field range of the cylinder, comparison between (a) spherical / cylindrical wave incidence and (b) plane wave incidence approximation.

However, in scenarios where the transmitter is in the near-field with respect to the diameter of trunk, the plane-wave incidence approximation is no longer valid. Intuitively this can be explained in Figure 7.3. The far-field radiation of antenna can be approximated as 0th order spherical Hankel wave, with the form of $E_i = A\frac{e^{ik_0 r}}{r}$, where r is the propagation distance, and A is a constant to ensure the incident E field to be E_0 at origin. A is denoted as $A = E_0 r/e^{ik_0 r}$. The wave propagation from transmitter to the trunk is depicted in Figure 7.3 (a), and plane wave incidence approximation is demonstrated in (b).

Sommerfeld identity [202] can be used to transfer the spherical wave function into cylindrical wave functions. With some efforts, the equivalent electric and magnetic surface currents can be written as:

$$\vec{J}_s^{TM}(a,\phi,z) = -\frac{\omega\varepsilon_1 A}{2}\int_{-\infty}^{\infty}[dk_z e^{ik_z z}\frac{k_\rho}{k_0}\sum_{n=-\infty}^{\infty}C_n' k_{1\rho}J_n'(k_{1\rho}a)e^{in\phi}\hat{z}], \tag{7.10}$$

$$\vec{J}_m^{TM}(a,\phi,z) = -\frac{iA}{2}\int_{-\infty}^{\infty}dk_z e^{ik_z z}\frac{k_\rho}{k_0}[\frac{k_z}{a}\sum_{n=-\infty}^{\infty}nC_n' J_n\,(k_{1\rho}a)e^{in\phi}\hat{z}$$

$$+ k_{1\rho}^2\sum_{n=-\infty}^{\infty}C_n' J_n\,(k_{1\rho}a)e^{in\phi}\hat{\phi})]. \tag{7.11}$$

The derivation and the expression for C_n' are describe in the Appendix. Note that (7.10) (7.11) require evaluating Sommerfeld integral at each point on the trunk's surface for all orders of

Bessel functions, and practically it needs hundreds of orders to ensure convergence. For mmWave band the trunk's surface can be discretized into hundreds of thousands of points, which makes the computation extremely extensive.

Alternatively, due to the fact that the distance from the transmitter to trunk is usually much larger than the wavelength, i.e. $k_\rho|\rho| \gg 1$, the spherical wave front can be approximated as cylindrical wave front for any observation point on the surface of the tree trunk:

$$\frac{e^{ik|\vec{r}-\vec{r}'|}}{|\vec{r}-\vec{r}'|} \approx \frac{e^{ik_z(z-z')}H_0^{(1)}(k_\rho|\vec{\rho}-\vec{\rho}'|)}{|\vec{r}-\vec{r}'|\sqrt{2/(i\pi k_\rho|\vec{\rho}-\vec{\rho}'|)}}, \tag{7.12}$$

where $\vec{r}' = \vec{\rho}' + z'\hat{z}$ is the source position of the spherical wave and $\vec{r} = \vec{\rho} + z\hat{z}$ denotes the observation point. The cylindrical wave with center at $\vec{\rho}'$ can be expanded as cylindrical eigenfunctions with center at $\vec{\rho}$ by:

$$H_0^{(1)}\left(k_\rho|\vec{\rho}-\vec{\rho}'|\right) = \sum_{n=-\infty}^{\infty} H_n^{(1)}\left(k_\rho\rho'\right)J_n\left(k_\rho\rho\right)e^{in(\phi-\phi')}, \qquad (\rho \le \rho') \tag{7.13}$$

Because the observation point is on the surface of trunk, and the source is outside the trunk, the condition $\rho \le \rho'$ is naturally satisfied. To simplify the calculation, the observation points with same k_z and k_ρ values can be treated as illuminated by the same cylindrical wave, and these points are on a conical surface with center at the source point. This conical surface intersecting with the trunk creates an ellipse as shown in Figure 7.4 (a). Assume with a small thickness, the elliptical small piece of trunk then is approximately illuminated by cylindrical wave with fixed k_ρ together with a propagating phase front in z direction with k_z. Therefore, the whole cylinder can be divided into small segments by conical surfaces with center at the source point as is shown in Fig. Figure 7.4 (b) and each segment is illuminated by different cylindrical wave. The angular step $d\theta$ is exaggerated in the figure and in simulation $d\theta = 0.2°$ is chosen for good accuracy.

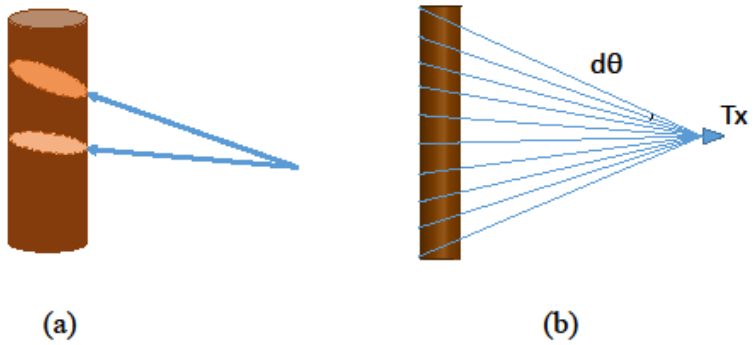

Figure 7.4. (a) Spherical wave incidence on one cross-section can be approximated by cylindrical wave incidence and (b) The trunk is divided by conical surfaces with center at the transmitter

After some algebra, the surface currents turn out to be the same form as (7.6), (7.7) with C_n replaced by C_n'', which is given by:

$$C_n = \frac{AH_n^{(1)}(k_\rho\rho')e^{-in\phi'}k_\rho}{k_{1\rho}^2\sqrt{\frac{2((z-z')^2+\rho'^2)}{i\pi k_\rho\rho'}}}\frac{H_n^{(1)}(k_\rho a)J_n'(k_\rho a)-H_n^{(1)\prime}(k_\rho a)J_n(k_\rho a)}{k_{1\rho}H_n^{(1)}(k_\rho a)J_n'(k_{1\rho}a)-k_\rho H_n^{(1)\prime}(k_\rho a)J_n(k_{1\rho}a)}, \quad (7.14)$$

Once the equivalent surface currents are computed, the scattering field at any position regardless of far-field or near-field condition can be evaluated by (7.3) numerically. Remarkably, the proposed cylindrical-wave incidence segmented-cylinder method (CISCM) can also be applied in far-field incidence situation. Compared to the plane-wave approximation for far-field incidence case, this approach will yield slightly more accurate results but need much more computations. Regarding the trade-off of accuracy and efficiency, the approach based on plane-wave approximation is chosen in numerical simulation for far-field incidence case.

7.3 Multiple Scattering Model of randomly distributed tree trunks

In some scenarios of vehicular communication, the communication channel can be interfered by more than one tree trunk. For example, in a scenario where two cars drives on a

curved road with many trees on the sides, the LOS link may be blocked by the trees as illustrated in Figure 7.5. As many trees locates on or near the LOS link between vehicles, the scattered field due to multiple scattering between trees cannot be ignored. Though the aforementioned current-integral based semi-analytic solutions can accurately evaluate the multiple scattered fields in the near-field range of tree trunks with free space Green's function, the calculation will become extremely expensive if applied to multiple scattering problem. With the assumption that the distance between transmitters / receivers and the trees are in the near field range of trees and only sacrifices small accuracy (will be discussed in the next section), the problem can be approximated as 2D scattering problem where the tree trunks are approximated as infinite long dielectric cylinders.

(a) (b)

Figure 7.5. (a) A photograph and (b) a 2D illustration of a curved road scenario where the vehicular communication link may be blocked by randomly distributed trees.

Many literatures [203][204] have studied the higher order scattered fields between metallic cylinders excited by a plane wave. In this thesis, a modal expansion-based approach for dielectric cylinders illuminated by cylindrical wave is presented. Assume the source s_0 locates at (x_0, y_0) and there are l cylinders locating at (x_1, y_1), …, (x_l, y_l) with radius of a_1,…,a_l, respectively.

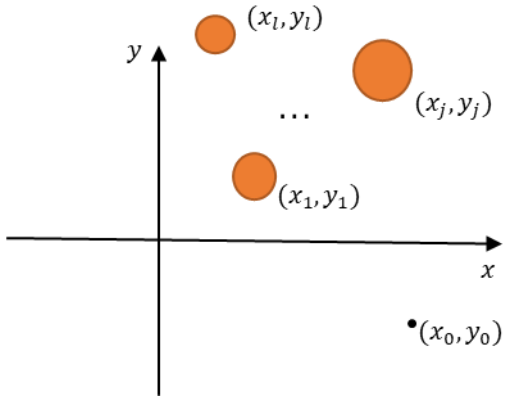

Figure 7.6. The coordinate system of the multiple scattering problem for dielectric cylinders

For simplicity, only TM case (vertical polarization) is considered in this analysis. The coordinate system for this problem is shown in Figure 7.6. The incident field at (x, y) from the source s_0 is given by:

$$E_{iz}^{(0)}(x,y) = H_0^{(1)}\left(k_\rho|\vec{\rho} - \vec{\rho}_0|\right) = H_0^{(1)}\left(k_\rho\sqrt{(x-x_0)^2 + (y-y_0)^2}\right), \tag{7.15}$$

where k_ρ is the wavenumber in free space. For any cylinder j, the incident field can be expanded as cylindrical eigen functions with center of (x_j, y_j) as given in (7.13). By applying boundary conditions that enforce the continuity of both electric fields and magnetic fields on the surface of cylinder, the first order scattered fields at (x, y) can be evaluated from:

$$E_{sj}^{(1)} = \sum_{n=-\infty}^{\infty} H_n^{(1)}\left(k_\rho\rho_{0j}\right)A_{j,n}k_\rho^2 H_n^{(1)}\left(k_\rho\rho_{rj}\right)e^{in(\phi_{rj}-\phi_{0j})}, \tag{7.16}$$

where ρ_{0j} denotes the distance between source s_0 and the center of cylinder j, $\rho_{0j} = \sqrt{\left(x_0 - x_j\right)^2 + \left(y_0 - y_j\right)^2}$, and ϕ_{0j} denotes the angle of source s_0 with respect to the center of cylinder j, $\phi_{0j} = \text{atan2}(y_0 - y_j, x_0 - x_j)$. Similarly, $\rho_{rj} = \sqrt{\left(x - x_j\right)^2 + \left(y - y_j\right)^2}$ and $\phi_{rj} =$

$\text{atan2}(y-y_j, x-x_j)$. $A_{j,n}$ is the modal coefficient corresponding to the n^{th} order Hankel function for plane wave incidence on cylinder j except the $(-i)^n$ term [185]:

$$A_{j,n} = \frac{k_\rho J_n'(k_\rho a_j) J_n(k_{1\rho} a_j) - k_{1\rho} J_n(k_\rho a_j) J_n'(k_{1\rho} a_j)}{k_\rho^2 k_{1\rho} H_n^{(1)}(k_\rho a_j) J_n'(k_{1\rho} a_j) - k_\rho^3 H_n^{(1)\prime}(k_\rho a_j) J_n(k_{1\rho} a_j)}. \tag{7.17}$$

where $k_{1\rho}$ denotes the wavenumber for the dielectric cylinder, a_j denotes the radius of cylinder j.

$E_{sj}^{(1)}$ can be rearranged as:

$$E_{sj}^{(1)} = \sum_{n=-\infty}^{\infty} F_{sj0,n}^{(1)} H_n^{(1)}(k_\rho \rho_{rj}) e^{in\phi_{rj}} = \vec{F}_{sj0} \cdot \vec{V}_{rj}, \tag{7.18}$$

where $F_{sj0,n}^{(1)} = H_n^{(1)}(k_\rho \rho_{0j}) A_{j,n} k_\rho^2 e^{-in\phi_{0j}}$, $\vec{F}_{sj0} = [F_{sj0,-N}^{(1)}, \dots, F_{sj0,N}^{(1)}]$, given that the infinite summation is truncated into $2N+1$ terms. The different cylindrical eigenfunctions of scattered fields from cylinder j to observation point r can form a vector $\vec{V}_{rj}$, and $\vec{V}_{rj}$ is defined as:

$$\vec{V}_{rj} = \left[H_{-N}^{(1)}(k_\rho \rho_{rj}) e^{-iN\phi_{rj}}, H_{-N+1}^{(1)}(k_\rho \rho_{rj}) e^{-i(N-1)\phi_{rj}}, \dots, H_N^{(1)}(k_\rho \rho_{rj}) e^{iN\phi_{rj}}\right]^T. \tag{7.19}$$

For integer n, the Bessel functions have the following property:

$$L_{-n}(x) = (-1)^n L_n(x), \tag{7.20}$$

where L_n can be J_n, J_n', $H_n^{(1)}$ or $H_n^{(1)\prime}$ in this problem. After some algebra, the $-n^{th}$ term and n term of $\vec{F}_{sj0}$ and $\vec{V}_{rj}$ can be simply related by the following equations:

$$F_{sj0,-n}^{(1)} e^{-in\phi_{0j}} = (-1)^n F_{sj0,n}^{(1)} e^{in\phi_{0j}}, \tag{7.21}$$

$$V_{rj,-n} e^{in\phi_{rj}} = (-1)^n V_{rj,n} e^{-in\phi_{rj}}, \tag{7.22}$$

Therefore, we only need to evaluate $F_{sj0,n}^{(1)}$ and $V_{rj,n}$ for $0 \le n \le N$, and the rest can be readily obtained. In the second order scattering analysis of cylinder k with respect to cylinder j, the incident fields on the surface of cylinder k is the same as the scattered field of cylinder j as given in (7.18). To obtain the scattered fields of cylinder k, the Graf's Addition Theorem of Bessel

functions [205] is applied to expressed the m^{th} order wave function $H_m^{(1)}(k_\rho\rho_{rj})e^{im\phi_{rj}}$ on the surface of cylinder k as a summation of cylindrical eigenfunctions with center at (x_k, y_k):

$$H_m^{(1)}(k_\rho\rho_{rj})e^{im\phi_{rj}} = e^{im(\pi+\phi_{jk})}\sum_{n=-\infty}^{\infty} H_{n-m}^{(1)}(k_\rho\rho_{jk})J_n(k_\rho\rho_{rk})e^{in(\phi_{rk}-\phi_{jk})}, \tag{7.23}$$

where ρ_{jk} and ϕ_{jk} denote the range and angle of the center of cylinder j with respect to the center of cylinder k, and ρ_{rk} and ϕ_{rk} are the range and angle of the observation point on the surface of cylinder k with respect to the center of cylinder k.

By applying the boundary condition, the second order scattered field of cylinder k by the m^{th} order cylindrical wave $H_m^{(1)}(k_\rho\rho_{rj})e^{im\phi_{rj}}$ from cylinder j can be given by:

$$E_{skj,m}^{(2)} = \sum_{n=-\infty}^{\infty} F_{skj,mn}^{(2)} H_n^{(1)}(k_\rho\rho_{rk})e^{in\phi_{rk}}, \tag{7.24}$$

where

$$\begin{aligned} F_{skj,mn}^{(2)} &= e^{im(\pi+\phi_{jk})}H_{n-m}^{(1)}(k_\rho\rho_{jk})A_{k,n}k_\rho^2 e^{-in\phi_{jk}} \\ &= (-1)^m H_{n-m}^{(1)}(k_\rho\rho_{jk})A_{k,n}k_\rho^2 e^{i(m-n)\phi_{jk}}. \end{aligned} \tag{7.25}$$

In real implementation, the number of orders of Bessel functions are truncated into the ranges $(-M \le m \le M, -N \le n \le N)$. We can define a vector $\vec{V}_{skj}^{(2)}$ as:

$$\vec{V}_j^{(2)} = \left[E_{skj,-M}^{(2)}, E_{skj,-M+1}^{(2)}, \ldots, E_{skj,M-1}^{(2)}, E_{skj,M}^{(2)}\right]^T, \tag{7.26}$$

Similarly, define a (2*M*+1) by (2*N*+1) matrix $\bar{\bar{F}}_{skj}$ with the element in m^{th} row and n^{th} column equal to $F_{skj,mn}^{(2)}$. Then the following expression can be obtained:

$$\vec{V}_j^{(2)} = \bar{\bar{F}}_{skj}\vec{V}_{rk}. \tag{7.27}$$

The total second order scattered field of cylinder k from cylinder j is:

$$E_{skj}^{(2)} = \sum_{m=-\infty}^{\infty} F_{sj0,m}^{(1)} E_{skj,m}^{(2)} = \vec{F}_{sj0} \cdot \vec{V}_j^{(2)}. \tag{7.28}$$

Notably, the coefficient vector $\vec{F}_{sj0}$ and matrix $\bar{\bar{F}}_{skj}$ are reusable in higher order scattered field calculation. Generally, in an L-cylinder problem, the v^{th} order solutions can be derived from the product of an adjacency matrix and the $(v-1)^{th}$ order solutions:

$$\begin{bmatrix} \vec{V}_1^{(v)} \\ \vec{V}_2^{(v)} \\ \dots \\ \vec{V}_L^{(v)} \end{bmatrix} = \begin{bmatrix} 0 & \bar{\bar{F}}_{s21} & \dots & \bar{\bar{F}}_{sL1} \\ \bar{\bar{F}}_{s12} & 0 & \dots & \bar{\bar{F}}_{sL2} \\ \dots & \dots & 0 & \dots \\ \bar{\bar{F}}_{s1L} & \bar{\bar{F}}_{s2L} & \dots & 0 \end{bmatrix} \begin{bmatrix} \vec{V}_1^{(v-1)} \\ \vec{V}_2^{(v-1)} \\ \dots \\ \vec{V}_L^{(v-1)} \end{bmatrix}, \tag{7.29}$$

$$E_s^{(v)} = \begin{bmatrix} \vec{F}_{s10} & \dots & \vec{F}_{sL0} \end{bmatrix} \cdot \begin{bmatrix} \vec{V}_1^{(v)} \\ \dots \\ \vec{V}_L^{(v)} \end{bmatrix}, \tag{7.30}$$

where $\vec{V}_k^{(1)} = \vec{V}_{rk}$, which is given by (7.19).

The entry of the adjacency matrix $\bar{\bar{F}}_{skj}$ denotes the EM coupling from cylinder j to cylinder k. In practical simulation, if two cylinders far apart from the direct link between transmitter and receiver, the contribution of multiple scattering can be very weak and therefore the corresponding entry of the adjacency matrix can be set as 0 to reduce the computational expense.

7.4 Numerical Results and Validation of the Single-Scattering Models for Tree Trunk

Depending on whether transmitter and receiver are in the far field of the trunk, different approaches are applied to obtain the scattered fields. In this section, validation of the accuracy of EM theoretical methods are discussed. Then, analysis on the scattered fields and path loss is presented.

7.4.1 Validation of Semi-exact Solution and SCIM

The semi-exact analytic solution in (7.9) is applied in the scenario where both the transmitter and receiver are in the far-field region of the trunk. To verify this method, the result is compared with that from a full-wave simulator based on method of moment (MoM). Here we use the commercial simulation software AnsysEM (HFSS). The full-wave simulation requires much more computational resources and time but has no approximation and very good accuracy. In the validation, the cylinder's dimension is set to be $4\lambda \times 10\lambda$(about 0.2 m × 0.5 m for 5.9 GHz) and relative permittivity is 10+5i in both the HFSS and the semi-exact solution. The results are shown in Figure 7.7. The root-mean-square error (RMSE) of the result from the two methods is 0.18 dB for VV polarization and 0.51 dB for HH polarization, which indicates that the semi-exact solution shows excellent agreement with that from MoM.

Similar to the semi-exact solution, SCIM method is also based on plane-wave incidence approximation to obtain equivalent surface currents. In fact, semi-exact solution is a special case of SCIM method when receiver is in far-field region of the trunk. Therefore, the results from these two methods should be the same for far-field receiver. In addition, suppose the receiver is very close to the trunk, then only a portion of trunk with height close to the observation point contributes to the scattered field. As a result the length of trunk no longer matters in this situation, and scattered E field will be similar to that for infinitely long cylinder. The scattered E field from infinitely-long cylinder is an analytic solution [185], and the detail of this solution is given in Appendix.

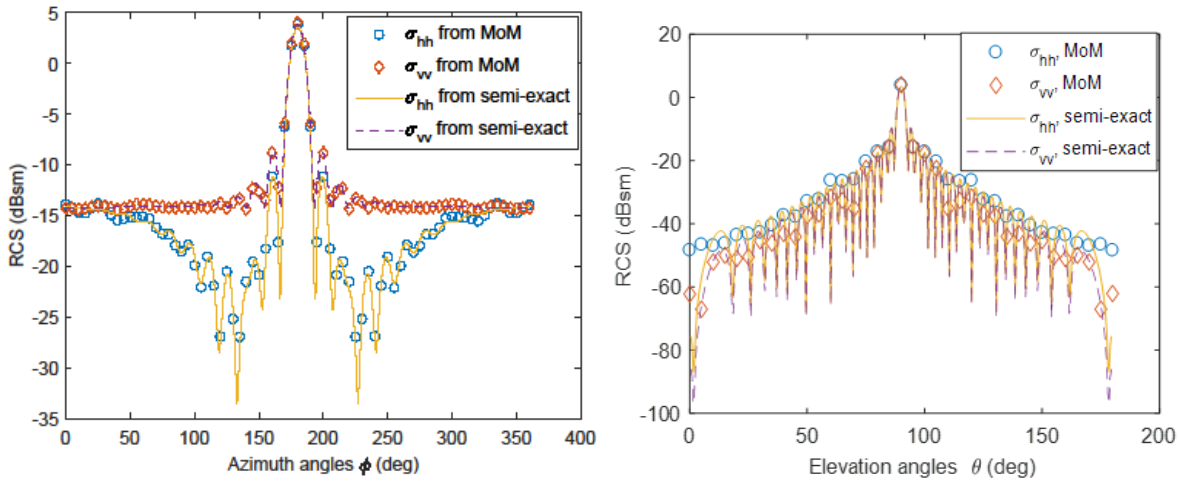

(a) (b)

Figure 7.7. Comparison of RCS simulation for semi-exact solution and MoM, for the cylinder with 4 λ diameter and 10 λ height, with scattering directions on (a) azimuth plane ($\theta_s = 90°$) and (b). elevation plane ($\theta_s = 180°$)

The comparison of the scattered E fields calculated by SCIM and two analytic solutions for receiver in the far field and very near range are depicted in Figure 7.8. The scattered E fields are normalized to the incident field $|E_0|$.

It is shown that E_s calculated by SCIM coincides with that by far-field analytic semi-exact solution in the far range and is very close to that derived from infinitely long cylinder solution for very near range. As a result, the accuracy of the surface integral method is validated.

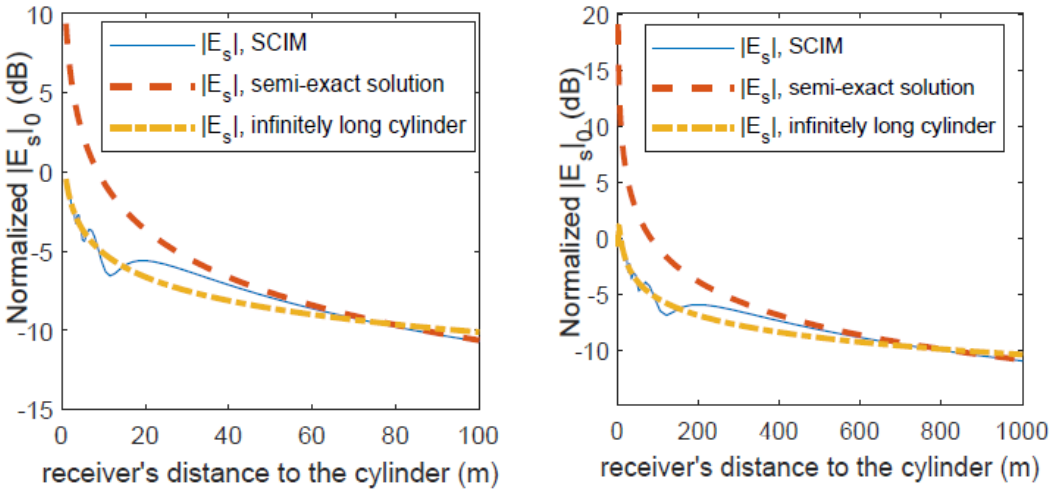

(a) (b)

Figure 7.8. Comparison of SCIM with analytic solutions for normalized $|E_s|$ as a function of distance between receiver and the trunk with plane wave incidence for 2 m long trunk with (a) 0.2 m radius at 5.9 GHz and (b) 0.1 m radius at 60 GHz.

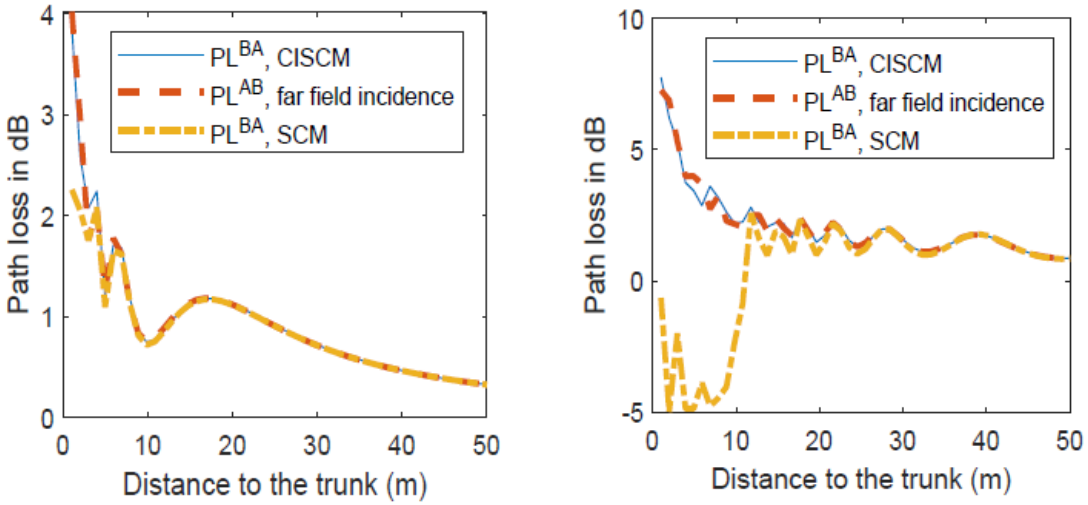

(a) (b)

Figure 7.9. Path loss as a function of distance to the trunk comparison for varying transmitter or receiver's position, while the other is located sufficiently far away for 2 m long and 0.2 diameter trunk with at (a) 5.9 GHz and (b) 60 GHz.

7.4.2 Validation of SCM and CISCM

For near-field incidence, the two methods SCM and CISCM mentioned in Sec. 7.2.4 are used to compute the scattered field. Since we have the accurate solution of scattered field from trunk with transmitter in the far-field and receiver in the near-field of trunk, the near-field incidence method can be verified by reciprocal property of EM wave in time-invariant linear media. Suppose two antennas are placed on the two sides of a tree trunk: one antenna denoted as antenna A locates in the far-field of the trunk, and the other denoted as antenna B is in the near-field of the trunk. Reciprocity states that the received signal at antenna A sent from antenna B should be the same as that at antenna B transmitted from antenna A if transmitted signal is the same. Therefore, the path loss should obey reciprocity as well.

Let antenna A be in the far field of trunk and antenna B be in the near field with distance to the trunk as a variable. The path loss for signal transmitted from antenna A to B denotes as PL^{AB}, and that from antenna B to A denotes as PL^{BA}. PL^{AB} can be accurately obtained by SCIM with plane wave incidence, and PL^{BA} is calculated based on the two methods under validation. Figure 7.9 depicts the path loss of PL^{AB} and PL^{BA} as a function of distance from antenna B to the trunk. The results show that at both 5.9 GHz and 60 GHz, the path loss calculated by CISCM has an excellent agreement with the far-field incidence solution for the range greater than 1 m. In addition, the solution based on SCM fails when the transmitter is in the near field of the cross-section of tree trunk (i.e., 1.6 m distance at 5.9 GHz and 16 m distance at 60 GHz for 0.2 m diameter). Reasonable accuracy is presented for the method with cylindrical wave incidence approximation if source is more than 1 m away from the trunk and the analysis shown in the following section are based on CISCM.

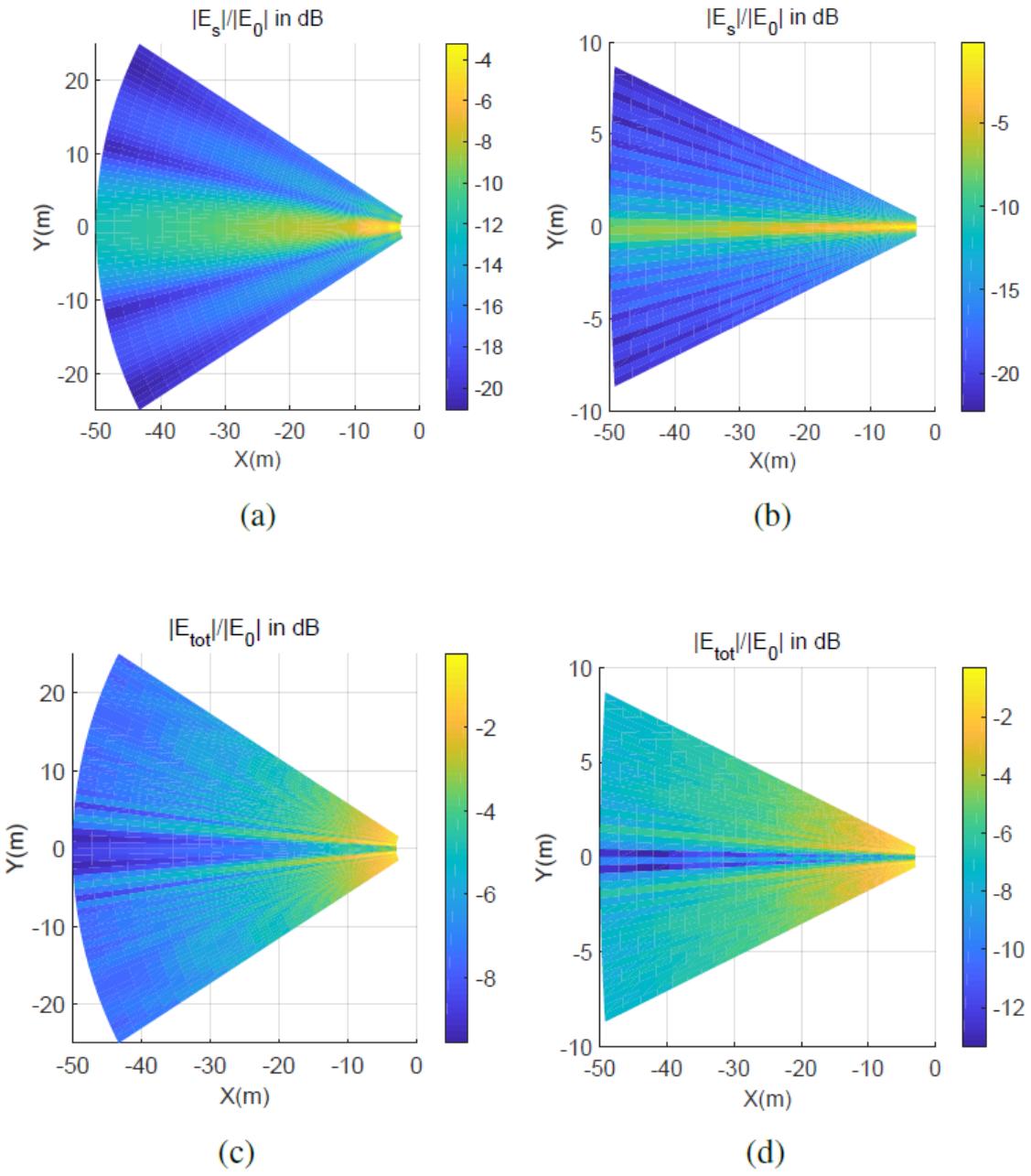

Figure 7.10. Scattered field for V2V foliage propagation at (a) 5.9 GHz, (b) 60 GHz, and the total field at (c) 5.9 GHz and (d) 60 GHz.

7.4.3 Scattered Fields and Path Loss Analysis

In the following discussion, the scattered field/path loss of signal is investigated for different receiver's locations, transmitter's locations, dimensions and dielectric properties of the trunk. To

examine how the scattered field and total field change with receiver's location, examples of the E fields normalized to the incident field at the center of the trunk are illustrated in Figure 7.10 at both 5.9 GHz and 60 GHz. In this example, the transmitter is located at 10 m away from the trunk (i.e., $d_1 = 10\ m$), and the radius and height of the trunk is 0.1 m and 2 m, respectively. The heights of the transmitter and the receiver are equal to 1 m. It shows that the scattered fields and total fields are nonlinear and fluctuating as functions of the distance and the azimuth angle. The azimuth directions of the fields are chosen to be from 150° to 210° for 5.9 GHz and 170° to 190° for 60 GHz, this is due to the fact that the normalized scattered power outside the ranges are negligible compared to LoS signal's power(<-20 dB).

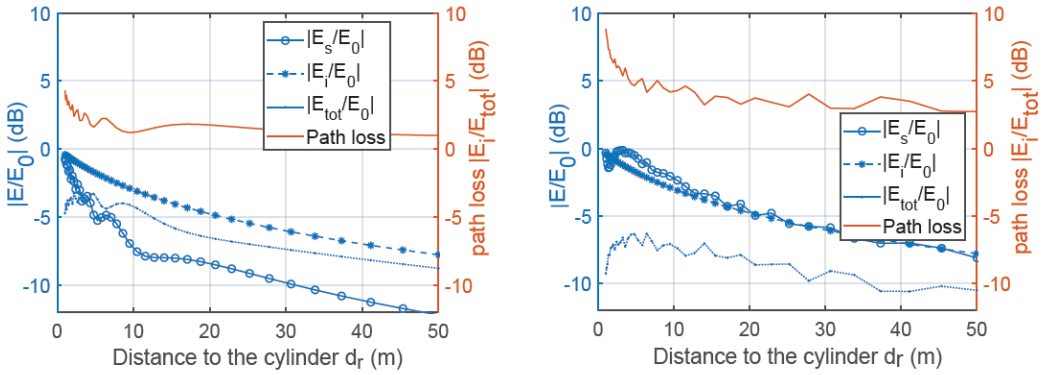

Figure 7.11. Incident, scattering and total E fields in forward scattering direction and path loss as a function of distance to the cylinder at (a) 5.9 GHz and (b) 60 GHz.

The normalized incident, scattered, total fields and the corresponding path loss in the forward scattering direction as a function of receiver's distance to the trunk are shown in Figure 7.11. It shows that for the same trunk the path loss at 60 GHz is much higher than that at 5.9 GHz. This is due to the fact that the short wavelength at 60 GHz behaves like light wave, where the total field is more substantially attenuated by the blockage, compared to that for the longer wavelength signal.

The relative permittivity of the tree trunk depends on the frequency and the water content of the tree, and thus it changes over seasons. The permittivity of trunk has small impact on the total field in the forward scattering direction as can be shown in Figure 7.12. This is because for an electric large lossy object like the tree trunk, when LoS is blocked, the EM wave can hardly penetrate through regardless of the permittivity. The total field is dominated by the diffraction, which mainly depends on the shape and dimension of the object.

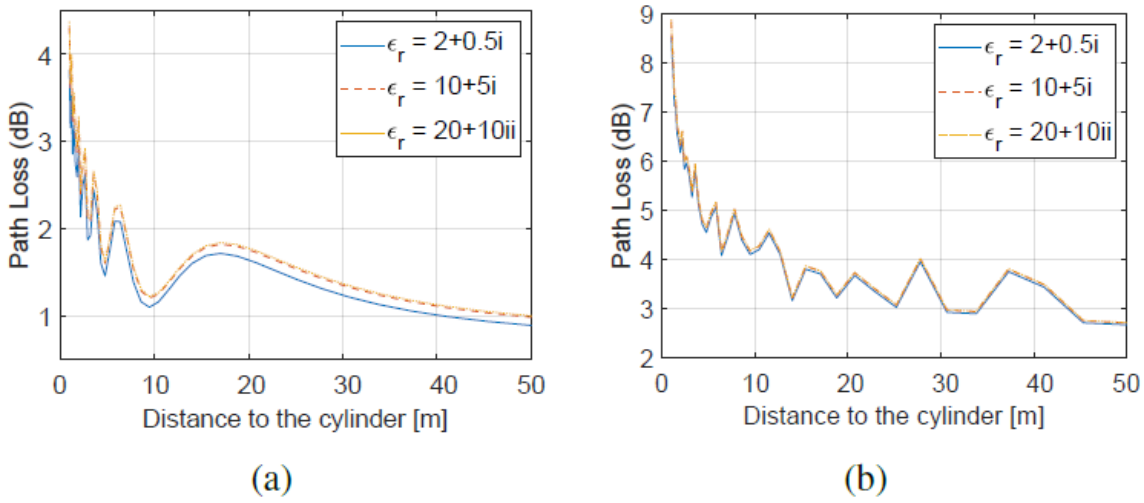

Figure 7.12. Comparison of the path loss in forward scattering direction with different permittivity at (a) 5.9 GHz and (b) 60 GHz.

The distance between transmitter and trunk affects the path loss as well. Figure 7.15 shows that the path loss for nearer transmitter is usually greater than that for further transmitter, intuitively, when the transmitter is placed closer to the trunk, wider angle of view will be blocked by the trunk, and remarkably, the path loss is not a linear or other simple function to the transmitter's distance. The same reason can be applied when considering larger radii of the trunk where higher path loss values are observed, which is shown in Figure 7.13 and Figure 7.14. It is shown that the path loss cannot be simply scaled with the dimensions of trunk. Notice the length of trunk doesn't affect the

path loss too much because both the transmitter and receiver are in the near-field range and only a portion of the trunk contributes to the attenuation of the communication link.

In summary, the path loss is a complex function of transmitter and receiver locations and the trunk's dimensions. Also the path loss has little dependence on the permittivity of the trunk as long as there is enough loss.

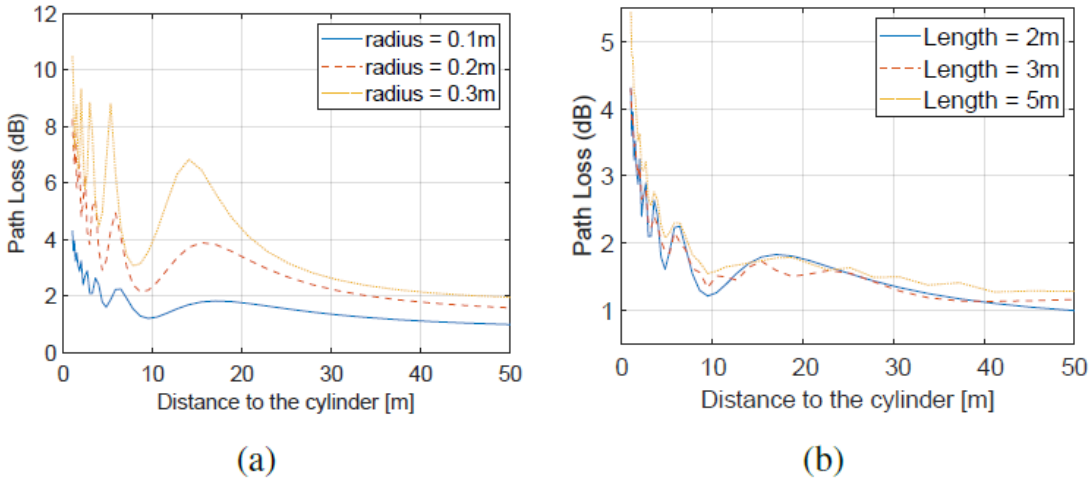

Figure 7.13. Comparison of the path loss in forward scattering direction with different (a) radii and (b) lengths of trunk at 5.9 GHz.

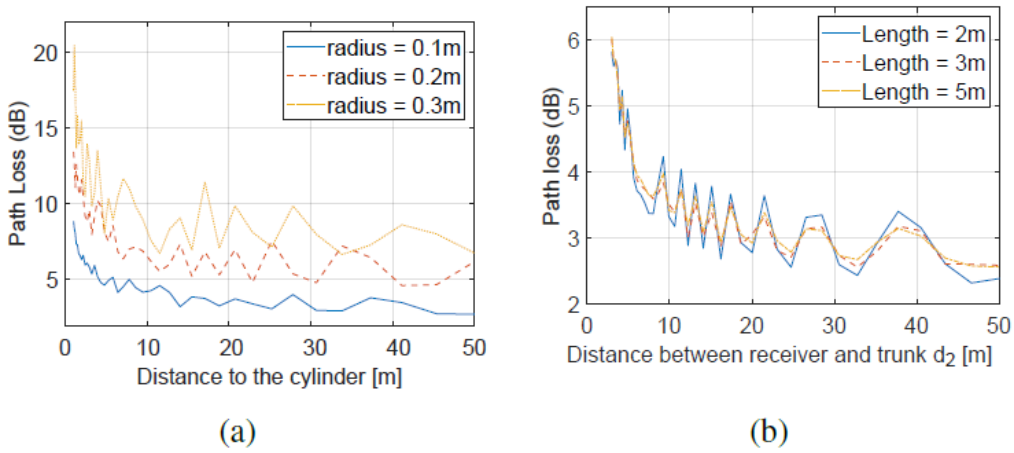

Figure 7.14. Comparison of the path loss in forward scattering direction with different (a) radii and (b) lengths of trunk at 60 GHz.

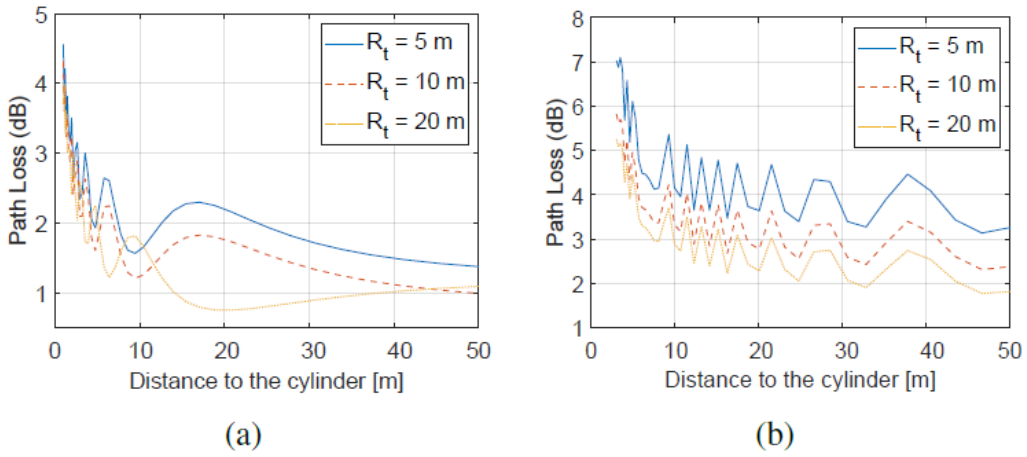

Figure 7.15. Comparison of the path loss in forward scattering direction with different distance to the trunk for transmitter Rt (a) at 5.9 GHz (b) at 60 GHz.

7.5 Artificial neural network model for the path loss of single tree trunk

For the example of scattered and total fields shown in Figure 7.10 (d_t = 10 m, radius = 0.1 m and length = 2 m), the path loss can be fitted by analytic functions with respect to receiver's distance to the trunk and its corresponding azimuth angle, as described in [182]. However, when generalized to arbitrary dimension of trunk and any position of the transmitter, the analytic curve-fitting functions become prohibitively complicated with compromised performance. To generate an accurate and easy-use model for the path loss, the artificial neural network (ANN) approach is applied.

In the following, the path loss is modeled as a function of the distance between transmitter and cylinder, distance between receiver and cylinder, azimuth angle, radius and length of the trunk with ANN. Then, we extract a macro-model to describe the overall link gain of V2V foliage propagation, which is promisingly useful for autonomous driving ITS.

ANNs can be treated as complicated mathematical functions to map input space $\vec{x}$ to output space Y. For this application, the input space $\vec{x}$ constructs as $[r_0, h, d_t, d_r, \phi_r]$, which

denote the radius of trunk, height of trunk, distance between transmitter and trunk, that between receiver and trunk and the azimuth angle of receiver, respectively. The output space *Y* is the path loss *PL* in dB ($10log_{10}|E\_i/E_{tot}|$) scale. The idea of ANN is to imitate the biological neural network, in which some intermediate variables are created. The intermediate variables are non-linear functions of inputs or other intermediate variables, and the final output is also a non-linear function of the intermediate variables.

The structure for the ANN model is shown in Figure 7.16, which is mainly composed of three parts: input layer, hidden layers and output layer. Each circle represents one variable, and the line with arrow from one circle to the other indicates the latter variable is a function of the former variable. Inputs $x_1, \ldots, x_5$ are normalized as $\vec{x}_i$ such that each variable has similar range from -1 to 1. The output of the neural network $\hat{y}$ is a normalized value as well, and can be mapped to the scale of path loss values *PL* inversely.

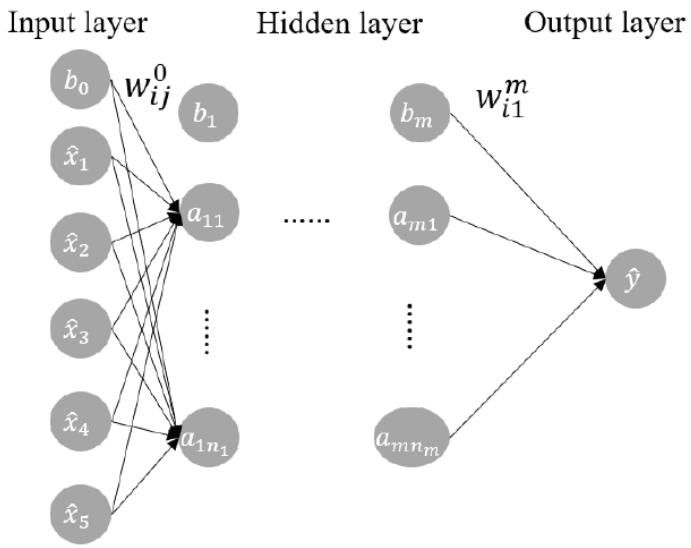

Figure 7.16. Structure of an artificial neural network with 5 inputs, 1 output and m hidden layers.

More than one million different datasets have been generated from EM models for curve-fitting. In training process, the datasets are randomly categorized into three parts: 70 % data are used to train the ANN, and 15 % are used in validation and the rest 15 % are testing data. The purpose of validation data is to ensure no over-fitting issue for a trained ANN, and that for testing data is to find the ANN with the best performance with many validated ANNs. The number of hidden layers and neurons is determined based on the performance of the ANN. The training process is implemented in Matlab, and Levenberg-Marquardt backpropagation algorithm is chosen as the training algorithm for its good performance and excellent time efficiency.

The correlation coefficient R and RMSE in dB are used to evaluate the performance of data fitting. Figure 7.17 shows the linear regression and correlation coefficient between the fitted and model path loss at 5.9 GHz with a neural network which contains two hidden layers and 10 neurons on each layer. It shows extremely strong correlation between the fitted data and model data, and very similar error performance for training, validation and test data indicates this neural network model is free from over-fitting problem. The RMSE between the fitted and model path loss of all dataset is 0.22 dB. Figure 7.18 depicts curve-fitting by this neural network for two examples with randomly chosen parameters. Reasonable agreement between fitted and model data is observed. Note that the range for ϕ is from 150° to 180° degree instead of 210°, this is due to the symmetry of trunk that the path loss at 180° + $\Delta\phi$ is the same as that at 180° - $\Delta\phi$.

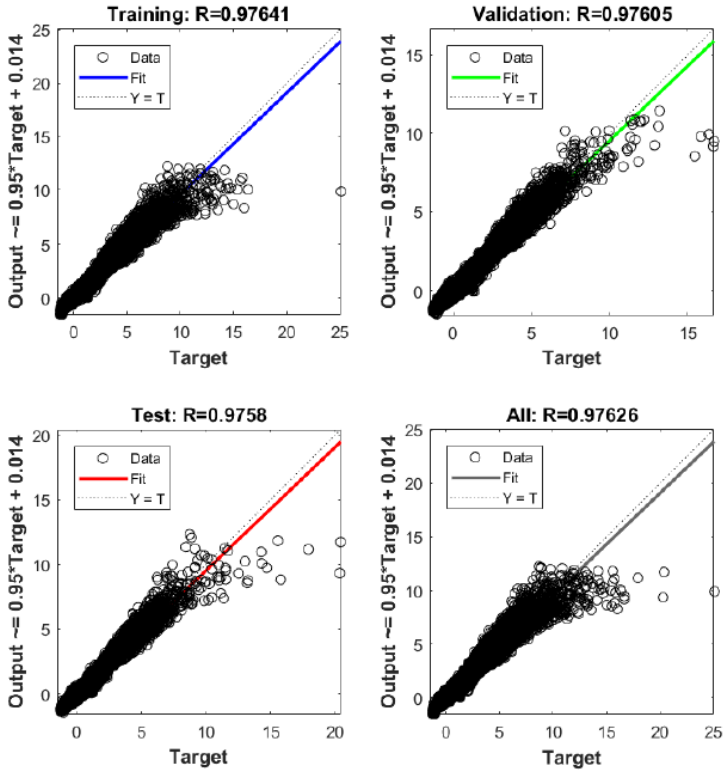
Training: R=0.97641
Validation: R=0.97605
Test: R=0.9758
All: R=0.97626
Data
Fit
Y = T
Output ~= 0.95*Target + 0.014
Target

(a)

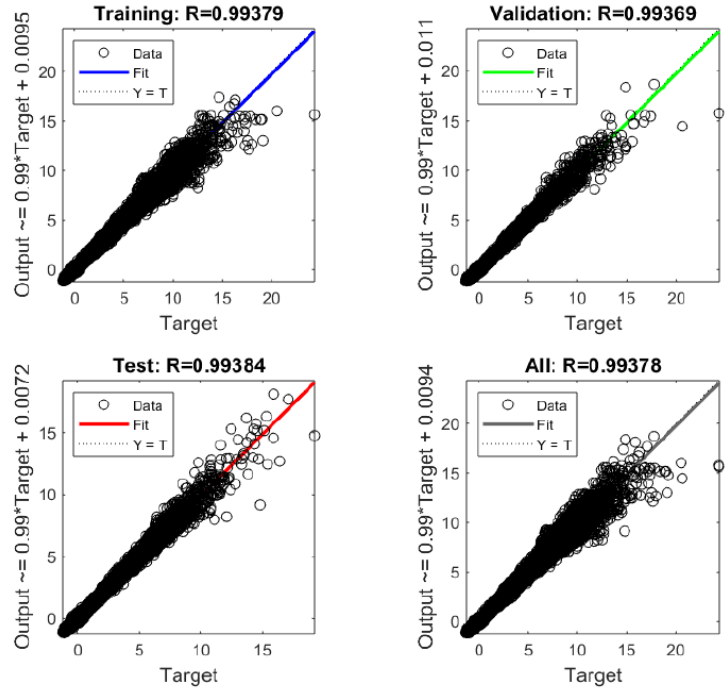
Training: R=0.99379
Validation: R=0.99369
Test: R=0.99384
All: R=0.99378
Data
Fit
Y = T
Output ~= 0.99*Target + 0.0095
Output ~= 0.99*Target + 0.011
Output ~= 0.99*Target + 0.0072
Output ~= 0.99*Target + 0.0094
Target

(b)

Figure 7.17. Data regression performance for curve-fitting of path loss of the ANN with two hidden layers at (a) 5.9 GHz and (b) 60 GHz.

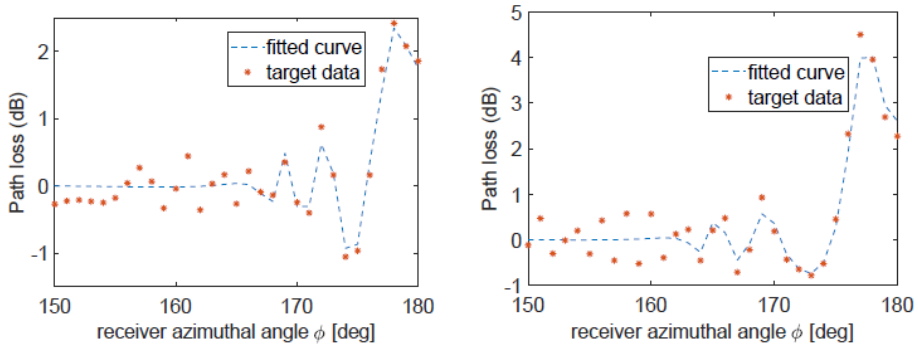

Figure 7.18. ANN Curve fitting of path loss at 5.9 GHz for examples of (a) radius = 0.1m, height = 3m, d_t = 8m and d_r = 26.9m and (b) radius = 0.2m, height = 2.0m, d_t = 28m and d_r = 5m.

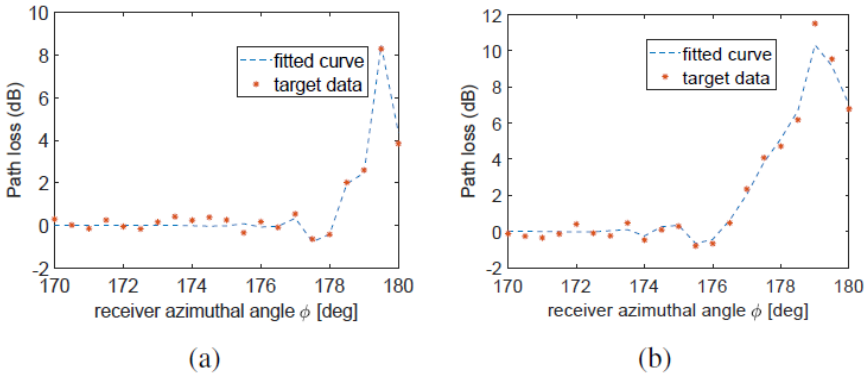

Figure 7.19. ANN Curve fitting of path loss at 60 GHz for examples of (a) radius = 0.1m, height = 2.2 m, d_t = 8 m and d_r = 35.7 m and (b) radius = 0.2m, height = 2.8m, d_t = 36 m and d_r = 5 m.

Similarly, we can generate ANN to fit the path loss data for 60 GHz. Because the function at 60 GHz is more irregular and unpredictable, structure with three hidden layers and 10 neurons in each layer is selected. The linear regression of fitted data is shown in Figure 7.17 (b). Similar to

5.9 GHz, excellent linearity between fitted data and model data is observed. The overall RMSE for path loss at 60 GHz fitted by this three hidden layers neural network is about 0.36 dB. Figure 7.19 gives two curve-fitting examples with randomly chosen parameters. In both examples the fitted and model data agree very well.

The average time for evaluating path loss through the proposed off-line ANN model is about 50 μs, which can enable the real-time assessment of communication channel. By contrast, the time for obtaining the similar path loss results from semi-analytical numerical simulation ranges from several seconds to several minutes, depending on the dimensions of tree trunk and frequency.

7.6 Simulation results and reduced multiple scattering model for multiple tree trunks

The permittivity of trunk is determined by the frequency f and gravimetric moisture content M_g. With the model given in [209], the permittivity of trunk is calculated as 33.2+9.75i at 5.9 GHz and 11.3+7.59i at 60 GHz, with the assumption that $M_g = 0.6$. Higher order scattered fields between cylinders can be evaluated by (7.29) and (7.30). The number of cylindrical eigenfunctions $\vec{V}_{rj}$ of each cylinder directly determine the calculation expense of this approach. It is known that the increase of number of eigenmodes $2N_j + 1$ will result in a more accurate solution. The optimal number of eigenmodes depends on both frequency and the radius of the cylinder. Here parametric study is used to find the optimal number of N as a function of ka, where N is the maximum order of eigenmode, k is the wavenumber in free space, and a is the radius of the cylinder. As the frequency band in our particular application is 5.9 GHz and 60 GHz, the study of number of eigenmodes are presented on these two bands. Figure 7.20 shows the path loss as a function of ($N/(ka)$), and ($2N$+1) is the number of eigenmodes. The path loss is obtained in a scenario where source and observation point are on the two side of the trunk and both are 5 m away from the trunk.

It shows that the path loss converges when N >1.2* ka in all scenarios, and in the following simulations, N =round(1.4* ka) is chosen. For example, for a 0.1 m radius cylinder, 33 modes (N=16) at 5.9 GHz and 327 modes (N = 163) at 60 GHz are selected for the cylinder in simulation.

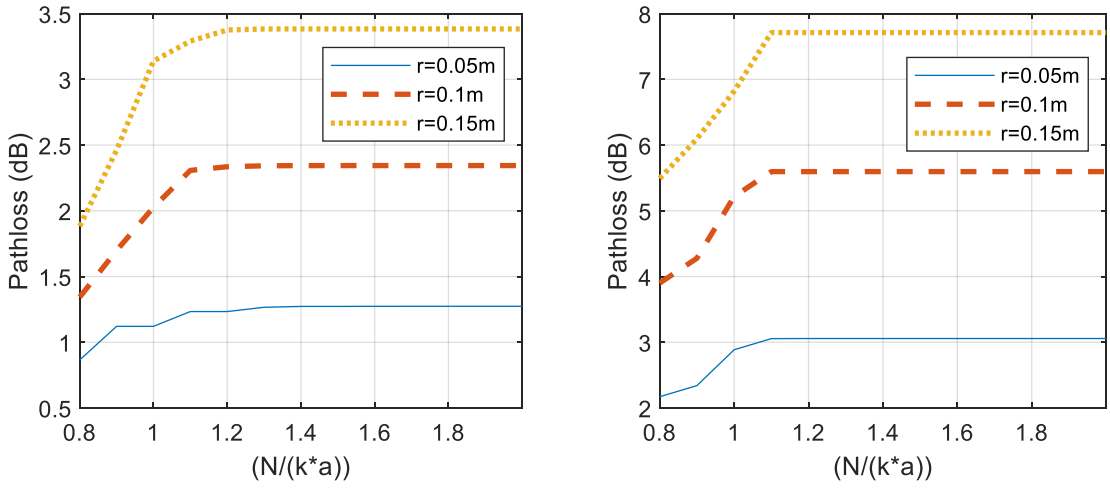

(a) (b)

Figure 7.20. Path loss of one trunk with different radii as a function of N/(ka) at (a) 5.9 GHz and (b) 60 GHz.

To demonstrate the multiple scattering effect between tree trunks, a two-cylinder scattering problem is examined first. In the first scenario, the source locates at (0,0), and the two tree trunks locate at (-0.1, 3.6) and (0, 4), respectively. Both tree trunks have 0.1 m radius. The path loss of *E* fields in dB scale at 5.9GHz and different locations with single and multiple scattering are shown in Figure 7.21. It shows that when one tree trunk is shaded by the other, the result based on single scattering method is not accurate and requires higher order scattering solutions. In this two-cylinder problem, second order solution can provide excellent accuracy as shown in Figure 7.21 (d). In another example shown in Figure 7.22 where two cylinders are not shaded by each other, even they are close the first order solution dominates in the scattered E fields as well as the path

loss. This feature can be used to determine whether the higher order scattering is significant between two given cylinders.

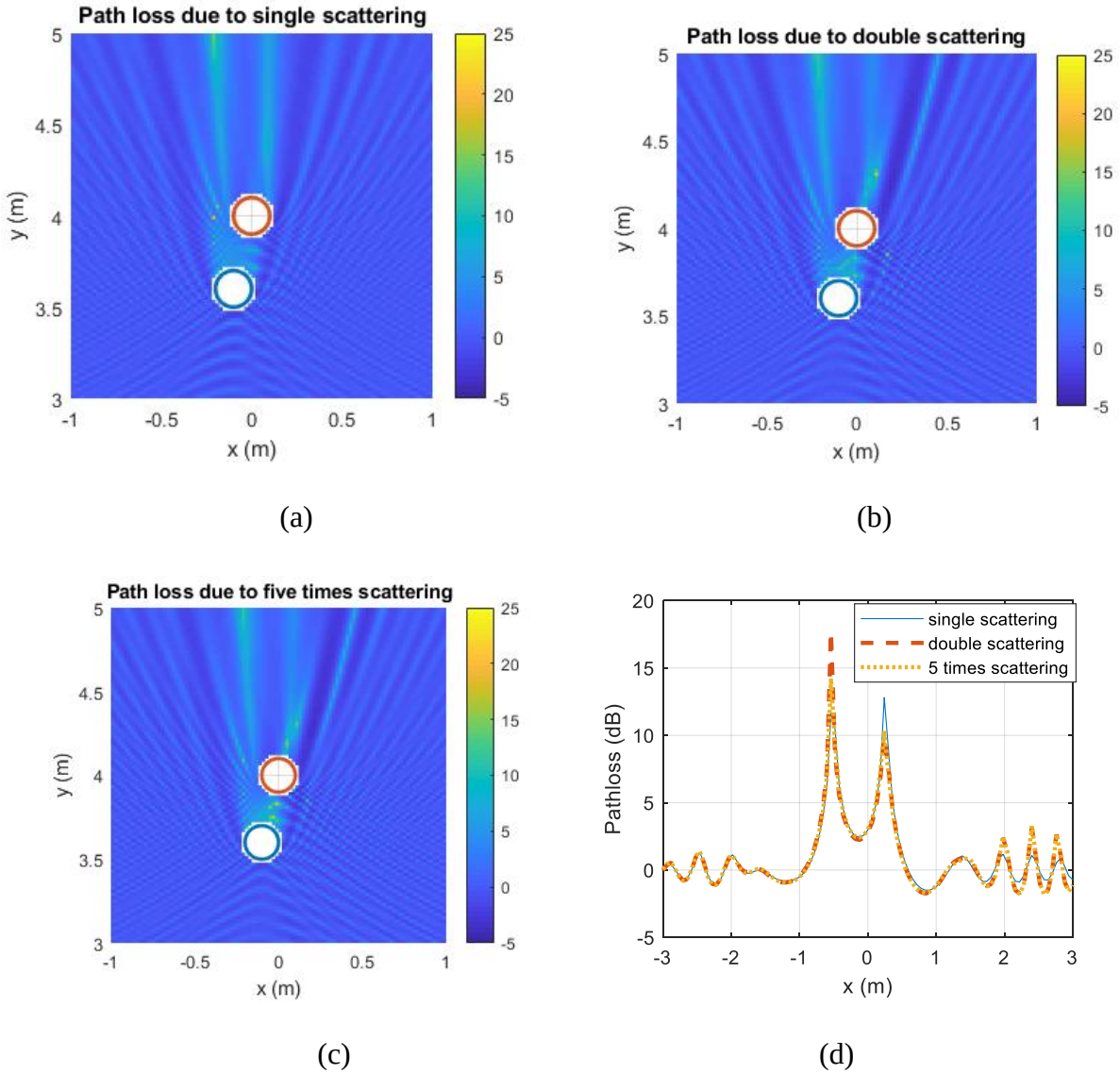

Figure 7.21. path loss of two overlapping tree trunks at 5.9 GHz with (a) single scattering, (b) double scattering and (c) five times scattering; (d) the path loss comparison between different orders of scattering at a function of receiver's x position, (y = 10m).

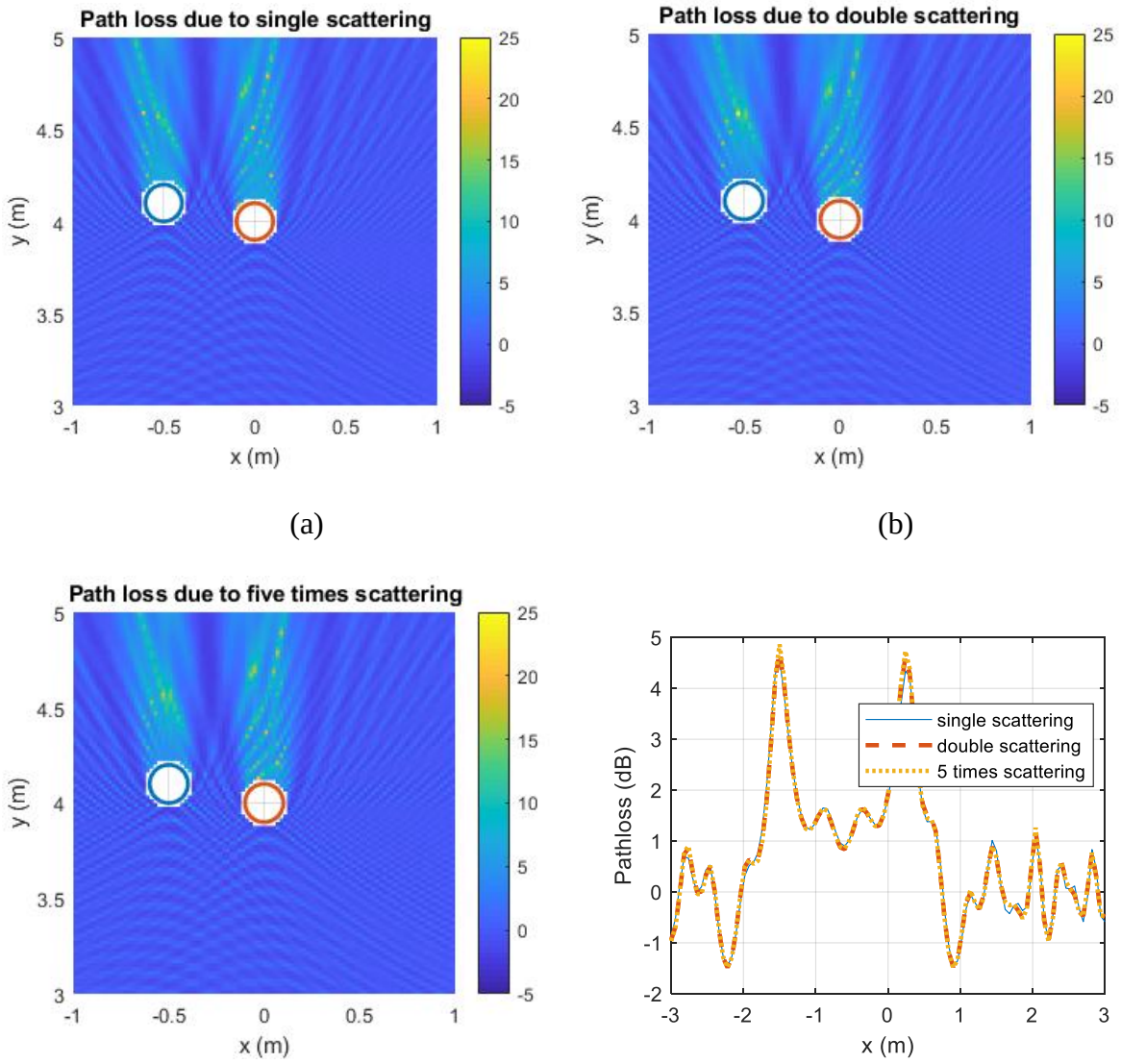

Figure 7.22. path loss of two non-overlapping tree trunks at 5.9 GHz with (a) single scattering, (b) double scattering and (c) five times scattering; (d) the path loss comparison between different orders of scattering at a function of receiver's x position, (y = 10m).

The accuracy of the analytic multiple scattering method is validated with full wave simulation method of moment (MoM). In the example of simulation, the source locates at (0 m, 0 m) and two dielectric cylinders with relative permittivity of (33+10i) and radius of 0.1 m locates at (0 m, 3 m) and (0 m, 4 m), respectively. The receiver's y position is at 10 m, and its x position

is sweeping as depicted in Figure 7.23 (a). The comparison of the pathloss between MoM and the multiple scattering solution at 5.9 GHz is shown in Figure 7.23 (b). It shows that the analytic 5th order solution has excellent agreement with the full-wave solution.

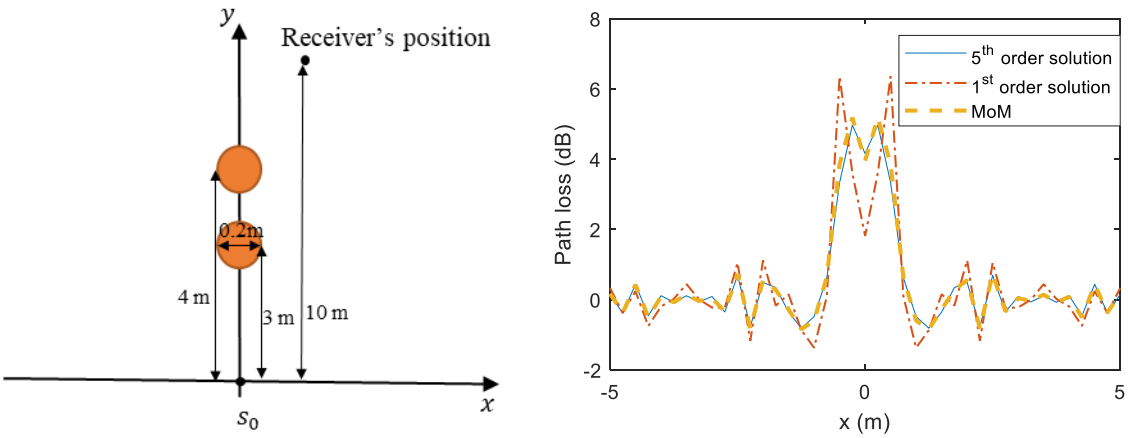

(a) (b)

Figure 7.23. The simulation setup (a) and (b) path loss as a function of receiver's x position comparison between analytic solution and method of moment solution for a two-cylinder scattering problem at 5.9 GHz.

The forest environment demonstrated in Figure 7.5 can be modeled as a random medium with randomly distributed dielectric cylinders. Intuitively, the path loss through this random medium is mainly determined by three parameters: the number density of trees ρ_{tree} (number of trees per m^2), the mean radius of tree trunks $\bar{a}$ and the foliage depth d. Under this complex environment, the path loss should be a random variable, and to analysis the statistical property of the path loss, Monte Carlo simulation are performed. Some examples of randomly generated tree distributions are shown in Figure 7.24. Figure 7.24 (a) depicts the sparse tree distribution with $\rho_{tree} = 0.1/m^2$ and $\bar{a} = 0.1m$, a more dense example is given in Figure 7.24 (b), where $\rho_{tree} = 0.7/m^2$, $\bar{a} = 0.07m$. As a reference, a typical forest in Michigan's Upper Peninsula has $\rho_{tree} = 0.17/m^2$, $\bar{a} = 0.07m$ [207]. The forest in both examples have 20 m by 10 m area, and the trees

are generated with the constraint that any pair of two trees are not too close to each other. Assuming both the transmitter and receiver are one the two side of the trees and are about 10 m away from the trees, e.g. the transmitter locates at (0,0), the trees distributed for y from 10m to 20m and the receivers' y positions are at 30 m. The path loss as a function of receiver's x position for the two randomly generated scenarios in Figure 7.24 are displayed in Figure 7.25. It shows that in the sparse tree environment, double-scattering solution is sufficient to provide an accurate result, but in a dense tree environment, it needs fifth order scattering solution to converge. Therefore, in the Monte-Carlo simulation, the scattered fields are evaluated based on fifth order scattering solutions. It can also be seen that the path loss fluctuates rapidly for a very small change of receiver's position, therefore statistical analysis has to be performed to obtain significant channel model.

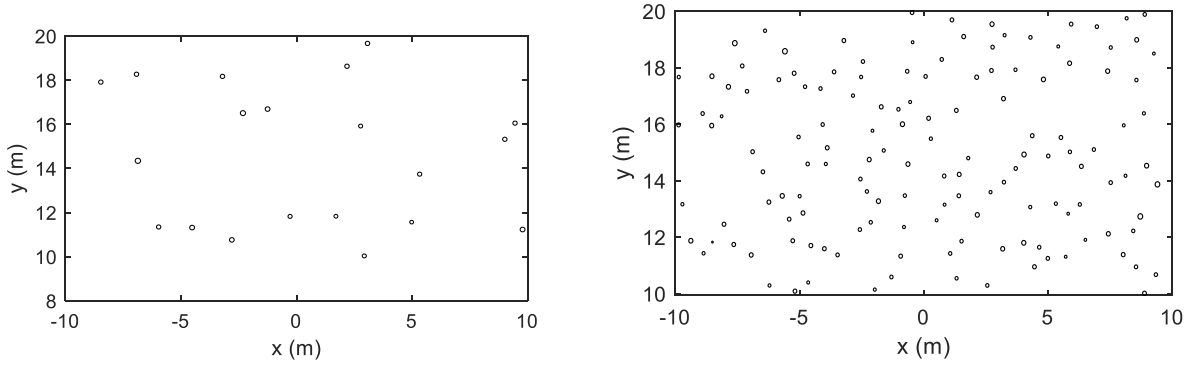

(a) (b)

Figure 7.24. The randomly generate dielectric cylinder distribution for (a) $\rho_{tree} = 0.1/m^2$, $\bar{a} = 0.1m$, $d = 10m$ and (b) $\rho_{tree} = 0.7/m^2$, $\bar{a} = 0.07m$, $d = 10m$.

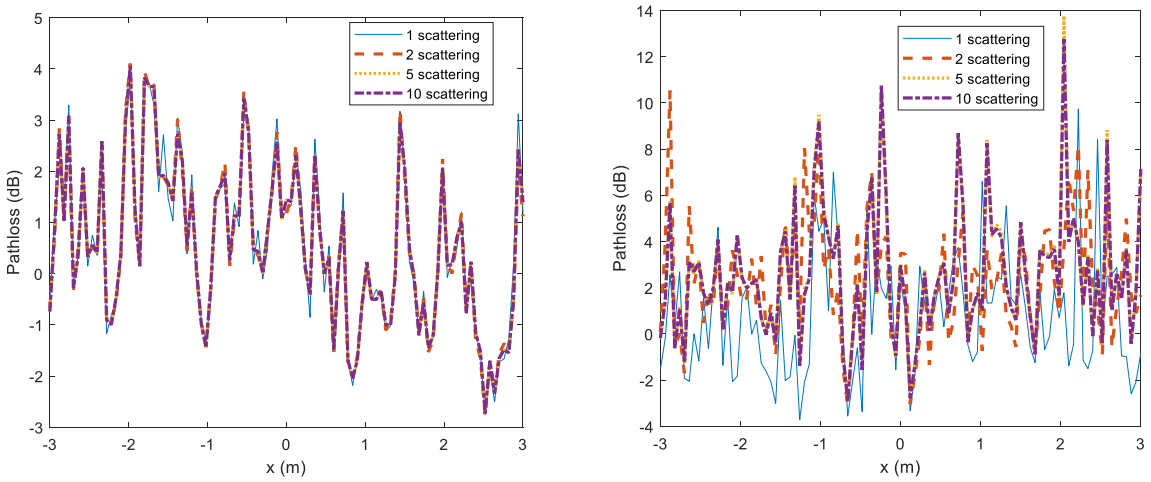

(a) (b)

Figure 7.25. The simulated path loss as a function of receiver's x position (receiver's y position at 30m,and transmitter at (0,0)) with different scattering orders for the trees with (a) $\rho_{tree} = 0.1/m^2$, $\bar{a} = 0.1m$, $d = 10m$ and (b) $\rho_{tree} = 0.7/m^2$, $\bar{a} = 0.07m$, $d = 10m$.

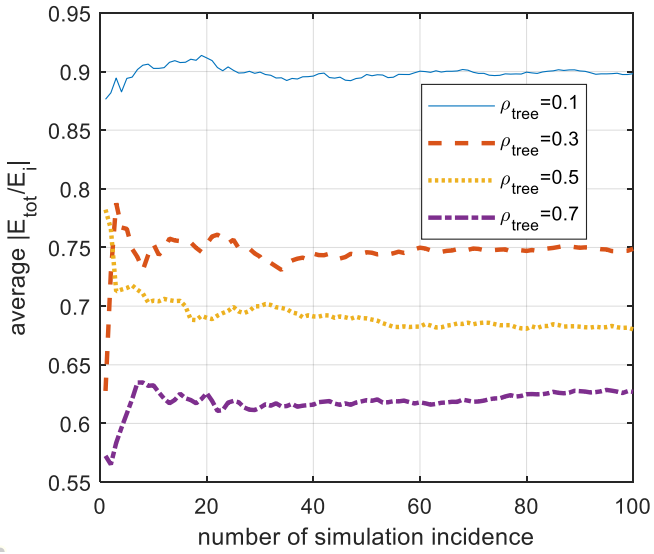

Figure 7.26. The simulated average $|E_{tot}/E_i|$ as a function of number of realizations for different ρ_{tree} and $\bar{a} = 0.07m$, $d = 10m$.

To determine how many realizations are required in the Monte-Carlo simulation, the average received total E field with respect to the incident E field as a function of number of

simulation realizations for different tree density with $\bar{a} = 0.07m$, $d = 10m$. It shows that for all scenarios, the averaged received relative E field or pathloss converges when the number of realizations is greater than 50. Therefore, in the parametric study, 50 realizations are performed for each scenario with different parameters.

The attenuation through the random medium can be considered as a random variable. It is better to find the statistical distribution of the random variable than just mean value and variance to describe the features of the random variable. For the scenario with each parameter, the path loss ($|E_i/E_{tot}|$) is fitted into many known statistical distributions: Gaussian, Lognormal and Weibull distribution. One example of the comparison of the fitting accuracy of different distribution for the path loss is shown in Figure 7.27. Fifty randomly generated forests with $\rho_{tree} = 0.3$, and $\bar{a} = 0.07m$, $d = 12m$ are simulated at 5.9 GHz to obtain the path loss data. The data are fitted to different distributions with linear scale and displayed in dB scale in Figure 7.27. It shows that the Lognormal distribution provides the best fit for the path loss. The PDF of Lognormal distribution is given by:

$$f(x|\mu,\sigma) = \frac{1}{x\sigma\sqrt{2\pi}} exp\left\{-\frac{(\ln x - \mu)^2}{2\sigma^2}\right\}. \tag{7.31}$$

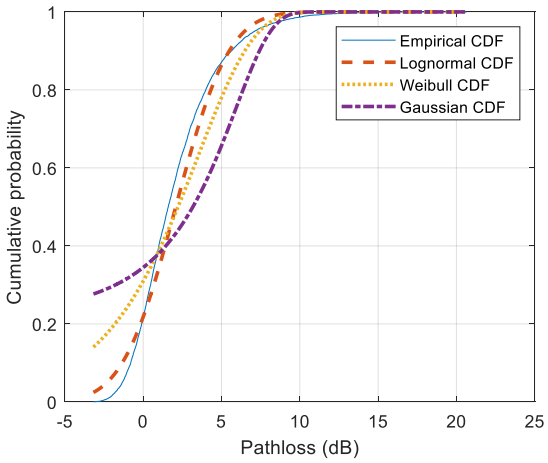

Figure 7.27. The comparison of the empirical CDF and the fitted CDF with Lognormal, Weibull and Gaussian distribution of path loss at 5.9 GHz for the forest with $\rho_{tree} = 0.3$, and $\bar{a} = 0.07m$, $d = 12m$.

Three parameters are considered in this forest V2V communication channel modeling, the tree density, mean tree radius and the foliage depth as mentioned above. To reveal the relation between each parameter and the V2V communication path loss, the control variates method is applied with the Monte-Carlo simulations. Figure 7.28 (a), (b) and (c) shows the Lognormal parameters fitted by the path loss data at 5.9 GHz from Monte-Carlo simulations as functions of foliage depth d, the mean tree radius $\bar{a}$ and the tree density ρ_{tree}, respectively.

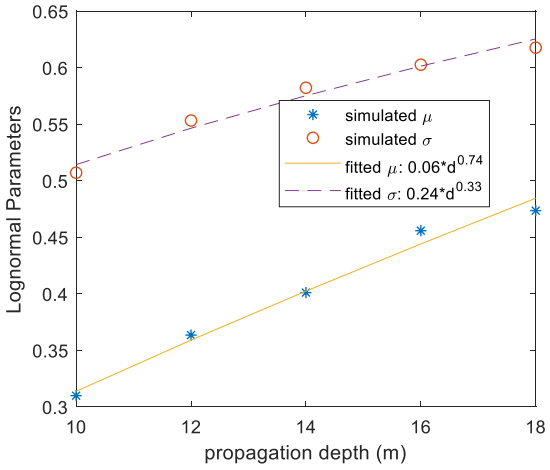

(a)

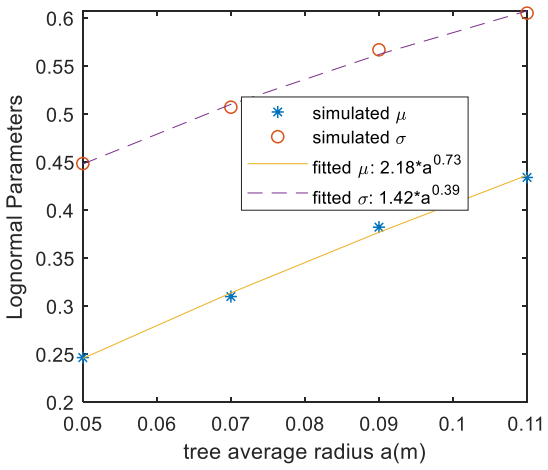

(b)

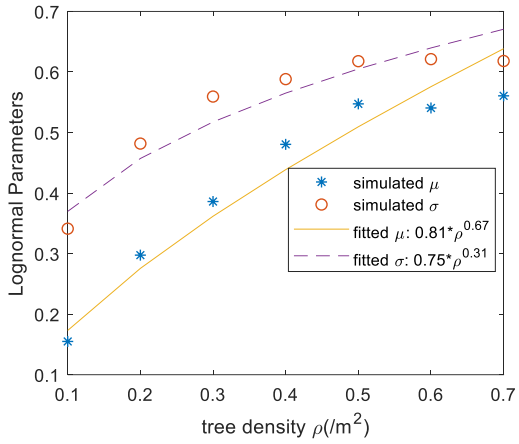

(c)

Figure 7.28. The Lognormal parameters μ and σ of path loss at 5.9 GHz (a) as functions of foliage depth d with $\rho_{tree} = 0.2$, and $\bar{a} = 0.07m$, (b) as functions of mean radius $\bar{a}$ with $\rho_{tree} = 0.2$ $d = 10m$ and (c) as functions of tree density ρ_{tree} with $\bar{a} = 0.07m$, $d = 12m$.

In this preliminary study, the Monte-Carlo simulations are performed for ρ_{tree} from 0.1 per m^2 to 0.7 per m^2, $\bar{a}$ from 0.05 m to 0.11 m and d from 10 to 18 m. Both the lognormal parameters μ and σ are fitted into the following expressions:

$$y = \beta_1 a^{\beta_2} d^{\beta_3} \rho^{\beta_4}, \quad y = \mu \text{ or } \sigma. \tag{7.32}$$

The mean path loss of the lognormal variable is given by:

$$\overline{PL} = \exp(\mu + \sigma^2/2). \tag{7.33}$$

After fitting to the simulated data, the values for β_0 to β_4 are given in Table 7 - 1, and the fitting performance is shown in Figure 7.29. It shows that the model has a reasonable accuracy to predict the statistical parameters of the tree trunks' path loss for vehicle communication.

Table 7 - 1. Fitted coefficient for the empirical model of μ and σ at 5.9 GHz

Parameters	β_1	β_2	β_3	β_4
Lognormal μ	0.868	0.484	0.514	0.537

Lognormal σ	0.71	0.232	0.273	0.226

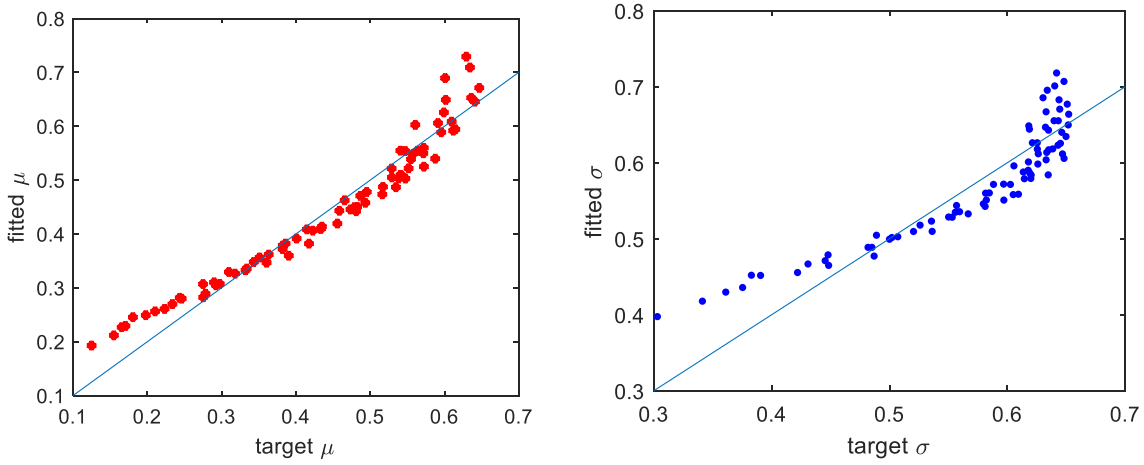

(a) (b)

Figure 7.29. The fitting performance of the empirical models for the Lognormal parameters (a) μ and (b) σ of path loss at 5.9 GHz.

7.7 Conclusion

In this paper, we provided an analytical free-space propagation model and semi-exact semi-closed-form scattered field expressions are derived for the far-field as well as near-field range of a single trunk and multiple scattering between trunks in V2V foliage propagation. The proposed path loss model is verified by full-wave solver and reciprocity.

Extensive numerical simulations on the scattered fields were carried out at 5.9 and 60 GHz. Then, we developed ANN curve-fitting model for the path loss of single trunk or any other cylindrical object, mainly as a function of the radius and length of trunk, distance of transmitter, distance and azimuth angle of receiver. The ANN curve-fitting model shows high accuracy with the numerical results. In a multiple-trunk scenario, the path loss is modeled as a Lognormal random variable. Finally, we extracted a macro-model for the total field of V2V foliage propagation, which

can be integrated as a useful tool to efficiently and accurately analyze real-time mmWave channel quality in vehicular communications.

A multiple-scattering model for tree trunks is developed to obtain the path loss in forest environment in the chapter as well. The

Appendix – A: Scattered *E* field of a cylinder in the far field region

Let the length of a cylinder to be *b* and the radius to *a*, the position of the current on the cylinder's surface is defined as,

$$\vec{r}' = a\cos\phi'\hat{x} + a\sin\phi'\hat{y} + z'\hat{z}. \tag{7.34}$$

The integral term Υ in (7.9) is given by,

$$\Upsilon = \int_{-\pi}^{\pi} \left[Z_0\vec{J}_\rho(a,\phi') - \hat{k}_s \times \vec{J}_{m\rho}(a,\phi')\right] e^{-ik_0\hat{k}_{s\rho}\cdot\vec{\rho}'} a d\phi' \tag{7.35}$$

where $\vec{J}_\rho(a,\phi')$ and $\vec{J}_{m\rho}(a,\phi')$ in TM case can be derived by,

$$\vec{J}_\rho(a,\phi') = \sum_{n=-\infty}^{\infty} e^{in\phi}(J_{snz}\hat{z} + J_{sn\phi}\hat{\phi}), \tag{7.36}$$

$$\vec{J}_{m\rho}(a,\phi') = \sum_{n=-\infty}^{\infty} e^{in\phi}(J_{mnz}\hat{z} + J_{mn\phi}\hat{\phi}). \tag{7.37}$$

Each term of the current with order n, $J_{snz}, J_{sn\phi}, J_{mnz}$ and $J_{mn\phi}$ are given by,

$$J_{snz} = i\omega\varepsilon_1 C_n k_{1\rho} J_n'(k_{1\rho}a), \tag{7.38}$$

$$J_{sn\phi} = 0, \tag{7.39}$$

$$J_{mnz} = -\frac{nC_n k_z}{a} J_n(k_{1\rho}a), \tag{7.40}$$

$$J_{mn\phi} = C_n k_{1\rho}^2 J_n(k_{1\rho}a), \tag{7.41}$$

where $\omega = 2\pi f$, ε_1 is the permittivity of the dielectric cylinder, C_n is given in (7.8) and $k_{1\rho}$ denotes the wavenumber in azimuth direction inside the cylinder, J_n and J_n' are the Bessel function of the first kind and its derivative with order of n.

To solve the integral Υ, we can first separate the *x*, *y* and *z* components:

$$\Upsilon = \Upsilon_x \hat{x} + \Upsilon_y \hat{y} + \Upsilon_z \hat{z}. \tag{7.42}$$

After lengthy algebra, each component of Υ is given by,

$$\Upsilon_x = 2\pi a \sum_{n=-\infty}^{\infty} e^{in\phi_s} i^n (Z_0 J_{sn\phi}(-I_{n\sin}) - k_{sy} J_{mnz} J_n(-k_{\rho s} a) + k_{sz} J_{mn\phi} I_{n\cos}) \tag{7.43}$$

$$\Upsilon_y = 2\pi a \sum_{n=-\infty}^{\infty} e^{in\phi_s} i^n (Z_0 J_{sn\phi}(I_{n\cos}) + k_{sx} J_{mnz} J_n(-k_{\rho s} a) + k_{sz} J_{mn\phi} I_{n\sin}) \tag{7.44}$$

$$\Upsilon_z = 2\pi a \sum_{n=-\infty}^{\infty} e^{in\phi_s} i^n (Z_0 J_{snz} J_n(-k_{\rho s} a) - J_{mnz}(k_{sx} I_{n\cos} + k_{sy} I_{n\sin})) \tag{7.45}$$

where $k_{\rho s} = k \sin\theta_s$, and $I_{n\sin}$, $I_{n\cos}$ are given by,

$$I_{n\cos} = -i\cos\phi_s J_n'(-k_{\rho s} a) + \frac{n \sin\phi_s}{k_{\rho s} a} J_n(-k_{\rho s} a), \tag{7.46}$$

$$I_{nsin} = -i\sin\phi_s J_n'(-k_{\rho s} a) - \frac{n \cos\phi_s}{k_{\rho s} a} J_n(-k_{\rho s} a), \tag{7.47}$$

Appendix – B: Surface current of a cylinder with spherical wave incidence

Spherical wave with center at $\vec{r}'$ and observation point at $\vec{r}$ can be expanded as an integral of cylindrical wave times a plane wave in z direction by Sommerfeld identity:

$$\frac{e^{ik|\vec{r}-\vec{r}'|}}{|\vec{r}-\vec{r}'|} = \frac{i}{2}\int_{-\infty}^{\infty} dk_z e^{ik_z(z-z')} H_0^{(1)}(k_\rho|\vec{\rho}-\vec{\rho}'|). \tag{7.48}$$

where $k_\rho = \sqrt{k^2 - k_z^2}$. Then the incident E field on the surface of trunk can be expressed as a summation of different cylindrical eigen-modes:

$$E_{iz}^{TM}(\rho,\phi,z)=\frac{Ai}{2}\int_{-\infty}^{\infty}\frac{dk_z e^{ik_z(z-z')}k_\rho}{k_0}\sum_{n=-\infty}^{\infty}H_n^{(1)}(k_\rho\rho')J_n(k_\rho\rho)e^{in(\phi-\phi')}. \tag{7.49}$$

where A is some constant related to the transmitted power. By applying boundary conditions for all eigen-modes and following the similar procedure for plane wave incidence, equivalent surface currents can be derived:

$$\vec{J}_s^{TM}(a,\phi,z)=-\frac{\omega\varepsilon_1 A}{2}\int_{-\infty}^{\infty}[dk_z e^{ik_z z}\frac{k_\rho}{k_0}\sum_{n=-\infty}^{\infty}C_n' k_{1\rho}J_n'(k_{1\rho}a)e^{in\phi}\hat{z}], \tag{7.50}$$

$$\vec{J}_m^{TM}(a,\phi,z)=-\frac{iA}{2}\int_{-\infty}^{\infty}dk_z e^{ik_z z}\frac{k_\rho}{k_0}[\frac{k_z}{a}\sum_{n=-\infty}^{\infty}nC_n'J_n\,(k_{1\rho}a)e^{in\phi}\hat{z}$$

$$+k_{1\rho}^2\sum_{n=-\infty}^{\infty}C_n'J_n\,(k_{1\rho}a)e^{in\phi}\hat{\phi})]. \tag{7.51}$$

where C_n' is given by:

$$C_n'=\frac{H_n^{(1)}(k_\rho\rho')e^{-in\phi'}k_\rho}{k_{1\rho}^2}\frac{H_n^{(1)}(k_\rho a)J_n'(k_\rho a)-H_n^{(1)\prime}(k_\rho a)J_n(k_\rho a)}{k_{1\rho}H_n^{(1)}(k_\rho a)J_n'(k_{1\rho}a)-k_\rho H_n^{(1)\prime}(k_\rho a)J_n(k_{1\rho}a)}, \tag{7.52}$$

Chapter 8 A Compact Broadband Horizontally Polarized Omnidirectional Antenna using Planar Folded Dipole Elements

8.1 Introduction

Omnidirectional antennas are widely used in mobile and wireless communication devices, such as cellphone base stations, WLAN routers and many portable devices. Since the bandwidth of antenna directly determines the data rate of communication, to satisfy the requirements for higher data rate and multiple-band communication, the system's antenna bandwidth also needs be largely increased. For example, the 5G network in the near future (around 2020) is expected to have peak data rate of 10 Gb/s for low mobility and 1Gb/s for high mobility nodes [215]. LTE in the mobile communication has more than 20 different frequency bands for different regions and carriers ranging from 698MHz to 960MHz (31.6%) and 1710MHz to 2690MHz (44.6%) [216]. In both cases wider bandwidth antennas are required. Also to improve the data rate, different diversity schemes, such as polarization and pattern diversity, broadband systems are being considered[217][218][219][220]. Other emerging applications are multistatic all-direction imaging radar systems that require omni-directional broadband antennas [221][222]. Usually, vertically polarized antennas, such as broadband biconical and mono-conical antennas, are used for these systems because of their simple structure and good omnidirectional radiation pattern. However, for more advanced communication and radar applications where polarization diversity is considered, a horizontally polarized (HP) omnidirectional antenna is also required to obtain higher efficiency in communication system and improved isolation between transmit and receive antennas in imaging radar systems.

Theoretically, loop antennas can generate good omnidirectional horizontal polarization since they are equivalent to magnetic dipoles (vertical magnetic current). However, small magnetic loop antennas provide very limited bandwidth. One design of this kind is the Alfred loop antenna [59][60], which provides less than 6% bandwidth. In [61], a MNG-TL loop antenna and its array are introduced. This antenna can generate good omnidirectional horizontally polarized (HP) radiation pattern, but its impedance bandwidth is less than 10% for a single element. A loop antenna with loaded capacitors and inductors is presented in [62]. It has multiple resonant frequencies with bandwidth less than 3% for each band. In [63], a segmented loop antenna is proposed, which has a -10 dB return loss bandwidth of less than 10%. Recently, many wider bandwidth omnidirectional HP antennas have been reported in the literature. A loop antenna with periodically capacitive loading is shown in [223]. This antenna is reported to have 31.2% bandwidth (2.17 to 2.97 GHz). Other than loop antennas, multipole broadband linearly polarized elements arranged in different orientations are proposed to achieve wider bandwidth. In [64], an antenna is proposed that contains four printed arc dipoles to form a circular shape, and provides a bandwidth of 31% (1.66 to 2.27 GHz). This antenna has a good omnidirectional property with gain variation less than 1.5 dB. A design using four printed pairs of flag-shaped dipoles with parasitic strips as radiators is presented in [65]. This antenna targets 4G LTE band with bandwidth of 41% (1.76 to 2.68 GHz). Parasitic strips are added to the antenna to obtain the reported bandwidth at the expense of increasing the antenna dimension ($0.59\lambda \times 0.59\lambda$, λ is for the lowest frequency of operation). Also azimuthal gain variation increases at high frequency portion of the operational band. Another design using four pairs of wide arc dipole is shown in [66]. This antenna is reported to have 34.1% bandwidth for one element, with peak gain of 1.7dBi. It is also shown that, by stacking the four-element array vertical direction, the gain can be increase to 7.2 dBi. These

antennas have significant bandwidth improvement compared to the traditional HP loop antenna, but their bandwidth is limited to about 40% or less. In [67], an 8-element omnidirectional array antenna is reported. It has 8 dipole elements printed on octagonal substrate. It has very wide bandwidth (62.5%), with the drawback of having a larger dimension ($0.79\lambda \times 0.79\lambda$, where λ is the wavelength at the lowest frequency of operation) and much higher gain variations of about 4.5 dB.

This paper reports on a compact HP omnidirectional antenna with an almost octave bandwidth. It is composed of four modified folded dipole antennas arranged around the perimeter of a small square box. The antenna presents a smaller form factor compared to other wideband HP omnidirectional antennas (size of $0.34\lambda \times 0.34\lambda$), while maintain a relatively low gain variation as a function of azimuth angle in the band of operation. The folded dipole antenna is chosen since it is reported to have a fractional bandwidth that can exceed 50% [68]. To compensate for the mutual coupling of different dipole elements and increase the bandwidth, some geometric modifications are made and analyzed. Four identical dipole elements are fed with microstrip baluns and connected by an appropriate matching network to a coaxial feed. The matching network, the baluns, and the geometrical modification of the elements are co-designed to mitigate the mutual coupling effects and achieve the required bandwidth while minimizing the antenna array dimension. Their distances are carefully chosen to achieve best omnidirectional property. The antenna's geometry, its principle of operation and its parametric study are discussed in Section II. The fabrication and the measurement results for return loss and radiation pattern are presented in Section III.

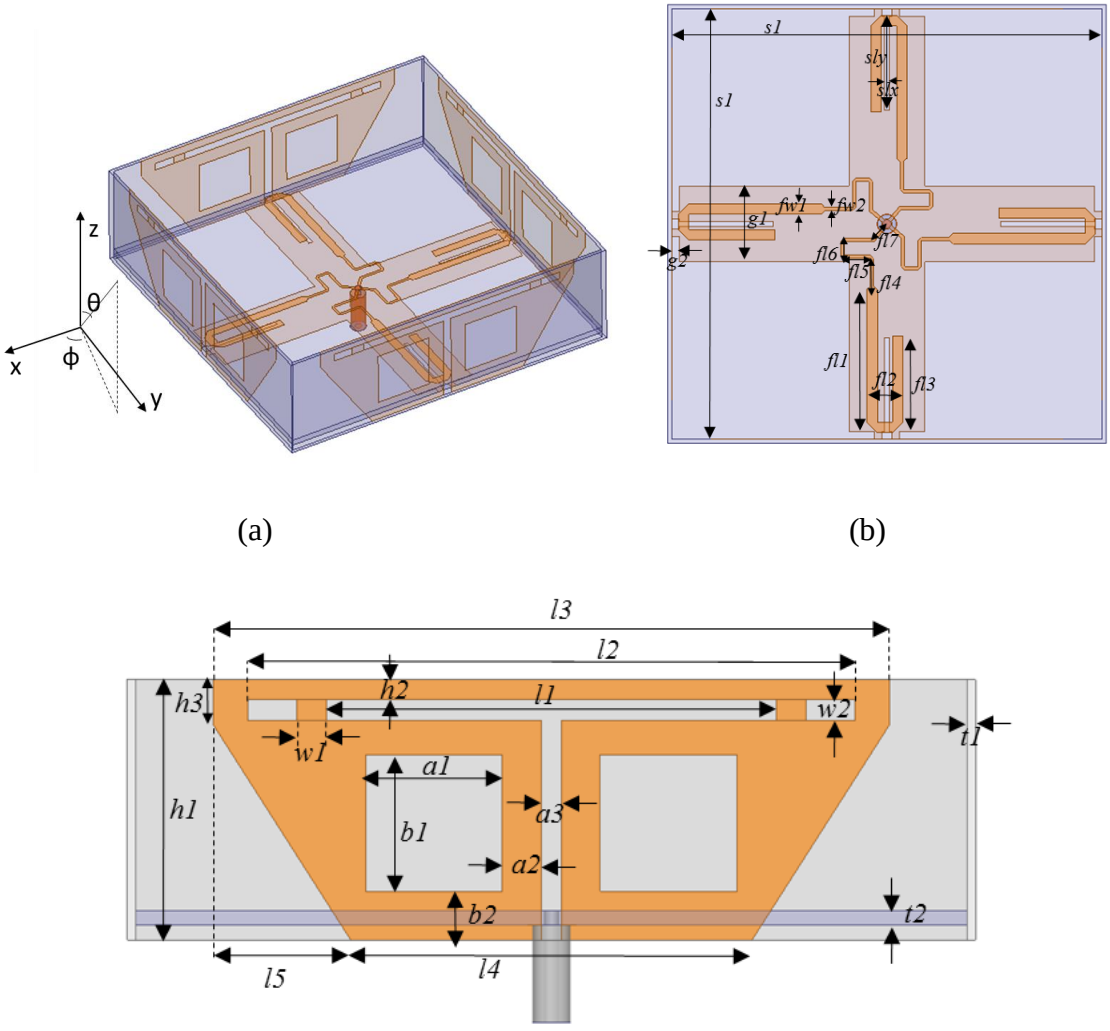

(a) (b)

(c)

Figure 8.1. Structure of the proposed antenna (a) overview, (b) top view, and (c) side view.

8.2 Antenna Architecture and Design

8.2.1 Antenna configuration

The structure of the proposed wideband, omni-directional, and horizontally polarized antenna is shown in Figure 8.1. The proposed antenna consists of an array of four modified folded dipole antennas and one feeding network with incorporated baluns. The geometry of the antenna is an open square box with four modified folded dipole elements on the side faces and baluns and

matching network on the bottom face. Both the antenna elements and the baluns are printed on Rogers RO4003C substrate ($\varepsilon r = 3.55$, $\tan\delta = 0.0027$).

The operation of the proposed antenna can be best explained by examining the performance of the elements of the square array. The folded dipoles are placed in the horizontal plane along the x- and y-axis to achieve horizontally polarized radiation. Each dipole is expected to have radiation null along the dipole axis with an approximate radiation pattern proportional to sine-squared function. The radiation patterns of the orthogonal elements, because of 90ºrotation, are hence proportional to cosine-squared function and as a result an omnidirectional radiation pattern is expected if the elements are fed equal in magnitude and phase or 180ºout of phase. The antenna can be viewed as two two-element arrays that are perpendicular to each other. Considering a pair of face-to-face antenna elements as one array, it becomes obvious that the two elements of this array should be positioned with a separation of about $\lambda/2$ and fed with the same power but 180º out of phase. This way the lateral dimension of the antenna is kept small and the far fields of the two elements at their respective boresights add up coherently. Another artifact of this arrangement is the creation of a null surface at the perpendicular bisector plane of the two elements which includes the z-axis. This is a desired feature as it allows the placement of the feed network on or near the perpendicular bisector plane without the mutual effect between the antenna elements and the feed network of the other pair.

8.2.2 Dipole elements' separations study

The radiated far-field from two parallel elements add up coherently in the boresight direction in case the separation between the two elements is 0.5λ. However, at other azimuthal angles, say at 45 degree offset from the boresight, there is no intuition about the azimuthal gain

deviation from its value at the boresight directions. The gain variation should be a function of elements' separation distance. To study the effect antenna separation and finding an optimal distance for best omnidirectional radiation pattern a simple analytical model for the square shape arrangement of dipole array is constructed. For simplicity, the model uses simple half wave dipole for each array element for which a sinusoidal current distribution is assumed. For this array the far field radiation pattern is calculated analytically using superposition. Figure 8.2 depicts the calculated radiation pattern for different separation between parallel dipole elements. In this simulation the antenna size is chosen to be 0.4λ and the separation between parallel dipoles is changed from 0.4λ to 0.6λ. It is shown that the smaller is the distance between the parallel antenna elements, the lower is the pattern variation as a function of azimuthal angle. Therefore, in order to achieve a better omnidirectional pattern from the square array, it is better to keep the separation as small as possible while adjusting the phase between the elements. In practice, there are two factors constraining the minimization of antenna separation. The first pertains to mutual coupling between the elements which increases with decreasing the separation and the second factor is related to the antenna size. Basically, making radiating elements small, the bandwidth becomes small [224][225]. After many simulations for minimizing the distance between elements while maintaining the bandwidth, the distance is chosen to be 85 mm, which is about 0.45λλ for the designed center frequency 1.6GHz. Figure 8.3 shows the return loss comparison for different separation distances. As we can see, if the distance is smaller than 85mm, it is very difficult to get the entire band below -10dB for S11.

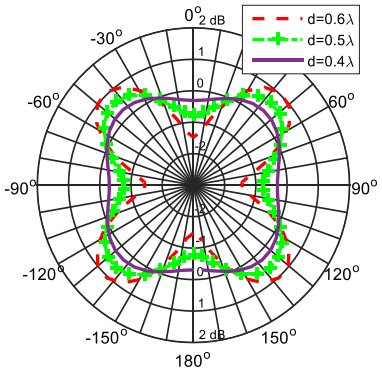

Figure 8.2. The calculated radiation pattern comparison for different distance between opposite antenna elements for idea half wavelength dipole.

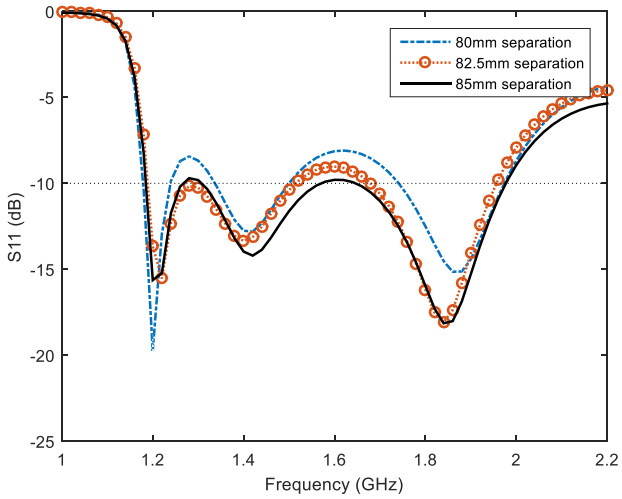

Figure 8.3. The simulated return loss for the antenna with different elements separation distances. Matching networks for all cases are optimized separated.

8.2.3 Modified folded dipole design and parametric study

To achieve a broadband operation, array elements themselves must be broadband. Folded dipole structure can provide higher bandwidth than ordinary dipoles, but such structure still does not provide the required bandwidth. The planar folded dipole antenna (PFDA) is chosen as radiation element because of its wide bandwidth (more than 50%), and its radiation pattern is very similar to that of an ordinary dipole antenna. The antenna can be considered as the superposition

of one wide-strip planar dipole and one folded dipole with different resonant frequencies which produce wider bandwidth [82]. One drawback of this geometry for the application at hand is the size of the elements. This prohibits designing the square array in a plane. To keep the spacing between the elements as small as possible, the PFDA elements are arranged in vertical direction, unlike the arrays used in [64]-[67], in such a way as to form a square box with each element on its four sides (see Figure 8.1).

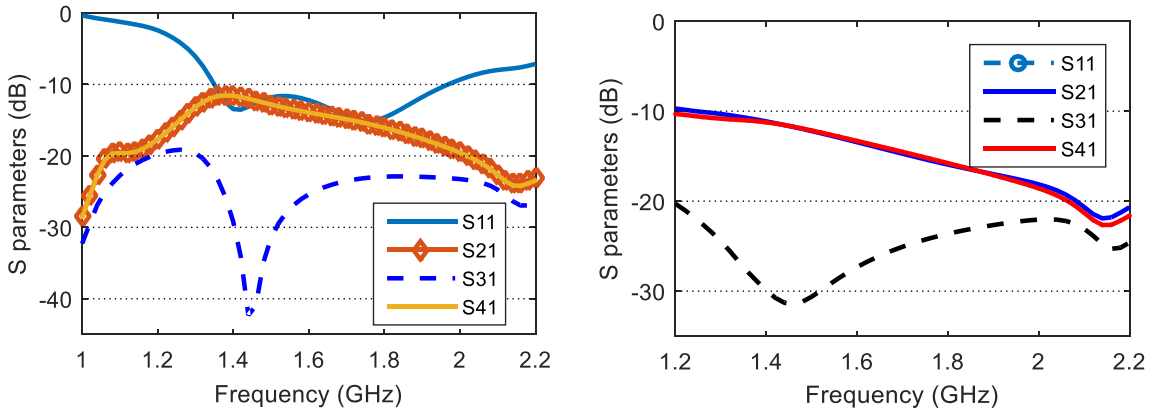

(a) (b)

Figure 8.4. S parameters for the four ordinary folded dipole antennas before matching network with (a) source impedance of 50 Ω, (b) source impedance equal to complex conjugate of input impedance of one element; S11 is below -35dB and not shown in (b).

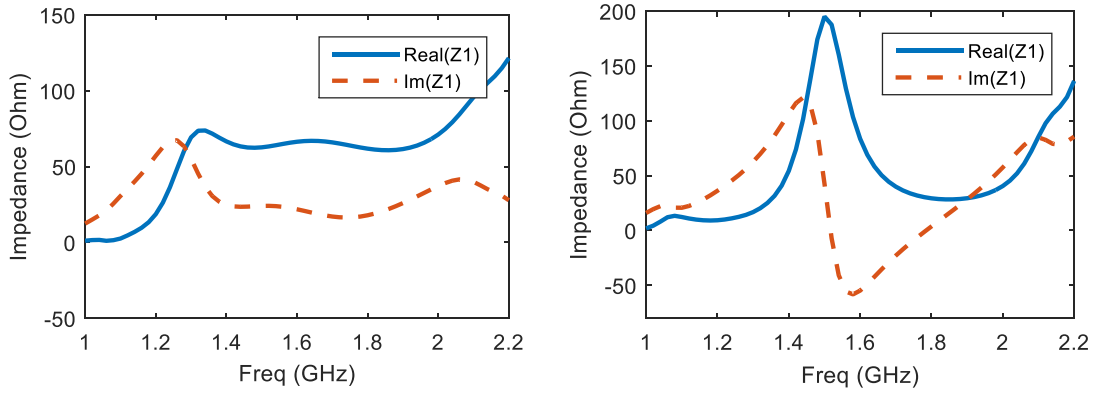

(a) (b)

Figure 8.5. The simulated impedance as a function of frequency for (a) a folded dipole in the array when other elements are terminated by 50 Ω (without returning power from other ports), and (b) a folded dipole when all other dipoles are also fed with the same power.

With the vertical architecture, the required spacing between parallel elements can be met; however, the vertical arrangement leads to increased mutual coupling among the four elements of the array. In arrays, high level of mutual coupling in turn results in performance degeneration of the antenna array [226]. To examine the effects of mutual coupling for the proposed geometry, the array is viewed as a four-port antenna where each port is connected to the input of the balun for each planar folded dipole element (the matching network is not considered here). The simulation is carried out using a commercial software (ANSYS HFSS). Figure 8.4 (a) shows the simulated S parameters for the four folded dipole antennas with the shape proposed in [82] choosing a source impedance of 50Ω. The port numbering is as follows: dipole 1 is adjacent to dipole 2 and 4, and opposite to dipole 3. Note that since the matching network is not part of the simulation, the condition for broadband operation is sought for by finding a smooth impedance response with frequency. As shown in Fig. 4, S21 and S41 are comparable to S11 at certain frequencies, which indicates a high level of the mutual coupling between adjacent elements.

Moreover, to examine the mutual coupling effect more accurately, another simulation is carried out in which the port impedance is chosen to be the complex conjugate of the antenna element for all frequencies. Under this ideal condition, S11 disappears and the parameters S21, S31 and S41 represent the coupling coefficients and are shown in Figure 8.4 (b). It can be seen that the coupling between adjacent elements is much higher than those between opposite elements. It should be noted that S21 and S41 are supposed to identical and the observed differences are due to numerical errors caused by asymmetric meshing of the geometry. The power from dipole 1 to dipole 2 and 4 is about -10 dB at 1.2GHz and decreases monotonically with frequency to a level of -18dB at 2GHz. This coupling phenomenon has a considerable effect on the overall return loss.

Before we solve this complex four ports coupling problem, let us simplify it first. The four dipole-elements are treated equally, and their radiation patterns are supposed to be symmetrical, so it means the four dipoles and their matching network should be identical. Thus, the matching of the four ports problem is equivalent to the matching of one port problem assuming that all other ports are fed identically (same source and same source impedance). The return loss for one port in this case is the sum of S11, S21, S31 and S41, as it considers the returning power from all other elements. To examine the effect of mutual coupling another simulation where one port is excited and other ports are matched to 50 Ω loads is also carried. The input impedance for this case will be referred to as "without returning power from other ports". Figure 8.5 shows the impedance comparison for the antenna with and without considering the returning power from other ports. When the coupling is included (all four ports excited) the impedance of the antenna shows sharp variations with frequency, and this of course leads to strong mismatch at certain frequencies which makes the task of broadband matching very difficult if not impossible. It is noted that the overall return loss behavior is influenced by the impedance mismatch of the antenna element itself and the mutual coupling among the elements. In the other words, the total return loss consists of the power returning from each antenna element, and the power coupled from one element to all other elements. In the four-port model mentioned above, those power are corresponding to the four S parameters. Notices that S parameters are all complex numbers and the total return loss is the sum of the phasors. So reducing all the four returning power is not the only way to reduce the total return loss, if we can change the S parameters such that they cancel each other over the desired band, then a low overall return-loss can be achieved.

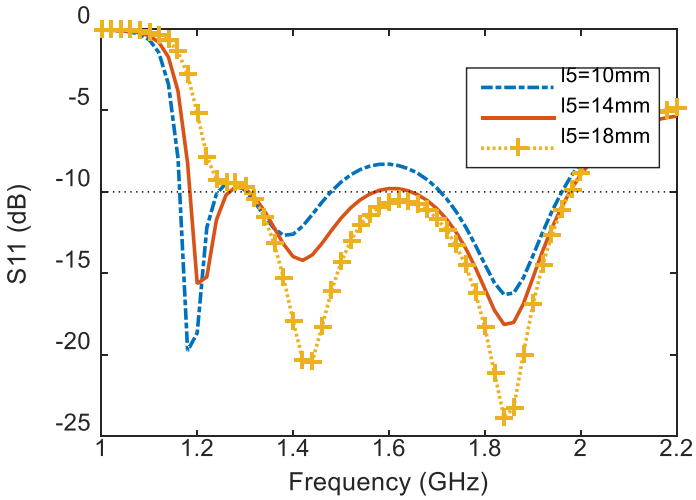

Figure 8.6. The simulated return loss for the antenna with different truncated corner's sizes, is the horizontal length of the corner.

Without increasing the distance between the elements, there is little that can be done to reduce this coupling unless the element configuration itself can be changed. However, changes in the element configuration can affect the input impedance as well. Therefore, to achieve a wideband operation, a configuration must be considered such that the variation in the impedance of the dipole elements as a function of frequency is compensated for by the frequency variations of the mutual coupling. One way to reduce coupling is to increase the separation between the edges of the adjacent elements. This can be done by tapering the edges of the ground planes, and by this approach the length of the dipoles and the distance between the elements can be preserved. This also to some extent allows for controlling the frequency response of the coupling simply by changing the tapering angle. The simulated S11 for the entire antenna with different corner taper angle is shown in Figure 8.6. Here $\ell 5$, referring to Figure 8.1(c), is varied to control the taper angle. $\ell 5 = 14mm$ is chosen since it can provide the widest bandwidth. Then other parameters of the folded antenna are further tuned to achieve a wider bandwidth for the array. Figure 8.7 shows the impedance of an optimized folded dipole with other elements terminated to match load (not considering the returning power coupled from other ports) and the impedance for a dipole antenna

when all ports are fed, which is of course four times of the entire antenna's impedance before matching. All tuning and optimizing process is done by trial and error. It is shown that although the impedance of a single element still varies sharply with frequency, the overall impedance of the four elements connected together has less variations with frequency. For more clear comparison, Figure 8.8 shows the return loss of the antenna in Smith Chart after considering the matching network for both the ordinary folded dipole elements and the modified dipole elements. We can observe that the bandwidth for the ordinary folded dipole array is only about 130 MHz, by contrast, the bandwidth for the modified dipoles is reached to about 800MHz.

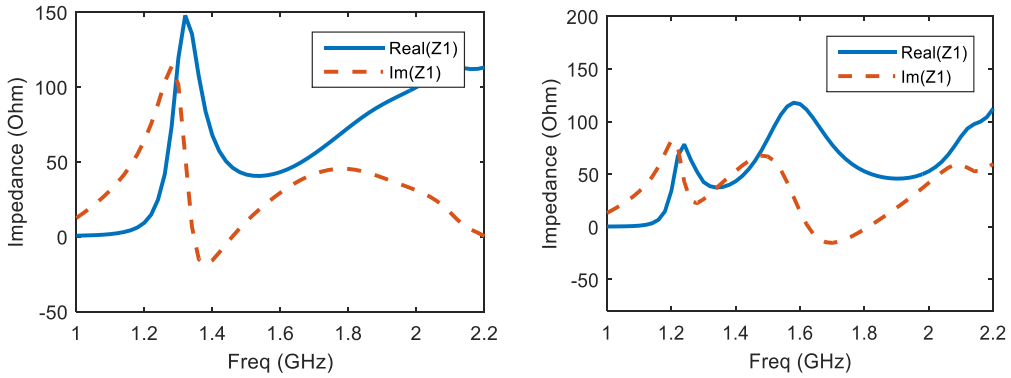

(a) (b)

Figure 8.7. The simulated impedance as a function of frequency for (a) one modified folded dipole antenna with other elements terminated to match load, and (b) one modified folded dipole antenna when other elements are fed with equal power.

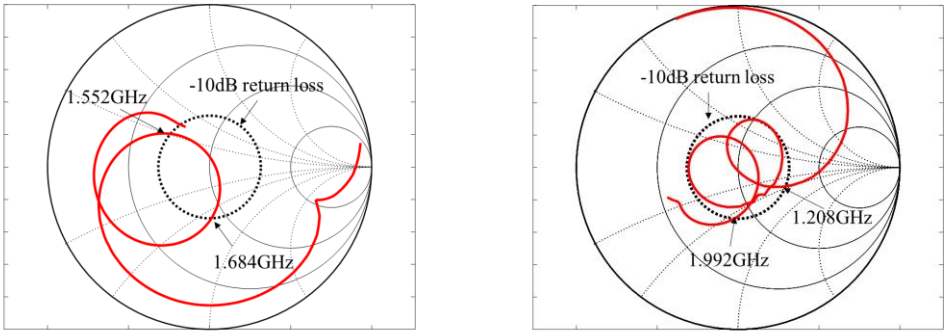

(a) (b)

Figure 8.8. The simulated S11 in Smith Chart of the HP antenna with (a) ordinary folded dipole, (b) modified structure folded dipole.

To keep the S11 below -10 dB for the entire band, other modifications are made to the PFDA including open windows on the ground planes of each element and providing inductive short circuits towards the end of the slot lines. To cut out windows in the ground plane with minimal effect on the antenna performance, the current distribution on the ground plane should be studied. The areas with lowest current density can be cut out to lower the multi-reflection of waves within the square box. Figure 8.9 (a) shows the current distribution over an ordinary PDFA at the center frequency. It is shown that the current density is high around the slot and near the edges. This suggests that the metal in the middle of the ground plane on each side of the feed can be removed with minimal effect on the input impedance and antenna radiation. Figure 8.9 (b) depicts the current distribution over the modified PDFA. Figure 8.10 shows the two return loss results for the antenna with and without windows. It is shown that the windows can help reducing the return-loss at certain frequencies within the band. The location of the two short circuits in the slot determines the frequencies of all the resonances. Figure 8.11 shows the return loss comparison for different shorts' locations. It is shown that when the distance between two shorts becomes smaller the first and third resonant frequencies become higher while the second resonance shifts to lower frequency. The current density distributions at different resonant frequencies are shown in Figure 8.12. It is noted that at the first and third resonant frequencies, the current is mainly concentrated around the edge of the slot, thus when the slot becomes shorter, the resonances shift to higher frequencies because of the shorter current path. For the second resonance the current leaks out further due to the inductive nature of the short to produce the second resonance. After optimization, $\ell_1 = 52mm$ is selected as the distance between two shorts.

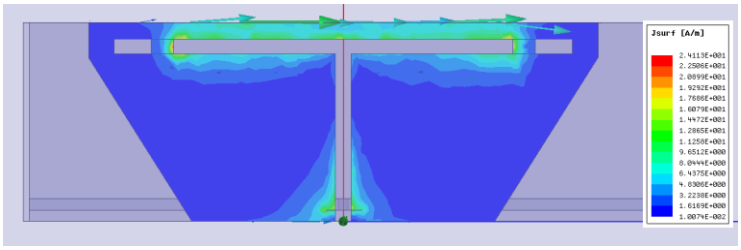

(a)

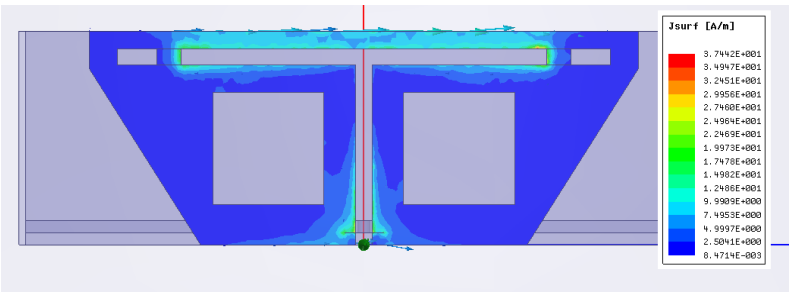

(b)

Figure 8.9. The current distribution on the dipole elements at the center frequency of the frequency band (1.6GHz) for (a) no windows, (b) with windows.

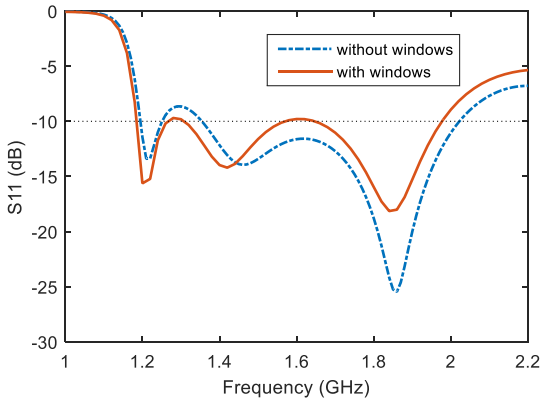

Figure 8.10. The simulated return loss for the antenna with windows and without windows at the center frequency (1.6GHz).

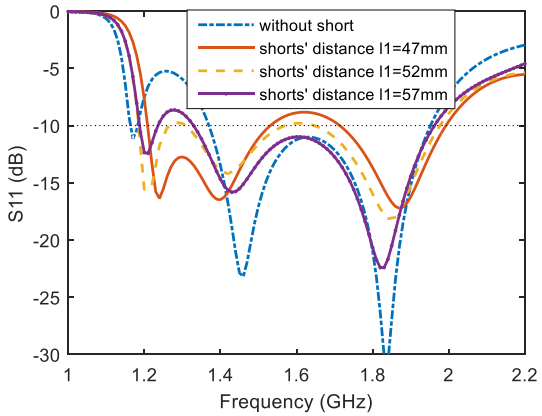

Figure 8.11. The simulated return loss of the antenna for different distance between two shorts.

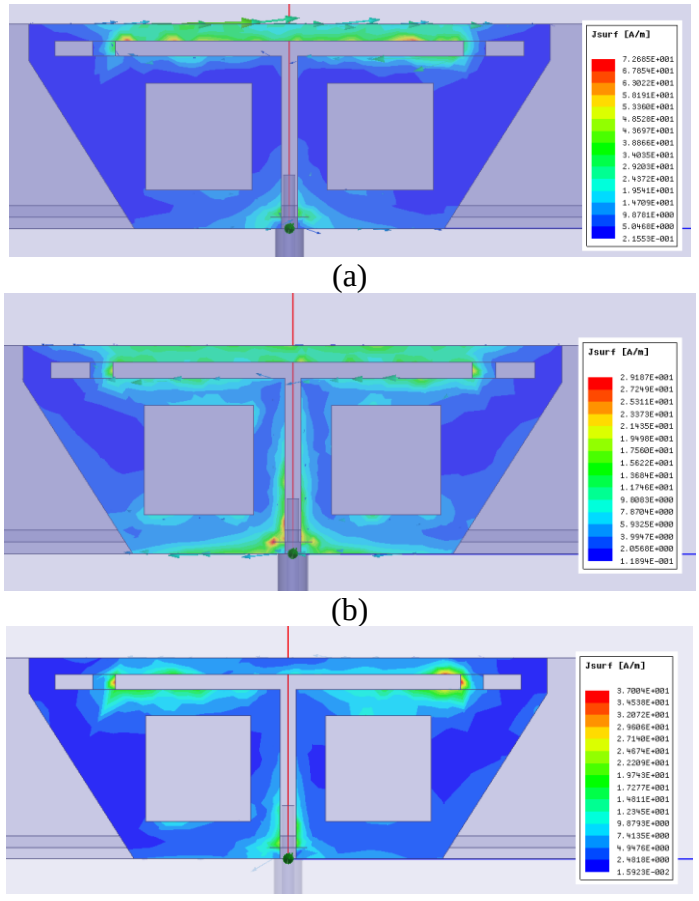

(a)

(b)

(c)

Figure 8.12. The current density distribution at (a) first resonance (1.22GHz), (b) second resonance (1.45GHz), and (c) third resonance (1.85GHz).

8.2.4 Baluns and matching network

The baluns and matching network are shown in Figure 8.1 (b). The balun used here is a classical broadband microstrip balun used for many applications [227][228]. The challenge here is to design balun that can also match the input impedance of the antenna over the desired wide band and can combine the four elements into a single port which is matched to a 50Ω coaxial line. This balun is also to achieve the desired 180^{o} phase shift between the parallel elements. The 180^{o} phase shift is conveniently achieved by choosing opposite directions for the microstrip crossings over the slots. The matching of microstrip to the antenna element is accomplished by choosing a proper slot gap and width for the co-planar strips. The matching network and combiner is constructed from four quarter-wavelength transformers as shown in Figure 8.1. In this design the width and the length of the transmission line are adjusted through trial and error to achieve the desired bandwidth. Usually the balun and the matching network result in reducing the bandwidth of the antenna, however, in this design, the entire antenna structure including the four dipole elements, the balun, the transmission line transformers are optimized together using full-wave analyses to achieve the widest bandwidth.

8.2.5 Overall Geometry of the proposed antenna

The electrical and metric dimensions for the entire antenna are, respectively, given by $0.34\lambda \times 0.34\lambda \times 0.11\lambda$ and $85\text{mm} \times 85\text{mm} \times 26.7\text{mm}$, where λ is the wavelength at the lowest frequency of operation. The folded dipole antennas and the feeding network are fabricated using printed circuit board technology. The substrate for the dipole antenna elements and the feeding network is chosen to have $\varepsilon_r = 3.55, \tan\delta = 0.0027$ $\varepsilon_r = 3.55$, $\tan\delta = 0.0027$ corresponding to commercial substrate RO3002C by Rogers. Also the thickness of the substrate for the dipole elements is chosen to be 0.813mm (32 mil) and that for the feeding network is chosen to be 1.525mm (60 mil). The

thicker substrate for the feeding network provides the required rigidity for the antenna structure and the thinner substrate for the modified dipoles ensure lower signal blockage from other array elements. After all the optimization and parameters study, all the parameters of the antenna are listed in Table 8-1.

Table 8 - 1. Geometric Parameters for the Proposed Antenna

s1	85mm	g1	15mm
g2	1.5mm	fw1	2.1mm
fw2	0.6mm	Sly	20mm
Slx	1mm	fl1	26.1mm
fl2	3mm	fl3	17mm
fl4	6.25mm	fl5	6.5mm
fl6	3.95mm	fl7	4.35mm
l1	52mm	l2	62mm
l3	69.6mm	l4	41.6mm
t1	0.808mm	t2	1.52mm
h1	26.7mm	h2	2.2mm
h3	4.7mm	w1	3mm
w2	2mm	a1	14mm
b1	14mm	a2	3.95mm
b2	5mm	a3	2.1mm

Different shape of the structure will also impact the azimuthal variations of directivity. Simulations imply that a circular or octagonal structure provide better omni-directionality for a given dimension. However, considering the coupling issues, it is found that the smallest distance between elements can best be achieved for square geometry which most affects the uniformity in the array's far-field radiation.

8.3 Experiment Results

The square array described in the previous section was fabricated for measurements and comparison against the simulation results. Figure 8.13 shows the prototype of the proposed

omnidirectional horizontally polarized antenna. All components of the antenna are fabricated with low cost PCB materials and different parts were soldered together to form the box structure. Figure 8.14 depicts both the measured and simulated reflection coefficient (S11) of the proposed antenna. The measured 10 dB return loss bandwidth is about 53.2% (from 1.19GHz to 2.05GHz). A very good agreement between the simulated and measure results is shown.

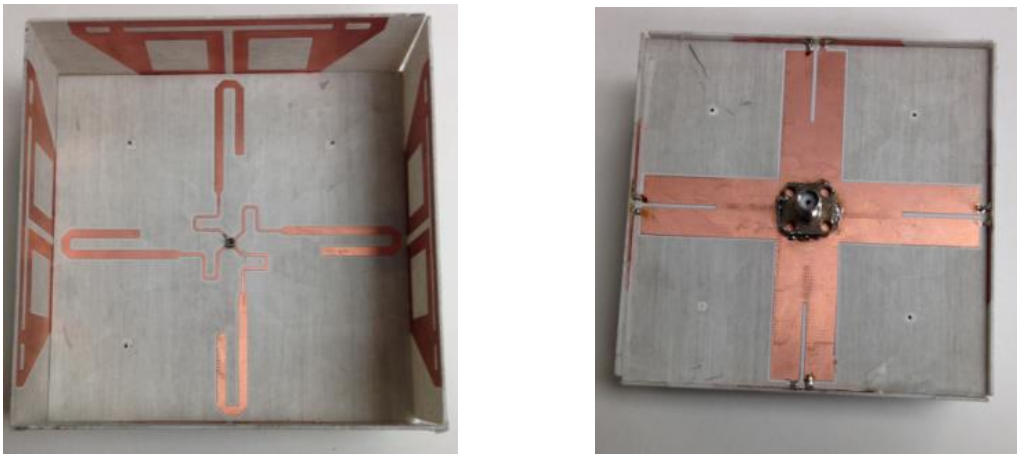

(a) (b)

Figure 8.13. The top view (a) and back view (b) of the prototype of the antenna.

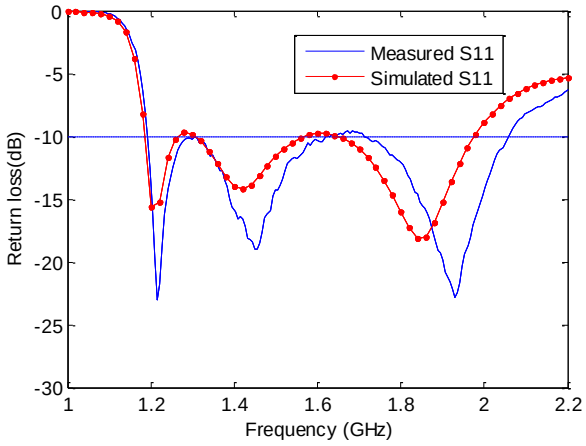

Figure 8.14. Return loss comparison of the measured and simulated result of the HP antenna.

For pattern and absolute gain measurements two double-ridged waveguide horn antennas operating in the band of 1-18GHz (model 3115 Double-Ridged guide antenna) are used. The

absolute gain is measured by the three-antenna gain measurement method. In this approach a calibrated vector network analyzer (VNA) is used to measure S21 in between pairs antennas inside the anechoic chamber of the University of Michigan. Using the distance and the setup unchanged, three measurements of S21's are obtained by permutation of the three antennas with unknown gains. Radiation patterns in E-plane (x-y plane) and H-plane (x-z plane) are shown in Fig. 15 and Fig 16. In azimuth plane, the RMS value for the gain is 0.30 dB, 0.32 dB, 0.52 dB and 0.73 dB for the frequency of 1.2 GHz, 1.5 GHz, 1.8 GHz and 2 GHz, respectively. The gain variations for the four frequencies are 1.1 dB, 1.15 dB, 1.85 dB and 2.8 dB, respectively. The isolation between the co-pol (HP) and cross-pol (VP) in all direction of azimuth plane is better than 20 dB for frequencies below 1.9 GHz, and it degrades to 15 dB for certain direction at 2 GHz but still better than 20 dB for most directions. Fig. 17 shows the co-pol and cross-pol gain comparison along x-axis direction as a function of frequency. It is shown that the gain is almost constant but with a slightly decreasing trend with frequency but the isolation between HP and VP is more than 20 dB for the entire desired frequency band from 1.2 GHz to 2GHz. The radiation efficiency and the total efficiency including the return loss are depicted in Fig. 18. It is shown at the desired band the radiation efficiency is more than 90% and the total efficiency is more than 80%.

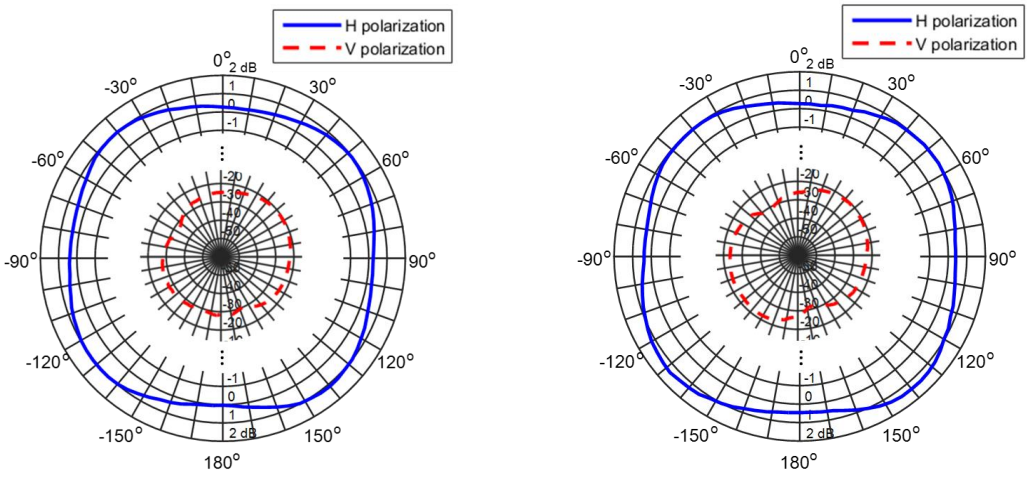

(a) (b)

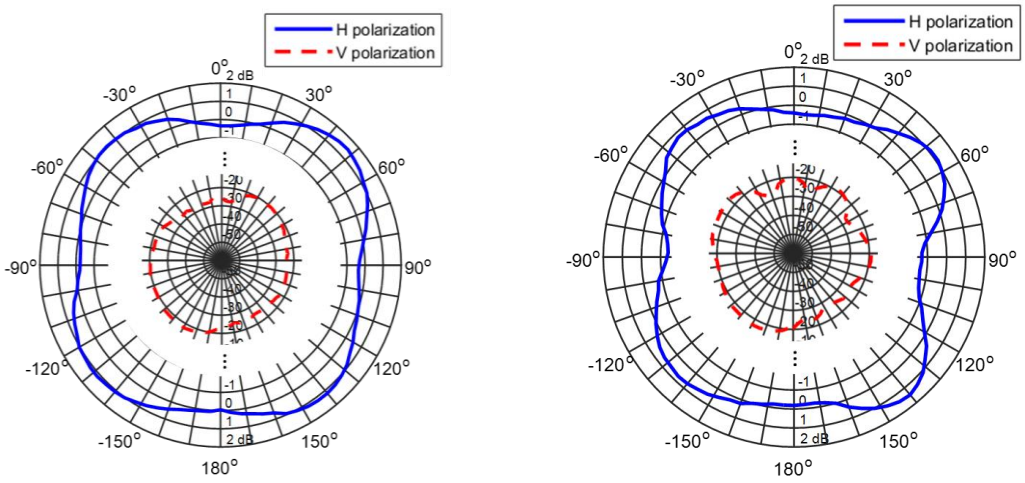

(c) (d)

Figure 8.15. Measured radiation pattern in x-y plane for the HP antenna at (a) 1.2GHz, (b) 1.5GHz, (c) 1.8GHz, and (d) 2GHz.

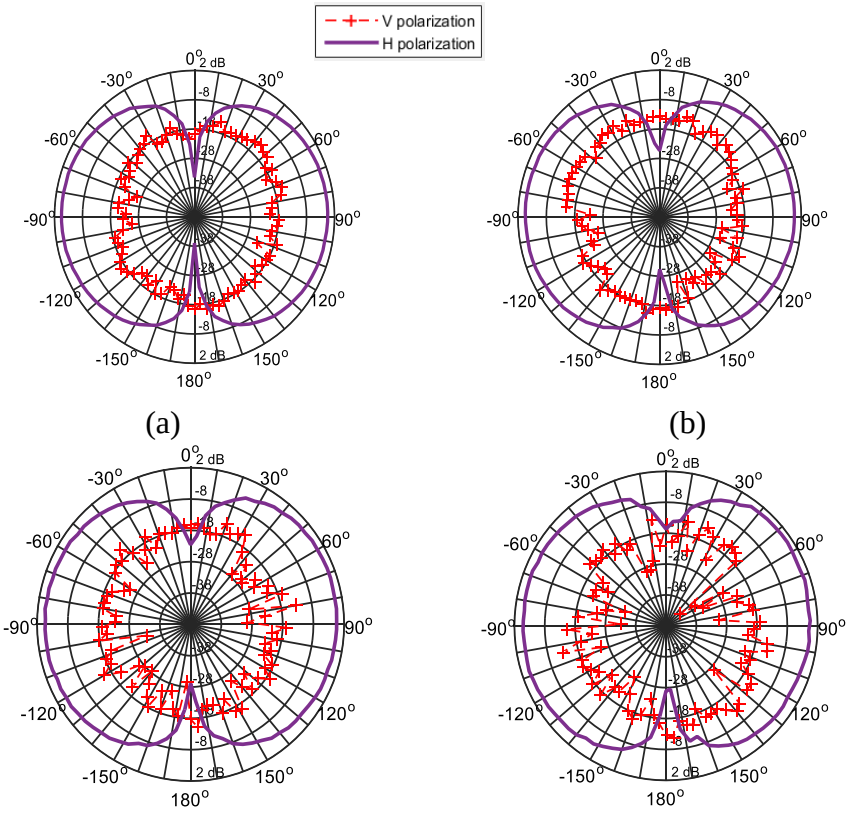

(a) (b)

(c) (d)

Figure 8.16. Measured radiation pattern in x-z plane for the HP antenna at (a) 1.2GHz, (b) 1.5GHz, (c) 1.8GHz, and (d) 2GHz.

Table II shows performance comparison for different broadband omnidirectional HP antennas. This shows a favorable performance of the proposed antenna considering the bandwidth, antenna dimensions, and gain variations in azimuth over the desired band. The proposed antenna provides a wide elevation beam width at the cost of lowering the gain in azimuth plane.

Table 8 - 2. Comparison of other broadband omnidirectional HP antennas and this work

Antenna	Dimension in term of wavelength of lowest operating frequency	Antenna type, number of radiation elements	-10 dB S11 bandwidth	Cross-pol isolation	Gain variation at center frequency	Peak gain at center frequency
[12]	0.34λ×0.34λ	Loop	31.2%	20 dB	Not mentioned	2.5 dBi
[13]	0. 57λ×0.57λ	Multiple radiators, 4	31%	20 dB	1.5dB	About 0 dBi
[14]	0.59λ×0.59λ	Multiple radiators, 4	41%	15 dB	Not mentioned	4 dBi
[15]	0.45λ×0.45λ	Multiple radiators, 4	34.1%	Not mentioned	3 dB	1.7 dBi
[16]	0.79λ×0.79λ	Multiple radiators, 8	62.5%	Not mentioned	~3 dB	~0 dBi
This work	0.34λ×0.34λ	Multiple radiators, 4	53.2%	20 dB	1.6 dB	1.2 dBi

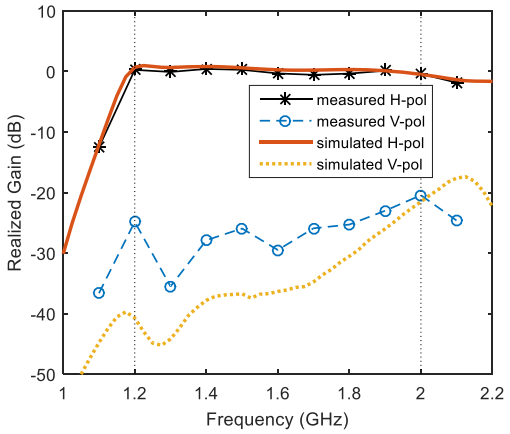

Figure 8.17. Measured and simulated realized co-pol (HP) and cross-pol (VP) gain for the proposed antenna in the x axis direction ($\phi = 0^{o}$) changing with frequency.

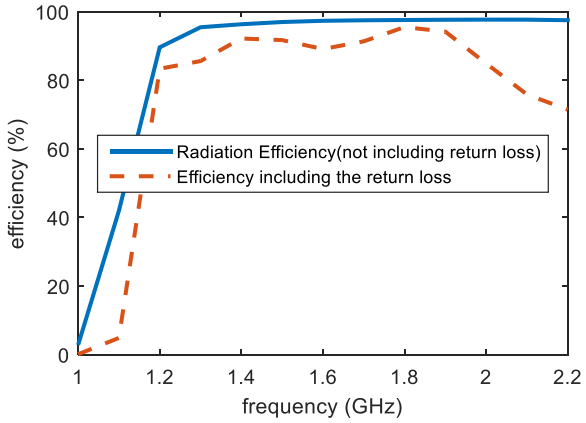

Figure 8.18. Simulated radiation efficiency and the total power efficiency including the return loss as a function of frequency.

8.4 Conclusion

This paper presents a compact broadband omnidirectional horizontally polarized antenna for UWB communication and radar applications. The antenna is composed of four printed broadband folded dipole antennas orientated perpendicular to each other and each covering a quadrant in the horizontal plane and one feeding network to match the antenna to a single 50 Ω port. The 10 dB the return loss bandwidth is about 53.2% (1.192GHz to 2.056 GHz), and the variation of the measured gain in all directions of horizontal plane is less than 2 dB for frequency of 1.2 GHz to 1.9 GHz, and slightly increases to 2.8 dB at 2 GHz. This antenna shows highest realized gain of 1.1 dBi at 1.2GHz and 1.2 dBi around 2 GHz. The isolation between HP and VP is more than 20 dB in all directions in the antenna H-plane over the frequency band of operation. Regarding the bandwidth performance, gain variations, and antenna dimensions, the proposed antenna shows considerable improvements over other similar type of antennas. This antenna meets the bandwidth requirement of the LTE system and probably is a good candidate for the 5G wireless network of the future. The gain of the antenna in azimuth plane can be increased by stacking a

number of these antennas to form a vertical array without compromising its bandwidth, polarization purity, and azimuthal pattern variations.

Chapter 9 Broadband Omnidirectional Circularly Polarized Antenna with Asymmetric Power Divider

9.1 Introduction

Prosperity of technology witnesses the exploding growing of the number of wireless connected devices and demand on high data rate. More than 20.4 billion Internet of Things (IoT) devices including smart personal devices, vehicles and industrial sensors will be installed by 2020 according to Gartner [229]. Examples like autonomous vehicles need extensive wireless communications in both vehicle to vehicle (V2V) and vehicle to infrastructure (V2I) scenarios to ensure best safety for the vehicles, and in the coming fifth generation (5G) telecom technology, more than 1Gb/s per device and 10 Gb/s data rate for base station are required. Wider bandwidth is a naturally solution to implement higher data rate, and since the frequency allocations for many communication purposes/standards are close to each other, wideband antennas are in favor for supporting multiband communication as well. For radar application, wide bandwidth is always desirable since the range resolution is directly proportional to the bandwidth of operation.

Circular polarization (CP) has been widely used in many communication systems include satellite communication, global positioning system (GPS) and radio frequency identification (RFID). In communication with circularly polarized EM wave, the signal strength is less affected by the orientation of device/antenna and multipath effect can be largely reduced compared to linear polarization [68]. Besides the mentioned advantages, in radar system, CP antenna can largely reduce the crosstalk between transmitter and receiver and enhance the performance of radar imaging [54].

Many wireless devices or systems require omnidirectional antennas for maximum signal coverage include the cellphone base station, WLAN router, vehicular communication, and in 2D all-direction synthetic aperture imaging radar [54]. Recently, several omnidirectional CP antennas have been reported [69]-[79]. In some omnidirectional CP dielectric resonator antenna (DRA) design [69][70], CP is created by adding parasitic slots [69] or dielectric wave polarizer [70] around an omnidirectional vertically polarized (VP) DRA. In such way the radiated VP fields are converted into CP fields. The DRA using parasitic slots [69] has usable bandwidth (overlapping of both axial ratio (AR) and impedance bandwidth) of 22% and the other design [70] produces a conical radiation pattern with usable bandwidth of 41%. Another omnidirectional CP antenna based on circular TE_{21}-type modes is reported in [71]. The antenna combines two orthogonal TE_{21} modes and forms a 16-element circular array to create omnidirectional CP. Besides, it utilizes low-pass/high-pass phase shifter to create wideband phase shifting for enhancing the bandwidth. This antenna has an effective bandwidth of 58%, but due to the return loss and resistive loss in feeding network, its efficiency is only around 65% for more than half of the entire bandwidth.

Circular polarized EM field can be realized by superposition of two perpendicular linearly polarized fields with same magnitude and 90° phase difference. The 90° phase difference is often achieved by the electrical length difference between the vertically polarized (VP) and horizontally polarized (HP) fields either in feeding or radiating stage. This setup has been successfully implemented in many omnidirectional CP antennas [72]-[79], [230]. When a circular patch antenna or DRA is feed at the center of the circle, TM modes can be excited to radiate VP fields, and the HP fields are generated by several rotationally symmetric monopole or dipole like radiators around the antenna [72]-[77]. Besides this type of CP antennas, a CP Antenna composed of four inverted L-shape monopoles is reported in[78], and the VP and HP fields are generated by the

horizontal and vertical part of the bended monopoles. For another compact omnidirectional CP antenna in [79], a slot antenna with fourfold parallel plate waveguide is designed to produce omnidirectional HP field, and VP field is excited by two PIFA antennas on the sides of the slot antenna. The antennas reported above have good omnidirectional CP property, but most have limited bandwidth (<10%).

One idea to increase the bandwidth is to create multipole resonances with different exciting modes [75], [76]. The usable bandwidth is increased to 14.4% [75] and 51.7% [76], however, these two antennas have a conical radiation pattern and do not generate CP field in horizontal plane. Recently, a wideband central-feed CP patch antenna is proposed [77]. Due to the symmetry of ground plane and antenna, this antenna's main beam is on azimuth plane, and it utilizes capacitive feed instead of direct feed to increase the bandwidth to about 30%.

For an omnidirectional CP antenna based on VP and HP radiators, the challenges of broad bandwidth (>50%) include broad impedance bandwidth for both VP and HP radiators, maintaining omnidirectional pattern within the band, and maintaining small magnitude difference and 90º phase difference between VP and HP fields for all operating frequencies. For a directional antenna, the VP and HP radiators can be the same antenna, but one is rotated by 90º. In this case an equal power divider can solve the problem. However, in omnidirectional antennas, VP and HP radiators are usually very different elements, and their gains and impedance as functions of frequency may have large discriminations as well. This increases the difficulty of designing the feeding network. Wilkinson power divider and its modified versions are widely used for splitting power equally or in arbitrary ratio [231]-[235]. The original Wilkinson power divider [232] has simple structure and good performance but only for equal power division and narrow band application. The theoretical analysis for multi-section Wilkinson power divider with arbitrary power split ratio is introduced

in [233]. It manipulates impedance of each transmission line while keeping their length to be λ/4 to obtain the optimal bandwidth performance. In [234], the dimensions of arbitrary ratio power divider are reduced by adding novel loading transmission lines. An optimization process based on method of least squares are applied to design a broadband multisection Wilkinson power divider with arbitrary power split ratio [235], but the quasi-Newton method based optimization can only guarantee to find the local optimal value. Many power divider designs in literatures can split power with arbitrary ratio, nevertheless, all the reported arbitrary ratios are constant with frequency, which cannot meet the requirement in this broadband CP antenna application.

In this paper, divide-and-conquer strategy is used in designing a broadband omnidirectional CP antenna. We first design a ring-shape ultra-wide band (UWB) monopole antenna based on a circular-shape UWB monopole antenna [238] and a broadband omnidirectional HP antenna [236] that can meet the impedance bandwidth requirement. Those antennas are carefully designed to achieve desired performances. Since the gain and impedance of VP and HP elements exhibit large differences, and those differences are also functions of frequency, an asymmetric Wilkinson power divider is studied and optimized by particle swarm optimization (PSO) to obtain the dedicated power split ratio as a function of frequency. The feeding network also includes a wideband Schiffman phase shifter to maintain almost 90º phase difference for the VP and HP electrical far fields over the entire band. The main beam for the proposed antenna is on azimuth plane and the usable bandwidth reaches 53.4%.

The chapter is organized as following. In Sec. 9.2, the entire antenna structure and geometric parameters are introduced, then the design and optimization process of each component including a double-ring shape UWB monopole antenna, a broadband omnidirectional HP antenna and a feeding network containing a dedicated optimized asymmetric power divider are presented

in detail. The parametric study of an asymmetric power divider is discussed as well. In Sec. 9.3, The simulation and measurement results of the proposed antenna are demonstrated and discussed. Finally, the concluding remarks are included in Sec. 9.4.

9.2 Antenna design and optimization

The proposed Broadband Omnidirectional Circularly Polarized (CP) Antenna is shown in Figure 9.1. It is designed to operate at L band from 1.2 GHz to 2 GHz. The dimensions for this antenna are 100mm×100mm×125mm, or 0.4λ×0.4λ×0.5λ, where λ is the wavelength as the lowest frequency of operation (1.2GHz). It is composed of an optimized broadband omnidirectional HP radiation element (from our previous work [236]), a double-ring shape UWB monopole antenna (VP element) and a very carefully designed feeding network that can divide the power properly between HP and VP components and maintain the required phase difference over the desired frequency band. Both the antenna elements and the feeding network are printed on Rogers RO4003C substrates (εr = 3.55, tanδ = 0.0027). The thickness of the substrate for the feeding network of HP radiators shown in Figure 9.1 (d) is 1.52 mm (60 mil) and the rest are printed on substrates with 0.81 mm (32 mil) thick. The geometric parameters of each components of the proposed antenna is given in Table 9 - 1.

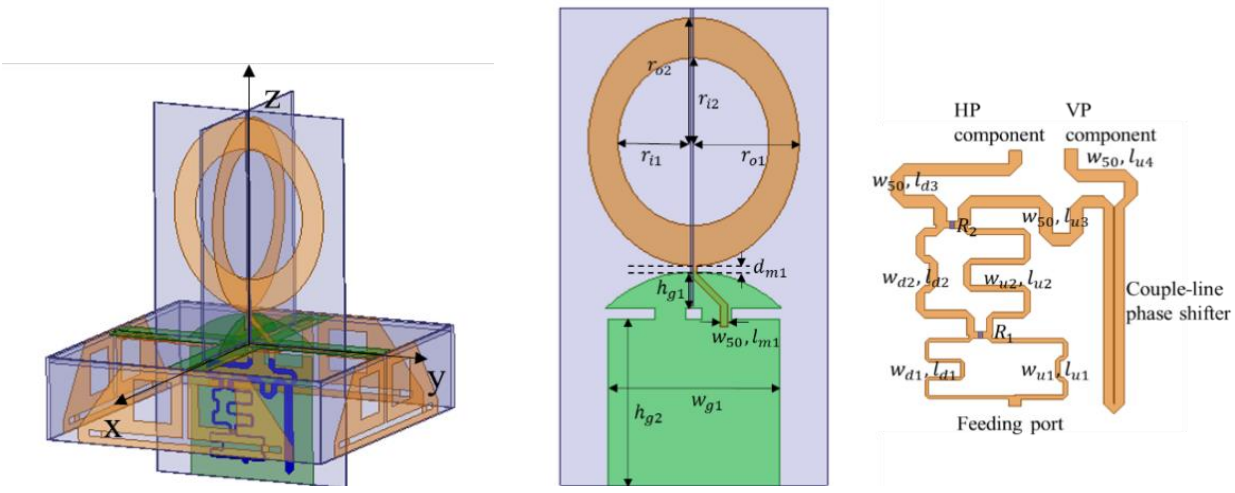

(a) (b) (c)

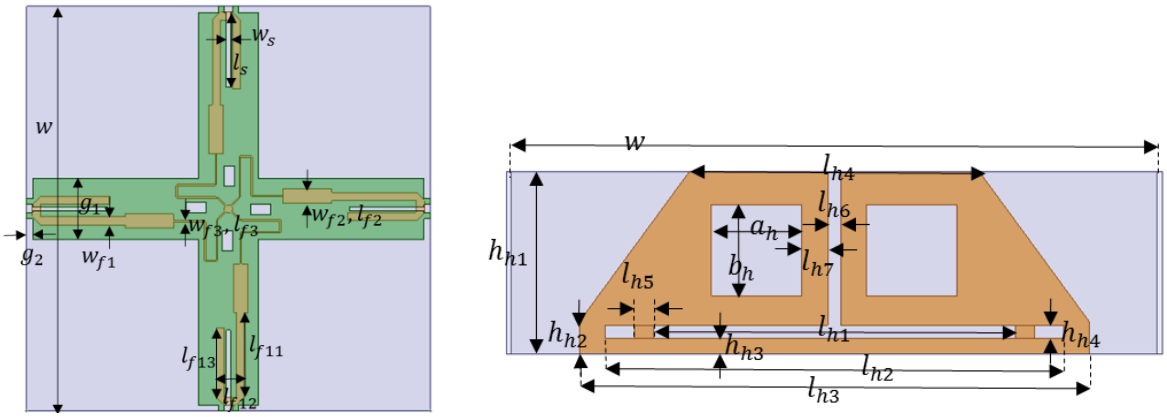

(d) (e)

Figure 9.1. The geometry of (a) the proposed CP antenna, (b) the double-ring monopole antenna, (c) the power divider-based feeding network, (d) feeding network for the four HP radiators and (e) one element of the HP radiator.

Table 9 - 1. Geometric Parameters

Parameters for double-ring monopole and ground plane			
r_{i1}	19.8 mm	w_{50}	1.81 mm
r_{i2}	22.0 mm	l_{m1}	11.25 mm
r_{o1}	27.63 mm	h_{g1}	9.41 mm
r_{o2}	32.5 mm	h_{g2}	43.45 mm
d_{m1}	1.6 mm	w_{g1}	45 mm
Parameters for power divider			
w_{d1}	0.35 mm	l_{d1}	34.67 mm
w_{u1}	0.47 mm	l_{u1}	24.16 mm
w_{d2}	0.79 mm	l_{d2}	22.69 mm
w_{u2}	0.66 mm	l_{u2}	41.88 mm
w_{50}	1.81 mm	l_{d3}	27.72 mm
R_1	300 Ω	l_{u3}	27.30 mm
R_2	150 Ω	l_{u4}	15.30 mm
Parameters for HP radiators' feeding network			
w	100 mm	l_{f12}	7 mm
w_s	1 mm	l_{f13}	17 mm
l_s	18.5 mm	w_{f2}	3.5 mm
g_1	15 mm	l_{f2}	12.03 mm
g_2	1.5 mm	w_{f3}	0.39 mm
w_{f1}	2 mm	l_{f3}	32.72 mm

l_{f11}	20.97 mm		
Parameters for HP radiator			
h_{h1}	28 mm	l_{h4}	45 mm
h_{h2}	5 mm	l_{h5}	3 mm
h_{h3}	2.4 mm	l_{h6}	2 mm
h_{h4}	2.1 mm	l_{h7}	4 mm
l_{h1}	56 mm	a_h	14 mm
l_{h2}	71 mm	b_h	14 mm
l_{h3}	79 mm		

9.2.1 Vertically polarized (VP) component design

Ultra-wideband (UWB) circular monopole antenna has been studied for more than a decade [237][238], and its broadband features in both impedance and omnidirectional property make it a good candidate for our vertically polarized component. The design of VP radiation element starts with a typical UWB monopole antenna as shown in Figure 9.2 (a). It is a ring shape monopole antenna feed by microstrip line and is printed on a double side PCB board, with antenna and ground on different sides. The design is modified from traditional UWB circular monopole antenna: the upper boundary of the ground plane is modified as elliptical shape to increase the symmetry of the current on the antenna. This ensures that the highest gain is on azimuth plane. This VP antenna can provide the required bandwidth and the isolation between VP and HP is more than 30 dB, but the gain variance in azimuth direction is as large as 1.5 dB at the center frequency (1.6 GHz).

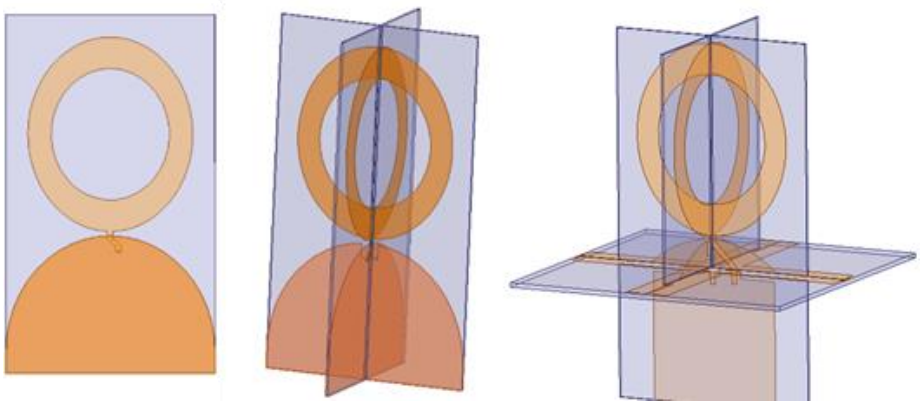

(a) (b) (c)

Figure 9.2. The geometry of (a) Ring UWB monopole antenna, (b) Two-cross-rings UWB monopole antenna and (c) the proposed monopole component for this CP antenna.

To improve its omnidirectional property, a geometry with two perpendicular ring radiators intersecting with each other is proposed as shown in Figure 9.2 (b). This geometry is further adjusted such that the feed structure for the HP antenna is also included as depicted in Figure 9.2 (c). The addition of ground traces on the horizontal plane assists further the monopole feature of the VP antenna and can enhance the uniformity of the radiation pattern in the horizontal plane. The three monopole antennas shown in Figure 9.2 are labeled as monopole-1, monopole-2 and monopole-3 antennas. The radiation pattern in azimuth plane for monopole-1, 2, 3 are shown in Figure 9.3. It shows that the double-ring geometry can reduce the gain variation significantly. All geometric parameters of the monopole antennas are carefully designed to make sure the return loss is greater than 10 dB for the entire required band. The normalized input impedance for monopole-3 antenna at different frequencies on a Smith chart are illustrated in Figure 9.4 (a). It shows that for this UWB antenna there is no obvious resonant frequency and the entire band has VSWR less than 2 (10 dB return loss). Figure 9.4 (b) depicts the radiation pattern on azimuth plane for monopole-3 antenna at three resonant frequencies (zero reactance): around 1.2 GHz, 1.4 GHz and 2 GHz. Excellent omnidirectional property is observed for the antenna at all frequencies, and the directivity at 1.2 GHz and 1.4 GHz are almost the same. The gain drops for about 0.7 dB at 2 GHz due to the fact that main beam moves up from the azimuth plane at high frequency.

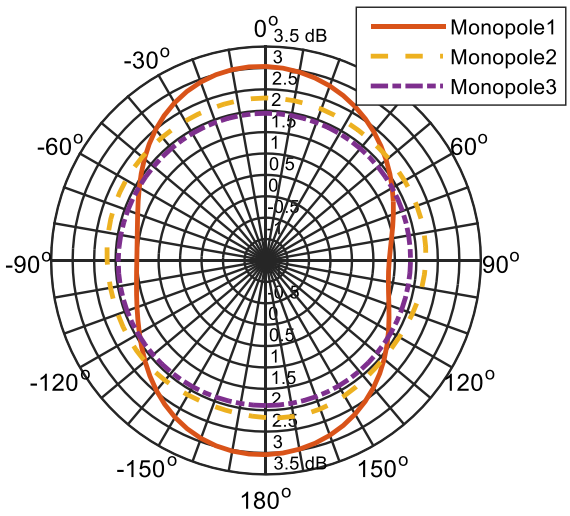

Figure 9.3. Radiation pattern in azimuth plane comparison at center frequency (1.6GHz) for the three monopole antennas.

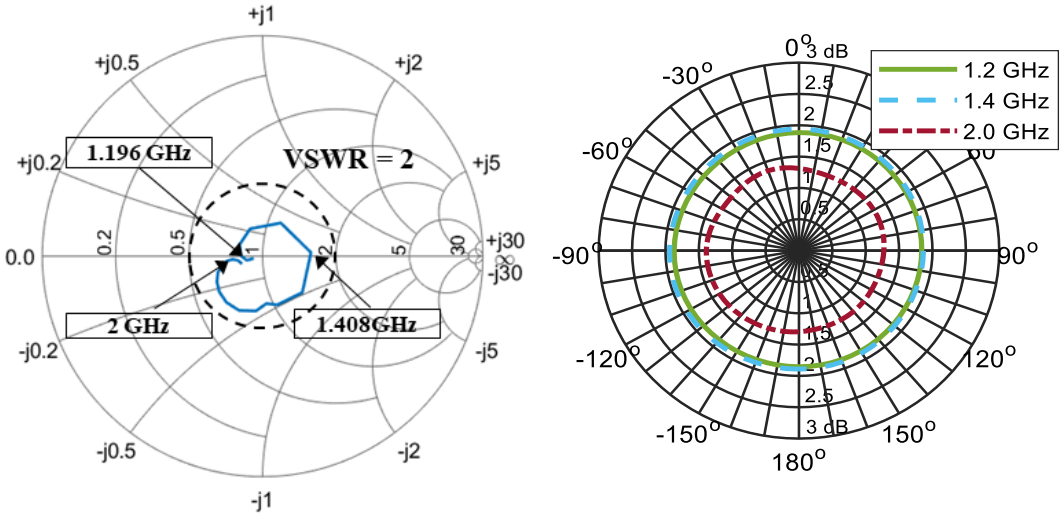

(a) (b)

Figure 9.4. (a) Return loss of monopole-3 antenna when terminated by 50 Ω impedance. (b) Radiation pattern on azimuth plane at different frequencies for monopole-3 antenna.

9.2.2 Horizontally polarized (HP) component design

The broadband HP omnidirectional antenna with planar folded dipole is selected as the HP radiation element. It has the required bandwidth, good omnidirectional property, and omnidirectional shape radiation pattern as we desired. In ordinary non-dispersive wave

propagation the phase term βd is linear with frequency, however, for the original proposed HP antenna [236], the phase of the radiated electric far field at the low frequency band (typically from 1.2GHz to 1.3GHz) is not linear with frequency as is shown in Figure 9.5. This is due to different resonant mechanism for the antenna at low frequency. The non-dispersive property is important for maintaining the 90º phase difference between VP and HP all over the band. In order to alleviate this problem, the HP antenna is scaled up to shift the dispersive response outside the operating band, and many parameters have been modified to keep the antenna's impedance bandwidth. The simulated results are provided in Figure 9.5. It shows that for w = 90mm, the phase deviated from normal propagation is more than 50 degrees at 1.2 GHz while those for w = 100mm and w = 110mm are about 20 degrees, which are acceptable for circular polarization criteria.

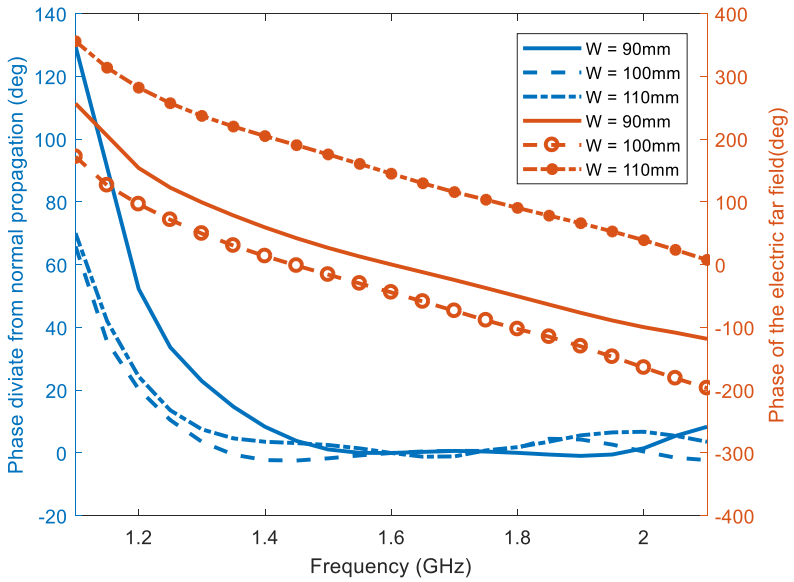

Figure 9.5. The phase of electrical far field at same distance and the phase deviation from normal propagation (linear function of frequency) as a function of frequency.

9.2.3 Simulation for combining VP and HP components

The geometry of the combined VP and HP components of the CP antenna is shown in Figure 9.6. When terminated by 50Ω impedance, the S parameters of the two components are given in Figure 9.7 (a). The return loss for VP component is greater than 10 dB for the entire band and that for HP antenna is greater than 10 dB for most part of the frequency band of interest. The coupling between VP and HP is lower than -25 dB and therefore good isolation between VP and HP is achieved with this geometry placement. The radiation pattern in H plane for both VP and HP components are shown in Figure 9.7 (b). The gain variation for different azimuth directions is about 0.6 dB for VP and 2 dB for HP. Their averaged gain has about 1.6 dB difference when both antenna components are feed with the same power. The comparison of dimensions between CP antenna and its linear polarized (LP) components are given in Table 9 - 2. The implementation of circular polarization is at the cost of increase in size as well.

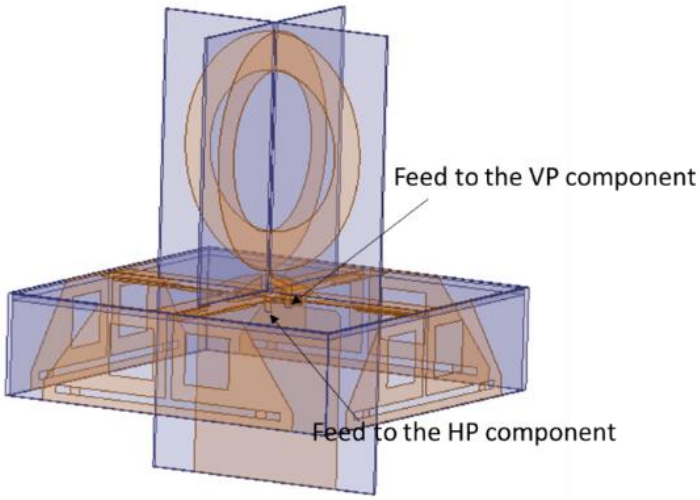

Figure 9.6. Geometry of the combination of VP and HP components without feeding network.

Due to the rotational symmetry of both VP and HP components, the largest variation of gain in azimuth plane is between $\phi=0^{o}$ and $\phi=45^{o}$, therefore analysis on these two directions is enough for examination of the omnidirectional property in the azimuth plane for this antenna. The

simulated realized gain of the VP and HP field for ϕ=0º and ϕ=45º as a function of frequency are given in Figure 9.8 (a). The gain for VP is almost constant for the frequency band from 1.2GHz to 2 GHz, while that for HP has a minimum at around 1.5GHz. The gain difference between VP and HP field are shown in Figure 9.8 (b). These results are used in designing the feeding network to divide the input power to VP and HP component as a function of frequency such that the VP and HP gain difference is as small as possible. Notice the gain differences change with different azimuth directions, and those at ϕ=0º and ϕ=45º have at most 2.5 dB difference within the band, so the goal for the feeding network is to have the power dividing ratio matching the average gain difference, which is the dot line shown in the figure.

Table 9 - 2. Dimensions of the CP antenna and its LP components

	CP antenna	HP component	VP component
x	100 mm	100 mm	100 mm
y	100 mm	100 mm	100 mm
z	125 mm	28 mm	75 mm

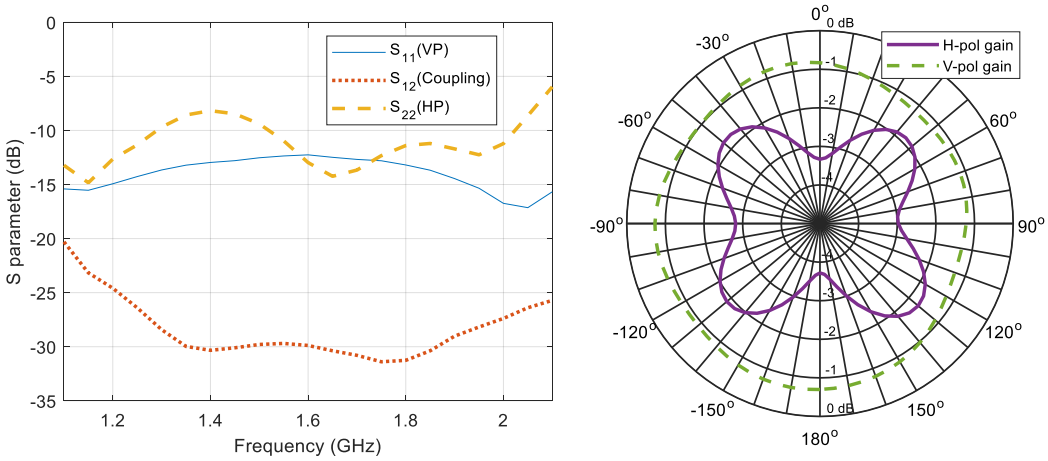

(a) (b)

Figure 9.7. (a) S parameters of the VP and HP components when terminated by 50 Ω ports, (b) the radiation pattern in azimuth plane for H polarization and V polarization components at center frequency (1.6GHz) when feed with the same power.

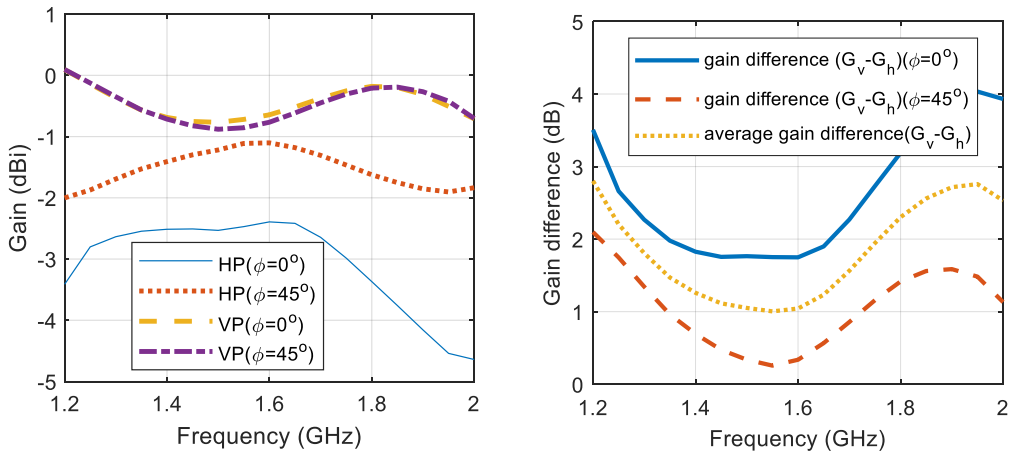

(a) (b)

Figure 9.8. (a) The simulated gain in horizontal plane for VP and HP at ϕ=0º and ϕ=45º as a function of frequency. (b) The gain differences of VP and HP at ϕ=0º, ϕ=45º and average over ϕ as a function of frequency.

Another important quantity for two orthogonal polarization waves to form circular polarization is the phase difference. Ideal for a nondispersive medium, the phase difference (βΔl) between VP and HP is a linear function of frequency and by adding a nondispersive transmission line in the VP's or HP's signal path for phase compensation, the phase difference will be constant zero for the entire band. Figure 9.9 depicts the phase difference between VP and HP fields after compensation at the center frequency. The phase differences are between -10º to 10º for the entire band, and it indicates that there is only small dispersion for both VP and HP component.

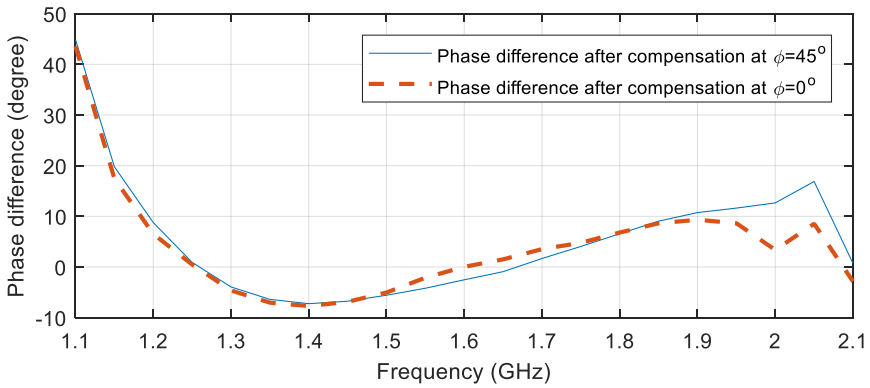

Figure 9.9. The phase difference for HP and VP after phase compensation by simple transmission line at ϕ=0º and ϕ=45º as a function of frequency.

9.2.4 Wideband phase shifter for feeding network

To achieve circular polarization, the feed network for this broadband circular polarized antenna is required to create 90º phase difference between VP and HP fields and compensate their gain difference such that both VP and HP fields have the same magnitude over the entire band.

A popular method to implement 90º phase difference is to utilize the propagation path difference of VP and HP signals in transmission line, antenna itself or wave propagation in the air. This solution is fine for narrow band design, but problem will arise for broadband application. It is noted that the phase difference ($\beta\Delta l$) between VP and HP is a linear function of frequency if the antenna and transmission line are nondispersive for EM signals propagating from feeding port to far field. Therefore, the phase difference between VP and HP is no longer 90º for the frequency other than the center frequency. For an ideal CP antenna with center frequency $\boldsymbol{f_0}$, the axial ratio as a function of frequency is depicted in Figure 9.10, given that the magnitudes of E fields for VP and HP are identical over the entire band. It shows that the maximum axial ratio bandwidth for a nondispersive CP antenna is 44% ($0.78\boldsymbol{f_0}$ to $1.22\boldsymbol{f_0}$) if nondispersive method is applied to create 90º phase difference. Therefore, more sophisticated phase shifting technique is required for broadband (>50% bandwidth) CP antenna.

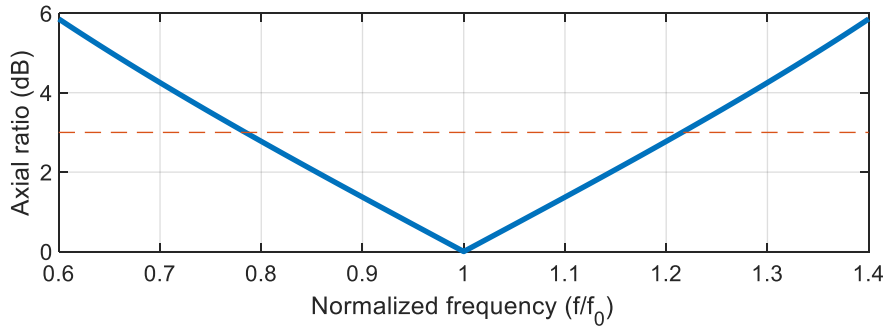

Figure 9.10. The phase difference for HP and VP after phase compensation by simple transmission line at ϕ=0º and ϕ=45º as a function of frequency.

Schiffman phase shifter [24] is used to create broadband 90º phase difference in this design. The schematic in Advanced Design System (ADS) is shown in Figure 9.11 (a). It is composed of a quarter wavelength couple line with one end shorted. It can create a broadband 90º phase difference compared to the response of a ¾ λ long transmission line, where λ is the wavelength for the central frequency. The simulated results are illustrated in Figure 9.11 (b). For the frequency from 1 to 2.2 GHz the phase difference between S_21 and S_43 is about 90±5°.

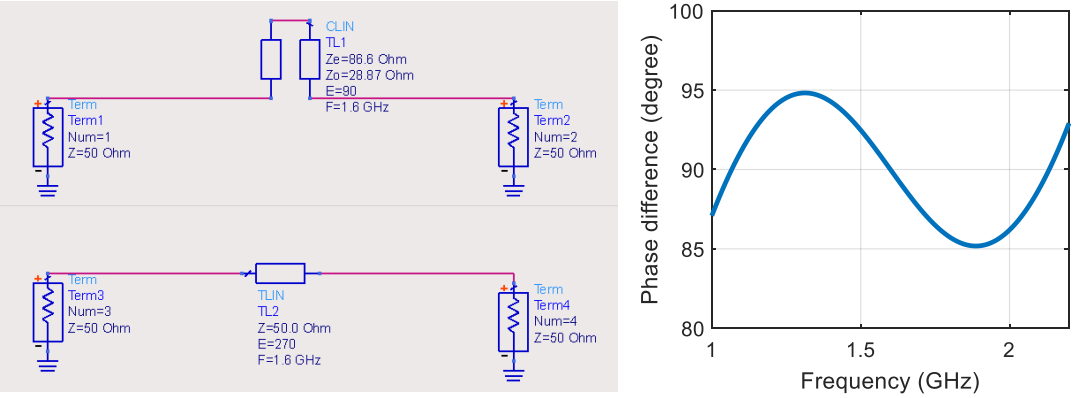

(a) (b)

Figure 9.11. (a) The schematic of the Schiffman phase shifter and (b) the phase difference between port 2 and 4, given that port 1 and 3 are in phase.

9.2.5 Analysis and optimization of an asymmetric power divider

As shown in Sec. 9.2.3, the gain difference between VP and HP changes with frequency. Thus the feed network should be capable to divide the power with a prescribed ratio varying with frequency.

It is found that when breaking the symmetry of the power divider (two splitting transmission lines have different impedance and length), the power dividing ratio is no longer constant with frequency. The drawbacks of this power divider are more loss in the resistors and there will be some power leakage between port 2 and port 3 shown in the left part of Figure 9.12 (large $|S_{32}|, |S_{23}|$).

The loss issue can be reduced by carefully optimizing the power divider and the power leakage is not a serious problem for this antenna application. Because in transmitting mode, the radiated power only depends on $|S_{21}|$ and $|S_{31}|$, and large value of $|S_{32}|$ or $|S_{23}|$ won't increase the return loss or reduce the radiation efficiency. In receiving mode, if the incident wave is circularly polarized as desired, the receiving efficiency should be the same as that in transmitting mode due to the reciprocity. In such case, the leakage power from port 2 to port 3 is actually cancelling the return loss from port 3 that to ensure maximum efficiency of power input from port 3 to port 1.

Since the power divider now is not symmetric, conventional "even-odd" mode analysis [231] cannot be applied here. Instead, since the n-stage Wilkinson power divider can be treated as cascaded 4-port network with transmission lines and shunt resistors, transmission matrix method (also known as ABCD matrix) is used to analyze this network. The three-port network Wilkinson power divider can be equivalent to a four-port network as is shown in Figure 9.12, with $V_1' = V_4' = V_1, I_1 = I1' + I_4'$ [235].

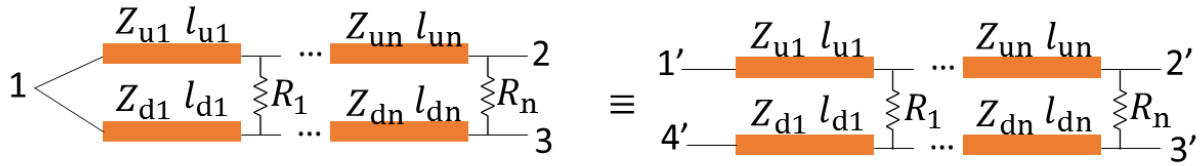

Figure 9.12. N-stage Wilkinson power divider and its equivalent 4-port network.

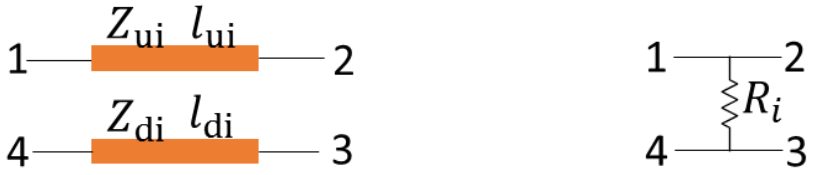

(a) (b)

Figure 9.13. The four-port schematic for (a) two transmission lines and (b) a shunted load.

The overall transmission matrix of the four-port network can be simply calculated by the multiplication of the transmission matrix of each component. The transmission matrix relates the voltages and currents in port 2 and 3 to those in port 1 and 4 in Figure 9.13, as described by:

$$[V_1, V_4, I_1, I_4]^T = [A][V_2, V_3, I_2, I_3]^T, \tag{9.1}$$

where A is the transmission matrix. The transmission matrix for two transmission lines (shown in Figure 9.13 (a)) A_{2tli} and that for a shunted load with impedance R_i (shown in Figure 9.13 (b)) A_{Ri} are given by [231]. Then the overall transmission matrix is:

$$[A'] = [A_{2tl1}][A_{R1}] \dots [A_{2tln}][A_{Rn}]. \tag{9.2}$$

The impedance matrix $[Z']$ of the four-port network shown in the right part of Figure 9.12 can be derived from its transmission matrix$[A']$ with some algebra. By applying the boundary condition $V_1' = V_4' = V_1, I_1 = I_1' + I_4'$,which means directly connecting port 1 and 4, the four port impedance matrix $[Z']$ can be reduced to three-port impedance matrix $[Z]$. Then the S matrix can be calculated from the impedance matrix together with the knowledge of the impedance of the three ports by:

$$[S] = [F]\big([Z] - [Z_p]\big)\big([Z] + [Z_p]\big)^{-1}[F]^{-1}, \tag{9.3}$$

where $[Z_p]$ is a diagonal matrix with element in ith row and ith column is the impedance of port i, Z_{pi}, and $[F]$ is also a diagonal matrix with element $F_{ii} = 1/(2\sqrt{\mathrm{Re}(Z_{pi})})$.

This reciprocal three-port S matrix contains 12 independent quantities (magnitude and phase of 6 S parameters S_{11}, S_{21}, S_{31}, S_{22}, S_{23} and S_{33}), and for our antenna application, four quantities are important: the return loss at port 1 ($|S_{11}|$), the power dividing ratio between port 2 and 3 ($|S_{21}|/|S_{31}|$,), the phase difference between port 2 and 3 ($\mathrm{Arg}(S_{21}/S_{31})$) and the power dissipate in resistors ($1 - |S_{11}|^2 - |S_{21}|^2 - |S_{31}|^2$).

Before optimizing the parameters of the power divider, a parametric analysis is performed to examine how the geometric parameters of asymmetric power divider impacts the performance. For simplicity, single stage power divider is taken as an example. The parameters for power divider include the impedance and length of the two transmission line arms and the resistance of the center resistor. In the captions of Figure 9.14 to Figure 9.16, the wavenumber β corresponds to the center frequency 1.6 GHz. If we only change the impedance of the lower transmission line $Z_d = 150\Omega$ and keep the rest parameters unchanged, this will result in unequally power splitting and the dividing ratio will be almost constant for the entire band as is shown in Figure 9.14.

Figure 9.15 depicts the simulated results for the single stage power divider with unequal length of transmission line. The dividing ratio between port 2 and 3 of this power divider is changing with frequency, with about 1dB at 1 GHz and -5 dB at 2 GHz. Notice it has drawback that the loss in resistor is large and the phase difference is a non-linear function of frequency. One way to reduce the loss in resistor is to increase its resistance, Figure 9.16 shows the results of the same power divider in Figure 9.15 except the impedance of the load increases to 1000 Ω. It can be seen that the power loss in resistor is largely decreased but it reduces the power dividing ratio as a function of frequency. In conclusion, the power dividing ratio depends on all the parameters of power divider, and asymmetric length of the two transmission lines is the key to make the power dividing ratio varying with frequency.

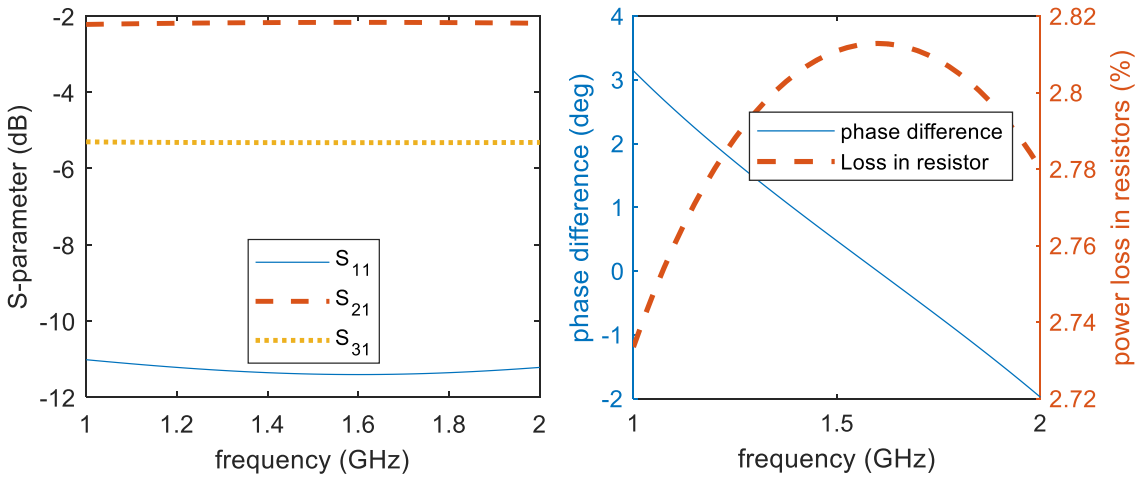

(a) (b)

Figure 9.14. Simulated results of (a) the S parameters and (b) phase difference between port 2 and 3 and power loss in resistive load for a single stage power divider with unequal Z_u and Z_d ($Z_u = 70.7\Omega$, $Z_d = 150\Omega$, $\beta l_u = \beta l_d = 90°$, $Z_L = 100\Omega$ and all port impedances are 50 Ω).

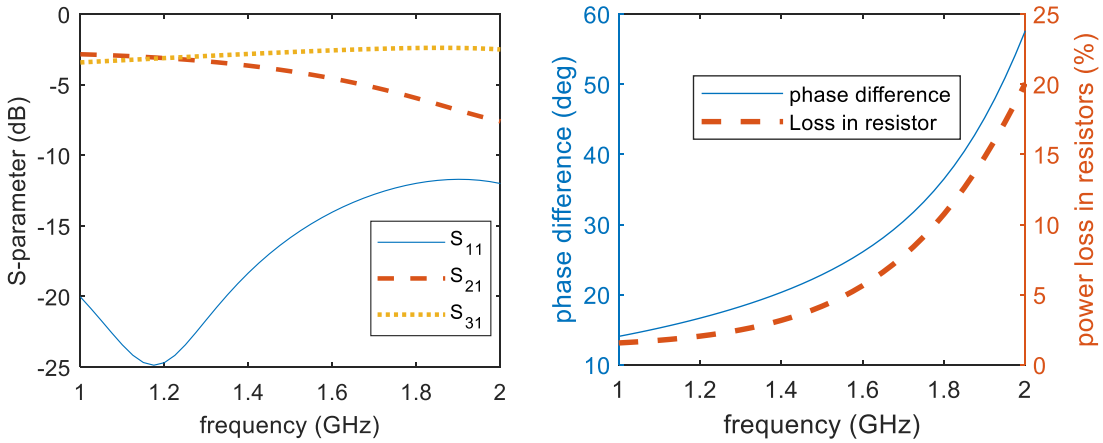

(a) (b)

Figure 9.15. Simulated results of (a) the S parameters and (b) phase difference between port 2 and 3 and power loss in resistive load for a single stage power divider with unequal l_u and l_d ($Z_u = Z_d = 70.7\Omega$, $\beta l_u = 90°, \beta l_d = 150°$, $Z_L = 100\Omega$ and all port impedances are 50 Ω).

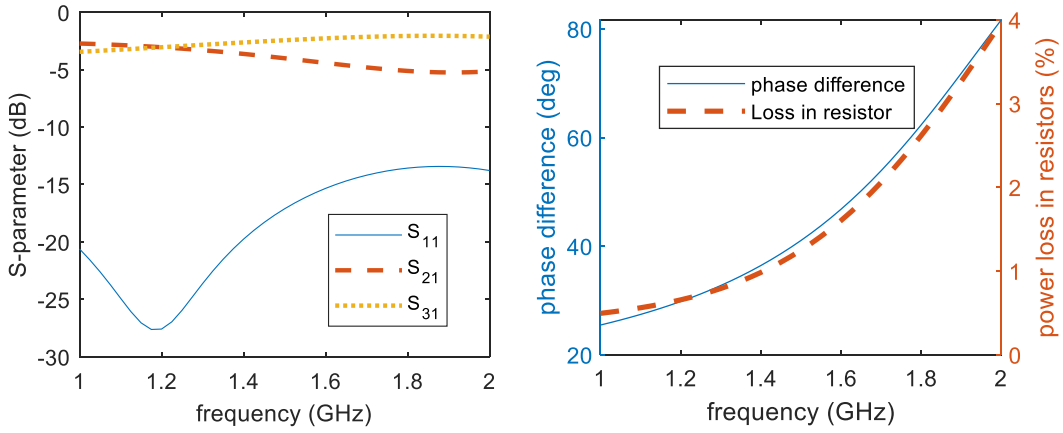

(a) (b)

Figure 9.16. Simulated results of (a) the S parameters and (b) phase difference between port 2 and 3 and power loss in resistive load for a single stage power divider with unequal l_u and l_d, and large resistive load ($Z_u = Z_d = 70.7\Omega$, $\beta l_u = 90°, \beta l_d = 150°$, $Z_L = 1000\Omega$ and all port impedances are 50 Ω).

It is difficult to optimize both the power dividing ratio and phase difference simultaneously for the power divider because both quantities highly depend on the length of upper and lower transmission line of the divider. To circumvent this problem, first two 50 Ω transmission lines are added to the end of the power divider to compensate for the phase difference. Then, all parameters of the power divider and the lengths of the transmission lines are optimized simultaneously. To monitor the power that goes into VP and HP components for optimization purpose, two hypothetical ideal directional couplers are used. For the convenience of cascading S parameters, here the two directional couplers are put in one block diagram. In Figure 9.17, the black numbers indicate the ports for the directional coupler block, and the red numbers refer to the ports for the entire system. In the block diagram, the S parameters for VP & HP antenna components are obtained from simulation shown in Sec.9.2.3.

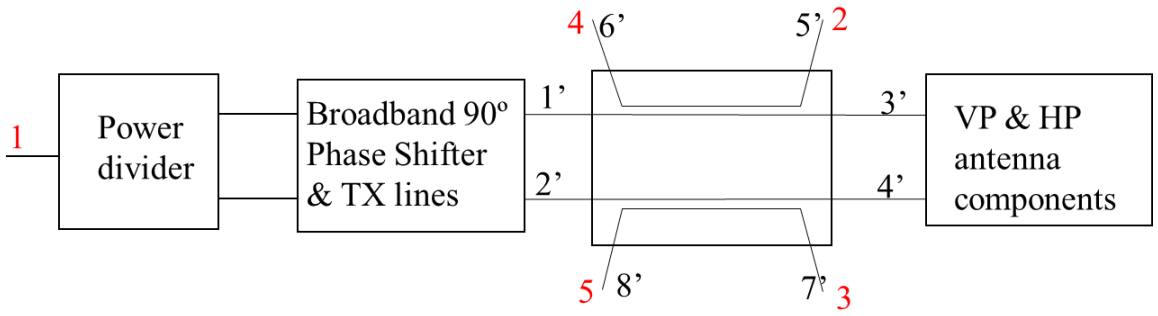

Figure 9.17. Block diagram of the feeding network with hypothetical ideal directional coupler.

The frequency independent S parameters for the hypothetical ideal directional couplers with all port terminated by 50 Ω impedance is given by:

$$[S] = \begin{bmatrix} 0 & 0 & 1 & 0 & 0 & 0 & 0 & 0 \\ 0 & 0 & 0 & 1 & 0 & 0 & 0 & 0 \\ 1 & 0 & 0 & 0 & 0 & 0 & 0 & 0 \\ 0 & 1 & 0 & 0 & 0 & 0 & 0 & 0 \\ 1 & 0 & 0 & 0 & 0 & 0 & 0 & 0 \\ 0 & 0 & 1 & 0 & 0 & 0 & 0 & 0 \\ 0 & 1 & 0 & 0 & 0 & 0 & 0 & 0 \\ 0 & 0 & 0 & 1 & 0 & 0 & 0 & 0 \end{bmatrix}, \tag{9.4}$$

The power ratio for VP and HP antenna components is $\left|\frac{S_{3\prime 1}}{S_{4\prime 1}}\right|^2$, and their phase difference is given by $Arg\left(\frac{S_{3\prime 1}}{S_{4\prime 1}}\right)$ for the entire system in Figure 9.17. Since the impedance of two components are not exact 50 Ω but functions of frequency, $\frac{S_{21}}{S_{31}}$ then is not equal to $\frac{S_{3\prime 1}}{S_{4\prime 1}}$. Instead, because of the linearity of this ideal directional coupler, those two quantities have the following relation:

$$\frac{S_{3\prime 1}}{S_{4\prime 1}} = g(f)\frac{S_{21}}{S_{31}}, \tag{9.5}$$

where the coefficient $g(f)$ is a function of frequency f.

Moreover, the ratio between the electrical far fields with VP and that with HP is linear to the ratio of feeding power for the VP and HP components for each frequency, and can be related by a coefficient $g_2(f)$, as is described by:

$$\frac{E_v}{E_h} = g_2(f)\frac{S_{3'1}}{S_{4'1}} = g_2(f)g(f)\frac{S_{21}}{S_{31}}. \tag{9.6}$$

It should be noted that the hypothetical directional couplers will not affect the performance of the system, and it is only used in simulation to optimize the power divider.

Regarding the bandwidth, power dividing ratio, loss in resistors and complexity of the network, a two-stage power divider is chosen to be optimized. The optimization goals for the power divider are to divide the power with ratio as desired function of frequency, keep the return loss and resistive loss minimum, and to maintain the phase difference to create circular polarization for VP and HP components. Practically, it is difficult to achieve all goals simultaneously, and for our application the most important property for the antenna is the omnidirectional circular polarization property, for other features like return loss or resistive loss of the feeding network can be tolerated within a certain range. More specifically, the return loss should be higher than 10 dB and the resistive loss in the circuit should be lower than 20%. The overall optimization cost function F is defined as the following equation:

$$\begin{aligned} \mathrm{F} = {} & a_1 R\left(|\mathrm{S}_{11}|^2 - |\mathrm{S}_{11}|^2_{\mathrm{req}}\right) + a_2 R(1 - |\mathrm{S}_{11}|^2 - |\mathrm{S}_{21}|^2 - |\mathrm{S}_{31}|^2 - 0.2) \\ & + a_3 \left| \left|\frac{S_{21}}{S_{31}}\right|^2 - \left|\frac{S_{21}}{S_{31}}\right|^2_{req} \right| + a_4 \left| Arg\left(\frac{S_{21}}{S_{31}}\right) - Arg\left(\frac{S_{21}}{S_{31}}\right)_{req} \right|, \end{aligned} \tag{9.7}$$

where $|\mathrm{S}_{11}|^2_{\mathrm{req}}$ is the required return loss and equals 0.1 (-10 dB), $R(x)$ is the ramp function, which is equal to x when x>0 and is equal to 0 when x<0. $\left|\frac{S_{21}}{S_{31}}\right|^2_{req}$ and $Arg\left(\frac{S_{21}}{S_{31}}\right)_{req}$ are the required

power ratio and phase difference derived from simulated results for the combined VP and HP components. They are functions of frequency. $\left(\frac{S_{21}}{S_{31}}\right)_{req}$ is given by:

$$\left(\frac{S_{21}}{S_{31}}\right)_{req} = \frac{\overline{E_v}/\overline{E_h}}{g_2(f)g(f)}, \tag{9.8}$$

where $\overline{E_v}/\overline{E_h}$ is the required average ratio between electric far field with V-pol and H-pol in all azimuthal directions and is equal to $1\angle -90°$ for circular polarization. Coefficients a_1 to a_4 in (9.7) are weighting parameters for each optimization goals. Here we set $a_1 = a_2 = 2$, $a_3 = a_4 = 1$. The optimization process is to minimize the value of F.

The impedance and electrical length of each transmission line is optimized by a process similar to particle swarm optimization (PSO) algorithm with random optimization (RO) algorithm in Advanced Design System (ADS). The process is described in Figure 9.18. In this application, the number of iterations m = 50 and when the optimization process finishes, the global optimal result and its corresponding $\vec{x}_{\text{loc}}$ are obtained. The feeding network is implemented by microstrip line and is printed on 0.81 mm thick PCB boards with substrate RO4003C ($\varepsilon_r = 3.55$, $\tan\delta = 0.0027$). The width and length of each microstrip line are calculated from its corresponding optimized impedance and electrical length, and the resistance of resistors R_1, R_2 is set to the value of 150 Ω and 300 Ω due to their availabilities. The geometry of the feeding network is shown in Figure 9.1(c), and the parameters including the width and length of the microstrip line is described in Table 9-1.

The magnitude and phase of the optimized and target S_{21}/S_{31} as a function of frequency are shown in Figure 9.19. The optimized feeding network has less than 0.7 dB deviation from the goal in the ratio of dividing power for two polarization components for the entire band (1.2 to 2 GHz). The return loss and resistive loss of the optimized feeding network when connected with

the VP and HP components is depicted in Figure 9.20 (a) and (b). Both return loss and resistive loss satisfy the requirement of 10 dB and less than 20% for all operating frequencies.

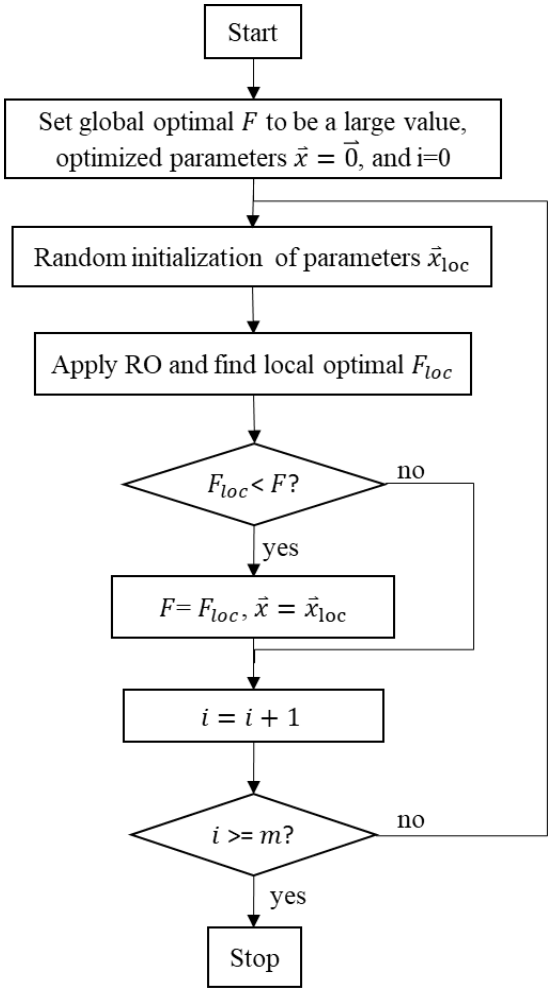

Figure 9.18. Optimization process for the feeding network.

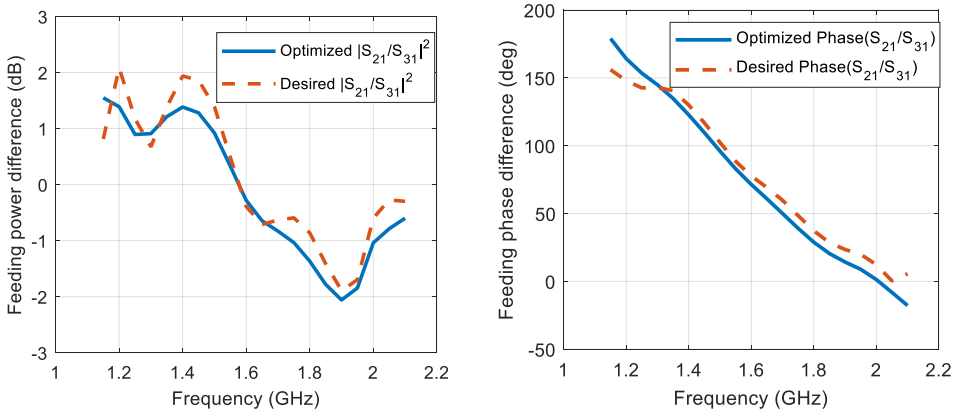

(a) (b)

Figure 9.19. The magnitude (a) and phase (b) for $\frac{S_{21}}{S_{31}}$ as functions of frequency comparison between the simulated result after optimization and the desired one (optimal circular polarization).

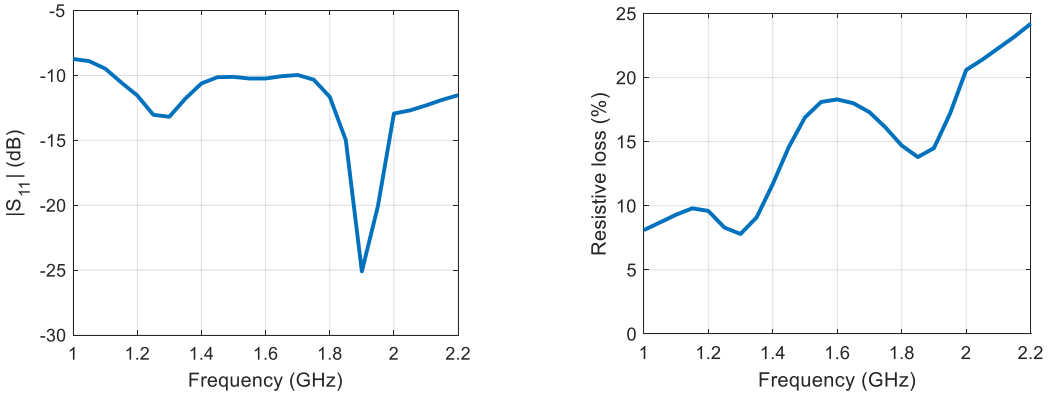

(a) (b)

Figure 9.20. The simulated (a) return loss $|S_{11}|^2$ and (b) resistive loss of the feeding network by circuit model in ADS after optimization.

9.3 Antenna simulation and measurement results

The optimized feeding network together with the VP and HP radiating components are simulated with full-wave simulation software AnsysEM (HFSS). It is fabricated and measured as well. The antenna is printed on printed circuit board (PCB) with substrate RO4003C (ε_r = 3.55, tanδ = 0.0027) and is fed with an SMA connector. The pictures of the exterior and inner structure are shown in Figure 9.21. The HP radiating components are on the inner side of the square box, and the feeding network is inside the box. The simulated and measured return loss for the entire antenna is depicted in Figure 9.22 (a). Good agreement is observed between simulation and measurement and the 10 dB return loss bandwidth is about 66.7% (1.05 to 2.1 GHz) from measurement result. Figure 9.22 (b) demonstrates the simulated radiation efficiency (only

considering resistive loss) and total efficiency (including both resistive loss and return loss). The resistive loss in full-wave simulation is higher than that from circuit simulation because the resistive loss in radiating element is not included in the circuit simulation. It is shown that the radiation efficiency is above 80 % and the total efficiency is above 70 % for the entire band from 1.2 to 2 GHz.

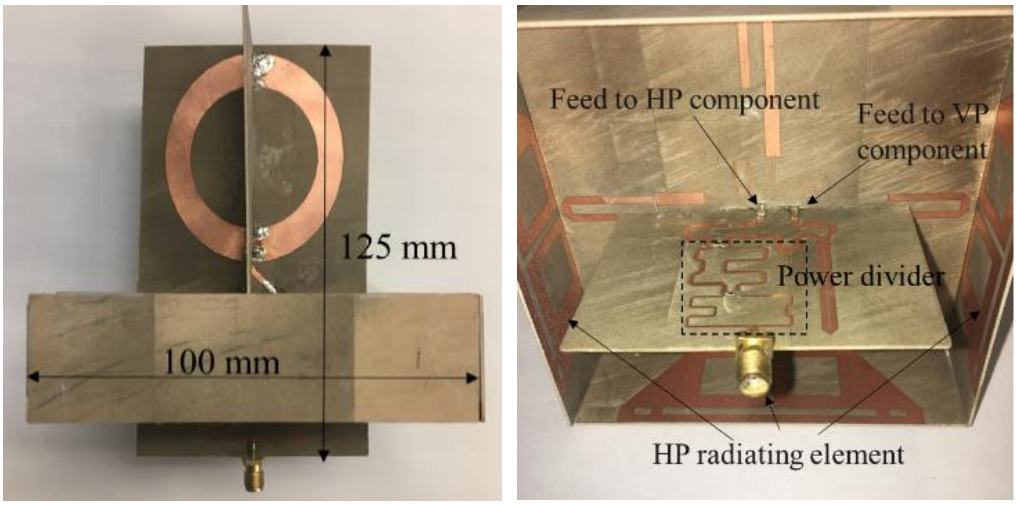

(a) (b)

Figure 9.21. Picture of (a) exterior and (b) inner structure of the proposed CP antenna.

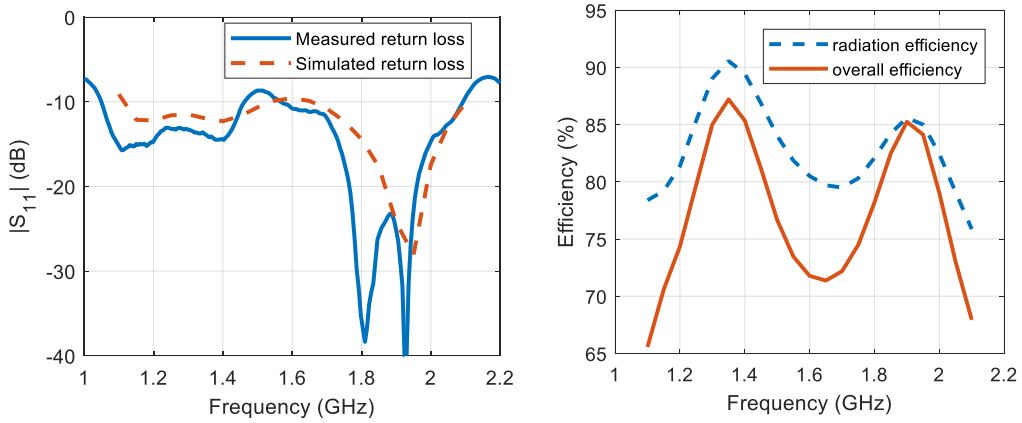

(a) (b)

Figure 9.22. (a) The simulated and measured $|S_{11}|$ and (b) the simulated radiation efficiency and overall efficiency for the proposed CP antenna.

The antenna's gain and radiation pattern in azimuth plane are measured in the anechoic chamber of the University of Michigan. To measure the circular polarized gain of this antenna, a linear polarized (LP) antenna with known gain is used as the receiver. The received VP and HP E-fields are measured in the same location, and the total E-field is the sum of both VP and HP E-fields, then by decomposing the total field into RHCP and LHCP components, the corresponding RHCP and LHCP gain can be obtained. The realized gain of this antenna for both RHCP and LHCP in azimuth plane for different frequencies are shown in Figure 9.23. Good agreement can be observed between simulated and measured results. The gain variations for RHCP are 1.3 dB and 1.8 dB at 1.3 GHz and 1.9 GHz respectively.

In Figure 9.24 (a), the solid and dash line represent the RHCP and LHCP gain averaged over all azimuth angles and the upper or lower bar denote the mean value plus or minus the standard deviation of gains for all azimuth angles at that frequency ($\mu_{gain} \pm \sigma_{gain}$). The average realized RHCP gain for all azimuth angles and frequency within the operating band is about -0.99 dBi and the peak gain is 0.9 dBi at 1.3 GHz. The isolation between the RHCP and LHCP averaged over all azimuth angles is more than 20 dB for frequencies larger than 1.25 GHz. The measured and simulated axial ratio results are depicted in Figure 9.24 (b). The upper and lower bars for measurement data denote the mean AR plus and minus the standard deviation of AR of all azimuth angles of one frequency ($\mu_{AR} \pm \sigma_{AR}$). The measured axial ratio averaged over azimuth directions is less than 2 dB for frequencies from 1.25 GHz to 2.15 GHz, and is less than 3 dB for frequencies from 1.215 GHz to 2.2 GHz (~57.7 % bandwidth). The usable bandwidth that includes the 10 dB return loss bandwidth and 3 dB axial ratio bandwidth on azimuth plane is 53.4% from 1.215 GHz to 2.1 GHz. The simulated radiation pattern for elevation plane is shown in Figure 9.25. It shows

the antenna pattern remains unchanged with frequency, and maximum RHCP gain occurs at θ=90º as desired.

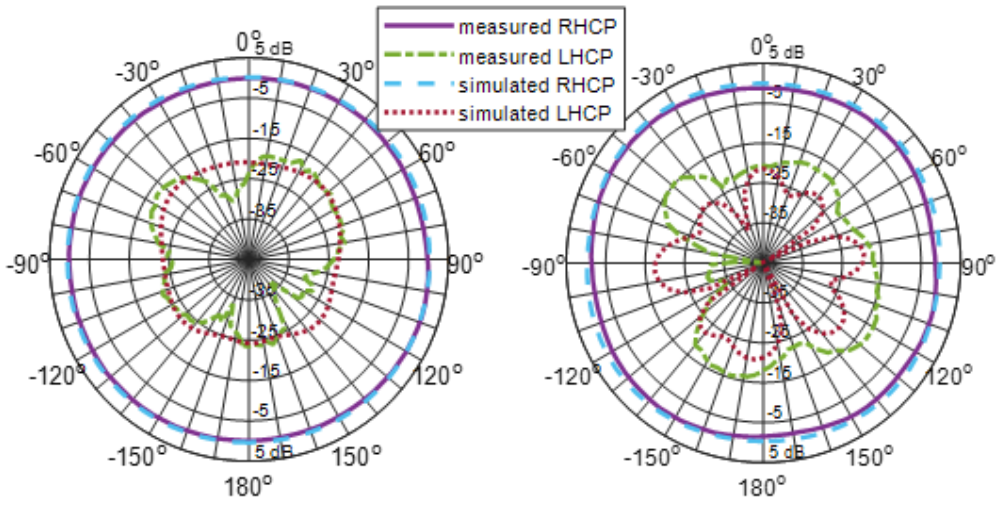

(a) (b)

Figure 9.23. The simulated and measured realized gain of RHCP and LHCP in azimuthal plane (x-y plane) for (a) 1.3 GHz, and (b) 1.9 GHz.

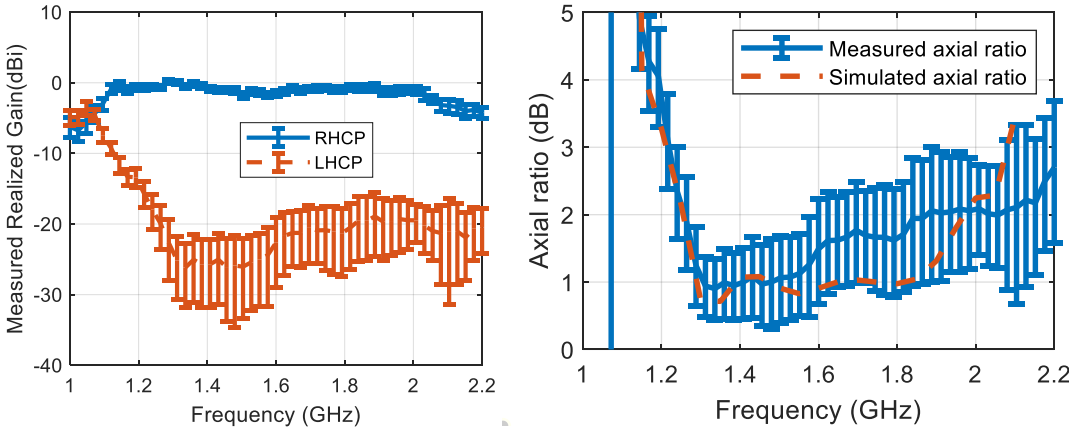

(a) (b)

Figure 9.24. (a) The measured realized gain of RHCP and LHCP in azimuthal plane (x-y plane) and (b) axial ratio as a function of frequency.

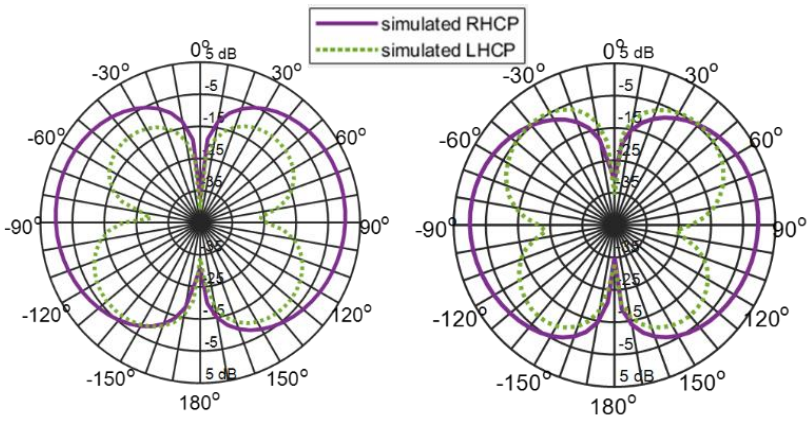

(a) (b)

Figure 9.25. The simulated realized gain of RHCP and LHCP in elevational plane (x-z plane) for (a) 1.3 GHz, and (b) 1.9 GHz.

Table 9 - 3. Comparison of different broadband omnidirectional CP antennas

Antenna	Dimension in term of wavelength of lowest operating frequency	Antenna type	Usable bandwidth	Maximum Gain and its corresponding elevation angle	Minimum efficiency within the band
[69]	0.32λ×0.32λ×0.26λ	DRA with wave polarizer	22%	1.48 dBi at 90º	84%
[70]	0.91λ×0.91λ×0.44λ	DRA with wave polarizer	41%	6.3 dBi at 30º	Not mentioned
[71]	0.92λ×0.92λ×0.18λ	Excitation of Two Orthogonal Circular TE_{21} Modes	58%	2 dBi at 50º	63%
[76]	0.63λ×0.63λ×0.11λ	Combination of VP and HP radiators	51.7%	1 dBi at 125º	Not mentioned
[77]	0.5λ×0.5λ×0.07λ	Combination of VP and HP radiators	31.3%	0.5 dBi at 90º	85%
This work	**0.4λ×0.4λ×0.5λ**	**Combination of VP and HP radiators**	**53.4%**	**0.9 dBi at 90º**	**72%**

The comparison between the proposed antenna and other broadband omnidirectional CP antennas is shown in Table III. Compared to other antenna designs in literature, the proposed antenna has the largest usable bandwidth for antennas whose maximum gain is on horizontal plane and has the most compact dimensions in azimuth plane for antennas with more than 30%

bandwidth. Therefore, the proposed antenna is favorable in applications that require omnidirectional CP on horizontal plane.

9.4 Conclusion

This chapter proposes a broadband omnidirectional circularly polarized antenna based on two dissimilar wideband VP and HP radiating components and a feeding network with a dedicated optimized asymmetric and frequency-dependent broadband power divider. Systematic analysis is performed for the asymmetric power divider and its ability of manipulating power dividing ratio as a function of frequency is investigated. An optimization process particle swarm optimization (PSO) algorithm is presented to obtain the optimal power divider for this application. The final design of antenna is simulated, fabricated and measured. The proposed antenna has an effective bandwidth (overlapping of 10 dB return loss bandwidth and 3 dB AR bandwidth) of 53.4% and average antenna gain of -1 dBi for all azimuthal angles and frequencies within the band. This antenna has the potential for application in next generation wireless communication and advanced bistatic radar systems that require omnidirectional CP antennas.

Chapter 10 Conclusion

10.1 Summary

This thesis presents many applications of electromagnetics for autonomous vehicles and demonstrates novel solutions to some existing problems related to electromagnetics for autonomous vehicles. In particular, three EM related areas for autonomous vehicles are studied: the automotive radar, the vehicular communication channel modeling, and antenna design.

In this thesis, the automotive radar related research includes the asymptotic numerical simulation approaches fast wideband PO and GO-PO, the MMW radar backscattering models for road surfaces from near grazing incidence, statistical models for the RCS of commonly seen traffic targets to enable real-time radar signal simulation, a fast multiple-source angle-of-arrival estimation algorithm and the radar target classification algorithms based on machine learning approaches. The proposed fast wideband PO methods and GO-PO methods can efficiently and accurately simulate the radar response for electrically very large targets, and provide the ability to quantitively study the radar response from targets with different parameters (e.g. weight and height for a pedestrian).

The radar backscattering from road surfaces are divided into two categories: surface scattering and volumetric scattering. The surface scattering is studied by Monte-Carlo simulations of many randomly generated dielectric rough surface with full-wave simulation software HFSS. In each simulation, the periodic boundary condition is enforced, and the tangential near fields are

collected. The scattered far field then is calculated from the tangential near fields by near-field far-field transformation. Finally, the backscattering coefficients with different polarizations are modeled as reduced functions of the rough surfaces' statistical features (RMS height and correlation length), dielectric constant and incident angle. The volumetric scattering is studied by measurement data and semi-empirical model with radiative transfer function.

By applying the PO or GO-PO method, the RCS of many traffic targets including pedestrians, vehicles and other targets are obtained. Because the RCS values fluctuate a lot with incident angle and frequency, the statistical information of the RCS for different types of targets are summarized. For advanced automotive radar like MIMO radar or imaging radar, the RCS of different parts of the radar targets are simulated and generalized into the statistical models. The entire radar target is modeled as a points cloud with the RCS of each point as a Gamma random variable. The statistical models of the targets then are applied in the real-time radar simulations. By using the parallel computing technique with GPU, one frame of MIMO radar simulation for all channels with 1.5 million data from 100 scatterers takes less than 100 ms to run on an ordinary PC (CPU: intel i7-7700, GPU: Nvidia GTX 1060).

Multiple-source AOA estimation is critical in MIMO radar signal processing when there are more than one targets with the same radial speed and range with respect to the radar. This thesis presents an analytic iterative multiple-source AOA estimation algorithm, which is much more efficient compared to many classical AOA estimation algorithm including MUSIC and ML. Besides, this approach doesn't require the knowledge of number of sources and can be applied in coherent signals and even single-snapshot condition.

Radar target classification can provide better reliability to autonomous driving compared to the state-of-art target classification methods based on cameras or lidars since the radar is more

robust than cameras or lidars under increment weather condition. Four radar target classification models are developed to be applied in different scenarios using different types of radar: the statistical RCS and time-domain RCS-based models can be applied to traditional radars at both short and long range, and the 2D/3D radar image-based models require a shorter range targets and a radar with imaging capability, but can provide much better classification accuracy.

The EM wave will not be totally blocked by cylindrical shape object even in MMW band due to the refraction. While the field scattering for infinite-long cylinder and the far field scattering for finite-length cylinder have been well-studied, the analysis of the near field scattering of a finite-length cylinder with a near-field point source has not been reported yet. This thesis provides a thorough analysis on the MMW channel model when the LoS is blocked by a cylindrical shape object regardless the position of transmitter and receiver. The channel model is reduced into an artificial neural network model for convenient usage. In the forest environment, the wave scattering between tree trunks is approximated as a 2D scattering problem. The multiple scatterings between cylinders have been studied analytically, and finally the path loss through a forest is modeled as functions of tree density, foliage depth and the mean radius of tree trunk.

In the last part of the thesis, two broadband (bandwidth > 50%) omnidirectional antenna designs are discussed. The first design is a compact horizontally polarized antenna, which contains four folded dipole radiators and utilizing their mutual coupling to enhance the bandwidth. The second one is a circularly polarized antenna. It is composed of one ultra-wide-band monopole, the compact HP antenna and a dedicatedly optimized asymmetric power divider-based feeding network. The asymmetric power divider is optimized by swarm particle optimization, and it has about 53% overlapping bandwidth for both impedance and axial ratio with peak RHCP gain of 0.9 dBi.

Bibliography

[1] A. Y. S. Lam, J. J. Q. Yu, Y. Hou and V. O. K. Li, "Coordinated Autonomous Vehicle Parking for Vehicle-to-Grid Services: Formulation and Distributed Algorithm," in *IEEE Transactions on Smart Grid*, vol. 9, no. 5, pp. 4356-4366, Sept. 2018.

[2] David Silver, "Waymo Has the Most Autonomous Miles, By A Lot", https://www.forbes.com/sites/davidsilver/2018/07/26/waymo-has-the-most-autonomous-miles-by-a-lot/#64903227ee53

[3] C. Ilas, "Electronic sensing technologies for autonomous ground vehicles: A review," *2013 8th International Symposium on advanced Topic in Electrical Engineering (ATEE)*, Bucharest, 2013, pp. 1-6.

[4] H. H. Meinel, "Automotive Millimeterwave Radar History and present Status," *1998 28th European Microwave Conference*, Amsterdam, Netherlands, 1998, pp. 619-629.

[5] J. Wenger, "Automotive radar - status and perspectives," *IEEE Compound Semiconductor Integrated Circuit Symposium, 2005. CSIC '05.*, Palm Springs, CA, USA, 2005, pp. 4 pp.-.

[6] R. H. Rasshofer, "Functional requirements of future automotive radar systems," *2007 European Radar Conference*, Munich, 2007, pp. 259-262.

[7] M. Schneider, "Automotive Radar – Status and Trends", Proc. German Microwave Conference GeMiC, pp. 144-147, Ulm, Germany, April 2005.

[8] M. Steinhauer, H. Ruob, H. Irion and W. Menzel, "Millimeter-Wave-Radar Sensor Based on a Transceiver Array for Automotive Applications," in *IEEE Transactions on Microwave Theory and Techniques*, vol. 56, no. 2, pp. 261-269, Feb. 2008.

[9] M. Lee and Y. Kim, "Design and Performance of a 24-GHz Switch-Antenna Array FMCW Radar System for Automotive Applications," in *IEEE Transactions on Vehicular Technology*, vol. 59, no. 5, pp. 2290-2297, Jun 2010.

[10] J. Hasch, E. Topak, R. Schnabel, T. Zwick, R. Weigel and C. Waldschmidt, "Millimeter-Wave Technology for Automotive Radar Sensors in the 77 GHz Frequency Band," in *IEEE Transactions on Microwave Theory and Techniques*, vol. 60, no. 3, pp. 845-860, March 2012.

[11] Inwoo Park, "Autonomous driving, Age of ADAS: Invest in sensor market", https://www.miraeassetdaewoo.com/bbs/download/2044977.pdf?attachmentId=2044977

[12] W. T. Buller, "Benchmarking Sensors for Vehicle Computer Vision Systems", http://mtri.org/automotivebenchmark.html

[13] J. Choi, V. Va, N. Gonzalez-Prelcic, R. Daniels, C. R. Bhat and R. W. Heath, "Millimeter-Wave Vehicular Communication to Support Massive Automotive Sensing," in *IEEE Communications Magazine*, vol. 54, no. 12, pp. 160-167, December 2016.

[14] M. Gerla, E. Lee, G. Pau and U. Lee, "Internet of vehicles: From intelligent grid to autonomous cars and vehicular clouds," *2014 IEEE World Forum on Internet of Things (WF-IoT)*, Seoul, 2014, pp. 241-246.

[15] S.K. Bhoi, and P. M. Khilar. "Vehicular communication: a survey." *IET networks* 3, no. 3 pp. 204-217. 2013.

[16] V. Va, T. Shimizu, G. Bansal, and R. W. Heath Jr., "Millimeter wave vehicular communications: A survey," *Foundations and Trends in Networking*, vol. 10, no. 1, 2016.

[17] S. K. Yong and C.-C. Chong. "An Overview of Multigigabit Wireless through Millimeter Wave Technology: Potentials and Technical Challenges". *EURASIP Journal on Wireless Communications and Networking*, 2007:1–10, 2007.

[18] F. Urlaby and D. Long, *Microwave Radar and Radiometric Remote Sensing*. Ann Arbor, MI, USA: Univ. of Michigan Press, 2014.

[19] V. Winkler, "Range Doppler detection for automotive FMCW radars," *2007 European Radar Conference*, Munich, 2007, pp. 166-169.

[20] A. Meta, P. Hoogeboom and L. P. Ligthart, "Signal Processing for FMCW SAR," in *IEEE Transactions on Geoscience and Remote Sensing*, vol. 45, no. 11, pp. 3519-3532, Nov. 2007.

[21] Kai-Bor Yu and D. J. Murrow, "Adaptive digital beamforming for angle estimation in jamming," in *IEEE Transactions on Aerospace and Electronic Systems*, vol. 37, no. 2, pp. 508-523, April 2001.

[22] K. Schuler, M. Younis, R. Lenz and W. Wiesbeck, "Array design for automotive digital beamforming radar system," *IEEE International Radar Conference, 2005.*, Arlington, VA, 2005, pp. 435-440.

[23] W. C. Gibson, *The Method of Moments in Electromagnetics*, 1st ed. London, U.K.: Chapman & Hall, 2008.

[24] J. M. Jin, *The finite element method in electromagnetics*. John Wiley & Sons; 2015.

[25] D. M. Sullivan, *Electromagnetic simulation using the FDTD* method. John Wiley & Sons, 2013.

[26] J. S. Asvestas, "The physical optics method in electromagnetic scattering." *Journal of Mathematical Physics* vol. 21, no. 2, pp. 290-299. 1980.

[27] F. Obelleiro, M. G. Araujo, and J. L. Rodriguez, "Iterative physical-optics formulation for analyzing large waveguide with lossy walls," *Microw. Opt. Tech. Lett.*, vol. 28, no. 1, pp. 21–26, Jan. 2001.

[28] M. Vahidpour and K. Sarabandi, “Millimeter-wave doppler spectrum of walking bodies,” *IEEE Trans. Geosc. Remote Sensing*, vol. 50, no. 7, pp. 2866–2879, Jul. 2012.

[29] H. Ling, R. -. Chou and S. -. Lee, "Shooting and bouncing rays: calculating the RCS of an arbitrarily shaped cavity," in *IEEE Transactions on Antennas and Propagation*, vol. 37, no. 2, pp. 194-205, Feb. 1989.

[30] Y. B. Tao, H. Lin, and H. J. Bao, “GPU-based shooting and bouncing ray method for fast RCS prediction,” *IEEE Trans. Antennas Propag.*, vol. 58, no. 2, pp. 494–502, 2010.

[31] R. G. Kouyoumjian and P. H. Pathak, “A uniform geometrical theory of diffraction for an edge in a perfectly conducting surface,” *Proc. IEEE*, vol. 62, pp. 1448-1461, Nov. 1974.

[32] P. H. Pathak, G. Carluccio and M. Albani, "The Uniform Geometrical Theory of Diffraction and Some of Its Applications," in *IEEE Antennas and Propagation Magazine*, vol. 55, no. 4, pp. 41-69, Aug. 2013.

[33] Gustafsson, F. Slip-based estimation of tire-road friction. *Automatica* 1997, no. 33, pp. 1087–1099.

[34] J. J. C. Aguilar, J. A. C. Carrillo, A. J. G. Fernandez, and E. C. Acosta, “Robust road condition detection system using in-vehicle standard sensors,” *Sensors*, vol. 15, no. 12, pp. 32056–32078, 2015.

[35] C. Ahn, H. Peng and H. E. Tseng, "Robust Estimation of Road Frictional Coefficient," in *IEEE Transactions on Control Systems Technology*, vol. 21, no. 1, pp. 1-13, Jan. 2013.

[36] J. Casselgren, M. Sjödahl, and J. LeBlanc, "Angular spectral response from covered asphalt," *Appl. Opt.* 46, pp. 4277-4288, 2007.

[37] Y. Sato, A. D. Kobay, I. Kageyama, K. Watanabe, Y. Kuriyagawa, and Y. Kuriyagawa, “Study on recognition method for road friction condition,” *JSAE Trans.*, vol. 38, pp. 51–56, 2007.

[38] V. V. Viikari, T. Varpula and M. Kantanen, "Road-Condition Recognition Using 24-GHz Automotive Radar," in *IEEE Transactions on Intelligent Transportation Systems*, vol. 10, no. 4, pp. 639-648, Dec. 2009.

[39] E. S. Li and K. Sarabandi, "Low grazing incidence millimeter-wave scattering models and measurements for various road surfaces," in *IEEE Transactions on Antennas and Propagation*, vol. 47, no. 5, pp. 851-861, May 1999.

[40] R. O. Schmidt, “Multiple emitter location and signal parameter estimation,” *IEEE Trans. Antennas Propag.*, vol. 34, no. 3, pp. 276–280, Mar. 1986.

[41] T.-J. Shan, M. Wax, and T. Kailath, “On spatial smoothing for direction-of-arrival estimation of coherent sources,” *IEEE Trans. Acoust., Speech, Signal Processing*, vol. ASSP-33, pp. 806-811, 1985.

[42] R. Roy and T. Kailath, “ESPRIT-estimation of signal parameters via rotational invariance techniques,” IEEE *Trans. Acoust., Speech, Signal Process.*, vol. 37, no. 7, pp. 984–995, July 1989.

[43] F. Athley, "Threshold region performance of maximum likelihood direction of arrival estimators," in *IEEE Trans. Signal Process*, vol. 53, no. 4, pp. 1359-1373, April 2005.

[44] Bartsch, A., Fitzek, F., and Rasshofer, R. H.: Pedestrian recognition using automotive radar sensors, *Adv. Radio Sci.*, 10, 45-55, 2012.

[45] J. I, Garber ED, Moses RL. “Radar target identification using the bispectrum: a comparative study”. *IEEE Transactions on Aerospace and Electronic Systems.* 31(1):69-77. Jan 1995.

[46] M. R. Akdeniz *et al*., "Millimeter Wave Channel Modeling and Cellular Capacity Evaluation," in *IEEE Journal on Selected Areas in Communications*, vol. 32, no. 6, pp. 1164-1179, June 2014.

[47] T. S. Rappaport *et al*., "Millimeter Wave Mobile Communications for 5G Cellular: It Will Work!," in *IEEE Access*, vol. 1, pp. 335-349, 2013.

[48] M. K. Samimi and T. S. Rappaport, "3-D Millimeter-Wave Statistical Channel Model for 5G Wireless System Design," in *IEEE Transactions on Microwave Theory and Techniques*, vol. 64, no. 7, pp. 2207-2225, July 2016.

[49] E. Ben-Dor et al., “Millimeter-Wave 60 GHz Outdoor and Vehicle AOA Propagation Measurements Using a Broadband Channel Sounder,” *Proc. IEEE GLOBECOM*, Dec. 2011, pp. 1–6.

[50] G. R. MacCartney, S. Deng, S. Sun and T. S. Rappaport, "Millimeter-Wave Human Blockage at 73 GHz with a Simple Double Knife-Edge Diffraction Model and Extension for Directional Antennas," *2016 IEEE 84th Vehicular Technology Conference (VTC-Fall)*, Montreal, QC, 2016, pp. 1-6.

[51] G. R. MacCartney, T. S. Rappaport and S. Rangan, "Rapid Fading Due to Human Blockage in Pedestrian Crowds at 5G Millimeter-Wave Frequencies," *GLOBECOM 2017 - 2017 IEEE Global Communications Conference*, Singapore, 2017, pp. 1-7.

[52] Yi-Cheng Lin and K. Sarabandi, "Electromagnetic scattering model for a tree trunk above a tilted ground plane," in *IEEE Transactions on Geoscience and Remote Sensing*, vol. 33, no. 4, pp. 1063-1070, July 1995.

[53] Tsenchieh Chiu and K. Sarabandi, "Electromagnetic scattering interaction between a dielectric cylinder and a slightly rough surface," in *IEEE Transactions on Antennas and Propagation*, vol. 47, no. 5, pp. 902-913, May 1999.

[54] B. Yektakhah and K. Sarabandi, "All-directions through the wall imaging using a small number of moving omnidirectional transceivers," *2017 IEEE International Geoscience and Remote Sensing Symposium (IGARSS)*, Fort Worth, TX, 2017, pp. 2416-2419.

[55] Constantine A. Balanis, *Antenna theory: analysis and design*. John wiley & sons, 2016.

[56] M. J. Ammann and Zhi Ning Chen, "Wideband monopole antennas for multi-band wireless systems," in *IEEE Antennas and Propagation Magazine*, vol. 45, no. 2, pp. 146-150, April 2003.

[57] Jianxin Liang, C. C. Chiau, Xiaodong Chen and C. G. Parini, "Study of a printed circular disc monopole antenna for UWB systems," in *IEEE Transactions on Antennas and Propagation*, vol. 53, no. 11, pp. 3500-3504, Nov. 2005.

[58] A. M. Abbosh and M. E. Bialkowski, "Design of Ultrawideband Planar Monopole Antennas of Circular and Elliptical Shape," in *IEEE Transactions on Antennas and Propagation*, vol. 56, no. 1, pp. 17-23, Jan. 2008.

[59] A. Alford and A. G. Kandoian, "Ultrahigh-frequency loop antennas," *Electr. Eng.*, vol. 59, no. 12, pp. 843–848, Dec. 1940.

[60] C.-C. Lin, L.-C. Kuo, and H.-R. Chuang, "A horizontally polarized omnidirectional printed antenna for WLAN applications," *IEEE Trans. Antennas Propag.*, vol. 54, no. 11, pp. 3551–3556, Nov. 2006.

[61] K. Wei, Z. Zhang, Z. Feng, and M. F. Iskander, "A MNG-TL loop antenna array with horizontally polarized omnidirectional patterns," *IEEE Trans. Antennas Propag.*, vol. 60, no. 6, pp. 2702–2710, Jun. 2012.

[62] A. L. Borja, P. S. Hall, Q. Liu, and H. Iizuka, "Omnidirectional loop antenna with left-handed loading," *IEEE Antennas Wireless Propag. Lett.*, vol. 6, pp. 495–498, Feb. 2007.

[63] X. Qing and Z. N. Chen, "Horizontally polarized omnidirectional segmented loop antenna," in *Proc. 6th Eur. Conf. Antennas Propag. (EUCAP'12),* Mar. 26–30, 2012, pp. 2904–2907.

[64] X. L. Quan, R. L. Li, J. Y. Wang, and Y. H. Cui, "Development of a broadband horizontally polarized omnidirectional planar antenna and its array for base stations," *Prog. Electromagn. Res.*, vol. 128, pp. 441–456, 2012.

[65] Y. Yu, F. Jolani, and Z. Chen, "A wideband omnidirectional horizontally polarized antenna for 4G LTE applications," *IEEE Trans. Antennas Wireless Propag.*, vol. 12, pp. 686–689, Jun. 2013.

[66] B. Wang, F.-S. Zhang, L. Jiang, Q. Li, and J. Ren, "A broadband omnidirectional antenna array for base station," *Prog. Electromagn. Res.* C, vol. 54, pp. 95–101, 2014.

[67] D. Wu, M. Zhao, Y. Fan, and Y. Zhang, "A wideband 8-element omnidirectional array for wireless system," *Microw. Opt. Technol. Lett.*, vol. 49, pp. 2944–2946, Dec. 2007.

[68] T. Manabe, Y. Miura, and T. Ihara, "Effects of antenna directivity and polarization on indoor multipath propagation characteristics at 60GHz," *IEEE J. Sel. Areas Commun.*, vol. 14, no. 3, pp. 441–448, 1996.

[69] Y. M. Pan and K. W. Leung, "Wideband Omnidirectional Circularly Polarized Dielectric Resonator Antenna With Parasitic Strips," in *IEEE Transactions on Antennas and Propagation*, vol. 60, no. 6, pp. 2992-2997, June 2012.

[70] Y. M. Pan and K. W. Leung, "Wideband circularly polarized dielectric bird-nest antenna with conical radiation pattern," IEEE Trans. Antennas Propag., vol. 61, no. 2, pp. 563-570, Feb. 2013.

[71] B. Yektakhah and K. Sarabandi, "A Wideband Circularly Polarized Omnidirectional Antenna Based on Excitation of Two Orthogonal Circular TE21Modes," in *IEEE Transactions on Antennas and Propagation*, vol. 65, no. 8, pp. 3877-3888, Aug. 2017.

[72] W. W. Li and K. W. Leung, "Omnidirectional Circularly Polarized Dielectric Resonator Antenna With Top-Loaded Alford Loop for Pattern Diversity Design," in *IEEE Transactions on Antennas and Propagation*, vol. 61, no. 8, pp. 4246-4256, Aug. 2013.

[73] B. C. Park and J. H. Lee, "Omnidirectional circularly polarized antenna utilizing zeroth-order resonance of epsilon negative transmission line," IEEE Trans. Antennas Propag., vol. 59, no. 7, pp. 2717–2721, Jul. 2011.

[74] B. Li, S. Liao and Q. Xue, "Omnidirectional Circularly Polarized Antenna Combining Monopole and Loop Radiators," in *IEEE Antennas and Wireless Propagation Letters*, vol. 12, pp. 607-610, 2013.

[75] W. Lin and H. Wong, "Circularly Polarized Conical-Beam Antenna With Wide Bandwidth and Low Profile," in *IEEE Transactions on Antennas and Propagation*, vol. 62, no. 12, pp. 5974-5982, Dec. 2014.

[76] D. Yu, S. Gong, Y. Wan, Y. Yao, Y. Xu and F. Wang, "Wideband Omnidirectional Circularly Polarized Patch Antenna Based on Vortex Slots and Shorting Vias," in *IEEE Transactions on Antennas and Propagation*, vol. 62, no. 8, pp. 3970-3977, Aug. 2014

[77] H. H. Tran, N. Nguyen-Trong and H. C. Park, "A Compact Wideband Omnidirectional Circularly Polarized Antenna Using TM01Mode With Capacitive Feeding," in *IEEE Antennas and Wireless Propagation Letters*, vol. 18, no. 1, pp. 19-23, Jan. 2019.

[78] Y. Yu, Z. Shen and S. He, "Compact Omnidirectional Antenna of Circular Polarization," in IEEE Antennas and Wireless Propagation Letters, vol. 11, pp. 1466-1469, 2012.

[79] J. Wu and K. Sarabandi, "Compact omnidirectional circularly polarized antenna," IEEE Trans. Antennas Propag., vol. 65, no. 4, pp. 1550–1557, Apr. 2017.

[80] Jia, Yangqing, et al. "Caffe: Convolutional architecture for fast feature embedding." *Proceedings of the 22nd ACM international conference on Multimedia*. ACM, 2014.

[81] A, Martín, P. Barham, J. Chen, Z Chen, A. Davis, J. Dean, M. Devin et al. "Tensorflow: A system for large-scale machine learning." In *12th {USENIX} Symposium on Operating Systems Design and Implementation ({OSDI} 16)*, pp. 265-283. 2016.

[82] S. Tanaka, Y. Kim, H. Morishita, S. Horiuchi, Y. Atsumi, and Y. Ido, “Wideband planar folded dipole antenna with self-balanced impedance property,” *IEEE Trans. Antennas Propag.*, vol. 56, no. 5, pp. 1223–1228, May 2008.

[83] Christiaan Huygens, *Treatise on light*. tredition, 2012.

[84] W. B. Gordon, "High frequency approximations to the physical optics scattering integral," in *IEEE Transactions on Antennas and Propagation*, vol. 42, no. 3, pp. 427-432, March 1994.

[85] Straßer, Wolfgang. “Schnelle Kurven- und Flächendarstellung auf grafischen Sichtgeräten*” PhD thesis* (1974-04-26*)*

[86] J. R. Rossignac and A. A. G. Requicha, "Depth-Buffering Display Techniques for Constructive Solid Geometry," in *IEEE Computer Graphics and Applications*, vol. 6, no. 9, pp. 29-39, Sept. 1986.

[87] Glassner, Andrew S., ed. *An introduction to ray tracing*. Elsevier, 1989.

[88] Thibault, William C., and Bruce F. Naylor. "Set operations on polyhedra using binary space partitioning trees." In *ACM SIGGRAPH computer graphics*, vol. 21, no. 4, pp. 153-162. ACM, 1987.

[89] Ulaby, Fawwaz Tayssir, David G. Long, William J. Blackwell, Charles Elachi, Adrian K. Fung, Chris Ruf, Kamal Sarabandi, Howard A. Zebker, and Jakob Van Zyl. *Microwave radar and radiometric remote sensing*. Vol. 4, no. 5. Ann Arbor: University of Michigan Press, 2014.

[90] Sarabandi, Kamal, Eric S. Li, and Abid Nashashibi. "Modeling and measurements of scattering from road surfaces at millimeter-wave frequencies." *IEEE Transactions on Antennas and Propagation* 45, no. 11 pp. 1679-1688, 1997.

[91] Tsang, Leung, Jin Au Kong, and Kung-Hau Ding. *Scattering of electromagnetic waves: theories and applications*. Vol. 27. John Wiley & Sons, 2004.

[92] Ogilvy, J. A., and J. R. Foster. "Rough surfaces: Gaussian or exponential statistics?." *Journal of Physics D: Applied Physics* 22, no. 9: 1243, 1989.

[93] Tsang, Leung, Jin Au Kong, Kung-Hau Ding, and Chi On Ao. *Scattering of electromagnetic waves: numerical simulations*. Vol. 25. John Wiley & Sons, 2004.

[94] S.O. Rice, “Reflection of electromagnetic wave by slightly rough surfaces,” *Communication in Pure and Applied Mathematics*, vol. 4, pp. 351-378, 1951.

[95] M. Nieto-Vesperinas, “Depolarization of electromagnetic waves scattered from slightly rough random surfaces: A study by means of the extinction theorem,” *J. Opt. Soc.*, 72(5), pp. 539-547, 1982.

[96] P. Beckmann and A. Spizzichino, *The Scattering of Electromagnetic Waves from Rough Surfaces*, Pergamon, New York, 1963.

[97] Hongxia Ye and Ya-Qiu Jin, "Parameterization of the tapered incident wave for numerical simulation of electromagnetic scattering from rough surface," in *IEEE Transactions on Antennas and Propagation*, vol. 53, no. 3, pp. 1234-1237, March 2005.

[98] Pak, Kyung, Leung Tsang, Chi H. Chan, and Joel Johnson. "Backscattering enhancement of electromagnetic waves from two-dimensional perfectly conducting random rough surfaces based on Monte Carlo simulations." *JOSA A* 12, no. 11 pp. 2491-2499, 1995.

[99] Chan, Chi-Hou, S. H. Lou, Leung Tsang, and Jin Au Kong. "Electromagnetic scattering of waves by random rough surface: A finite-difference time-domain approach." *Microwave and Optical Technology Letters* 4, no. 9 pp. 355-359, 1991.

[100] L. Kuang and Y. Jin, "Bistatic Scattering From a Three-Dimensional Object Over a Randomly Rough Surface Using the FDTD Algorithm," in *IEEE Transactions on Antennas and Propagation*, vol. 55, no. 8, pp. 2302-2312, Aug. 2007.

[101] Jiangfeng Wu, "Radar Sub-surface Sensing for Mapping the Extent of Hydraulic Fractures and for Monitoring Lake Ice and Design of Some Novel Antennas" *PhD Thesis*, 2016

[102] W. H. Bragg, W. L. Bragg, "The Reflexion of X-rays by Crystals". *Proceedings of the Royal Society of London. Series A, Containing Papers of a Mathematical and Physical Character*, pp. 428-438, 1913.

[103] Park, Sung Y., and Anil K. Bera. "Maximum entropy autoregressive conditional heteroskedasticity model." *Journal of Econometrics* 150, no. 2 pp. 219-230, 2009.

[104] Tsang, L., J. A. Kong, and R. T. Shin, "Radiative Transfer Theory for Active Remote Sensing of a Layer of Nonspherical Particles," *Radio Sci.*, 19, pp. 629-642, 1984.

[105] K. Sarabandi, Class Lecture, Topic: "Radiative transfer theory", EECS 730, College of Engineering, University of Michigan, Ann Arbor, Winter, 2012.

[106] Joel Palmius, software: *MakeHuman 1.1.0*, http://www.makehumancommunity.org/ , 2016

[107] "The 3dsMax-friendly BVH release of CMU's motion capture database" https://sites.google.com/a/cgspeed.com/cgspeed/motion-capture/3dsmax-friendly-release-of-cmu-motion-database , 2009

[108] Software, Blender v2.70, https://www.blender.org/, 2014

[109] P. Swerling, "Probability of Detection for Fluctuating Targets". *ASTIA Document Number AD 80638*. March 17, 1954.

[110] D. A. Shnidman, "Expanded Swerling target models," in *IEEE Transactions on Aerospace and Electronic Systems*, vol. 39, no. 3, pp. 1059-1069, July 2003.

[111] P. Swerling "Recent developments in target models for radar detection analysis". *AGARD Avionics Tech. Symp. Proc*. 1970 May 25.

[112] Shi W, Shi XW, Xu L. “RCS Characterization of Stealth Target Using X 2 Distribution and Lognormal Distribution”. *Progress In Electromagnetics Research.* 2012.

[113] Shi W, Shi XW, Xu L. “Radar cross section (RCS) statistical characterization using Weibull distribution”. *Microwave and Optical Technology Letters*. ;55(6):1355-8. Jun. 2013.

[114] M. Sekine, T. Musha, Y. Tomita, T. Hagisawa, T. Irabu and E. Kiuchi, "Log-Weibull distributed sea clutter," in *IEE Proceedings F - Communications, Radar and Signal Processing*, vol. 127, no. 3, pp. 225-228, June 1980.

[115] A. A. Alaqeel, A. A. Ibrahim, A. Y. Nashashibi, H. N. Shaman and K. Sarabandi, "Experimental Characterization of Multi-Polarization Radar Backscatter Response of Vehicles at J -Band," in *IEEE Transactions on Intelligent Transportation Systems*, vol. 20, no. 9, pp. 3337-3350, Sept. 2019.

[116] C. Zhang and T. Chen, "Efficient feature extraction for 2D/3D objects in mesh representation," *Proceedings 2001 International Conference on Image Processing (Cat. No.01CH37205)*, Thessaloniki, Greece, pp. 935-938 vol.3, 2001.

[117] Vale, C. David, and Vincent A. Maurelli. "Simulating multivariate nonnormal distributions." *Psychometrika* 48, no. 3 pp. 465-471, 1983.

[118] Stackoverflow, “Sample from multivariate normal/Gaussian distribution in C++”,[on line] https://stackoverflow.com/questions/6142576/sample-from-multivariate-normal-gaussian-distribution-in-c, 2012.

[119] Lewandowski, Daniel, Dorota Kurowicka, and Harry Joe. "Generating random correlation matrices based on vines and extended onion method." *Journal of multivariate analysis* 100, no. 9 pp. 1989-2001, 2009.

[120] Gentle, J. E. "Cholesky Factorization." §3.2.2 in *Numerical Linear Algebra for Applications in Statistics.* Berlin: Springer-Verlag, pp. 93-95, 1998.

[121] Newey, Whitney K., and Kenneth D. West. "A simple, positive semi-definite, heteroskedasticity and autocorrelationconsistent covariance matrix.", 1986.

[122] Weisstein, Eric W. "Distribution Function." From *MathWorld*--A Wolfram Web Resource. http://mathworld.wolfram.com/DistributionFunction.html.

[123] Weisstein, Eric W. "Normal Distribution." From *MathWorld*--A Wolfram Web Resource. http://mathworld.wolfram.com/NormalDistribution.html .

[124] Unreal Engine 4, https://www.unrealengine.com/en-US/.

[125] “OpenMP C and C++ Application Program Interface", [online] https://www.openmp.org/wp-content/uploads/cspec20.pdf, 2002.

[126] Nvidia, C. U. D. A. "Nvidia cuda c programming guide." *Nvidia Corporation* 120, no. 18 : 8, 2011.

[127] T. E. Tuncer and B. Friedlander, *Classical and Modern Direction-of-Arrival Estimation*. New York, NY, USA: Elsevier, 2009.

[128] P. Hacker and B. Yang, "Single snapshot DOA estimation," *Adv. Radio Sci.* 8, no. 16, pp. 251–256, 2010.

[129] M. D. Zoltowski, G. M. Kautz, and S. D. Silverstein, "Beam space ROOTMUSIC," *IEEE Trans. Signal Process.*, vol. 41, no. 1, pp. 344–364, Feb. 1993.

[130] Han, Fang-Ming, and Xian-Da Zhang. "An ESPRIT-like algorithm for coherent DOA estimation." *IEEE Antennas and Wireless Propagation Letters* no. 4, pp. 443-446, 2005.

[131] Rife, D. C. and Boorstyn, R. R.: "Single-Tone Parameter Estimation from Discrete-Time Observations", *IEEE Trans. on Information Theory*, 20, 591–598, 1974.

[132] Rife, D. C. and Boorstyn, R. R.: "Multiple Tone Parameter Estimation from Discrete-Time Observations", *The Bell System Technical Journal*, 55, 1389–1411, 1976.

[133] I. Ziskind and M. Wax, "Maximum likelihood localization of multiple sources by alternating projection," *IEEE Trans. Acoust., Speech, Signal Process.*, vol. 36, pp. 1560–1577, Oct. 1988.

[134] Amjadi, S. Mohammad, Mahbub Hoque, and Kamal Sarabandi. "An Iterative Array Signal Segregation Algorithm: A method for interference cancelation and multipath mitigation in complex environments." *IEEE Antennas and Propagation Magazine* 59, no. 3 pp: 16-32, 2017.

[135] Amjadi, S. Mohammad, and Kamal Sarabandi. "Superresolution DOA estimation with circular arrays using signal segregation algorithm in conjunction with a nulls-synthesis method." *IEEE Transactions on Antennas and Propagation* 66, no. 6 pp: 3108-3121, 2018.

[136] Liu, Zhang-Meng, Zhi-Tao Huang, and Yi-Yu Zhou. "An efficient maximum likelihood method for direction-of-arrival estimation via sparse Bayesian learning." *IEEE Transactions on Wireless Communications* 11, no. 10 pp. 1-11, 2012.

[137] Khan, Aftab, Stephen Wang, and Ziming Zhu. "Angle-of-arrival estimation using an adaptive machine learning framework." *IEEE Communications Letters* 23, no. 2 (2018): 294-297.

[138] Xiao, Xiong, Shengkui Zhao, Xionghu Zhong, Douglas L. Jones, Eng Siong Chng, and Haizhou Li. "A learning-based approach to direction of arrival estimation in noisy and reverberant environments." In *2015 IEEE International Conference on Acoustics, Speech and Signal Processing (ICASSP)*, pp. 2814-2818. IEEE, 2015.

[139] A. Das, W. S. Hodgkiss and P. Gerstoft, "Coherent Multipath Direction-of-Arrival Resolution Using Compressed Sensing," in *IEEE Journal of Oceanic Engineering*, vol. 42, no. 2, pp. 494-505, April 2017.

[140] M. A. Matin, A. I. Sayeed, "A Design Rule for Inset-fed Rectangular Microstrip Patch Antenna", *WSEAS Transactions on Communications*, Vol. 9, Issue. 1, pp. 63-72, Jan. 2010.

[141] R. Hussain and S. Zeadally, “Autonomous Cars: Research Results, Issues, and Future Challenges,” in *IEEE Commun. Surv. & Tut.*, vol. 21, no. 2, pp. 1275-1313, 2019.

[142] Sarabandi, K., and E.S. Li, “Polarimetric Characterization of Debris and Faults in the Highway Environment at Millimeter-Wave Frequencies,” *IEEE Trans. Antennas Propag.,* vol. 48, no. 11, pp. 1756-1768, November 2000.

[143] Sarabandi, K., and E. Li, “Characterization of Optimum Polarization for Multiple Target Discrimination Using Genetic Algorithms,” *IEEE Trans. Antennas Propag,* vol. 45, no. 12, pp. 1810-1817, December 1997.

[144] Q. Zhu, L. Chen, Q. Li, M. Li, A. Nüchter and J. Wang, "3D LIDAR point cloud based intersection recognition for autonomous driving," *2012 IEEE Intelligent Vehicles Symposium*, Alcala de Henares, 2012, pp. 456-461.

[145] S. A. Bagloee, M. Tavana, M. Asadi, and T. Oliver, “Autonomous vehicles: Challenges, opportunities, and future implications for transportation policies,” *J. Mod. Transp.*, vol. 24, no. 4, pp. 284–303, Dec. 2016.

[146] J. Van Brummelen, M. O’Brien, D. Gruyer, and H. Najjaran, “Autonomous vehicle perception: The technology of today and tomorrow,” *Transp. Res. C, Emerg. Technol.*, vol. 89, pp. 384–406, Apr. 2018.

[147] K. Eykholt, I. Evtimov, E. Fernandes, B. Li, A. Rahmati, C. Xiao, A. Prakash , T. Kohno, D.Song. “Robust physical-world attacks on deep learning visual classification”. In *Proceedings of the IEEE Conference on Computer Vision and Pattern Recognition* pp. 1625-1634. 2018.

[148] K. Kidono, T. Miyasaka, A. Watanabe, T. Naito and J. Miura, “Pedestrian recognition using high-definition LIDAR”. In *2011 IEEE Intelligent Vehicles Symposium (IV)* (pp. 405-410). June, 2011.

[149] J. Choi, S. Ulbrich, B. Lichte and M. Maurer, "Multi-Target Tracking using a 3D-Lidar sensor for autonomous vehicles," *16th International IEEE Conference on Intelligent Transportation Systems (ITSC 2013)*, The Hague, 2013, pp. 881-886.

[150] A. Zyweck and R. E. Bogner, "Radar target classification of commercial aircraft," in *IEEE Transactions on Aerospace and Electronic Systems*, vol. 32, no. 2, pp. 598-606, April 1996.

[151] Kim, K-T., and H. T. Kim. "One-dimensional scattering centre extraction for efficient radar target classification." *IEE Proceedings-Radar, Sonar and Navigation* 146, no. 3 pp. 147-158, 1999.

[152] P. Ferrazzoli, L. Guerriero and G. Schiavon, "Experimental and model investigation on radar classification capability," in *IEEE Transactions on Geoscience and Remote Sensing*, vol. 37, no. 2, pp. 960-968, March 1999.

[153] Pierce, L.E., K. Sarabandi, and F.T. Ulaby, “Application of an Artificial Neural Network in a Canopy Scattering Inversion,” *International Journal of Remote Sensing*, vol. 15, no. 16, 3263-3270, 1994.

[154] J. Ding, B. Chen, H. Liu and M. Huang, "Convolutional Neural Network With Data Augmentation for SAR Target Recognition," in *IEEE Geoscience and Remote Sensing Letters*, vol. 13, no. 3, pp. 364-368, March 2016.

[155] S. Chen and H. Wang, "SAR target recognition based on deep learning," *2014 International Conference on Data Science and Advanced Analytics (DSAA)*, Shanghai, 2014, pp. 541-547.

[156] S. Heuel and H. Rohling, "Pedestrian classification in automotive radar systems," *2012 13th International Radar Symposium*, Warsaw, 2012, pp. 39-44.

[157] S. Heuel and H. Rohling, "Two-stage pedestrian classification in automotive radar systems," *2011 12th International Radar Symposium (IRS)*, Leipzig, 2011, pp. 477-484.

[158] Bartsch, A., Fitzek, F., and Rasshofer, R. H. “Pedestrian recognition using automotive radar sensors”, *Adv. Radio Sci.*, 10, 45–55, https://doi.org/10.5194/ars-10-45-2012 , 2012.

[159] A. Krizhevsky, I. Sutskever, and G. Hinton, “Imagenet classification with deep convolutional neural networks,” in *Proc. Advances in Neural Information Processing Systems (NIPS)*, 2012, pp. 1097–1115.

[160] J. Long, E. Shelhamer, and T. Darrell, “Fully Convolutional Networks for Semantic Segmentation,” in *Proc IEEE Comput Soc Conf Comput Vis Pattern Recognit (CVPR)*, 2015.

[161] R. Girshick, J. Donahue, T. Darrell, and J. Malik, “Rich feature hierarchies for accurate object detection and semantic segmentation,” in *Proc IEEE Comput Soc Conf Comput Vis Pattern Recognit (CVPR)*, 2014.

[162] S. Kim, S. Lee, S. Doo and B. Shim, "Moving Target Classification in Automotive Radar Systems Using Convolutional Recurrent Neural Networks," *2018 26th European Signal Processing Conference (EUSIPCO)*, Rome, 2018, pp. 1482-1486.

[163] S. Lim, S. Lee, J. Yoon and S. Kim, "Phase-Based Target Classification Using Neural Network in Automotive Radar Systems," *2019 IEEE Radar Conference (RadarConf)*, Boston, MA, USA, 2019, pp. 1-6.

[164] Angelov, Aleksandar, Andrew Robertson, Roderick Murray-Smith, and Francesco Fioranelli. "Practical classification of different moving targets using automotive radar and deep neural networks." *IET Radar, Sonar & Navigation* 12, no. 10, pp. 1082-1089, 2018.

[165] J. Lombacher, K. Laudt, M. Hahn, J. Dickmann, and C. Wohler, “Semantic radar grids,” in *IEEE Intelligent Vehicles Symposium (IV)*. pp. 1170–1175, 2017.

[166] O. Schumann, M. Hahn, J. Dickmann, and C. Wohler, “Semantic ¨ segmentation on radar point clouds,” in *2018 21st International Conference on Information Fusion*. IEEE, pp. 2179–2186, 2018.

[167] X. Cai and K. Sarabandi, "A Machine Learning Based 77 GHz Radar Target Classification for Autonomous Vehicles," *2019 IEEE International Symposium on Antennas and Propagation and USNC-URSI Radio Science Meeting*, Atlanta, GA, USA, 2019, pp. 371-372.

[168] T. Wu, T. S. Rappaport, and C. M. Collins, "The human body and millimeter-wave wireless communication systems: Interactions and implications," in *2015 IEEE International Conference on Communications (ICC)*, June 2015, pp. 2423–2429

[169] S. Gabriel, R. W. Lau, and C. Gabriel, "The dielectric properties of biological tissues: III. Parametric models for the dielectric spectrum of tissues," *Physics in medicine and biology*, vol. 41, no.11, pp. 2271, 1996.

[170] S. I. Alekseev, and M. C. Ziskin, "Human skin permittivity determined by millimeter wave reflection measurements," *Bioelectromagnetics*, vol. 28, no. 5, pp. 331-339, 2007.

[171] C. Matzler, "Microwave (1–100 GHz) dielectric model of leaves," *IEEE Trans. Geosci. Remote Sensing*, vol. 32, pp. 947–949, Sept. 1994.

[172] E. Bel Kamelet al., "RCS modeling and measurements for automotive radar applications in the W band," *11th European Conference on Antennas and Propagation (EUCAP)*, Paris, 2017.

[173] Alaqeel, A., A. Ibrahim, A. Nashashibi, H. Shaman, and K. Sarabandi, "Experimental Characterization of Polarimetric Radar Backscatter Response of Vehicles at J-Band," *IEEE Trans. Intell. Transp. Syst.*, vol. 20, no. 9, pp. 3337-3350, September 2019.

[174] LeCun, Yann, and Yoshua Bengio. "Convolutional networks for images, speech, and time series." *The handbook of brain theory and neural networks* 3361, no. 10, 1995.

[175] Krizhevsky, Alex, Ilya Sutskever, and Geoffrey E. Hinton. "Imagenet classification with deep convolutional neural networks." In *Advances in neural information processing systems*, pp. 1097-1105. 2012.

[176] Marco Peixeiro, "Introduction to Convolutional Neural Networks (CNN) with TensorFlow" online resource: https://towardsdatascience.com/

[177] The MathWorks, *MATLAB Statistics and Machine Learning Toolbox*. Natick, Massachusetts, United States. Available at: https://www.mathworks.com/products/statistics.html.

[178] S. Mumtaz, K. M. S. Huq, M. I. Ashraf, J. Rodriguez, V. Monteiro,and C. Politis, "Cognitive vehicular communication for 5G," *IEEE Communications Magazine*, vol. 53, no. 7, pp. 109–117, July 2015.

[179] R. C. Daniels and R. W. Heath, "60 GHz wireless communications: Emerging requirements and design recommendations," *IEEE Vehicular Technology Magazine*, vol. 2, no. 3, pp. 41–50, Sept 2007.

[180] S. Kaul, K. Ramachandran, P. Shankar, S. Oh, M. Gruteser, I. Seskar, and T. Nadeem, "Effect of antenna placement and diversity on vehicular network communications," *4th IEEE Conf. Sensor, Mesh and Ad Hoc Comm. Networks*, pp. 112–121, 2007.

[181] M. di Bernardo, A. Salvi, and S. Santini, “Distributed consensus strategy for platooning of vehicles in the presence of time-varying heterogeneous communication delays,” *IEEE Trans. Intell. Transp. Syst.*, vol. 16, no. 1, pp. 102–112, Feb 2015.

[182] X. Cai, C. Han, and K. Sarabandi, “Phenomenology of Foliage Effect on 5G Millimeter-Wave V2V Communications,” in *Proc. of IEEE GLOBECOM*, 2018.

[183] M. A. Karam, A. K. Fung, and Y. M. M. Antar, “Electromagnetic wave scattering from some vegetation samples,” *IEEE Transactions on Geoscience and Remote Sensing*, vol. 26, no. 6, pp. 799–808, Nov 1988.

[184] Y. L. De Jong and M. H. Herben, “A tree-scattering model for improved propagation prediction in urban microcells,” *IEEE Transactions on Vehicular Technology*, vol. 53, no. 2, pp. 503–513, 2004.

[185] K. Sarabandi, *Electromagnetic scattering from vegetation canopies*. 1989.

[186] K. Sarabandi, P. F. Polatin, and F. T. Ulaby, “Monte carlo simulation of scattering from a layer of vertical cylinders,” *IEEE Transactions on Antennas and Propagation*, vol. 41, no. 4, pp. 465–475, April 1993.

[187] F. Wang and K. Sarabandi, “A physics-based statistical model for wave propagation through foliage,” *IEEE Transactions on Antennas and Propagation*, vol. 55, no. 3, pp. 958–968, March 2007.

[188] A. A. E. El-Rouby, F. T. Ulaby, and A. Y. Nashashibi, “Mmw scattering by rough lossy dielectric cylinders and tree trunks,” *IEEE Transactions on Geoscience and Remote Sensing*, vol. 40, no. 4, pp. 871–879, Apr 2002.

[189] R. F. S. Caldeirinha and M. O. Al-Nuaimi, “Microwave propagation modeling and measurement of scattering and absorption inside a canopy using the fdtd technique,” *IEEE Transactions on Antennas and Propagation*, vol. 63, no. 1, pp. 280–293, Jan 2015.

[190] Y. S. Meng, Y. H. Lee, and B. C. Ng, “Empirical near ground path loss modeling in a forest at vhf and uhf bands,” *IEEE transactions on antennas and propagation*, vol. 57, no. 5, pp. 1461–1468, 2009.

[191] J. A. Azevedo and F. E. Santos, “An empirical propagation model for forest environments at tree trunk level,” *IEEE Transactions on Antennas and Propagation*, vol. 59, no. 6, pp. 2357–2367, 2011.

[192] Attenuation in vegetation,” Int. Telecommun. Union, Geneva, Switzerland, Recommendation P.833-8, Sep. 2013. [Online]. Available: http://www.itu.int/rec/R-REC-P.833/en

[193] Weissberger, M. A., “An initial critical summary of models for predicting the attenuation of radio waves by foliage,” ECAC-TR81-101, Electromagn. Compat. Analysis Center, Annapolis, MD, 1981.

[194] R. Isermann and M. M¨unchhof, *Identification of Dynamic Systems: An Introduction with Applications*. Springer Berlin Heidelberg, 2011.

[195] P. J. Werbos et al., "Backpropagation through time: what it does and how to do it," *Proceedings of the IEEE*, vol. 78, no. 10, pp. 1550–1560, 1990.

[196] J. H. Holland et al., *Adaptation in natural and artificial systems: an introductory analysis with applications to biology, control, and artificial intelligence*. MIT press, 1992.

[197] S. Shanmuganathan and S. Samarasinghe, *Artificial neural network modelling*. Springer, 2016, vol. 628.

[198] B. Yegnanarayana, *Artificial neural networks*. PHI Learning Pvt. Ltd., 2009.

[199] A. Krizhevsky, I. Sutskever, and G. E. Hinton, "Imagenet classification with deep convolutional neural networks," F. Pereira, C. J. C. Burges, L. Bottou, and K. Q. Weinberger, Eds. Curran Associates, Inc., 2012, pp. 1097–1105. [Online]. Available: http://papers.nips.cc/paper/4824imagenet-classification-with-deep-convolutional-neural-networks.pdf.

[200] T. Mikolov, M. Karafi´at, L. Burget, J. ˇCernock`y, and S. Khudanpur, "Recurrent neural network based language model," in *Eleventh annual conference of the international speech communication association*, 2010.

[201] S. Ballantine, "Reciprocity in electromagnetic, mechanical, acoustical, and interconnected systems," *Proceedings of the Institute of Radio Engineers*, vol. 17, no. 6, pp. 927–951, June 1929.

[202] W. C. Chew, *Waves and Fields in Inhomogenous Media*. Wiley-IEEE Press, Feb. 1999.

[203] Twersky, Vic. "Multiple scattering of radiation by an arbitrary configuration of parallel cylinders." *The Journal of the Acoustical Society of America* 24, no. 1, pp: 42-46, 1952.

[204] D. E. Lawrence, "Accurate substrate integrated waveguide modeling using an exact analytical formulation for multiple cylinder scattering," *2016 IEEE MTT-S International Microwave Symposium (IMS)*, San Francisco, CA, 2016, pp. 1-4.

[205] M. Abramowitz and I. A. Stegun, *Handbook of Mathematical Functions*, Dover, 1046 pp. 1964.

[206] ANSYS, "ANSYS HFSS SBR+", [online] https://www.ansys.com/-/media/ansys/corporate/resourcelibrary/brochure/ansys-sbr-plus.pdf, 2020.

[207] Yi-Cheng Lin and K. Sarabandi, "A Monte Carlo coherent scattering model for forest canopies using fractal-generated trees," in *IEEE Transactions on Geoscience and Remote Sensing*, vol. 37, no. 1, pp. 440-451, Jan. 1999.

[208] Y. L. C. de Jong and M. H. A. J. Herben, "A tree-scattering model for improved propagation prediction in urban microcells," in *IEEE Transactions on Vehicular Technology*, vol. 53, no. 2, pp. 503-513, March 2004.

[209] F. T. Ulaby and M. A. Elrayes, “Microwave dielectric spectrum of vegetation, Part II: Dual-dispersion model,” *IEEE Trans. Geosci. Remote Sensing*, vol. GE-25, pp. 550–557, May 1987.

[210] C.Mätzler, “Microwave (1–100 GHz) dielectric model of leaves,” *IEEE Trans. Geosci. Remote Sensing*, vol. 32, pp. 947–949, Sept. 1994.

[211] J.M. Chen, and T.A. Black, “Defining leaf area index for non‐flat leaves”. *Plant, Cell & Environment*, vol. 15, pp. 421-429, 1992.

[212] S. Hur *et al*., "Proposal on Millimeter-Wave Channel Modeling for 5G Cellular System," in *IEEE Journal of Selected Topics in Signal Processing*, vol. 10, no. 3, pp. 454-469, April 2016.

[213] B. Ai *et al*., "On Indoor Millimeter Wave Massive MIMO Channels: Measurement and Simulation," in *IEEE Journal on Selected Areas in Communications*, vol. 35, no. 7, pp. 1678-1690, July 2017.

[214] T. S. Rappaport, S. Sun, R. Mayzus, H. Zhao, Y. Azar, K. Wang, G. N. Wong, J. K. Schulz, M. Samimi, and F. Gutierrez, “Millimeter wave mobile communications for 5G cellular: It will work!” *IEEE Access*, vol. 1, pp. 335–349, 2013.

[215] C.-X. Wang, F. Haider, X. Gao, X.-H. You, Y. Yang, D. Yuan, H. Aggoune, H. Haas, S. Fletcher, and E. Hepsaydir, “Cellular architecture and key technologies for 5G wireless communication networks,” *IEEE Commun.* Mag., vol. 52, no. 2, pp. 122–130, Feb. 2014.

[216] E. Dahlman, S. Parkvall, and J. Sköld, "4G: LTE/LTEAdvanced for Mobile Broadband: LTE/LTE-Advanced for Mobile Broadband", *Academic Press*, Apr. 2011.

[217] J. F. Valenzuela-Vald & eacutes "Evaluation of true polarization diversity for MIMO systems", *IEEE Trans. Antennas Propag.*, vol. 57, pp.2746 -2755 2009.

[218] Elsherbini, A., and K. Sarabandi, “Dual Polarized Coupled Sectorial Loops Antennas for UWB Applications,” *IEEE Antennas and Wireless Propagation Letters,* vol. 10*,* pp.75-78, 2011.

[219] Elsherbini, A., and K. Sarabandi, “UWB High-Isolation Directive Coupled Sectorial Loops Antenna Pair,” *IEEE Antennas and Wireless Propagation Letters,* Vol.10 pp. 215-218, 2011.

[220] Oh, J., and K. Sarabandi, “Compact, Low Profile, Common Aperture Polarization and Pattern Diversity Antennas,” *IEEE Transactions on Antennas and Propagation,* vol. 62, no. 2, pp. 569-576, Feb. 2014.

[221] Ali, F.; Urban, A.; Vossiek, M., "A high resolution 2D omnidirectional synthetic aperture radar scanner at K band," *Microwave Conference (EuMC), 2010 European* , vol., no., pp.1694,1697, 28-30 Sept. 2010.

[222] Y. Abe, S. Kidera and T. Kirimoto, “Accurate and Omni-directional UWB Radar Imaging Algorithm with RPM Method Extended to Curvilinear Scanning Model,” *IEEE Geoscience and Remote Sensing Letters*, vol. 9, no. 1, pp. 144–148, 2011.

[223] Kunpeng Wei; Zhijun Zhang; Feng, Z., "Design of a Wideband Horizontally Polarized Omnidirectional Printed Loop Antenna," *Antennas and Wireless Propagation Letters, IEEE* , vol.11, no., pp.49,52, 2012.

[224] Bukhari, H., and Sarabandi, K.: 'Ultra-wideband printed slot antenna with graded index superstrate', *IEEE Trans. Antennas Propag.*, 2013, 61, (10), pp. 5278–5282.

[225] D. Sievenpiper, D. Dawson, M. Jacob, T. Kanar, S. Kim, J. Long, and R. Quarfoth, "Experimental validation of performance limits and design guidelines for small antennas," *IEEE Trans. Antennas Propag.*, vol. 60, no. 1, pp. 8–19, Jan. 2012.

[226] Hoi-Shun Lui; Hon Tat Hui; Mook-Seng Leong, "A Note on the Mutual-Coupling Problems in Transmitting and Receiving Antenna Arrays," *Antennas and Propagation Magazine, IEEE* , vol.51, no.5, pp.171,176, Oct. 2009.

[227] RongLin Li; Wu, T.; Bo Pan; Kyutae Lim; Laskar, J.; Tentzeris, M.M., "Equivalent-Circuit Analysis of a Broadband Printed Dipole With Adjusted Integrated Balun and an Array for Base Station Applications," *Antennas and Propagation, IEEE Transactions on* , vol.57, no.7, pp.2180,2184, July 2009.

[228] B. Edward and D. Rees, "A broadband printed dipole with integrated balun," *Microw. J.*, pp. 339–344, May 1987.

[229] R. Szumny, K. Kurek and J. Modelski, "Attenuation of multipath components using directional antennas and circular polarization for indoor wireless positioning systems," *EuRAD 2007*, Munich, pp. 1680-1683. 2007.

[230] J. Oh and K. Sarabandi, "A Topology-Based Miniaturization of Circularly Polarized Patch Antennas," *IEEE Trans. Antennas Propag.*, vol. 61, no. 3, pp. 1422-1426, March 2013.

[231] D. M. Pozar, *Microwave Engineering*, 2nd ed. New York: Wiley, 1998.

[232] E. J. Wilkinson, "An N-Way Hybrid Power Divider," *IRE Trans. Microw. Theory Tech.*, vol. 8, no. 1, pp. 116-118, January 1960.

[233] M. M. Honari, L. Mirzavand, R. Mirzavand, A. Abdipour and P. Mousavi, "Theoretical Design of Broadband Multisection Wilkinson Power Dividers With Arbitrary Power Split Ratio," *IEEE Trans. Compon., Packag., Manuf. Technol*, vol. 6, no. 4, pp. 605-612, April 2016.

[234] J. Li and B. Wang, "Novel Design of Wilkinson Power Dividers With Arbitrary Power Division Ratios," I*EEE Trans. Ind. Electron.*, vol. 58, no. 6, pp. 2541-2546, June 2011.

[235] H. Oraizi and A. -. Sharifi, "Design and optimization of broadband asymmetrical multisection wilkinson power divider," *IEEE Trans. Microw. Theory Techn.*, vol. 54, no. 5, pp. 2220-2231, May 2006.

[236] X. Cai and K. Sarabandi, "A Compact Broadband Horizontally Polarized Omnidirectional Antenna Using Planar Folded Dipole Elements," *IEEE Trans. Antennas Propag.*, vol. 64, no. 2, pp. 414-422, Feb. 2016.

[237] J. Liang, C. C. Chiau, X. Chen and C. G. Parini, "Study of a printed circular disc monopole antenna for UWB systems," *IEEE Trans. Antennas Propag.*, vol. 53, no. 11, pp. 3500-3504, Nov. 2005.

[238] A. M. Abbosh and M. E. Bialkowski, "Design of Ultrawideband Planar Monopole Antennas of Circular and Elliptical Shape," *IEEE Trans. Antennas Propag.*, vol. 56, no. 1, pp. 17-23, Jan. 2008.

[239] B. M. Schiffman, "A New Class of Broad-Band Microwave 90-Degree Phase Shifters," *IRE Trans. Microw. Theory Tech*., vol. 6, no. 2, pp. 232-237, April 1958.